frontiers | Research Topics

Cutting-edge technology in veterinary medicine

Edited by
Laura Elizabeth Selmic, Mindaugas Tamosiunas and Blaz Cugmas

Published in
Frontiers in Veterinary Science

ISSN 1664-8714
ISBN 978-2-8325-5592-7
DOI 10.3389/978-2-8325-5592-7

About Frontiers

Frontiers is more than just an open access publisher of scholarly articles: it is a pioneering approach to the world of academia, radically improving the way scholarly research is managed. The grand vision of Frontiers is a world where all people have an equal opportunity to seek, share and generate knowledge. Frontiers provides immediate and permanent online open access to all its publications, but this alone is not enough to realize our grand goals.

Frontiers journal series

The Frontiers journal series is a multi-tier and interdisciplinary set of open-access, online journals, promising a paradigm shift from the current review, selection and dissemination processes in academic publishing. All Frontiers journals are driven by researchers for researchers; therefore, they constitute a service to the scholarly community. At the same time, the *Frontiers journal series* operates on a revolutionary invention, the tiered publishing system, initially addressing specific communities of scholars, and gradually climbing up to broader public understanding, thus serving the interests of the lay society, too.

Dedication to quality

Each Frontiers article is a landmark of the highest quality, thanks to genuinely collaborative interactions between authors and review editors, who include some of the world's best academicians. Research must be certified by peers before entering a stream of knowledge that may eventually reach the public - and shape society; therefore, Frontiers only applies the most rigorous and unbiased reviews. Frontiers revolutionizes research publishing by freely delivering the most outstanding research, evaluated with no bias from both the academic and social point of view. By applying the most advanced information technologies, Frontiers is catapulting scholarly publishing into a new generation.

What are Frontiers Research Topics?

Frontiers Research Topics are very popular trademarks of the *Frontiers journals series*: they are collections of at least ten articles, all centered on a particular subject. With their unique mix of varied contributions from Original Research to Review Articles, Frontiers Research Topics unify the most influential researchers, the latest key findings and historical advances in a hot research area.

Find out more on how to host your own Frontiers Research Topic or contribute to one as an author by contacting the Frontiers editorial office: frontiersin.org/about/contact

Cutting-edge technology in veterinary medicine

Topic editors

Laura Elizabeth Selmic — The Ohio State University, United States

Mindaugas Tamosiunas — University of Latvia, Latvia

Blaz Cugmas — University of Latvia, Latvia

Citation

Selmic, L. E., Tamosiunas, M., Cugmas, B., eds. (2024). *Cutting-edge technology in veterinary medicine*. Lausanne: Frontiers Media SA.

doi: 10.3389/978-2-8325-5592-7

Table of contents

frontiers | Frontiers in Veterinary Science

TYPE Case Report
PUBLISHED 03 April 2023
DOI 10.3389/fvets.2023.966513

OPEN ACCESS

EDITED BY
Laura Elizabeth Selmic,
The Ohio State University, United States

REVIEWED BY
Takeshi Aikawa,
Aikawa Veterinary Medical Center, Japan
Zbigniew Adamiak,
Vet Clinic Białystok, Poland

*CORRESPONDENCE
Masakazu Shimada
✉ masakazu42710@gmail.com

SPECIALTY SECTION
This article was submitted to Veterinary Surgery and Anesthesiology, a section of the journal Frontiers in Veterinary Science

RECEIVED 11 June 2022
ACCEPTED 20 March 2023
PUBLISHED 03 April 2023

CITATION
Shimada M, Nagashima T, Michishita M, Yazawa D and Hara Y (2023) Case report: Limb-sparing surgery of tibial chondrosarcoma with frozen autologous bone graft using liquid nitrogen in a dog. *Front. Vet. Sci.* 10:966513. doi: 10.3389/fvets.2023.966513

Case report: Limb-sparing surgery of tibial chondrosarcoma with frozen autologous bone graft using liquid nitrogen in a dog

Masakazu Shimada[1]*, Tomokazu Nagashima[2], Masaki Michishita[2], Daisuke Yazawa[1] and Yasushi Hara[1]

[1]Division of Veterinary Surgery, Department of Veterinary Science, Faculty of Veterinary Medicine, Nippon Veterinary and Life Science University, Musashino, Tokyo, Japan, [2]Division of Veterinary Pathology, Department of Veterinary Science, Faculty of Veterinary Medicine, Nippon Veterinary and Life Science University, Musashino, Tokyo, Japan

Chondrosarcoma is the second most common primary bone tumor after osteosarcoma in dogs. Chondrosarcoma has a good prognosis owing to its low metastatic rate and long survival time, even with amputation alone. However, amputation risks reducing the quality of life in patients with other orthopedic diseases of the non-affected limb, neurological diseases, or large body size. Limb-sparing surgery with frozen autologous bone grafting using liquid nitrogen allows bone quality to be maintained in the normal bone area while killing tumor cells, thereby preserving the affected limb. Thus, it is expected to maintain the quality of life. We describe herein limb-sparing surgery for tibial chondrosarcoma with frozen autologous bone graft using liquid nitrogen in an 8-year and 8-month-old castrated male bulldog weighing 29.2 kg. The patient had chondrosarcoma of the left tibia, suspected cranial cruciate ligament rupture of the right stifle, and degenerative lumbosacral stenosis. In such a case, amputation would increase the burden on the non-affected limb or spine, which could cause difficulty in walking; therefore, we performed limb-sparing surgery. Postoperatively, although a circumduction gait associated with stifle arthrodesis remained, the patient maintained the quality of life for 20 months, and the owner was satisfied with the results.

KEYWORDS

chondrosarcoma, limb-sparing surgery, liquid nitrogen autologous graft, stifle arthrodesis, dog

1. Introduction

Chondrosarcoma (CSA) is the second most common primary bone tumor after osteosarcoma, but its incidence is low at ∼10% (1, 2). CSA most commonly occurs in the nasal cavity (28.8%) and limbs (17.5%) (3). Previous reports have shown that CSA has a longer survival time and lower metastasis rate than osteosarcoma (1).

Limb-sparing surgery can maintain quality of life (QOL) in patients expected to have significant difficulty walking after limb amputation, such as patients with other orthopedic diseases in the unaffected limb, patients with neurological diseases, or patients with large body size (4, 5). There are several techniques for limb-sparing surgery in veterinary medicine; these include allogeneic cortical bone grafting, endoprosthesis, stereotactic radiosurgery and fixation, and lateral manus translation (6–9). However, there may be limitations in the availability of allogeneic cortical bone and implants to be used at different hospitals and limitations in biomechanical strength.

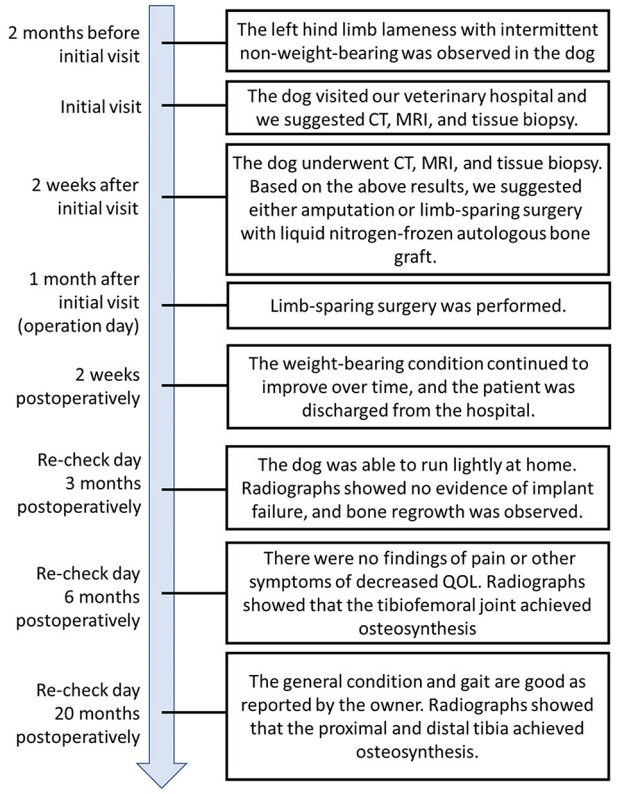

FIGURE 1
Timeline with relevant data from the episode of care. CT, computed tomography; MRI, magnetic resonance image.

The reuse of parts of bone tumors has been reported in human medicine. In recent years, limb-sparing surgery using liquid nitrogen freezing, which is readily available and minimizes the loss of bone strength, has been reported for bone tumors (10, 11). This surgery is expected to have good osteoconductive and osteoinductive capabilities with less adverse immune responses because autologous bone can be used. However, reports on the use of liquid nitrogen for freezing bone tumors in animals are rare but have been reported for the scapula in a cat and the mandible in a dog (12, 13). However, there have been no long-term postoperative observations of CSA reported to date. The burden on the unaffected limbs after amputation is a particular concern because CSA has a promising long-term outcome, which makes a focus on the QOL of the patients important.

2. Case description

An 8-year, 8-month-old castrated male bulldog weighing 29.2 kg was referred to our hospital with a primary complaint of lameness with intermittent inability to bear weight in the left hind limb for 2 months (Figure 1). The patient had also presented with lameness in the right hind limb 5 months prior that subsequently improved without treatment. The patient was able to walk in the hospital but did not want to walk for a long time. On palpation, cranial drawer and tibial compression tests of the left stifle joint were positive, and the stifle joint showed pain on extension. The cranial drawer and tibial compression tests of the right stifle joint were negative. In addition, lordosis test showed a painful reaction, and both hind limbs showed decreased conscious proprioception. Radiography revealed increased radiolucency of the proximal left tibia (Figures 2A, B). The right stifle showed mild cranial displacement of the tibia and findings suggestive of osteoarthritis (Figures 2C, D). The findings of the thoracolumbar radiograph were indicative of spondylosis deformans in several vertebrae, including the lumbosacral vertebrae. Chest radiography revealed no findings suggestive of metastasis. Based on these results, the left stifle was suspected to have a bone tumor based on bone resorption of the proximal tibia, and the right stifle was suspected to have a ruptured cranial cruciate ligament associated with osteoarthritis. Degenerative lumbosacral stenosis was also suspected in the lumbosacral joint. As such, concurrent computed tomography (CT), magnetic resonance imaging (MRI), and tissue biopsy of the left tibia, and MRI of the lumbosacral joint were recommended.

In this case, CSA was suspected as a result of biopsy. Subsequently, we report CSA of the proximal tibia treated with limb-sparing surgery using an autologous bone graft after freezing by liquid nitrogen and stifle arthrodesis that resulted in a favorable prognosis.

CT showed bone resorption in the left proximal tibia (Figure 2E). In addition, the same region showed a high signal intensity in the MR T2-weighted images (T2WI; Figure 2F). Evaluation of the lungs revealed no findings suggestive of tumor metastasis, even on CT. The intervertebral foramen of the lumbosacral joint was bilaterally narrowed during the extension on T2WI. Although tissue biopsy revealed a suspected chondroma or CSA, a definitive diagnosis could not be made due to the small amount of material collected (Figure 2G). Based on the above results, we suggested either amputation or limb-sparing surgery with liquid nitrogen-frozen autologous bone graft, and the owner requested limb-sparing surgery.

Surgery was performed one month after the initial visit. Anesthesia was induced with propofol [4 mg/kg intravenous (IV)] and midazolam hydrochloride (0.3 mg/kg IV), and endotracheal intubation was performed. Anesthesia was maintained with isoflurane and oxygen, and a ventilator ensured respiratory management. After induction of anesthesia, 0.5% bupivacaine (0.2 ml/kg) and morphine (0.1 μg/kg) were administered epidurally for analgesia, and continuous infusion of remifentanil (5–15 μg/kg/h) was administered intraoperatively. Cefmetazole sodium (25 mg/kg, IV) antibiotic was first administered ∼1 h before the incision and at 90-min intervals during the perioperative period (14).

The stifle joint was approached laterally. A skin incision was made from the greater trochanter to the tarsal joint along the femur and tibia. After incising the joint capsule, the ligaments (cruciate ligament, collateral ligament, and meniscofemoral ligament) and tendons (tendons of the long digital extensor and popliteus) of the tibiofemoral joint were removed from the femoral attachment. The patellar tendon was resected at the patellar apex (Figures 3A, B). The muscles around the proximal tibia were dissected off, and the tibia was osteotomized ∼3 cm distal to the area of high signal intensity on T2WI (Figure 3C). Tissue was collected from the medullary cavity of the distal end of the proximal

10.3389/fvets.2023.966513

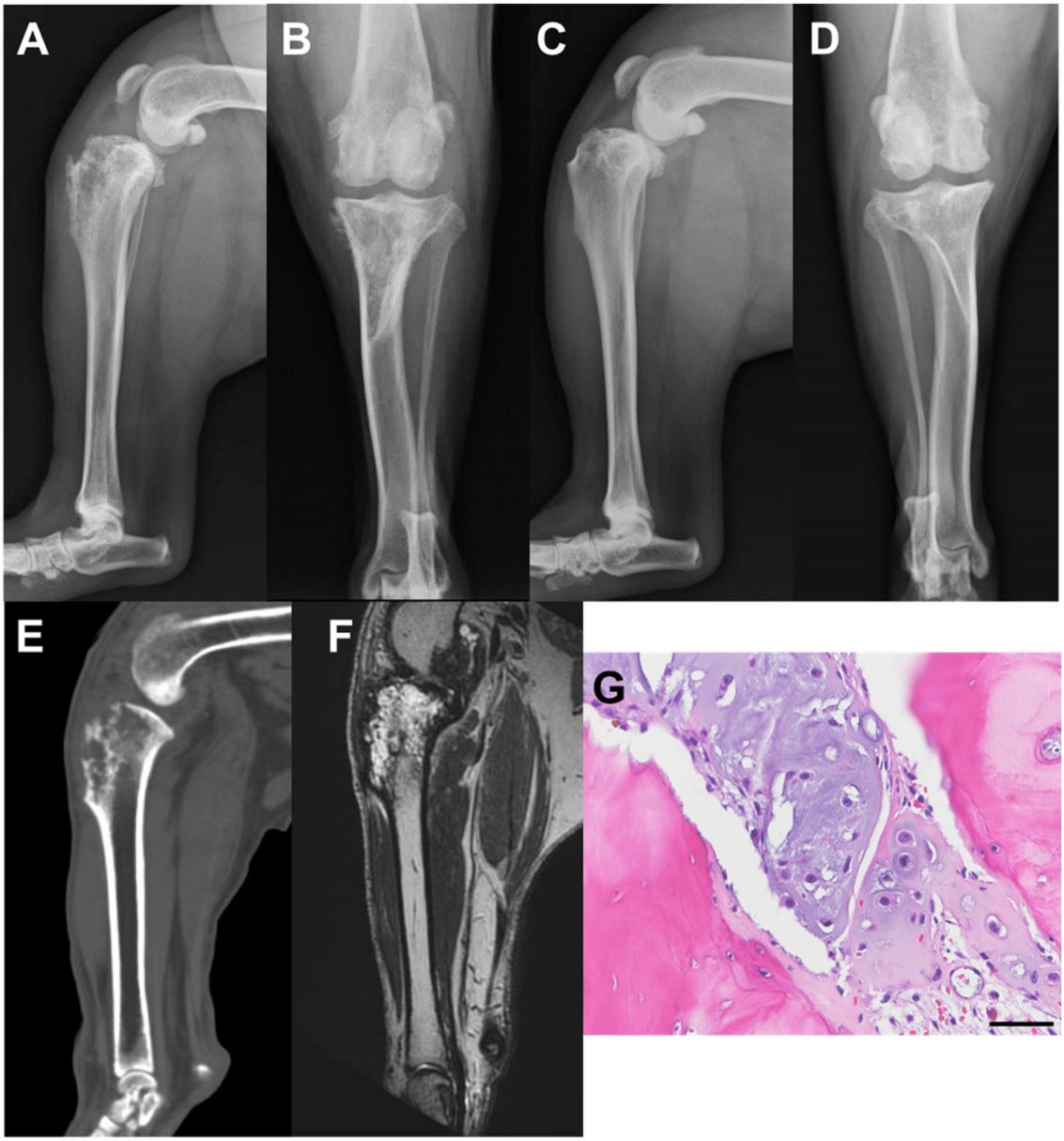

FIGURE 2
Radiographic images of the stifle joints at the time of initial examination: computed tomography (CT), magnetic resonance (MR), and histological images. **(A)** Mediolateral image of the left stifle; **(B)** Craniocaudal image of the left stifle; **(C)** Mediolateral image of the right stifle; **(D)** Craniocaudal image of the right stifle; **(E)** The left stifle joint midsagittal section on CT; **(F)** The left stifle joint midsagittal section in MR T2-weighted image; **(G)** Microscopic findings of hematoxylin-eosin staining (scale bar: 50 μm).

tibial fragment and a portion of the tumor lesion for histological diagnosis. Thereafter, the removed proximal tibia was immersed in liquid nitrogen for 20 min, at room temperature for 15 min, and in a 30°C-physiological saline solution for 15 min, according to previous reports (Figure 3D) (10). The subsequent process resulted in the collapse of the tumor lesion (tibial tuberosity) (Figure 3E). After osteotomy of the proximal articular surface of the tibia and distal articular surface of the femur, stifle arthrodesis was performed as 135 degrees of the femorotibial joint angle. A 2.0-mm diameter dynamic compression plate (Mizuho Medical Co., Ltd., Tokyo, Japan) was used to temporarily fix the proximal and distal fragments of the tibia. Subsequently, the cross-pin method was used to fix the tibiofemoral joint using a 1.6-mm diameter Kirschner wire (Johnson & Johnson, New Brunswick, NJ, USA; Figure 3F). A 3.5-mm diameter locking compression plate (Johnson & Johnson) was placed on the cranial side of the stifle, then the dynamic compression plate used for temporary fixation was removed. A 3.5-mm diameter string of pearls plate (Veterinary Orthopedic Implants, Saint Augustine, FL, USA) was placed laterally (Figure 3G). The patella was fixed to the medial femoral condyle using a 2.0 mm diameter self-tapping cortical screw (Johnson & Johnson) in lag fashion. The tibial tuberosity

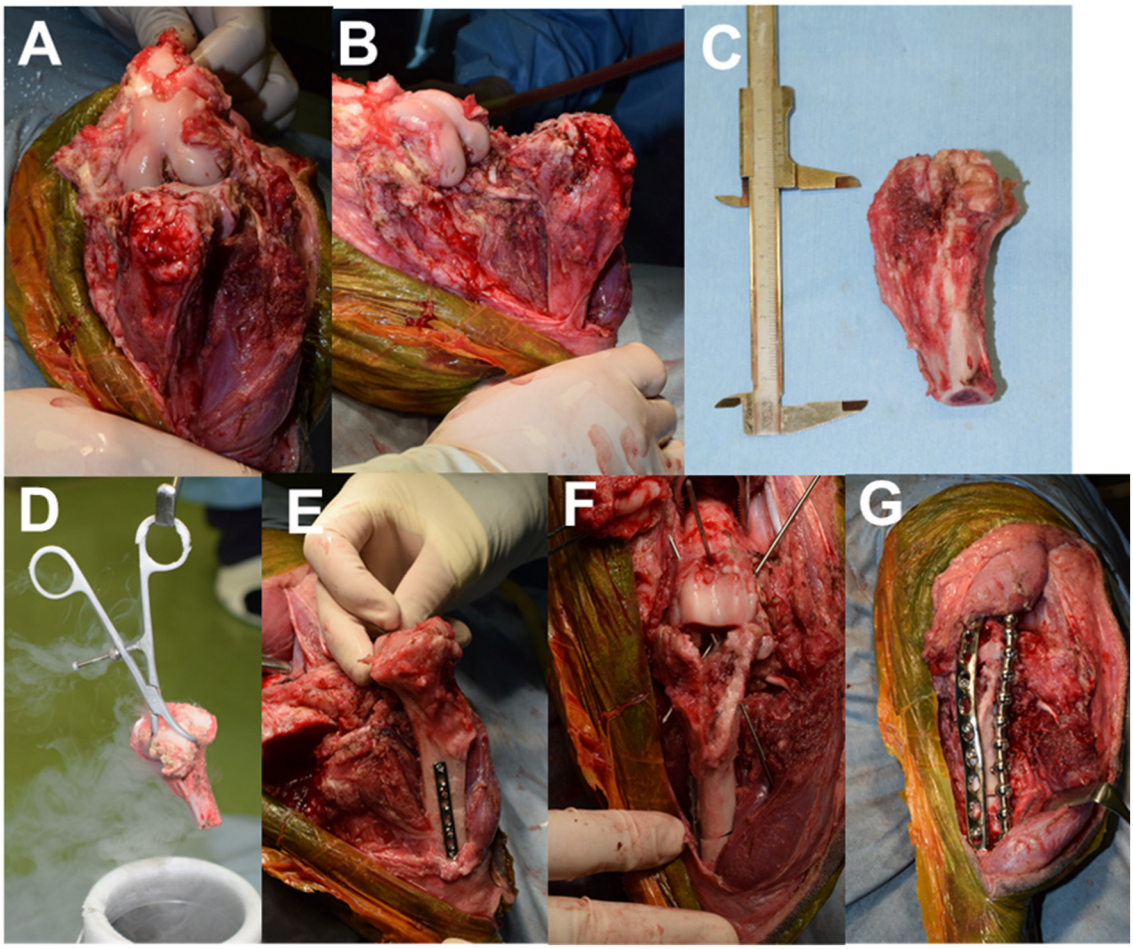

FIGURE 3
Intraoperative images. **(A)** Cranial view after removing soft tissue around the tibia; **(B)** Medial view after removing soft tissue around the tibia; **(C)** Resected proximal tibia; **(D)** proximal tibia frozen using liquid nitrogen; **(E)** Tibial tuberosity collapsed after freezing. **(F)** Fixation of the tibiofemoral joint with K-wire; **(G)** Arthrodesis with two plates.

that collapsed during the freezing process was supplemented with bioabsorbable artificial bone made of β-Tricalcium phosphate (Olympus Terumo Biomaterials Corp., Tokyo, Japan).

Postoperative radiographs are shown in Figures 4A, B. A fentanyl patch was used for postoperative analgesic management. In addition, a continuous infusion of fentanyl (1–2 μg/kg/h) and medetomidine (0.5–1 μg/kg/h) was administered for 12 h after surgery. After icing, the Robert Jones bandage technique was performed, which was continued for 1 week with daily changes. For antibiotic control, cefmetazole sodium (25 mg/kg, IV) was continued at 12-h intervals for 2 weeks. The tissue taken intraoperatively from the lesion was histologically diagnosed as CSA, which was classified as grade 1 based on previous literature (15). The tissue in the medullary cavity at the distal end of the proximal tibial fragment did not reveal any neoplastic lesions. On the third postoperative day, the weight-bearing ability of the affected limb was observed, and the patient walked around the hospital voluntarily. The weight-bearing ability continued to improve over time, and the patient was discharged from the hospital 2 weeks postoperatively.

Three months postoperatively, the patient was able to run lightly at home. Radiographic images did not show evidence of implant failure, and bone regrowth was observed; however, bone healing was not yet fully achieved. Six months postoperatively, there were no findings of pain or other symptoms of decreased QOL, metastasis, or recurrence. Radiographs showed that the tibiofemoral joint achieved osteosynthesis, and the proximal and distal tibia showed bone activity, but osteosynthesis was incomplete. Currently, 20 months have passed since the surgery, and the general condition and gait are good as reported by the owner. Radiographs showed that the proximal and distal tibia achieved osteosynthesis. Although circumduction gait remained during the postoperative period, the weight-bearing status was good, and the owner was satisfied with the results (Figures 4C, D).

3. Discussion

In the present case, CSA of the proximal tibia treated with limb-sparing surgery using frozen autologous bone graft with liquid

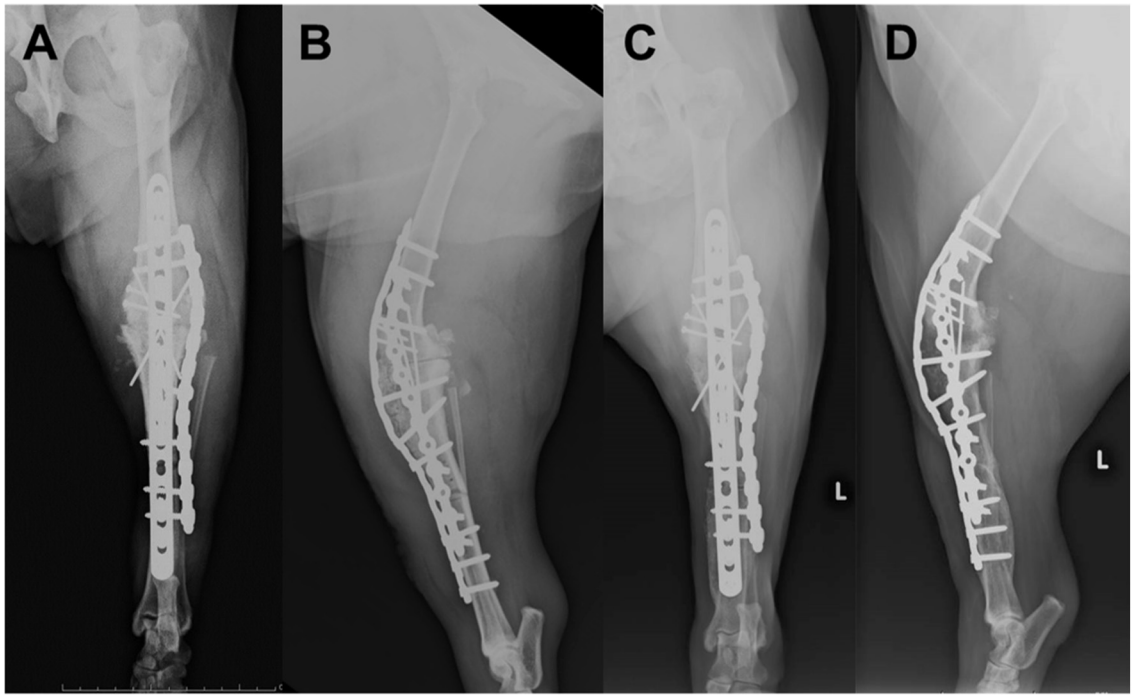

FIGURE 4
Postoperative radiographs of the left stifle; **(A)** Mediolateral image after surgery; **(B)** Craniocaudal image after surgery; **(C)** Mediolateral image at 20 months postoperatively; **(D)** Craniocaudal image at 20 months postoperatively.

nitrogen and stifle arthrodesis resulted in a favorable outcome. Postoperatively, although a circumduction gait associated with stifle arthrodesis remained, the patient could maintain a high QOL during the 20-month follow-up period, and the owner was satisfied with the results.

CSA has good prognosis owing to its low metastatic rate and long survival time, with a median survival time of 979 days, even with amputation alone (15). However, the gait changes drastically with amputation. Although hindlimb amputation has been suggested to have a smaller effect on the unaffected limb than forelimb amputation (16), changes in gait and weight-bearing capacity of the forelimb, especially the contralateral forelimb; increase in weight-bearing capacity of the contralateral hindlimb; increase in lateral flexion of the spine; and extension of the lumbosacral joint have been observed after hindlimb amputation (16–18). In the current case, cranial cruciate ligament rupture of the right stifle joint was suspected, and degenerative lumbosacral stenosis was also present. It was predicted that amputation was associated with a risk of postoperative gait disturbance due to the progression of stifle osteoarthritis in the contralateral limb and an increase in the burden of lumbosacral disease. In a previous case of stifle arthrodesis treated using a frozen cortical bone allograft for CSA in a German Shepherd dog, while circumduction gait persisted during the 17-month postoperative follow-up period, the patient could use the affected limb and had an excellent outcome (19). In the present study, the patient could use the affected limb for an extended period (20 months) after surgery, QOL was maintained, and the owner was satisfied with the outcomes. However, there is a lack of research on gait changes caused by stifle arthrodesis; therefore, further long-term follow-up studies on patient gait are needed.

CSA shows high water content and signal intensity on T2WI (20, 21). In the present case, preoperative T2WI imaging was used to localize the tumor. Autoclave and pasteurization methods can be used to reuse bone from tumor sites in humans; however, these techniques require special equipment and strict temperature control, and there are concerns about bone fragility and loss of osteoinductive capacity (11, 22). The liquid nitrogen freezing method used in this study has been shown to kill tumor cells without reducing the strength of normal bone in previous reports (11). However, when the CSA was frozen with liquid nitrogen in the present case, the tumor area became fragile and collapsed. Here, the tumor was localized mainly in the tibial tuberosity. The cortical bone on the caudal aspect, which is the compression side of the stifle joint, was maintained. This may have been one of the factors that allowed the stifle to remain fixed. However, depending on the site of tumor occurrence, the choice of surgical method may need to be considered in patients with CSA. Additionally, preoperative T2WI may be helpful for surgical planning.

In conclusion, limb-sparing surgery with frozen autologous bone grafting using liquid nitrogen can be an alternative to amputation. Thus, the usefulness of this treatment for CSA should be clarified in long-term outcome studies with a large sample size.

4. Patient perspective

In this case, a chondrosarcoma developed at the proximal end of the tibia, and joint preservation was not possible. The patient

could use the affected limb with joint immobilization, which may be a more favorable outcome than amputation. However, gait changes associated with joint immobilization may affect other orthopedic and neurological conditions, and will require follow-up over time.

Data availability statement

The original contributions presented in the study are included in the article/supplementary material, further inquiries can be directed to the corresponding author.

Ethics statement

Written informed consent was obtained from the owner for the participation and publication of this case report.

Author contributions

MS contributed to study design, acquisition of data, data analysis, interpretation, and drafted manuscript. TN and MM contributed to acquisition of data, data analysis, and interpretation. DY contributed to study design, data analysis, and interpretation. YH contributed to conception of study, study design, acquisition of data, data analysis, and interpretation. All authors also revised and approved the submitted manuscript.

Funding

MS reports grants from AO VET seed grants program (No. 115492) outside of the submitted work in the past.

Acknowledgments

We gratefully acknowledge the work of past and present members of the Animal Medical Center of Nippon Veterinary and Life Science University. We also thank Editage (www.editage.com) for English language editing.

Conflict of interest

The authors declare that the research was conducted in the absence of any commercial or financial relationships that could be construed as a potential conflict of interest.

Publisher's note

References

1. Brodey RS, Sauer RM, Medway W. Canine bone neoplasms. *J Am Vet Med Assoc.* (1963) 143:471–95.

2. Ling GV, Morgan JP, Pool RR. Primary bone rumors in the dog: a combined clinical, radiographic, and histologic approach to early diagnosis. *J Am Vet Med Assoc.* (1974) 165: 55–67.

3. Popovitch CA, Weinstein MJ, Goldschmidt MH, Shofer FS. Chondrosarcoma: a retrospective study of 97 dogs (1987–1990). *J Am Anim Hosp Assoc.* (1994) 30:81–5.

4. Boston SE. Musculoskeletal neoplasia and limb-sparing surgery. In: Johnson SA, Tobias KM, editors. *Veterinary Surgery: Small Animal*, 2nd ed. Saint Louis, MO: Elsevier (2017), p. 134 7–1372.

5. Szewczyk M, Lechowski R, Zabielska K. What do we know about canine osteosarcoma treatment? Review [Review]. *Vet Res Commun.* (2015) 39:61–7. doi: 10.1007/s11259-014-9623-0

6. Liptak JM, Dernell WS, Ehrhart N, Lafferty MH, Monteith GJ, Withrow SJ. Cortical allograft and endoprosthesis for limb-sparing surgery in dogs with distal radial osteosarcoma: a prospective clinical comparison of two different limb-sparing techniques. *Vet Surg.* (2006) 35:518–33. doi: 10.1111/j.1532-950X.2006.00185.x

7. Covey JL, Farese JP, Bacon NJ, Schallberger SP, Amsellem P, Cavanaugh RP, et al. Stereotactic radiosurgery and fracture fixation in 6 dogs with appendicular osteosarcoma. *Vet Surg.* (2014) 43:174–81. doi: 10.1111/j.1532-950X.2014.12082.x

8. Séguin B, Pinard C, Lussier B, Williams D, Griffin L, Podell B, et al. Limb-sparing in dogs using patient-specific, three-dimensional-printed endoprosthesis for distal radial osteosarcoma: a pilot study. *Vet Comp Oncol.* (2020) 18:92–104. doi: 10.1111/vco.12515

9. Séguin B, Walsh PJ, Ehrhart EJ 3rd, Hayden E, Lafferty MH, Selmic LE. Lateral manus translation for limb-sparing surgery in 18 dogs with distal radial osteosarcoma in dogs. *Vet Surg.* (2019) 48:247–56. doi: 10.1111/vsu.13132

10. Zekry KM, Yamamoto N, Hayashi K, Takeuchi A, Higuchi T, Abe K, et al. Intercalary frozen autograft for reconstruction of malignant bone and soft tissue tumours. *Int Orthop.* (2017) 41:1481–7. doi: 10.1007/s00264-017-3446-x

11. Yamamoto N, Tsuchiya H, Tomita K. Effects of liquid nitrogen treatment on the proliferation of osteosarcoma and the biomechanical properties of normal bone. *J Orthop Sci.* (2003) 8:374–80. doi: 10.1007/s10776-002-0626-3

12. Okamura Y, Heishima K, Motegi T, Sasaki J, Goryo M, Nishida H, et al. Mandibular reconstruction by using a liquid nitrogen-treated autograft in a dog with an oral tumor. *J Am Anim Hosp Assoc.* (2017) 53:167–71. doi: 10.5326/JAAHA-MS-6339

13. Akasaka M, Honnami M, Mochizuki M. Efficacy of frozen autograft treated with liquid nitrogen in limb-sparing surgery in feline scapular osteosarcoma: a case report. *J Vet Med Sci.* (2019) 81:1152–6. doi: 10.1292/jvms.18-0498

14. Hagen CRM, Singh A, Weese JS, Marshall Q, Linden AZ, Gibson TWG. Contributing factors to surgical site infection after tibial plateau leveling osteotomy: a follow-up retrospective study. *Vet Surg.* (2020) 49:930–9. doi: 10.1111/vsu.13436

15. Farese JP, Kirpensteijn J, Kik M, Bacon NJ, Waltman SS, Seguin B, et al. Biologic behavior and clinical outcome of 25 dogs with canine appendicular chondrosarcoma treated by amputation: a Veterinary Society of Surgical Oncology retrospective study. *Vet Surg.* (2009) 38:914–9. doi: 10.1111/j.1532-950X.2009.00606.x

16. Kirpensteijn J, van den Bos R, van den Brom WE, Hazewinkel HA. Ground reaction force analysis of large breed dogs when walking after the amputation of a limb. *Vet Rec.* (2000) 146:155–9. doi: 10.1136/vr.146.6.155

17. Hogy SM, Worley DR, Jarvis SL, Hill AE, Reiser RF 2nd, Haussler KK. Kinematic and kinetic analysis of dogs during trotting after amputation of a pelvic limb. *Am J Vet Res.* (2013) 74:1164–71. doi: 10.2460/ajvr.74.9.1164

18. Cole GL, Millis D. The effect of limb amputation on standing weight distribution in the remaining three limbs in dogs. *Vet Comp Orthop Traumatol.* (2017) 30:59–61. doi: 10.3415/VCOT-16-05-0075

19. Vasseur PB. Limb salvage in a dog with chondrosarcoma of the tibia. *J Am Vet Med Assoc.* (1985) 187:620–3.

20. Roynard PF, Bilderback A, Falzone C, Stefanacci JD, Cherubini GB. Magnetic resonance imaging, treatment and outcome of canine vertebral chondrosarcomas. Six cases. *J Small Anim Pract.* (2016) 57:610–6. doi: 10.1111/jsap.12554

21. Vanel M, Blond L, Vanel D. Imaging of primary bone tumors in veterinary medicine: which differences? *Eur J Radiol.* (2013) 82:2129–39. doi: 10.1016/j.ejrad.2011.11.032

22. Ehara S, Nishida J, Shiraishi H, Tamakawa Y. Pasteurized intercalary autogenous bone graft: radiographic and scintigraphic features. *Skelet Radiol.* (2000) 29:335–9. doi: 10.1007/s002560000205

frontiers | Frontiers in Veterinary Science

TYPE Original Research
PUBLISHED 28 April 2023
DOI 10.3389/fvets.2023.1179762

OPEN ACCESS

EDITED BY
Laura Elizabeth Selmic,
The Ohio State University, United States

REVIEWED BY
Giovanni Mogicato,
Ecole Nationale Vétérinaire de Toulouse (ENVT), France
Theresa Elizabeth Pancotto,
Virginia Tech, United States

*CORRESPONDENCE
Jeremy R. Mortier
✉ jeremy.mortier@vet-alfort.fr

†PRESENT ADDRESS
Jeremy R. Mortier,
École Nationale Vétérinaire de Maisons-Alfort, Paris, France

RECEIVED 04 March 2023
ACCEPTED 10 April 2023
PUBLISHED 28 April 2023

CITATION
Mortier JR, Maddox TW, Blackwood L, La Fontaine MD and Busoni V (2023) Dynamic contrast-enhanced computed tomography perfusion parameters of canine suspected brain tumors at baseline and during radiotherapy might be different depending on tumor location but not associated with survival. *Front. Vet. Sci.* 10:1179762. doi: 10.3389/fvets.2023.1179762

Dynamic contrast-enhanced computed tomography perfusion parameters of canine suspected brain tumors at baseline and during radiotherapy might be different depending on tumor location but not associated with survival

Jeremy R. Mortier[1,2*†], Thomas W. Maddox[1], Laura Blackwood[1], Matthew D. La Fontaine[3] and Valeria Busoni[2]

[1]Small Animal Teaching Hospital, Institute of Infection, Veterinary and Ecological Sciences, University of Liverpool, Neston, United Kingdom, [2]Diagnostic Imaging Section, Department of Clinical Sciences, Faculty of Veterinary Medicine, University of Liège, Liège, Belgium, [3]The Netherlands Cancer Institute, Amsterdam, Netherlands

Introduction: Treatment of brain tumors in dogs can be associated with significant morbidity and reliable prognostic factors are lacking. Dynamic contrast-enhanced computed tomography (DCECT) can be used to assess tumor perfusion. The objectives of this study were to assess perfusion parameters and change in size of suspected brain tumors before and during radiotherapy (RT) depending on their location and find a potential correlation with survival.

Methods: Seventeen client-owned dogs with suspected brain tumors were prospectively recruited. All dogs had a baseline DCECT to assess mass size, blood volume (BV), blood flow (BF), and transit time (TT). Twelve dogs had a repeat DCECT after 12Gy of megavoltage RT. Survival times were calculated.

Results: Intra-axial masses had lower BF (p=0.005) and BV (p<0.001) than extra-axial masses but not than pituitary masses. Pituitary masses had lower BF (p=0.001) and BV (p=0.004) than extra-axial masses. The volume of the mass was positively associated with TT (p=0.001) but not with BF and BV. Intra-axial masses showed a more marked decrease in size than extra-axial and pituitary masses during RT (p=0.022 for length, p=0.05 for height). Extra-axial masses showed a greater decrease in BF (p=0.011) and BV (p=0.012) during RT than pituitary masses and intra-axial masses. Heavier dogs had a shorter survival time (p=0.011). Perfusion parameters were not correlated with survival.

Conclusion: DCECT perfusion parameters and change in size of brain masses during RT might be different based on the location of the mass.

KEYWORDS

perfusion parameters, dynamic contrast enhanced computed tomography, brain tumor, dogs, radiotherapy, response to treatment

1. Introduction

Brain tumors are a common cause of central neurological signs in dogs and associated with high morbidity (1). Radiotherapy (RT) (with or without surgical excision) or debulking is widely recognized as the treatment of choice, both to alleviate clinical signs and improve survival time (2–11). The survival advantage of surgery is controversial, and surgery is technically demanding and associated with significant morbidity (12–14). Survival times after RT are variable and affected by both treatment and tumor type, but a recent systematic review reported median survival times of 348 days, 226 days and 351 days for the extra-axial, intra-axial and pituitary masses, respectively (15). Radiotherapy is expensive, constraining for clients and can be associated with significant side effects due to early and late radiation toxicity (16, 17). It is therefore vital to find or develop good prognostic factors that would allow for optimal patient selection. Very few imaging-derived characteristics have been associated with the prognosis, although it seems that large masses (2, 7, 18), poorly defined and irregular margins, T2w heterogeneity, presence of drop metastasis (19), mass effect, and cyst-like lesions are negative prognostic factors (7). A decrease in size of the mass at 6 weeks after RT is also associated with a longer survival (20).

In human medicine, functional imaging is increasingly used in the diagnosis, treatment planning and prognostication of brain tumors, and includes magnetic resonance spectroscopy, diffusion-weighted magnetic resonance imaging (MRI), perfusion-weighted MRI and dynamic contrast-enhanced computed tomography (DCECT) (21, 22). Dynamic contrast-enhanced computed tomography provides quantitative information about tumor physiology that cannot be obtained using conventional imaging, in particular the blood volume (BV), blood flow (BF), and transit time (TT) of masses. In human medicine, it can be used to refine grading and prognostication of brain tumors, as well as assessing response to treatment (23, 24). To date, two studies in veterinary medicine described the use of DCECT in dogs with cerebral mass lesions, showing promising results in differentiating the type of masses and in assessing response to treatment (25, 26).

The aims of this study were (1) to compare DCECT-derived perfusion parameters among intra-axial, extra-axial and pituitary tumors, (2) to assess if pretreatment perfusion parameters are associated with survival, and (3) to describe early changes in perfusion parameters and size of the masses during RT in a subset of them. Our hypotheses were that extra-axial and pituitary tumors will have higher BF and BV than intra-axial tumors, that baseline perfusion parameters might be associated with survival time and that we can observe early changes in perfusion parameters and mass volume during RT.

2. Materials and methods

This is a prospective cross-sectional study. Ethical approval was granted by the Committee on Research Ethics at the Institute of Veterinary Science of the University of Liverpool (VREC560a).

Abbreviations: BF, blood flow; BV, blood volume/fractional vascular volume; CT, computed tomography; CTV, clinical target volume; DCECT, dynamic contrast-enhanced computed tomography; GTV, gross tumor volume; MRI, magnetic resonance imaging; PTV, planning target volume; TT, transit time; NSAID, non-steroidal anti-inflammatory drugs; RT, radiotherapy.

2.1. Case selection

Client-owned dogs presented to the Small Animal Teaching Hospital (SATH) of the University of Liverpool for suspected brain tumors were prospectively enrolled from January 2017 to January 2020. Owner consent allowing for diagnostic tests including DCECT was obtained before inclusion into the study. To meet the inclusion criteria, dogs must have a brain mass on MRI and a presumptive diagnosis of brain tumor made by the attending board-certified radiologist and neurologist based on the imaging and clinical findings, but a final diagnosis of brain tumor made by histology was not necessary. Dogs must have undergone at least a baseline DCECT. Dogs who had already received RT, surgery or chemotherapy were excluded. Dogs receiving other non-chemotherapeutic medical treatments for their neurological signs (anti-inflammatory and anti-epileptic medication) were not excluded.

2.2. Clinical data

Treatment received at the time of DCECT, heart rate and systolic blood pressure during DCECT, treatment administered to treat the suspected brain tumor and survival time from the referral consultation were recorded. Treatment administered before the consultation was categorized as corticosteroids, non-steroidal anti-inflammatory drugs (NSAID) and other (paracetamol, anti-epileptic medication, trilostane) or none. Treatments received for the brain mass were categorized as RT or palliative (1 dog).

2.3. Dynamic contrast-enhanced computed tomography

All dogs were anesthetized. Premedication varied depending on the attending anesthetist, but most dogs received medetomidine (0.003 to 0.01 mg/kg) in association with butorphanol, lidocaine, buprenorphine or methadone. One dog received acepromazine (0.03 mg/kg) instead of medetomidine. Dogs were then induced using propofol or alfaxolone (to effect) and anesthesia was maintained using sevoflurane. Dynamic contrast-enhanced CT was performed using an 80-slice CT scan (Aquilion Prime 80, Canon Medical System) with dogs in sternal recumbency. Dogs for which owners elected for RT were positioned using a thermoplastic mask and a bite block as part as the RT planning (25).

Pre-contrast scans of the head were performed. Scanning parameters were 120 kV, variable mAs using Automatic Exposure Control, pitch factor 0.625, and images were reconstructed at 1 mm slice thickness using bone and soft tissue reconstruction algorithms. Dynamic contrast-enhanced CT planning was done using the pre-contrast soft tissue reconstruction in a soft tissue window (window width: 200 HU, window level 40 HU). A 4-cm length field of view was chosen to include the whole mass.

A 60-s continuous scan starting with intravenous injection of 2 mL/kg body weight of iodinated contrast medium (Ioversol 300 mg/mL iodine) using a power injector set at 3 mL/s injection rate (maximal allowable injection pressure set at 150 psi) and followed by a bolus flush of saline 1 mL/kg at the same injection rate. Scanning parameters were 80 kV, 200 mA, 0.75 s rotation time, 0.5 mm scan slice

thickness, 1 s time interval and 2 mm reconstruction slice thickness. Images were reconstructed using a soft tissue reconstruction algorithm.

A post-contrast scan of the head was performed immediately after DCECT (90 s after intravenous injection of iodinated contrast medium), using the same scanning parameters as for the pre-contrast scan.

A second DCECT using the same anesthetic protocol (all under general anesthesia) and the same scanning technique was performed, after receiving 12 Gy of radiation.

2.4. Radiation therapy

Radiotherapy was administered using a linear accelerator (VitalBeam, Varian Medical Systems, Palo Alto, California). Definitive RT was administered with 12 fractions of 4 Gy on a Monday, Wednesday, Friday basis. All treatments were carried out at 6MV and were 3D planned by a European College of Veterinary Internal Medicine board-certified veterinary oncologist and radiation oncologist (LB). Planning was performed from CT images using Eclipse 15.1 (Varian Medical Systems, Palo Alto, California), with the intention to include at least 95% of the planning treatment volume in the 95 to 105% isodose, or 97% of the planning treatment volume in the 97 to 103% isodose. Gross tumor volume (GTV) and clinical target volume (CTV) were defined using CT and MRI. Gross tumor volume was contoured based on T1-weighted (or T1-weighted after IV administration of gadolinium) images. A margin of 1–2 mm of normal tissue, including questionable tissue, was added to the GTV to create the CTV. The CTV-margin was extended three-dimensionally by 3–5 mm to define the planning target volume (PTV). Organs at risk were contoured (tympanic bullae, brain, spinal cord, optic chiasma). Plans utilized 3 to 5 coplanar beams, with beam collimation using multileaf collimator beam modification and dynamic wedges where appropriate. Dogs were immobilized as described for the CT scans. Portal imaging was carried out at least twice during the treatment protocol to verify position.

2.5. Images and perfusion analysis

Conventional CT images of the head were reviewed by a European College of Veterinary Diagnostic Imaging board-certified veterinary radiologist (JM) blinded to the clinical data of the dogs, using a Macintosh workstation and an image viewer (OsirixMD, Pixmeo). Images were viewed using both a soft tissue window (window width: 200 HU, window level: 40 HU) and a brain window (window width: 100 HU and window level: 50 HU). Multiplanar reconstruction was performed for each dog. Length, width, and height with planes parallel and orthogonal to those of the head were measured and the volume of the mass (using the ellipsoid formula $V = 4/3 \times \pi \times L \times W \times H$) was calculated. In 2 dogs with an intra-axial lesion, the mass was not sufficiently visible on CT and T2w MRI sequences in transverse, sagittal and dorsal planes were used for initial morphological assessment. One of these dogs had a repeat DCECT but the mass could not be measured on the images. Masses were first classified as extra-axial, intra-axial or pituitary based on their location, relationship to the rest of the brain parenchyma and contrast-enhancement (Figure 1).

Dynamic contrast-enhanced CT images were analyzed using an adiabatic approximation to the tissue homogeneity (ATH) model implemented with MATLAB™ (MathWorks, Massachusetts), designed as part of a previous study (27). An arterial input function was first contoured, and a time-attenuation curve was displayed to verify it had a shape consistent with arterial blood flow. The artery selected for the arterial input function was the lingual artery as it was the largest artery that was consistently included in the field of view and not surrounded by bone. To appropriately contour the artery without selecting peripheral lingual tissue the image was zoomed in and contoured on the arterial phase (veins not contrast-enhanced). Only the center of the artery was included when possible. The brain mass was then contoured manually slice by slice on every slice containing suspected tumoral tissue (Figure 2). Care was taken not to include bone or cerebral vessels within the contouring. Therefore, when present, the small part of the mass in contact with a cerebral vessel was excluded from contouring. For the two intra-axial masses not clearly visible on CT, side-by-side comparison of the MRI and CT images were performed to contour the mass as accurately as possible using the perfusion software. Perfusion parameters obtained from the analysis were blood flow (volume flow rate) and transit time (TT, time to traverse vasculature). Blood volume (BV) was then calculated using the following formula: $BV = TT \times BF$. Perfusion analysis was performed by one trained operator (JM).

2.6. Statistical analysis

Statistical analyzes were performed using the statistical software programs SPSS 24.0 (SPSS Inc., Chicago, Illinois, United States) and R (R version 3.2.0, The R Foundation for Statistical Computing). Dependent (outcome) and independent variables were derived from signalment data, clinical data and CT examinations. Descriptive statistics were calculated for data as required; categorical variables were summarized as frequencies with 95% confidence intervals (95% CI) and continuous variables as medians with interquartile ranges (IQR). Categorical variables with multiple categories, categories containing small numbers, or both, were reviewed and groupings amalgamated if necessary. The distribution of continuous variables was assessed for deviation from normal both graphically and with the Kolmogorov–Smirnov test.

The three primary individual outcomes considered were BF, TT and BV, with associations between these continuous variables and the collected independent variables estimated with linear regression. All independent variables showing potential association with an outcome on univariable analysis (p-value <0.25) were considered for inclusion in the final multivariable model for that outcome. Variables showing evidence of correlation (correlation coefficient > 0.7), were examined and only the variable with the smallest p-value was selected for entry in the multivariable models developed. Final models were developed with a manual backwards stepwise methodology with retention of variables with p-values < 0.05. Additionally, for the 12 dogs that were re-scanned, linear regression was used to compare the change in tumor parameters (length, width, height, volume, BF, BV, TT) between pituitary, extra-and intra-axial tumors and to evaluate associations between tumor volume and perfusion parameters (BF, BV, TT).

Survival times were calculated from the time of the first consultation at the SATH until death; dogs alive at the time of data

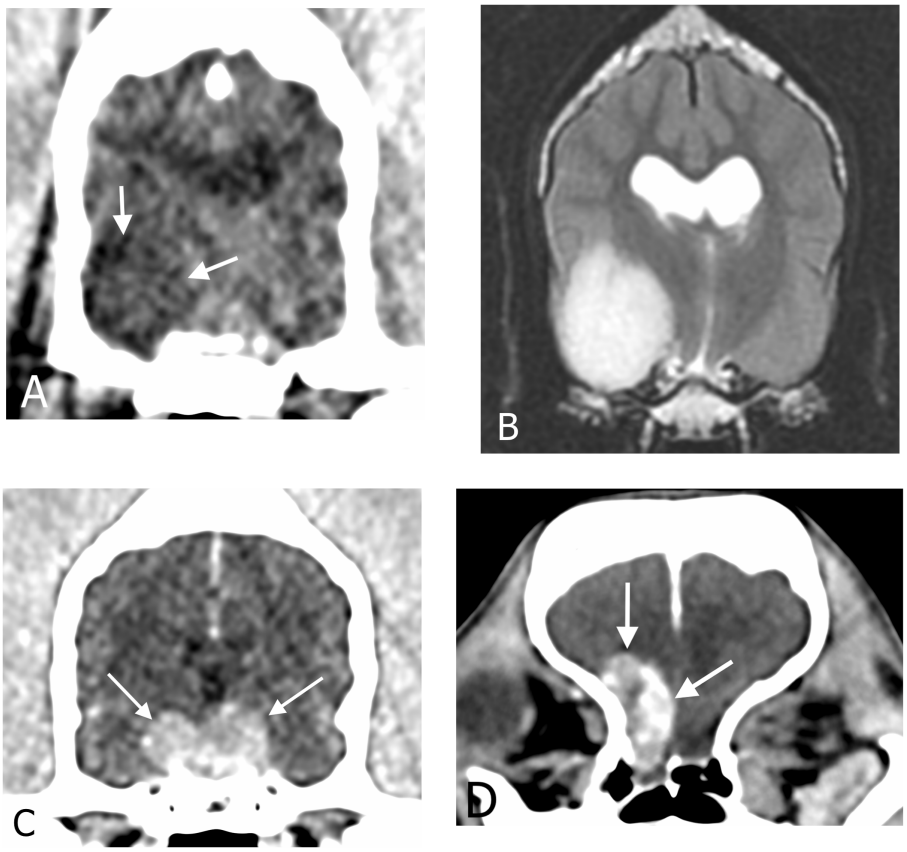

FIGURE 1
Transverse CT images in soft tissue reconstruction and brain window (WL 50 HU, WW 100HU) showing **(A)** an intra-axial mass, **(C)** a pituitary mass and **(D)** an extra-axial mass. **(B)** Transverse T2-weighted magnetic resonance image of the same intra-axial mass as in **(A)**.

collection were considered as censored, as were dogs lost to follow-up (censored at the date of last known contact). Median survival times were calculated from Kaplan–Meier product limit (survival) analysis. Univariable comparison of survival times and associations between survival and independent variables were examined with the Log Rank test for categorical variables and Cox proportional hazard regression analysis for continuous variables. Multivariable regression models were constructed with the same approach as above, including all variables with univariable p-value <0.25 and a backward stepwise approach with retention of p-values <0.05.

3. Results

3.1. Clinical data

Seventeen dogs met the inclusion criteria. There were 4 neutered females, 3 entire males and 10 neutered males. Breeds included 4 cross breeds, 3 Staffordshire bull terriers, 2 Labrador retrievers and 1 dog of each breed including cocker spaniel, boxer, Cavalier King Charles spaniel, Dalmatian, Jack Russel terrier, pug, West Island white terrier and dachshund. Median age of the dogs was 9.9 (6.6–14.3) years; median weight was 19.9 (6.6–59.6) kg.

There were 7 pituitary masses, 6 extra-axial masses and 4 intra-axial masses. Among the extra-axial masses, 4 were localized against the basicranium, 1 at the cerebellar convexity and 1 at the cerebral convexity. Among the intra-axial masses, 2 were within the temporal cortex, 1 within the cerebellum and 1 within the thalamus.

Nine dogs received corticosteroids (4 extra-axial, 2 intra-axial, 2 pituitary), 1 dog received NSAID (1 pituitary), 2 dogs received "other" treatments (one paracetamol and gabapentin; one trilostane) and 5 dogs had no treatment at the time of presentation (2 pituitary, 2 extra-axial, 1 intra-axial).

Twelve/17 dogs had repeat DCECT. There were 5 pituitary masses, 5 extra-axial masses and 2 intra-axial masses. Five dogs could not have repeat DCECT for logistical reasons. One did not received RT, DCECT failed in 1 dog and the remaining dogs were not considered stable enough to undergo the procedure.

At repeat DCECT, 10/12 dogs were receiving corticosteroids, 1 dog was on phenobarbital (1 intra-axial) only and 1 dog was not receiving any medical treatment (1 extra-axial). Most dogs were receiving analgesics in addition to the aforementioned treatment.

Sixteen/17 dogs had RT, and 1 dog did not receive any treatment for the suspected brain tumor. Median time between first DCECT and start of RT was 6 days (3–31).

Twelve/17 dogs had a record of their heart rate during the baseline DCECT, at the time of injection of contrast medium. All were

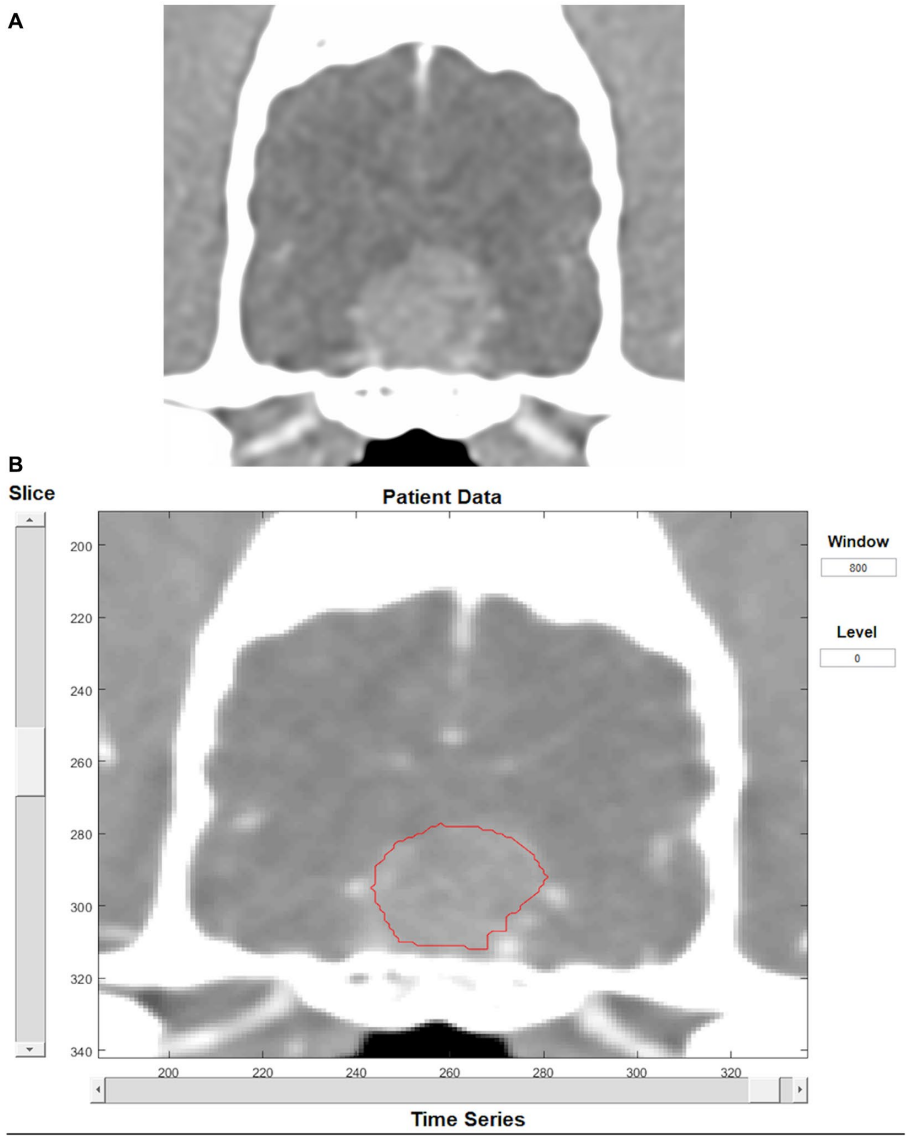

FIGURE 2
Transverse CT image in soft tissue reconstruction showing a pituitary mass **(A)**. Same image as displayed by the perfusion software, showing tumor contouring **(B)**.

considered appropriate by the attending anesthetist and ranged from 40 to 110 bpm (median 68 bpm). Similarly, systolic blood pressure was obtained for 12 dogs and ranged from 90 to 130 mmHg (median 115 mmHg).

3.2. Baseline DCECT

Median mass length, width, height, and volume were 1.4 cm (0.8–3.2), 1.2 cm (0.6–2.2), 1.2 cm (0.4–2.1) and 8.2 cm^3 (1.4–29.6), respectively. Median volume was 16 cm^3 (1.8–25.5) for pituitary masses, 9.4 cm^3 (1.5–15.8) for extra-axial masses, and 8 cm^3 (1.4–29.6) for intra-axial masses.

Median BV was 3.6 ml/100 g (0.7–11), median BF was 33.4 ml/100 g/min (2.8–116.1) and median TT was 7.2 s (4.1–15.7). Results for the different locations of masses are shown in Table 1. Intra-axial masses had a significantly lower BF ($p = 0.005$) and BV ($p < 0.001$) than extra-axial masses but not than pituitary masses. Similarly, pituitary masses had significantly lower BF ($p = 0.001$) and BV ($p = 0.004$) than extra-axial masses. The volume of the mass was positively associated with TT ($p = 0.001$) but not with BF and BV. There was no statistical association between any other imaging characteristic of the masses and the perfusion parameters.

3.3. Repeat DCECT

Median change in volume, length, height, width for each type of mass is shown in Table 2. There were statistically significant differences in the change of length and height but not width and volume between extra-axial, intra-axial and pituitary masses during the course of RT. More specifically, intra-axial tumors showed a more marked

decrease in size than extra-axial and pituitary tumors during RT ($p = 0.022$ for the length and $p = 0.05$ for the height).

The median change in perfusion parameters for each type of mass are presented in Table 3. There were statistically significant differences in the change of BF and BV but not TT between extra-axial, intra-axial and pituitary masses during the course of RT. More specifically, extra-axial tumors showed a more marked decrease in BF ($p = 0.011$) and BV ($p = 0.012$) than pituitary tumors and intra-axial tumors.

There was no statistically significant association between tumor volume change and change in BF, BV or TT.

3.4. Survival analysis

At the end of the study, 11 dogs were deceased, all due to progression of their intracranial mass, and six were either still alive or lost to follow-up.

The median survival time was 186 days (95%CI 0–496) for all dogs. The only dog who did not receive RT had a survival time of 175 days. There was no statistical difference in survival time between intra-axial, extra-axial and pituitary masses.

On multivariate analysis, only the weight of the dog was associated with survival ($p = 0.011$). More specifically, heavier dogs had a shorter survival time. Perfusion parameters were not significantly associated with survival in the final statistical model.

4. Discussion

The perfusion parameters of presumed brain tumors were significantly different depending on their location. Extra-axial masses had higher BF and BV than intra-axial and pituitary masses. In the early course of RT (after administration of 12 Gy), intra-axial masses showed a greater decrease in size than masses of the other groups, and extra-axial masses had a more marked decrease in BF and BV than masses of the other groups.

A study on 16 dogs with various types of brain masses (including 3 meningiomas and 7 gliomas but no pituitary masses) showed that meningiomas had the highest BV among all masses, although their results were not statistically significant (25). The authors also found that the permeability surface area ratio (PS) was higher in meningioma than in other brain masses, but they did not calculate BF. Although the DCECT scanning protocol was similar to the one used in the present study, the method of perfusion analysis was not described in detail and may have been different, making comparisons of the results difficult. Higher BF and BV in extra-axial masses compared to intra-axial masses is consistent with expectations, as the former are located outside the blood–brain barrier, therefore tend to be hypervascular and have permeable capillaries (29). Although perfusion imaging is not commonly used to differentiate intra-axial from extra-axial masses in human medicine, their findings were comparable to those of this study (29, 30). Pituitary masses are also considered extra-axial and frequently have strong contrast enhancement (31), suggesting hypervascularity, therefore high BV and BF would have been expected. In the present study, their perfusion values were high but not significantly different from those of intra-axial masses. This may be due to the small number of cases. Perfusion imaging is rarely performed on pituitary adenomas in human beings, therefore comparison with human studies is not possible (32).

A more recent study investigated the change in volume and perfusion parameters of brain tumors (confirmed and suspected) before and approximately 3 months and 6 months after RT (26). They found a significant decrease in tumor volume, BF, BV, and PS after RT, maintained or further decreased at second recheck. These results combined with those of this study suggest that the decrease in DCECT perfusion parameters occurs early during RT and is at least maintained if not progressing further during the first 6 months after treatment.

The fact that intra-axial masses showed a greater decrease in size than extra-axial and pituitary masses was interesting and unexpected. However, this result should be interpreted with caution given the small number of dogs in this group and the technical difficulty in accurately measuring intra-axial masses on CT. Imaging follow-up

TABLE 1 Median baseline perfusion parameters of brain tumors in dogs depending on their location.

Mass location	Blood volume (min; max) (mL/100g)	Blood flow (min; max) (mL/100g/min)	Transit time (min; max) (s)
Intra-axial	1.7 (0.7; 2.5)	22.4 (2.8; 33.4)	4.8 (4.1; 5.1)
Extra-axial	7.1* (3.8; 11)	54* (34.4; 116.1)	6.9 (5.2; 9.5)
Pituitary	3.6 (1.8; 4.3)	22.6 (9.6; 50)	8.8 (4.6; 12.4)

*$p < 0.05$.

TABLE 2 Median change in the size of brain masses after 12Gy of radiation therapy depending on their location.

Mass location	Change in volume (min; max) (cm^3)	Change in length (min; max) (cm)	Change in height (min; max) (cm)	Change in width (min; max) (cm)
Extra-axial	−1.6 (−1.7; 0.9)	0 (−0.2; 0)	0 (0; 0.6)	0 (−0.8; 0)
Intra-axial	−8.2 (−1; −0.1)	−0.3* (−1.3; −0.3)	−0.3* (−1.5; −0.3)	−0.4 (−1; −0.1)
Pituitary	−0.1 (−5; 0.1)	−0.1 (−0.3; 0.1)	0 (−0.3; 0)	−0.1 (−0.1; 0.1)

*$p < 0.05$.

TABLE 3 Median change in perfusion parameters of brain masses after 12Gy of radiation therapy depending on their location.

Mass location	Change in blood volume (min; max) (mL/100g)	Change in blood flow (min; max) (mL/100g/min)	Change in transit time (min; max) (s)
Extra-axial	−2.4* (−3.1; −1.4)	−24.7* (−54.6; −11.4)	1,5 (−0.42; 2.19)
Intra-axial	0.3 (0.1; 2.1)	18.2 (−2.5; 50.4)	−1.1 (−12.4; 0.6)
Pituitary	0.6 (−2.1; 1.6)	6.4 (3.7; 38.3)	−1.1 (−7.3; 1.6)

*$p < 0.05$.

during or after treatment of brain tumor is rare and unstandardized in veterinary research and studies assessing the association between change in volume, type of tumor and survival are scarce. It seems that a reduction in size of gliomas 6 weeks after RT is associated with longer survival (20). These results were not consistent with a previous study on various brain tumors that suggested that pituitary masses could be associated with a greater decrease in volume than other tumor types (glioma, meningioma and trigeminal nerve sheath tumors) 3 months after RT (26). It is therefore possible that gliomas have a greater initial size reduction, but that pituitary tumors have a greater delayed response. Direct tumor toxicity of RT through DNA damage is related to cell multiplication, and more aggressive tumors with fast-multiplying cells generally respond better to RT (33). On the other hand, indirect RT toxicity through its action on tumor microenvironment (such as vascularization and local immune system) could explain a delayed response (34). It could be hypothesized that the intra-axial masses in this study could be more aggressive than the extra-axial and pituitary masses, therefore have a better early response to treatment but also a faster tumor repopulation.

Extra-axial masses had a greater decrease in BF and BV during RT than the other tumor groups. This could simply be explained by the fact that extra-axial masses were more perfused at baseline, therefore the toxicity of RT on vascularity could have been more pronounced in this group. However, the response of the tumor microenvironment to RT is a complex and still poorly understood topic, and oversimplified assumptions should be avoided. Relationships between baseline perfusion parameters, their variation after treatment and prognosis have been investigated in people with high-grade gliomas. High-grade gliomas tend to have higher baseline perfusion parameters than low-grade gliomas, while lower post-treatment perfusion parameters were associated with a better prognosis (23, 24, 35–39). In the current study, the fact that the baseline and follow-up perfusion parameters were not associated with the change in size of the mass and the survival of the dogs could be due to the small population of dogs, the fact that all brain masses were considered as a single group when assessing the statistical relationship between these parameters, but also because of the variability of clinical signs associated with brain masses, leading to humane euthanasia regardless of response to treatment or aggressivity of the tumor. A study in a much larger population would be needed to further assess the potential prognostic role of DCECT perfusion parameters in brain tumors.

Heavier dogs had shorter survival in this study, regardless of tumor location. There is no clear reason to explain this finding, but it could simply be that heavier dogs with severe neurological clinical signs would be less manageable by their owners, therefore euthanized earlier in the course of the disease. Alternately, it could also represent a bias due to the small number of dogs included.

This study has many limitations. The main one is the small number of dogs, limiting the statistical power. A second limitation is the absence of confirmation and characterization of the masses. Using only the imaging characteristics, it is often impossible to differentiate between meningioma and histiocytic sarcoma, between pituitary adenoma and carcinoma, and between types and grades of gliomas (31, 40, 41). Unfortunately, brain biopsy requires specific equipment and experience and is not routinely performed in veterinary medicine, and a post-mortem examination is often declined by the owners. The accuracy of MRI has been reported to be as high as 100% in predicting the presence of a brain tumor (40), and 70 to 96% accurate in predicting the correct tumor type (42, 43). However, several studies in the veterinary literature report that other types of lesions such as cerebral vascular accidents can be misdiagnosed as gliomas on MRI (44, 45). Therefore, the diagnosis of brain tumor remains presumptive in this study.

Some dogs received ant-inflammatory drugs before first or repeat DCECT, or before both; other did not. The effects of anti-inflammatory drugs on DCECT perfusion parameters have not been studied, yet their anti-COX-2 activity have an anti-angiogenic action and could be responsible for changes in the perfusion parameters (46).

The technique of DCECT images acquisition and analysis used in this study also has some inherent limitations. The DCECT protocol used meets the human recommendations except for the injection rates of contrast medium and saline flush. Indeed, due to catheter size limitations leading to overpressure during injection, a 5 ml/s injection rate was not feasible. However, the smaller size of dogs compared to human beings likely balances out this limitation. Finally, intra and inter-observer variability have not been calculated in this study but would have been interesting, especially since it represents the highest contributor to overall variability in DCECT (47). A study found a coefficient of variation within patient ranging from 22 to 30% due to variability of the arterial input function area under the curve and variability in the tumor area under the curve in dogs with nasal tumors, using the same perfusion analysis software as the one used in this study (27). On the other hand, patients' blood pressure was not found to have a significant impact on the perfusion analysis.

Contouring of masses close to the calvarium obliged to exclude a sliver of tissue to avoid including bone in the perfusion analysis. Another important technical limitation is the fact that in two dogs with an intra-axial mass, contouring was performed where the observer subjectively thought the mass was based on MRI studies, and therefore might have been inaccurate.

In conclusion, this study found an association between the location of intracranial masses and the perfusion parameters at baseline (extra-axial masses have higher BF and BV than intra-axial and pituitary masses) and during RT (with extra-axial tumors showing

a higher decrease in BF and BV than pituitary and intra-axial tumors), and between the location of the mass and the size reduction during RT (with intra-axial tumors showing a higher decrease in size than extra-axial and pituitary tumors). Functional imaging, including DCECT, is of increasing availability in veterinary medicine yet still poorly studied. Further research in this field might be extremely valuable, with potential to help refine the diagnosis and prognosis, guide the choice of treatment, assess the treatment response, and detect recurrence in dogs with brain tumors.

Data availability statement

The raw data supporting the conclusions of this article will be made available by the authors, without undue reservation.

Ethics statement

The animal study was reviewed and approved by Research Ethics at the Institute of Veterinary Science of the University of Liverpool (VREC560a). Written informed consent was obtained from the owners for the participation of their animals in this study.

Author contributions

JM, TM, VB, LB, and ML: conception and design. JM and LB: acquisition of data. JM and TM: analysis and interpretation of data. JM, LB, and TM: drafting the article. JM, TM, VB, LB, and ML: revising article for intellectual content, final approval of the completed article, and agreement to be accountable for all aspects of the work in ensuring that questions related to the accuracy or integrity of any part of the work are appropriately investigated and resolved. All authors contributed to the article and approved the submitted version.

Funding

The authors received a research grant from the University of Liège for this work (FSR 2018).

Conflict of interest

The authors declare that the research was conducted in the absence of any commercial or financial relationships that could be construed as a potential conflict of interest.

Publisher's note

All claims expressed in this article are solely those of the authors and do not necessarily represent those of their affiliated organizations, or those of the publisher, the editors and the reviewers. Any product that may be evaluated in this article, or claim that may be made by its manufacturer, is not guaranteed or endorsed by the publisher.

References

1. Foster ES, Carrillo JM, Patnaik AK. Clinical signs of tumors affecting the rostral cerebrum in 43 dogs. *J Vet Intern Med*. (1988) 2:71–4. doi: 10.1111/j.1939-1676.1988.tb02796.x

2. Kent MS, Bommarito D, Feldman E, Theon AP. Survival, neurologic response, and prognostic factors in dogs with pituitary masses treated with radiation therapy and untreated dogs. *J Vet Intern Med*. (2007) 21:1027–33. doi: 10.1111/j.1939-1676.2007.tb03060.x

3. Berlato D, Zwingenberger AL, Ruiz-Drebing M, Pradel J, Clark N, Kent MS. Canine meningiomas treated with three-dimensional conformal radiation therapy require magnetic resonance imaging to avoid a geographic miss. *Vet Radiol Ultrasound*. (2018) 59:777–85. doi: 10.1111/vru.12653

4. Dolera M, Malfassi L, Bianchi C, Carrara N, Finesso S, Marcarini S, et al. Frameless stereotactic radiotherapy alone and combined with temozolomide for presumed canine gliomas. *Vet Comp Oncol*. (2018) 16:90–101. doi: 10.1111/vco.12316

5. Kelsey KL, Gieger TL, Nolan MW. Single fraction stereotactic radiation therapy (stereotactic radiosurgery) is a feasible method for treating intracranial meningiomas in dogs. *Vet Radiol Ultrasound*. (2018) 59:632–8. doi: 10.1111/vru.12636

6. Hansen KS, Zwingenberger AL, Théon AP, Kent MS. Long-term survival with stereotactic radiotherapy for imaging-diagnosed pituitary tumors in dogs. *Vet Radiol Ultrasound*. (2019) 60:219–32. doi: 10.1111/vru.12708

7. Debreuque M, de Fornel P, David I, Delisle F, Ducerveau MN, Devauchelle P, et al. Definitive-intent uniform megavoltage fractioned radiotherapy protocol for presumed canine intracranial gliomas: retrospective analysis of survival and prognostic factors in 38 cases (2013–2019). *BMC Vet Res*. (2020) 16:412. doi: 10.1186/s12917-020-02614-x

8. Moirano SJ, Dewey CW, Haney S, Yang J. Efficacy of frameless stereotactic radiotherapy for the treatment of presumptive canine intracranial gliomas: a retrospective analysis (2014-2017). *Vet Comp Oncol*. (2020) 18:528–37. doi: 10.1111/vco.12573

9. Monforte Monteiro SR, Rossmeisl JH, Russell J, Holmes MA, Wessmann A, Morris J, et al. Effect of radiotherapy on freedom from seizures in dogs with brain tumors. *J Vet Intern Med*. (2020) 34:821–7. doi: 10.1111/jvim.15695

10. Van Asselt N, Christensen N, Meier V, Rohrer Bley C, Laliberte S, Poirier VJ, et al. Definitive-intent intensity-modulated radiation therapy provides similar outcomes to those previously published for definitive-intent three-dimensional conformal radiation therapy in dogs with primary brain tumors: a multi-institutional retrospective study. *Vet Radiol Ultrasound*. (2020) 61:481–9. doi: 10.1111/vru.12868

11. Carter GL, Ogilvie GK, Mohammadian LA, Bergman PJ, Lee RP, Proulx DR. CyberKnife stereotactic radiotherapy for treatment of primary intracranial tumors in dogs. *J Vet Intern Med*. (2021) 35:1480–6. doi: 10.1111/jvim.16086

12. Axlund TW, McGlasson ML, Smith AN. Surgery alone or in combination with radiation therapy for treatment of intracranial meningiomas in dogs: 31 cases (1989-2002). *J Am Vet Med Assoc*. (2002) 221:1597–600. doi: 10.2460/javma.2002.221.1597

13. Keyerleber MA, McEntee MC, Farrelly J, Thompson MS, Scrivani PV, Dewey CW. Three-dimensional conformal radiation therapy alone or in combination with surgery for treatment of canine intracranial meningiomas. *Vet Comp Oncol*. (2015) 13:385–97. doi: 10.1111/vco.12054

14. Hara Y. Transsphenoidal surgery in canines: safety, efficacy and patient selection. *Vet Med*. (2020) 11:1–14. doi: 10.2147/vmrr.s175995

15. Hu H, Barker A, Harcourt-Brown T, Jeffery N. Systematic review of brain tumor treatment in dogs. *J Vet Intern Med*. (2015) 29:1456–63. doi: 10.1111/jvim.13617

16. Brearley MJ, Jeffery ND, Phillips SM, Dennis R. Hypofractionated radiation therapy of brain masses in dogs: a retrospective analysis of survival of 83 cases (1991-1996). *J Vet Intern Med*. (1999) 13:408–12. doi: 10.1111/j.1939-1676.1999.tb01454.x

17. Griffin LR, Nolan MW, Selmic LE, Randall E, Custis J, LaRue S. Stereotactic radiation therapy for treatment of canine intracranial meningiomas. *Vet Comp Oncol*. (2016) 14:e158–70. doi: 10.1111/vco.12129

18. van Rijn SJ, Galac S, Tryfonidou MA, et al. The influence of pituitary size on outcome after transsphenoidal hypophysectomy in a large cohort of dogs with pituitary-dependent hypercortisolism. *J Vet Intern Med*. (2016) 30:989–95. doi: 10.1111/jvim.14367

19. José-López R, Gutierrez-Quintana R, Fuente C, Manzanilla EG, Suñol A, Pi Castro D, et al. Clinical features, diagnosis, and survival analysis of dogs with glioma. *J Vet Intern Med*. (2021) 35:1902–17. doi: 10.1111/jvim.16199

20. Garcia Mora JK, Robertson J, Hsu F, et al. Comparison of linear and volumetric criteria for the determination of therapeutic response in dogs with intracranial gliomas. *J Vet Intern Med*. (2022) 36:1066–74. doi: 10.1111/jvim.16406

21. Kimura M, da Cruz LCH. Multiparametric MR imaging in the assessment of brain tumors. *Magn Reson Imaging Clin N Am*. (2016) 24:87–122. doi: 10.1016/j.mric.2015.09.001

22. TPC Y, Bauman G, Yartsev S, Fainardi E, Mac Donald D, Lee TY. Dynamic perfusion CT in brain tumors. *Eur J Radiol*. (2015) 84:2386–92. doi: 10.1016/j.ejrad.2015.02.012

23. Shankar JJS, Woulfe J, da Silva V, Nguyen TB. Evaluation of perfusion CT in grading and prognostication of high-grade gliomas at diagnosis: a pilot study. *Am J Roentgenol*. (2013) 200:W504–9. doi: 10.2214/AJR.12.8967

24. Yeung TPC, Wang Y, He W, et al. Survival prediction in high-grade gliomas using CT perfusion imaging. *J Neuro-Oncol*. (2015) 123:93–102. doi: 10.1007/s11060-015-1766-5

25. MacLeod AG, Dickinson PJ, LeCouteur RA, Higgins RJ, Pollard RE. Quantitative assessment of blood volume and permeability in cerebral mass lesions using dynamic contrast-enhanced computed tomography in the dog. *Acad Radiol*. (2009) 16:1187–95. doi: 10.1016/j.acra.2009.03.015

26. Zwingenberger AL, Pollard RE, Taylor SL, Chen RX, Nunley J, Kent MS. Perfusion and volume response of canine brain tumors to stereotactic radiosurgery and radiotherapy. *J Vet Intern Med*. (2016) 30:827–35. doi: 10.1111/jvim.13945

27. la Fontaine MD, McDaniel LS, Kubicek LN, Chappell RJ, Forrest LJ, Jeraj R. Patient characteristics influencing the variability of distributed parameter-based models in DCE-CT kinetic analysis. *Vet Comp Oncol*. (2017) 15:105–17. doi: 10.1111/vco.12143

28. Treggiari E, Maddox TW, Gonçalves R, Benoit J, Buchholz J, Blackwood L. Retrospective comparison of three-dimensional conformal radiation therapy vs. prednisolone alone in 30 cases of canine Infratentorial brain tumors. *Vet Radiol Ultrasound*. (2017) 58:106–16. doi: 10.1111/vru.12440

29. Hakyemez B, Yildirim N, Erdoğan C, Kocaeli H, Korfali E, Parlak M. Meningiomas with conventional MRI findings resembling intraaxial tumors: can perfusion-weighted MRI be helpful in differentiation? *Neuroradiology*. (2006) 48:695–702. doi: 10.1007/s00234-006-0115-y

30. Kremer S, Grand S, Remy C, Esteve F, Lefournier V, Pasquier B, et al. Cerebral blood volume mapping by MR imaging in the initial evaluation of brain tumors. *J Neuroradiol*. (2002) 29:105–13.

31. Pollard RE, Reilly CM, Uerling MR, Wood FD, Feldman EC. Cross-sectional imaging characteristics of pituitary adenomas, invasive adenomas and adenocarcinomas in dogs: 33 cases (1988-2006). *J Vet Intern Med*. (2010) 24:160–5. doi: 10.1111/j.1939-1676.2009.0414.x

32. Bashari WA, Senanayake R, Fernández-Pombo A, Gillett D, Koulouri O, Powlson AS, et al. Modern imaging of pituitary adenomas. *Best Pract Res Clin Endocrinol Metab*. (2019) 33:101278. doi: 10.1016/j.beem.2019.05.002

33. Baskar R, Dai J, Wenlong N, Yeo R, Yeoh KW. Biological response of cancer cells to radiation treatment. *Front Mol Biosci*. (2014) 1. doi: 10.3389/fmolb.2014.00024

34. Hirata E, Sahai E. Tumor microenvironment and differential responses to therapy. *Cold Spring Harb Perspect Med*. (2017) 7:1, 24–14. doi: 10.1101/cshperspect.a026781

35. Beppu T, Sasaki M, Kudo K, Kurose A, Takeda M, Kashimura H, et al. Prediction of malignancy grading using computed tomography perfusion imaging in nonenhancing supratentorial gliomas. *J Neuro-Oncol*. (2011) 103:619–27. doi: 10.1007/s11060-010-0433-0

36. Maarouf R, Sakr H. A potential role of CT perfusion parameters in grading of brain gliomas. *Egypt J Radiol Nucl Med*. (2015) 46:1119–28. doi: 10.1016/j.ejrnm.2015.07.002

37. Ahmad N, Shaukat A, Rehan A, Rashid S. Diagnostic accuracy of perfusion computed tomography in cerebral glioma grading. *J Coll Physicians Surg Pak*. (2016) 26:562–5.

38. Jain R, Narang J, Griffith B, Bagher-Ebadian H, Scarpace L, Mikkelsen T, et al. Prognostic vascular imaging biomarkers in high-grade gliomas. Tumor permeability as an adjunct to blood volume estimates. *Acad Radiol*. (2013) 20:478–85. doi: 10.1016/j.acra.2012.11.011

39. Satheesh Kumar E, Ramesh D, Kailasanathan N. The role of CT perfusion parameters in grading of brain gliomas in correlation with histopathology. *Int J Contemp Med Res*. (2017) 4:540–4.

40. Bentley RT, Ober CP, Anderson KL, Feeney DA, Naughton JF, Ohlfest JR, et al. Canine intracranial gliomas: relationship between magnetic resonance imaging criteria and tumor type and grade. *Vet J*. (2013) 198:463–71. doi: 10.1016/j.tvjl.2013.08.015

41. Wada M, Hasegawa D, Hamamoto Y, Yu Y, Fujiwara-Igarashi A, Fujita M. Comparisons among MRI signs, apparent diffusion coefficient, and fractional anisotropy in dogs with a solitary intracranial meningioma or histiocytic sarcoma. *Vet Radiol Ultrasound*. (2017) 58:422–32. doi: 10.1111/vru.12497

42. Ródenas S, Pumarola M, Gaitero L, Zamora À, Añor S. Magnetic resonance imaging findings in 40 dogs with histologically confirmed intracranial tumours. *Vet J*. (2011) 187:85–91. doi: 10.1016/j.tvjl.2009.10.011

43. Thomas WB, Wheeler SJ, Kramer R, Kornegay JN. Magnetic resonance imaging features of primary brain tumors in dogs. *Vet Radiol Ultrasound*. (1996) 37:20–7. doi: 10.1111/j.1740-8261.1996.tb00807.x

44. Cervera V, Mai W, Vite CH, Johnson V, Dayrell-Hart B, Seiler GS. Comparative magnetic resonance imaging findings between gliomas and presumed cerebrovascular accidents in dogs. *Vet Radiol Ultrasound*. (2010) 52:33–40. doi: 10.1111/j.1740-8261.2010.01749.x

45. Young BD, Fosgate GT, Holmes SP, Wolff CA, Chen-Allen AV, Kent M, et al. Evaluation of standard magnetic resonance characteristics used to differentiate neoplastic, inflammatory, and vascular brain lesions in dogs. *Vet Radiol Ultrasound*. (2014) 55:399–406. doi: 10.1111/vru.12137

46. Mander K, Finnie J. Tumour angiogenesis, anti-angiogenic therapy and chemotherapeutic resistance. *Aust Vet J*. (2018) 96:371–8. doi: 10.1111/avj.12747

47. Ng CS, Wei W, Ghosh P, Anderson E, Herron DH, Chandler AG. Observer variability in CT perfusion parameters in primary and metastatic tumors in the lung. *Technol Cancer Res Treat*. (2018) 17:1–9. doi: 10.1177/1533034618769767

frontiers | Frontiers in Veterinary Science

TYPE Original Research
PUBLISHED 14 September 2023
DOI 10.3389/fvets.2023.1238549

OPEN ACCESS

EDITED BY
Blaz Cugmas,
University of Latvia, Latvia

REVIEWED BY
Joaquín Araos,
Cornell University, United States
Roberto Rabozzi,
CVRS Policlinico Veterinario Roma Sud, Italy
Katerina Tomsič,
University of Ljubljana, Slovenia

*CORRESPONDENCE
Vaidehi V. Paranjape
✉ vparanjape@vt.edu

RECEIVED 12 June 2023
ACCEPTED 21 August 2023
PUBLISHED 14 September 2023

CITATION
Paranjape VV, Henao-Guerrero N, Menciotti G and Saksena S (2023) Performance of four cardiac output monitoring techniques vs. intermittent pulmonary artery thermodilution during a modified passive leg raise maneuver in isoflurane-anesthetized dogs.
Front. Vet. Sci. 10:1238549.
doi: 10.3389/fvets.2023.1238549

Performance of four cardiac output monitoring techniques vs. intermittent pulmonary artery thermodilution during a modified passive leg raise maneuver in isoflurane-anesthetized dogs

Vaidehi V. Paranjape[1]*, Natalia Henao-Guerrero[1], Giulio Menciotti[1] and Siddharth Saksena[2]

[1]Department of Small Animal Clinical Sciences, Virginia-Maryland College of Veterinary Medicine, Virginia Polytechnic Institute and State University, Blacksburg, VA, United States, [2]Department of Civil and Environmental Engineering, Virginia Polytechnic Institute and State University, Blacksburg, VA, United States

Objective: This study investigated the performance among four cardiac output (CO) monitoring techniques in comparison with the reference method intermittent pulmonary artery thermodilution (iPATD) and their ability to diagnose fluid responsiveness (FR) during a modified passive leg raise (PLR_M) maneuver in isoflurane-anesthetized dogs undergoing acute blood volume manipulations. The study also examined the simultaneous effect of performing the PLR_M on dynamic variables such as stroke distance variation (SDV), peak velocity variation (PVV), and stroke volume variation (SVV).

Study design: Prospective, nonrandomized, crossover design.

Study animals: Six healthy male Beagle dogs.

Methods: The dogs were anesthetized with propofol and isoflurane and mechanically ventilated under neuromuscular blockade. After instrumentation, they underwent a series of sequential, nonrandomized steps: Step 1: baseline data collection; Step 2: removal of 33 mL kg^{-1} of circulating blood volume; Step 3: blood re-transfusion; and Step 4: infusion of 20 mL kg^{-1} colloid solution. Following a 10-min stabilization period after each step, CO measurements were recorded using esophageal Doppler (ED_{CO}), transesophageal echocardiography (TEE_{CO}), arterial pressure waveform analysis ($APWA_{CO}$), and electrical cardiometry (EC_{CO}). Additionally, SDV, PVV, and SVV were recorded. Intermittent pulmonary artery thermodilution ($iPATD_{CO}$) measurements were also recorded before, during, and after the PLR_M maneuver. A successful FR diagnosis made using a specific test indicated that CO increased by more than 15% during the PLR_M maneuver. Statistical analysis was performed using one-way analysis of variance for repeated measures with *post hoc* Tukey test, linear regression, Lin's concordance correlation coefficient (ρc), and Bland–Altman analysis. Statistical significance was set at $p < 0.05$.

Results: All techniques detected a reduction in CO ($p < 0.001$) during hemorrhage and an increase in CO after blood re-transfusion and colloid infusion ($p < 0.001$) compared with baseline. During hemorrhage, CO increases with the PLR_M maneuver were as follows: 33% for iPATD ($p < 0.001$), 19% for EC ($p = 0.03$), 7% for APWA ($p = 0.97$), 39% for TEE ($p < 0.001$), and 17% for ED ($p = 0.02$). Concurrently,

decreases in SVV, SDV, and PVV values ($p < 0.001$) were also observed. The percentage error for TEE, ED, and EC was less than 30% but exceeded 55% for APWA. While TEE_{CO} and EC_{CO} slightly underestimated $iPATD_{CO}$ values, ED_{CO} and $APWA_{CO}$ significantly overestimated $iPATD_{CO}$ values. TEE and EC exhibited good and acceptable agreement with iPATD. However, CO measurements using all four techniques and iPATD did not differ before, during, and after PLR_M at baseline, blood re-transfusion, and colloid infusion.

Conclusion and clinical relevance: iPATD, EC, TEE, and ED effectively assessed FR in hypovolemic dogs during the PLR_M maneuver, while the performance of APWA was unacceptable and not recommended. SVV, SDV, and PVV could be used to monitor CO changes during PLR_M and acute blood volume manipulations, suggesting their potential clinical utility.

KEYWORDS

arterial pressure waveform analysis, canine, electrical cardiometry, esophageal doppler, general anesthesia, fluid responsiveness, hypovolemia, transesophageal echocardiography

1. Introduction

Circulatory shock can pose as a life-threatening event, occurring because of inadequate blood flow and oxygen delivery to tissues. Amidst such hemodynamic instability, the cornerstone of treatment lies in fluid therapy, which ameliorates venous return, cardiac preload, cardiac output (CO), and tissue oxygen utilization (1). Over the past two decades, the concept of "fluid responsiveness" (FR), rooted in the Frank-Starling cardiac curve, has garnered significant attention, targeting the challenges of precisely dosing fluid therapy. Following a fluid bolus, an increase of more than 10–15% in CO or stroke volume signifies FR, as there are heightened cardiac preload and ventricular filling pressures. By contrast, minimal changes occur with fluid nonresponsiveness (2–5). FR evaluation uses static or dynamic indices. Static indices such as central venous pressure and pulmonary artery occlusion pressure, although established as cardiac filling pressures, lack a strong correlation with FR (6, 7). Dynamic indices such as stroke volume variation (SVV) and pulse pressure variation depend on heart-lung interactions induced by mechanical ventilation and measure the subsequent effect of positive-pressure ventilation on fluctuations in stroke volume across a respiratory cycle. While these indices hold clinical relevance in both human medicine (2–4) and veterinary medicine (8, 9), their accuracy diminishes during spontaneous breathing, low tidal volume ventilation, cardiac rhythm disturbances, right-sided heart failure, and open chest conditions (2, 10, 11). In such scenarios, researchers have introduced the "passive leg raising" test that can trigger a preload challenge similar to a traditional fluid bolus or heart-lung interactions, effectively predicting FR based on multiple trials and meta-analyses (12–15).

Historically, passive leg raising was employed as an emergency measure during acute circulatory crises or hemorrhagic events in human patients. This simple bedside test shifts a patient from a semi-recumbent to a horizontal trunk position, raising the lower limbs at 30–45° (2, 16, 17). This gravitational shift causes the movement of approximately 150–300 mL of blood volume from the lower body to cardiac chambers, mimicking a fluid bolus' effects (18, 19). This transient and reversible hemodynamic change eliminates the risk of volume overload. In an ideal scenario, real-time cardiovascular assessment is crucial to capture brief circulatory adjustments during passive leg raising (2, 16, 17). Transthoracic or transesophageal echocardiography has been routinely used in diverse human populations to precisely monitor the real-time cardiovascular response to this test (2, 12–14, 16). A replication of the 45° passive leg raising test during cardiopulmonary resuscitation in an experimental porcine model of prolonged ventricular fibrillation yielded comparable outcomes to those of standard positioning in terms of spontaneous circulation return and 24-h survival rates. Animals undergoing passive leg raising exhibited notably better neurological alertness scores (20).

Until recently, only limited literature has been available on this maneuver in veterinary species. Recognizing inter-species variations in pelvic limb conformation, size, and blood volume distribution, a modified passive leg raise (PLR_M) maneuver was developed and demonstrated in anesthetized pigs (21) and dogs (22). During acute hemorrhage, the inclination of the pelvic limbs and caudal abdomen at 15° in pigs and 30° in dogs caused a significant CO increase of more than 25%, measured through intermittent pulmonary artery thermodilution ($iPATD_{CO}$). While $iPATD_{CO}$ is often regarded as the "gold standard" for veterinary research (23–25), its application in clinical settings is hindered by complications, expertise requirements, extensive training, and costly equipment setup (26). Real-time minimally invasive (e.g., esophageal Doppler [ED_{CO}], transesophageal echocardiography [TEE_{CO}], arterial pressure waveform analysis [$APWA_{CO}$]) or noninvasive (e.g., electrical cardiometry [EC_{CO}]) methods that provide continuous, reproducible CO measurements remain unvalidated for assessing PLR_M in animals.

The objectives of the present study were as follows: (1) gaging the agreement between invasive $iPATD_{CO}$ and ED_{CO}, TEE_{CO}, $APWA_{CO}$, and EC_{CO} for monitoring CO changes in response to PLR_M in anesthetized dogs subjected to hemodynamic effects from induced blood volume changes; (2) evaluating the ability of ED_{CO}, TEE_{CO}, $APWA_{CO}$, and EC_{CO} to identify more than 15% $iPATD_{CO}$ increase, indicative of FR; and (3) investigating the correlation between EC and ED-derived dynamic variables like SVV, stroke distance variation (SDV), and peak velocity variation (PVV) with $iPATD_{CO}$

measurements during PLR_M analysis. The following hypotheses were proposed: (1) strong and acceptable agreement will be observed between ED_{CO}, TEE_{CO}, $APWA_{CO}$, EC_{CO}, and $iPATD_{CO}$; (2) all test methods will detect more than 15% increase in CO signifying FR; and (3) SVV, SDV, and PVV will demonstrate correlation with $iPATD_{CO}$ readings during PLR_M.

2. Materials and methods

2.1. Ethics statement

This prospective, nonrandomized, crossover experimental study involving dogs was reviewed and granted approval by the Institutional Animal Care and Use Committee of Virginia Tech University (protocol number 20-235).

2.2. Animals in the study

Six adult, sexually intact male, healthy Beagles aged 13–16 months and weighing 10.5 ± 0.3 kg (mean ± standard deviation), bred specifically for research, were included in this investigation. A comprehensive physical examination, complete blood count, and serum chemistry panel were conducted on all dogs. The dogs were deemed healthy as no abnormalities were observed in the blood test results or during the cardiopulmonary examination. Following an extensive review of pertinent literature on human studies detecting a positive CO response to the passive leg raising test (2, 12–15), published data on the PLR_M maneuver in pigs (21), and an unpublished pilot study involving dogs, an *a priori* power analysis affirmed that a sample size of at least six dogs would be necessary to detect a significant 15% difference in CO, assuming a statistical power of 0.8 and an alpha level of 0.05 (G*Power 3.1, Heinrich-Heine-Universität Düsseldorf, Germany). An effect size greater than 0.8, derived from these animal studies, indicated a substantial difference effect. The dogs were individually housed in kennels under controlled temperature conditions and were acclimatized to the laboratory environment for 2 weeks. Food was withheld for 12 h before the experimental procedures, while access to water was maintained. A physical examination was conducted for all dogs on the day of general anesthesia.

2.3. Anesthetic induction and standard anesthetic monitoring

The determination of the order in which each dog underwent the experiment on a given day was randomized using a tool available at: https://www.randomizer.org/. On the designated study day, intravenous (IV) catheterization of the right cephalic vein was performed. This was followed by preoxygenation using a facemask to administer oxygen at a flow rate of 4Lmin^{-1}. General anesthesia was induced facemask to administer IV propofol (Propoflo 10 mg mL^{-1}, Zoetis Inc., MI, United States), titrated until orotracheal intubation could be accomplished with an appropriately sized, cuffed endotracheal tube. After securing the airway, the dog was connected to an anesthesia workstation integrated with a ventilator (Datex-Ohmeda Aestiva 5/7900, GE Healthcare, WI, United States) through a circle anesthetic breathing circuit. Anesthetic maintenance was achieved using isoflurane (Fluriso, VetOne, ID, United States) in oxygen (1–2 L min^{-1}), targeting an end-tidal concentration of isoflurane between 1.5 and 1.7%. The dogs were placed in a right lateral recumbent position. End-tidal isoflurane concentration and end-tidal carbon dioxide concentration were continuously monitored using a calibrated side-stream infrared gas analyzer linked to a multiparameter monitor (Datex-Ohmeda S/5 Compact anesthesia monitor; GE Healthcare). Using the same monitor, Standard lead II electrocardiogram, heart rate (HR), esophageal temperature, and peripheral hemoglobin oxygen saturation were also recorded at 5-min intervals throughout the experiment, as part of routine anesthetic monitoring and record keeping. Body temperature was maintained between 36.7°C and 38.1°C during anesthesia using a forced-air warming blanket and a circulating water-heating system.

Arterial catheterization of the dorsal pedal artery was performed to measure invasive systolic, diastolic, and mean arterial blood pressures. The catheter was connected to a disposable pressure transducer through non-compliant short tubing (15.24 cm) filled with heparinized saline (2 IU mL^{-1}) and connected to a three-way Luer lock stopcock. The transducer was positioned at a height approximating the right atrium location. Neuromuscular paralysis was initiated to prevent patient-ventilator dyssynchrony, with an initial IV dose of 0.4 mg kg^{-1} rocuronium (rocuronium bromide 10 mg mL^{-1}, Pfizer, NY, United States), followed by a continuous rate infusion of 0.4 mg kg^{-1} h^{-1}. Supramaximal stimulation of the common peroneal nerve was generated using a peripheral nerve stimulator (Stimpod 450X, Xavant Technology, Pretoria, SA) to assess the effectiveness of the blockade. Mechanical ventilator settings were adjusted to a volume-controlled mode set at 12 mL kg^{-1}, with an inspiratory-to-expiratory ratio ranging from 1:2 to 1:3, and the respiratory rate was adjusted to maintain end-tidal carbon dioxide concentration between 30 and 40 mmHg. Throughout the experiment, no maintenance crystalloid fluids were administered to prevent potential blood volume changes that could skew hemodynamic data.

2.4. Instrumentation for EC_{CO} measurements

The technique employed by the ICON monitor (Osypka Medical Inc., CA, United States) for continuous hemodynamic data monitoring, including EC_{CO} and SVV readings, is referred to as electrical cardiometry. After preparing the skin areas by clipping and cleaning, four Cardiotronic (Osypka Medical Inc.) electrocardiographic electrodes with adhesive patches were positioned. Two electrodes were placed on the left aspect of the neck (at the level of the common carotid artery), and the other two electrodes were attached to the left thoracic area (at the level of the T8-T13 vertebrae), as previously described in published studies (27–29). These electrodes were then connected to the ICON EC monitor through a cable. The ICON EC monitor was synchronized with a laptop using the iControl™ software application (Osypka Medical Inc.) and an external communication cable, facilitating efficient data management. The ICON monitor employed the Electrical Velocimetry™ (Osypka Medical Inc.) physiological model to assess changes in thoracic electrical bioimpedance during cardiac systole, thereby capturing

volumetric changes in the aorta. Detailed information on the physiology and algorithmic calculations used for EC_{CO} derivation can be found in other studies (28, 29). Additionally, the computation of SVV was automated with ICON internal software using a specific formula.

$$SVV\,(\%) = \frac{SV_{max} - SV_{min}}{(SV_{max} + SV_{min})/2} \times 100$$

where SV_{max} and SV_{min} are the maximum and minimum stroke volume (mL), respectively, over one respiratory cycle.

At each data point, the EC_{CO} ($L\,min^{-1}$) and SVV (%) data were recorded as an averaged value over a 1-min interval, as configured in the internal database settings.

2.5. Instrumentation for $iPATD_{CO}$ measurements

Subsequently, the dogs were positioned in dorsal recumbency and maintained in this posture throughout the course of the experiment. Areas of approximately 4 × 4 cm over the left and right jugular veins were clipped and prepared with aseptic techniques. A 5 Fr 13-cm double-lumen central venous catheter (MILA International Inc., KY, United States) was introduced into the left jugular vein to draw a consistent blood volume during acute hemorrhagic shock and to facilitate blood transfusion and colloid solution administration during correction of hypovolemia. Concurrently, a 6 Fr 8.5 cm hemostasis introducer (Fast-Cath, Abbott Cardiovascular, MN, United States) was positioned in the right jugular vein, through which a 5 Fr 75 cm pulmonary artery Swan Ganz catheter (132FS, Edwards Lifesciences Corp., CA, United States) was inserted. Both the proximal and distal ports of the pulmonary artery catheter were connected to additional disposable pressure transducers. These transducers were calibrated and positioned in a manner analogous to the arterial pressure transducer. The pulmonary artery catheter was cautiously advanced through the right atrium and right ventricle until its distal port was situated within the pulmonary artery. The positioning accuracy was affirmed by monitoring characteristic pressure waveforms and values, using the CO monitor (Carescape B850, GE Healthcare, IL, United States). Measurement of the pulmonary artery wedge aided the assessment of left ventricular filling and left atrial pressure, pertaining to a concurrent independent research study. For the determination of $iPATD_{CO}$, a 3-mL chilled (2–5°C) bolus of 0.9% sodium chloride solution was injected at the end of the expiration phase for <3 s through the proximal injectate port. The appropriate computation constant was selected on the CO monitor screen based on the catheter model, injectate volume, and temperature, as advised by the manufacturers. The catheter thermistor measured core body temperature as well as the difference in blood temperature downstream, which the CO monitor converted into a dilution curve through a modified Stewart-Hamilton equation. At each data timepoint, a CO reading represented the mean of three consecutive measurements within a 10% variation range. The injections were manually executed consistently by the same individual, with a minimum interval of 90 s between each injection.

2.6. Instrumentation for arterial pressure waveform analysis-based CO measurements

The LiDCOplus monitor (LiDCO Ltd., Cambridge, UK) employed the PulseCO algorithm based on pulse power analysis to continuously determine real-time CO values. This algorithm relied on arterial pressure waveforms and lithium dilution for intermittent calibration. To calibrate, a 0.006 $mmol\,kg^{-1}$ IV bolus of lithium chloride (LiDCO Ltd.) was injected through the central venous catheter in the left jugular vein. The concentration of lithium was measured by a lithium ion-sensitive electrode sensor connected to a three-way stopcock on the indwelling arterial catheter (30, 31). Blood samples were collected using a peristaltic pump at a flow rate of 4 $mL\,min^{-1}$ across the sensor. The packed cell volume and serum sodium concentration, which were correction factors required by the LiDCO monitor, were analyzed using a benchtop blood gas machine just before CO measurement. The resultant lithium concentration vs. time was employed to calculate plasma flow using the Stewart-Hamilton equation. The calibration CO value ($L\,min^{-1}$) was determined using the following formula (32, 33):

$$LiDCO\,(L/min) = \frac{\text{Lithium chloride dose}\,(mmol) \times 60}{\text{area of curve corrected for sodium concentration}\,(mmol\,L-1) \times (1 - \text{packed cell volume})}$$

The PulseCO algorithm integrated a time-based autocorrelation and transformed the arterial waveform into a volume-time waveform, accounting for compliance and aortic volume. The root mean square method, independent of waveform morphology, estimated the effective value (approximately 0.7 times the original amplitude) of this volume waveform, calculating the "nominal stroke volume." This was then scaled to an "actual stroke volume" using a patient-specific calibration derived from the lithium dilution CO measurement, considering the individual's age, height, and weight (33–35). The $APWA_{CO}$ (arterial pressure waveform analysis-based CO) was automatically calculated as the product of stroke volume and heart rate (HR), continuously monitored and recorded by the LiDCOplus monitor. At each data point, the recorded value for PulseCO was an average over a 1-min interval.

2.7. Instrumentation for TEE_{CO} measurements

A multiplane transesophageal transducer (Canon i6SVX2–1.8-6mHz, Canon Medical Systems, CA, United States) was inserted into the esophagus, reaching a mid-esophageal position. The image plane was digitally rotated forward until a mid-esophageal long-axis view was obtained (36, 37). The image was optimized for clear visualization of the left ventricular outflow tract (LVOT), the sinus of Valsalva, and the proximal portion of the ascending aorta. The "zoom" function of the ultrasound machine (Aplio i900, Canon Medical Systems, CA, United States) was employed to enhance the visibility of these structures. Electrocardiogram-triggered cine-loop, encompassing three consecutive cardiac cycles, was stored for subsequent offline analysis. Subsequently, the probe was advanced to a deep

trans-gastric position and its tip was anteflexed to obtain a short-axis view of the left ventricle. The image plane was further rotated forward to visualize the LVOT in a position as parallel as possible to a Doppler gate. This image plane remained fixed for the rest of the procedure. At predetermined time points, a pulsed wave-Doppler gate was positioned in the LVOT, just below the aortic valve, in accordance with the American Society of Echocardiography Guidelines (38). Care was exercised to position the gate at the same location where the LVOT measurements were taken. Spectral Doppler traces spanning at least three cardiac cycles were stored for subsequent analysis. Continuous-wave Doppler was employed in a similar manner when the Nyquist limit was reached to acquire LVOT Doppler spectrograms. The acquired images and cine-loops were imported into a workstation equipped with specialized cardiac analysis software (Tomtec Arena, Tomtec Imaging Systems, Germany). All measurements were conducted over three consecutive cardiac cycles, and the average values were used for statistical analysis. LVOT diameter was measured from zoomed images captured from the mid-esophageal long-axis view, selecting a mid-systolic frame just below the aortic valve. The LVOT cross-sectional area (LVOTArea) was then calculated as $\pi \times (\text{LVOT diameter}/2)^2$. To minimize sources of error, given that LVOTArea was not anticipated to vary significantly over the study duration, the LVOTArea was measured only once for each dog (38). For each acquired Doppler spectrogram, the velocity time integral of three consecutive beats was measured using the embedded function of the software program. Instantaneous heart rate (HR) was also measured by the embedded function of the software, calculating the time between two consecutive envelope peaks. At each time point, TEE_{CO} was calculated as follows: velocity time integral × LVOTArea × HR.

2.8. Instrumentation for ED_{CO} measurements

The esophageal Doppler veterinary monitoring system (CardioQ-EDMV+, Deltex Medical, UK), equipped with a 4.02-MHz continuous Doppler ultrasound emitting probe (K9P, Deltex Medical), was utilized to estimate stroke distance (cm), SDV (%), and PVV (%). The probe, measuring 120 cm in length, featured 6 depth markers to aid in guiding the insertion depth and ensuring proper probe placement. Following lubrication with aqueous gel, the probe was introduced into the oral cavity alongside the existing TEE probe and gently advanced into the esophagus. Further insertion continued until the probe tip reached a position approximately aligned with the fifth to sixth thoracic vertebra, coinciding with peak aortic blood flow. Once a characteristic triangular waveform, accompanied by a distinct maximal pitch Doppler "whip crack" sound, was visualized, the probe was stabilized in that position to confirm peak blood flow from the descending thoracic aorta. The working principle of this method, Doppler waveform analysis, and the derived variables have been recently documented in canine studies (25). The CardioQ-EDMV+ monitor did not automatically display quantified ED_{CO} values. Therefore, the LVOTArea measured using TEE was used to calculate ED_{CO} ($L\,min^{-1}$) with the following formula, referencing a study conducted in canines (39):

$$ED_{CO}\left(L/\min\right) = \text{LVOTArea}\left(cm^2\right) \times \text{Stroke distance}\left(cm\right) \times \text{HR}\left(\text{beats}\,\min^{-1}\right)$$

During each mechanical breath delivered by the ventilator, SDV and PVV were automatically computed by an internal software program, and the results were continuously displayed on the CardioQ-EDMV+ monitor screen (25). Before data collection at each time point, a minimum of 3 min was allowed to ensure a consistent, high-quality signal and Doppler waveform. The average values for stroke distance, SDV, and PVV over a 1-min cycle were recorded.

$$\text{SDV}\left(\%\right) = \frac{\text{Stroke Distance}_{max} - \text{Stroke Distance}_{min}}{\left(\text{Stroke Distance}_{max} + \text{Stroke Distance}_{min}\right)/2} \times 100$$

$$\text{PVV}\left(\%\right) = \frac{PV_{max} - PV_{min}}{\left(PV_{max} + PV_{min}\right)/2} \text{X}\,100$$

2.9. Study timeline and performing PLR_M maneuver

After completing the instrumentation process and confirming the proper functioning of all CO equipment, each dog underwent a sequential nonrandomized study design to induce acute alterations in blood volume. The experiment followed a four-step sequence (Figure 1): Step 1 involved obtaining baseline data corresponding to euvolemia; Step 2 initiated acute hemorrhage by withdrawing 33 mL kg^{-1} of circulating blood volume from the left jugular catheter over a 15-min period (induction of hypovolemia). The removed blood was stored in blood collection bags coated with citrate phosphate dextrose adenine as an anticoagulant. Step 3 encompassed autologous blood transfusion through the left jugular catheter over 15 min using an infusion pump (to restore lost blood volume); Step 4 comprised the administration of a 20 mL kg^{-1} IV bolus of 6% hydroxyethyl starch (VetStarch 130/0.4 in 0.9% sodium chloride, Zoetis Inc.) as a colloid solution into the left jugular vein over a 15-min period (induction of hypervolemia). After each step, a 10-min period was provided for hemodynamic stabilization. The purpose of subjecting the dogs to various blood volume phases was to induce significant CO changes during each step, creating a physiological context to demonstrate and simultaneously assess the presence or absence of FR using the various CO techniques.

The Passive Leg Raise Maneuver (PLR_M), as depicted in Figure 2, was executed according to the recently characterized detailed description in dogs (22). Hemodynamic data were collected under each step three times: before performing the PLR_M maneuver (Pre-PLR_M; see Figure 2A), after 5 min of the PLR_M maneuver involving elevating the pelvic limbs and caudal abdomen at a 30° angle (PLR_M; Figure 2B), and after returning the original position for 5 min (Post-PLR_M; Figure 2A).

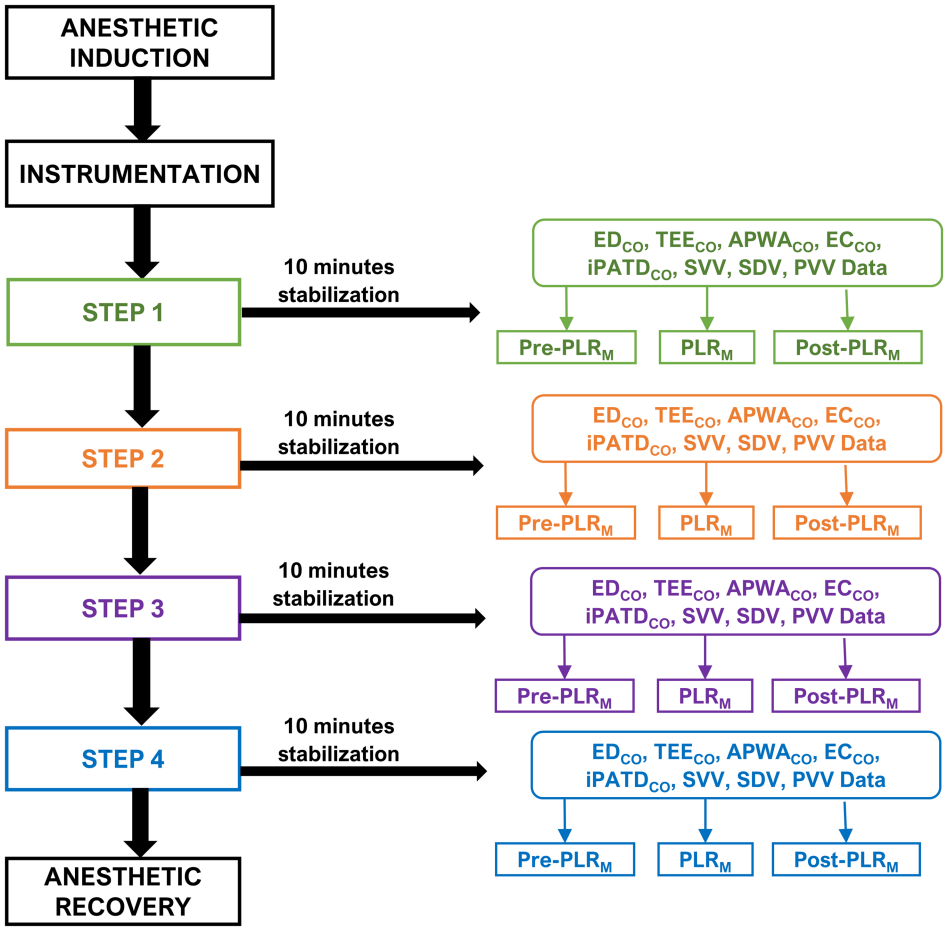

FIGURE 1
Timeline of the experimental study design and cardiac output data: The timeline of this experimental study design and cardiac output data was obtained through various techniques such as minimally invasive esophageal Doppler (ED_{CO}), transesophageal echocardiography (TEE_{CO}), arterial pressure waveform analysis ($APWA_{CO}$), noninvasive electrical cardiometry (EC_{CO}), and the gold standard intermittent pulmonary artery thermodilution ($iPATD_{CO}$). The evaluation was conducted during a modified passive leg raise (PLR_M) maneuver in six healthy anesthetized Beagle dogs. After anesthesia induction and instrumentation, each dog underwent a sequential nonrandomized four-step sequence: Step 1: baseline data collection; Step 2: induction of hypovolemia by withdrawing 33 mL kg^{-1} of circulating blood volume over a 15-min period; Step 3: autologous blood transfusion over 15 min; and Step 4: administering a 20 mL kg^{-1} intravenous bolus of a colloid solution over 15 min. A 10-min stabilization period was implemented after each step and before data collection. In each step, hemodynamic data were collected three times: before the PLR_M maneuver (Pre-PLR_M); after 5 min of being in the PLR_M maneuver, wherein the elevation of the pelvic limbs and caudal abdomen was assessed at 30° (PLR_M); and after 5 min of returning to the original position (Post-PLR_M). The final data were obtained, the jugular and arterial catheters were removed, and anesthetic recovery was initiated.

2.10. Summary for data collection

To ensure unbiased data collection, each researcher was assigned to collect data from a specific CO monitoring technique and remained unaware of the data recorded by others. One researcher was responsible for altering body positions during the PLR_M maneuver. While the order for collecting CO data from the four test methods in the study (EC, APWA, TEE, and ED) was randomized (using https://www.randomizer.org/), $iPATD_{CO}$ measurements were consistently performed after acquiring CO data from the other CO techniques. This sequencing was designed to prevent the fluid volume from multiple 0.9% saline injections for $iPATD_{CO}$ potentially affecting data from the test methods. Moreover, preserving the required sodium concentrations for LiDCOplus CO calibration in determining $APWA_{CO}$ values was essential, which could be influenced by the administration of 0.9% saline injections.

Calibration of CO by the LiDCOplus monitor for estimating $APWA_{CO}$ values was conducted before Step 1, Step 3, and Step 4. The data recorded under each step for studying the effects of the PLR_M maneuver (Pre-PLR_M, during PLR_M, and Post-PLR_M) are summarized as follows:

I. ICON electrical cardiometry monitor measured EC_{CO} and SVV values.
II. LiDCOplus monitor with the PulseCO algorithm for pulse power analysis- measured $APWA_{CO}$ values.
III. Transesophageal echocardiography probe measured velocity time integral and LVOTArea to calculate TEE_{CO} measurements.
IV. CardioQ-EDMV+ esophageal Doppler monitor measured stroke distance, SDV, and PVV values.
V. Carescape B850 intermittent pulmonary artery thermodilution monitor measured $iPATD_{CO}$ values.

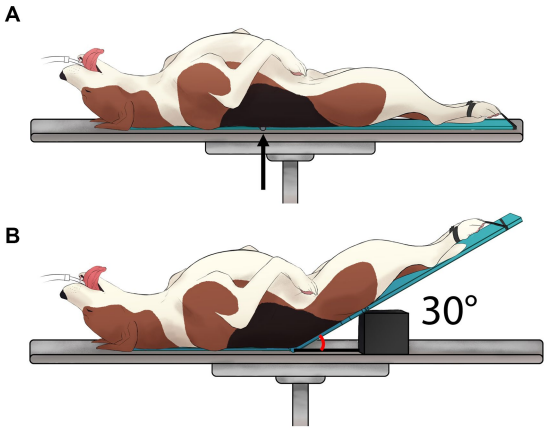

FIGURE 2
Graphical illustration of the modified passive leg raise (PLR_M) maneuver: A visual depiction of the PLR_M maneuver that was performed in six healthy, anesthetized dogs according to the detailed description published recently in a canine model (22). The PLR_M maneuver involved two states: **(A)** Before performing the PLR_M maneuver, and **(B)** the PLR_M maneuver itself, achieved by raising the caudal abdomen and pelvic limbs at 30° relative to the horizontal surface of the table [Created by V. Paranjape and J. Mauragis]. This image is reproduced with permission from Source: Paranjape et al. (22).

2.11. Anesthetic recovery

Subsequent to the final data collection, rocuronium administration was ceased. A train-of-four ratio ≥0.9, consistent spontaneous ventilation, and generation of more than 3 cmH_2O negative pressure during spontaneous inspiration were taken as indicators of recovery from rocuronium-induced neuromuscular block. The pulmonary artery, jugular, and arterial catheters were removed with careful application of external pressure on the catheter sites to prevent bleeding and hematoma formation. Anesthetic recovery was marked by discontinuing the isoflurane vaporizer. Following extubation, all dogs received 0.3 $mg\,kg^{-1}$ IV methadone (methadone hydrochloride injection 10 $mg\,mL^{-1}$, Akorn, IL, United States), and they were transferred to individual kennels. Cardiopulmonary parameters were monitored, and catheter sites were periodically observed over the subsequent 96 h. Pain scores were assessed using the Glasgow composite pain scale short form, along with physical examination and noninvasive blood pressure measurements. Additional administration of 0.25 $mg\,kg^{-1}$ IV methadone was considered if needed based on pain scores.

2.12. Statistical analysis

The normality of variables across the sequential steps (baseline, hemorrhage, autologous blood transfusion, and hydroxyethyl starch infusion) for each CO measurement method (iPATD, EC, APWA, TEE, and ED) was assessed using the Shapiro–Wilk and D'Agostino-Pearson tests. All variables were determined to be normally distributed and are presented as mean ± standard deviation. A one-way analysis of variance for repeated measures was employed to compare differences between the sequential steps during acute blood volume manipulation for all variables, with the Greenhouse and Geisser correction applied when sphericity assumptions were not met. *Post hoc* Tukey adjustment was applied for multiple pairwise comparisons. Student *t*-tests were also conducted for pairwise comparisons, with significance set at $p < 0.05$ for all analyses. According to the definition of FR (2–5), the test methods were deemed successful in diagnosing FR in response to the PLR_M only if there was a more than 15% increase in CO values during the PLR_M maneuver compared to Pre-PLR_M CO values.

To calculate bias, the difference between $iPATD_{CO}$ and CO values for each of the other methods (EC_{CO}, $APWA_{CO}$, TEE_{CO}, and ED_{CO}) was expressed as a percentage of the average CO values between $iPATD_{CO}$ and the specific method. This relative bias was represented as a percentage of average CO values, utilizing a formula previously reported (24). Relative bias was considered positive when CO values were underestimated by other methods in comparison to $iPATD_{CO}$, and negative when CO values were overestimated. Limits of agreement were calculated as relative bias ±1.96 × standard deviation to encompass 95% confidence intervals. The absolute value of relative bias for each observation was compared with a 30% threshold to calculate the count of observations within the acceptable performance range. The percentage error was expressed as 1.96 × standard deviation of bias/mean CO × 100, calculated for all test methods, and compared with the acceptable range (<30%) proposed in the literature (40).

The relationships between the reference method $iPATD_{CO}$ and test methods (iPATD, EC, APWA, TEE, and ED) were analyzed using linear regression, and concordance was assessed using Lin's concordance correlation coefficient (ρc), where perfect concordance equated to a value of 1 (41). Agreement between $iPATD_{CO}$ and individual test methods was evaluated through the Bland–Altman (BA) method (42), and a polar plot was employed to visualize the agreement (43, 44). In cases where bias between CO values of test methods and reference ($iPATD_{CO}$) depended on the magnitude of the original measurement, a BA analysis for nonuniform differences was performed, and the bias was regressed linearly against the average bias. The distance from the center indicated the absolute values of the mean change in ($[\Delta CO_{PATD} + \Delta CO_{EC}]/2$), while the angle with the horizontal (0° radial) indicated disagreement. A good trend was evident when data were situated within 10% of mean CO values. Commercial statistical software (SAS version 9.4; SAS Institute Inc.) was utilized for all analyses, with BA and polar plots generated using available software (Excel, Microsoft Corp.; Polar Plot 2 analysis add-in; accessed 11 December, 2022)[1].

3. Results

The anesthetic induction, maintenance, and recovery phases proceeded without adverse events for all dogs. In each case, iPATD instrumentation and placement of the thermodilution catheter were successfully executed without any reported complications. No missing data were noted for iPATD, EC, APWA, TEE, and ED. The experimental procedures were completed successfully across all dogs. The dogs maintained normothermia throughout the anesthetic period

1 https://andypope.info/charts/polarplot3.html

(37.2 ± 0.6°C). No discernible differences were noted in total anesthesia time ($p = 0.51$), time spent during hemorrhage ($p = 0.46$), time spent during blood transfusion ($p = 0.89$), and colloid administration ($p = 0.66$) among the dogs.

Compared with baseline Pre-PLR_M CO values, significant reductions ($p < 0.001$) in hemorrhage Pre-PLR_M CO values were detected by iPATD, EC, APWA, TEE, and ED. Following blood transfusion and colloid infusion, Pre-PLR_M CO values were notably higher ($p < 0.001$) than baseline measurements, consistent across all test methods, including iPATD. Throughout baseline, blood transfusion, and colloid infusion, $iPATD_{CO}$ measurements displayed no disparity between the Pre-PLR_M, PLR_M, and Post-PLR_M readings. This trend was mirrored in EC_{CO}, $APWA_{CO}$, TEE_{CO}, and ED_{CO} measurements. During blood volume depletion, $iPATD_{CO}$ showed an approximately 33% increase during the PLR_M maneuver as compared to Pre-PLR_M CO measurements. When evaluating the test methods, EC, APWA, TEE, and ED identified an approximate increase in PLR_M CO values of 19% ($p = 0.03$), 7% ($p = 0.97$), 39% ($p < 0.001$), and 17% ($p = 0.02$), respectively. Thus, alongside iPATD, only EC, TEE, and ED could successfully diagnose FR in response to the maneuver in hypovolemic dogs. Derived dynamic variables from EC (SVV) and ED (SDV and PVV) accurately tracked changes in CO values resulting from acute blood volume manipulation (Table 1). Commencement of acute hemorrhage induced significant increases in SVV, SDV, and PVV values ($p < 0.001$) compared with baseline. Following volume replacement with blood and colloids, these variables returned to baseline levels. However, no differences were observed between Pre-PLR_M, PLR_M, and Post-PLR_M readings for these variables during Steps 1, 3, and 4. By contrast, during hypovolemia, the maneuver led to a significant decrease in SVV, SDV, and PVV ($p < 0.001$) compared with Pre-PLR_M values. Returning the abdomen and legs to the horizontal position significantly increased these values, moving them closer to Pre-PLR_M readings ($p < 0.001$).

For each dog, pairs of CO measurements were obtained using iPATD and EC, APWA, TEE, and ED techniques at Pre-PLR_M, PLR_M, and Post-PLR_M timepoints, during baseline, hemorrhage, autologous blood transfusion, and colloid infusion. Thus, 12 pairs of CO comparisons between iPATD and the four test methods were collected for each dog, amounting to 72 pairs per test method across all six dogs. Percentage error, relative bias, LOA, and Lin's concordance correlation coefficient for all test methods across all time points are presented in Table 2. TEE, ED, and EC exhibited percentage errors within the acceptable range (<30%) established as a standard (40), while APWA showed >55% error in performance across time points and during sequential manipulation of blood volume. Lin's concordance correlation, indicating test method data reproducibility, was the highest for TEE (>0.90) and EC (>0.90), followed by ED (0.61–0.66), and the lowest for APWA (0.41–0.45). In comparison to $iPATD_{CO}$ measurements, TEE_{CO} (Figure 3A) and EC_{CO} (Figure 3B) consistently displayed underestimation (positive relative bias; slope < 1 about Y = X on regression line) across time points and during sequential blood volume manipulation. Conversely, ED_{CO} (Figure 3C) and $APWA_{CO}$ (Figure 3D) consistently demonstrated significant overestimation of $iPATD_{CO}$ measurements (negative relative bias; slope > 1 about Y = X on regression line).

BA analysis for TEE_{CO} (Figure 4A) showed a negative trend (slope = −0.16; intercept = 0.45) between bias and average CO data, indicating underestimation for lower CO values and slight overestimation at higher CO values. EC_{CO} BA analysis (Figure 4B) revealed a positive trend (slope = 0.22; intercept = −0.33) between bias and average CO data, suggesting increased bias at higher CO values. Slight overestimation was observed for lower CO values, with slight

TABLE 1 Mean ± standard deviation of hemodynamic variables stroke volume variation (SVV), stroke distance variation (SDV), and peak velocity variation (PVV) derived from electrical cardiometry (EC) and esophageal Doppler (ED) monitors recorded in six healthy, mechanically ventilated, isoflurane-anesthetized dogs undergoing sequential manipulation of blood volume: Step 1: baseline; Step 2: acute hemorrhage by withdrawing circulating blood volume (33 mL kg^{-1}); Step 3: autologous blood transfusion; and Step 4: 20 mL kg^{-1} intravenous bolus of 6% hydroxyethyl starch (colloid). Data were collected immediately before performing the modified passive leg raise (PLR_M) maneuver (Pre-PLR_M), after 5 min of PLR_M (PLR_M), and 5 min after the abdomen and limbs were returned to the horizontal position (Post-PLR_M).

Variable	Step	Time of data collection		
		Pre-PLR_M	PLR_M	Post-PLR_M
SVV (%) derived from EC	1	9 ± 3	10 ± 2	10 ± 2
	2	22 ± 4*	15 ± 3*, a	25 ± 2*, b
	3	8 ± 2†	9 ± 1†	10 ± 1†
	4	6 ± 1†	5 ± 1†	5 ± 1†
SDV (%) derived from ED	1	10.4 ± 0.5	11.2 ± 0.3	11.5 ± 0.2
	2	19.2 ± 0.6*	12.7 ± 0.7*, a	21.4 ± 0.5*, b
	3	8.1 ± 0.8†	7.7 ± 0.6†	7.9 ± 0.7†
	4	5.5 ± 0.4*, †	5.1 ± 0.2*, †	5.4 ± 0.5*, †
PVV (%) derived from ED	1	6.2 ± 0.2	6.4 ± 0.5	6.5 ± 0.7
	2	16.8 ± 0.7*	9.8 ± 0.4*, a	14.1 ± 0.5*, b
	3	7.3 ± 0.8†	7.1 ± 0.5†	7.5 ± 0.7†
	4	4.4 ± 0.5†	4.1 ± 0.6†	3.8 ± 0.6†

*Significant difference from step 1 at the same time point ($p < 0.05$). †Significant difference from step 2 at the same time point ($p < 0.05$).
[a]Significant difference from Pre-PLR_M within the same step ($p < 0.05$). [b]Significant difference from PLR_M within the same step ($p < 0.05$).
SVV, Stroke Volume Variation; SDV, Stroke Distance Variation; PVV, Peak Velocity Variation.

TABLE 2 Percentage error (%), mean ± standard deviation (SD) of the relative bias (%), limits of agreement (%), and Lin's concordance correlation coefficient (ρ_c) for the cardiac output (CO) values measured using the test methods transesophageal echocardiography (TEE_{CO}), arterial pressure waveform analysis ($APWA_{CO}$), esophageal Doppler (ED_{CO}), and electrical cardiometry (EC_{CO}) in comparison with the reference method intermittent pulmonary artery thermodilution.

CO values from test method	Timepoint	Percentage error (%)	Relative bias (%) Mean ± SD	Limits of agreement (%)	Lin's concordance (ρ_c)
TEE_{CO}	Pre-PLR_M	27.1	14.2 ± 18.0	−21.1 to 49.5	0.94
	PLR_M	27.2	10.4 ± 15.7	−20.4 to 41.1	0.93
	Post-PLR_M	26.5	11.7 ± 14.0	−15.7 to 39.0	0.94
$APWA_{CO}$	Pre-PLR_M	64.2	−24.3 ± 43.3	−109.2 to 60.6	0.45
	PLR_M	57.8	−26.0 ± 40.3	−105.0 to 53.0	0.42
	Post-PLR_M	55.6	−34.5 ± 41.2	−115.2 to 46.2	0.41
ED_{CO}	Pre-PLR_M	26.8	−31.0 ± 17.6	−65.5 to 3.4	0.66
	PLR_M	20.8	−31.1 ± 13.2	−57.0 to −5.1	0.61
	Post-PLR_M	23.7	−34.4 ± 17.9	−69.5 to 0.8	0.64
EC_{CO}	Pre-PLR_M	24.4	3.1 ± 12.9	−22.1 to 28.4	0.93
	PLR_M	23.1	3.8 ± 10.6	−16.9 to 24.5	0.92
	Post-PLR_M	24.5	0.8 ± 14.4	−27.5 to 29.0	0.94

These data were obtained from six healthy, mechanically ventilated, isoflurane-anesthetized dogs undergoing sequential manipulation of blood volume: Step 1: baseline; Step 2: acute hemorrhage by withdrawing circulating blood volume (33 mL kg^{-1}); Step 3: autologous blood transfusion; and Step 4: 20 mL kg^{-1} intravenous bolus of 6% hydroxyethyl starch (colloid). Data were collected at three timepoints in each step: immediately before performing the modified passive leg raise (PLR_M) maneuver (Pre-PLR_M), 5 min after PLR_M (PLR_M), and 5 min after the abdomen and limbs were returned to the horizontal position (Post-PLR_M).

underestimation at higher CO values. Overall, good agreement emerged between TEE, EC, and iPATD, with only a few observations falling outside the limits of agreement, and bias magnitude relatively small across a range of CO values. BA analysis for ED_{CO} (Figure 4C) showcased a very weak negative trend (slope = −0.04; intercept = −0.59) between bias and average CO data, suggesting uniform bias distribution across a broad CO range, with a relatively higher magnitude of consistent overestimation. $APWA_{CO}$ BA analysis (Figure 4D) demonstrated a strong negative trend (slope = −0.46; intercept = 0.30) between bias and average CO data, indicating consistent overestimation across a wide CO range, with bias increasing at higher CO values. Consequently, only satisfactory agreement was observed between ED, APWA, and iPATD, with a few observations lying outside the limits of agreement.

Polar plot analysis revealed strong trending patterns for TEE_{CO} (Figure 5A), EC_{CO} (Figure 5B), and ED_{CO} (Figure 5C), with <20% of data points situated outside the limits of good agreement (i.e., 10% = 0.198 Lmin-1 as mean $iPATD_{CO}$ = 1.98 Lmin-1). Contrarily, the trending ability of $APWA_{CO}$ was poor, with >50% of data points located outside the limits of good agreement, as depicted in the polar plot (Figure 5D).

4. Discussion

During the past two decades, the dependability of the passive leg-raising test has been substantiated across a diverse range of human patients, including those with sepsis in line with the Surviving Sepsis Campaign (45), and in patients with COVID-19 manifesting with acute respiratory failure (46). Furthermore, its predictive efficacy persists in patients featuring spontaneous ventilation, cardiac arrhythmias, and right ventricular failure (2, 47). A novel adaptation of the traditional passive leg raise has recently been applied to veterinary contexts, wherein both the pelvic limbs and caudal abdomen are elevated, prompting a significant redistribution of blood volume from the caudal region toward the central compartment. In healthy mechanically ventilated isoflurane-anesthetized pigs (21) and Beagle dogs (22), employing the PLR_M maneuver at angles of 15° and 30° accurately gaged FR during acute hemorrhagic shock, yielding an increase in $iPATD_{CO}$ of more than 30% (pigs) and 28% (dogs), respectively. In instances of euvolemia and hypervolemia, marginal variations in CO were observed, indicating fluid nonresponsiveness. Remarkably, the percentage CO increase attributed to PLR_M surpassed the conventional 15% benchmark from human studies (2–4), highlighting the credibility of outcomes in these two animal studies (21, 22). In our investigation, as we examined the impact of PLR_M amidst moderate–severe hypovolemia, TEE, EC, and ED successfully diagnosed FR by detecting a > 15% CO elevation, akin to the reference iPATD method. Other hemodynamic variables derived from EC (such as SVV) and ED (such as SDV and PVV) exhibited close alignment with fluctuations in $iPATD_{CO}$ values stemming from abrupt blood volume shifts and responses to the PLR_M maneuver. This correspondence harmonizes with previously reported canine literature (25, 27, 48–50). The TEE, ED, and EC displayed an acceptable percentage error range, while APWA exhibited the lowest Lin's concordance. Generally, TEE and EC displayed good agreement with iPATD, maintaining a consistent trending pattern across a broad spectrum of CO values.

A comprehensive meta-analysis conducted on critically ill human patients, exploring the prognostic value of CO changes induced by the passive leg raising (at angles of 30–45°), reported pooled sensitivity and specificity values of 89.4 and 91.4%, respectively, based on the analysis of 351 fluid boluses. The pooled area under the curve stood at 0.95, with the prediction threshold for fluid responsiveness ranging from 8 to 15%. The alterations in CO resulting from the passive leg raise test correlated well with the CO increase facilitated

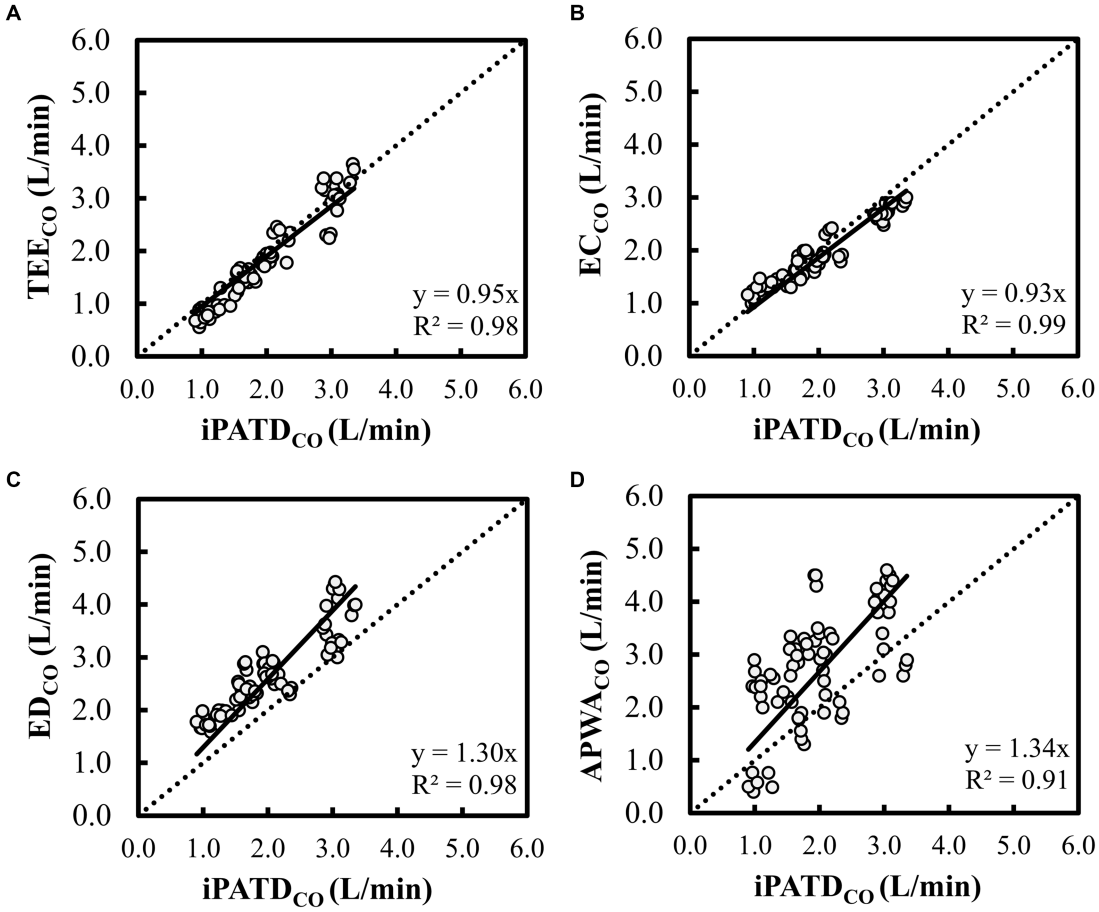

FIGURE 3
Scatterplot of cardiac output (CO) measurements using **(A)** transesophageal echocardiography (TEE_{CO}), **(B)** electrical cardiometry (EC_{CO}), **(C)** esophageal Doppler (ED_{CO}), and **(D)** arterial pressure waveform analysis ($APWA_{CO}$) against the reference method intermittent pulmonary artery thermodilution ($iPATD_{CO}$) in six healthy, anesthetized dogs across three timepoints (before, during, and after the modified passive leg raise maneuver) and during sequential acute manipulations to the blood volume, thus yielding 72 paired observations (circles) per test method. The dotted line equates to the best-fit correlation. When compared with $iPATD_{CO}$ measurements, TEE_{CO} and EC_{CO} displayed consistent slight underprediction (slope < 1 about Y = X on regression line), while ED_{CO} and $APWA_{CO}$ showed constant significant overprediction of $iPATD_{CO}$ measurements (slope > 1 about Y = X on regression line).

by fluid infusion, effectively distinguishing between fluid responders and nonresponders (12). Correspondingly, Monnet et al. (14) identified 21 studies encompassing 991 adult patients, scrutinizing the hemodynamic effects of 995 fluid challenges. The study yielded a notably significant pooled correlation coefficient of 0.76 ($p < 0.001$) between CO readings influenced by the test and those by fluid administration. The optimal threshold mean was a CO elevation of more than 10 ± 2%, reflective of test performance. Across multiple clinical trials (12–15), primary variables for precise hemodynamic response detection encompassed CO, cardiac index, stroke volume, stroke volume index, or aortic blood flow. The techniques commonly employed for direct measurement of these variables involved calibrated pulse contour analysis, echocardiography, ED, iPATD, transpulmonary thermodilution, bioimpedance, bioreactance, and APWA. Therefore, the advanced hemodynamic monitoring techniques selected for our study were iPATD (considered the gold standard), TEE, EC, ED, and APWA, ensuring congruence with published human patient findings.

Minimally invasive TEE not only delivers precise, swift, and reliable CO measurements but also assesses derived parameters such as respiratory variations in superior and inferior vena cava diameter, maximal Doppler velocity in the LVOT, left ventricular ejection fraction, LVOT velocity–time integral, and ventricular end-diastolic area ratio. These parameters have demonstrated utility in investigating the effects of the passive leg raise test within human medicine (51). While TEE's specific evaluation for FR in dogs has not been explored, its precision in CO estimation is well documented (52). Nonetheless, TEE does entail substantial training, skill, and high equipment costs, rendering it potentially less accessible at the bedside. Conversely, noninvasive EC is extensively employed in both adults and children owing to its simplicity, convenience, and continuous hemodynamic monitoring. However, its diagnostic value in the context of the passive leg raise test remains relatively unexplored. In pediatric patients undergoing cardiac surgery, EC-derived stroke volume and cardiac index were evaluated for FR prediction and effectiveness of the passive leg raise test, demonstrating accuracy in guiding

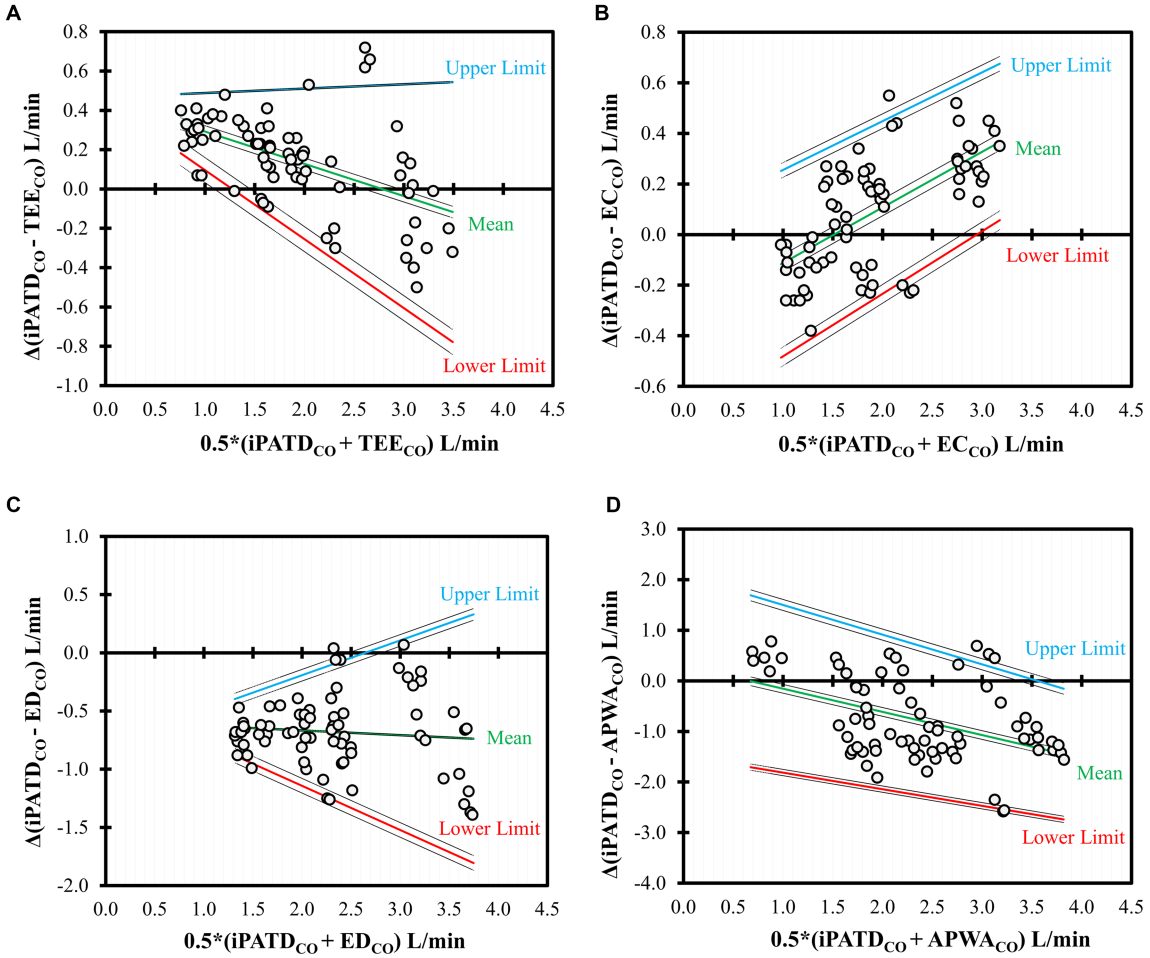

FIGURE 4
Bland–Altman analysis of the nonuniform differences in cardiac output (CO) measurements using **(A)** transesophageal echocardiography (TEE_{CO}), **(B)** electrical cardiometry (EC_{CO}), **(C)** esophageal Doppler (ED_{CO}), and **(D)** arterial pressure waveform analysis ($APWA_{CO}$) as compared with the reference method intermittent pulmonary artery thermodilution ($iPATD_{CO}$) in six healthy, anesthetized dogs across three timepoints (before, during, and after the modified passive leg raise maneuver) and during sequential acute manipulations to the blood volume, which yielded 72 paired observations (circles) per test method. Each circle represents an individual comparison of the difference with the mean, and the central line represents the nonuniform mean bias of the difference. The solid lines indicate the mean (green) as well as the upper (blue) and lower (red) limits of agreement, and the dashed lines indicate the 95% confidence intervals around these values.

circulatory function (53). Similarly, thoracic electrical bioimpedance cardiography exhibited good discriminatory ability in predicting responders to the passive leg raise in critical situations. Among key parameters, a secondary derivative of impedance wave slope displayed the highest predictive capacity for responder identification (54). It is essential to note that the EC technique's Electrical Velocimetry™ model leverages the volume of electrically participating tissue based on anthropometric measures such as body mass and height, to estimate the electrically participating volume of the thorax. Predominantly influenced by patient weight, the mass-based volumetric equivalent of thoracic blood volume was determined using human subjects in both stable normal states and unstable cardiopulmonary disease states (55, 56). Consequently, the translation of this patient constant, derived from human data, to canines might account for potential errors reported in our EC analysis. Overall, the performance of TEE and EC in our study dogs indicated these methods could be used interchangeably with iPATD in assessing the PLR_M maneuver.

When interpreting ED_{CO} values, despite the percentage error remaining within acceptable bounds, this method consistently exhibited an overestimation of $iPATD_{CO}$ measurements and displayed lower data reproducibility. Notably, the precision of measuring descending aortic blood velocity is significantly influenced by the alignment between the Doppler ultrasound beam and blood flow direction, termed the angle of insonation (57, 58). When employing ED, the sole approach to ensuring precise alignment lies in optimizing signal quality, manifested as a constant, distinct aortic waveform featuring the highest peak velocity, accompanied by a pronounced pitch "whip crack" sound. As the angle between the Doppler beam and blood flow widens, the inaccuracy in blood velocity measurements escalates due to the cosine error in the Doppler equation, coupled with deviation from the assumed angle of insonation (57–59). Furthermore,

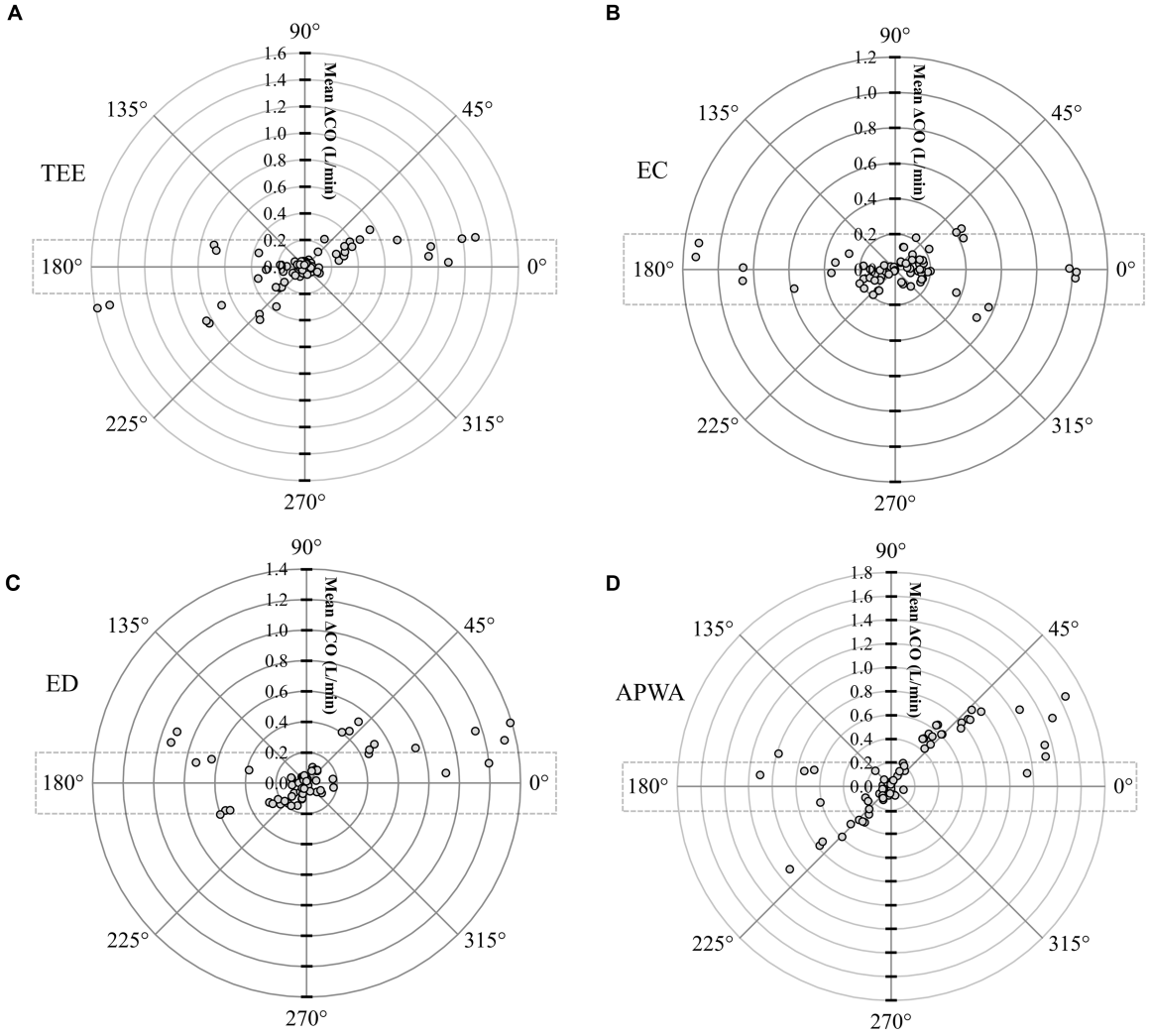

FIGURE 5
Polar plot representing changes in cardiac output (CO) measurements evaluated by **(A)** transesophageal echocardiography (TEE_{CO}), **(B)** electrical cardiometry (EC_{CO}), **(C)** esophageal Doppler (ED_{CO}), and **(D)** arterial pressure waveform analysis ($APWA_{CO}$) as compared with the reference method intermittent pulmonary artery thermodilution ($iPATD_{CO}$) in six healthy, anesthetized dogs across three timepoints (before, during, and after the modified passive leg raise maneuver) and during sequential acute manipulations to the blood volume, thus yielding 72 paired observations (circles) per test method. Dotted lines represent 10% agreement boundaries (i.e., 10% = 0.198 L m i n - 1 as mean $iPATD_{CO}$ = 1.98 L m i n - 1). The distance from the center represents the absolute values of the mean change in CO (|ΔiPATD$_{CO}$ + ΔTest method CO|/2), and the angle from the horizontal 0° radial axis represents the disagreement. Polar plot analysis revealed a good trending pattern for TEE_{CO}, EC_{CO}, and ED_{CO} across the wide range of CO values, as <20% of the data points were located outside the limits of good agreement. By contrast, the trending ability of $APWA_{CO}$ was poor, as >50% of the data points were located outside the limits of good agreement.

the ED veterinary monitoring system (CardioQ-EDMV+) lacks direct CO display, necessitating the use of the TEE-measured cross-sectional area of the LVOT to calculate ED_{CO}, as previously described in dogs (39). In contrast to TEE, however, the ED_{CO} probe tip location, and consequently the flow traces' origin, do not stem from the LVOT but from a segment of the descending aorta. Additionally, the potential discrepancy between the LVOT area and descending aorta area, the location where ED_{CO} traces were derived, could introduce variability and error into measurements. The ED human monitoring system (Cardio-Q ODM+) provides continuous CO measurements grounded in a human nomogram derived from patient age, height, and weight, correlating with the relationship between descending aortic blood velocity and $iPATD_{CO}$ values (58). When used in animals, this human-based monitor might contribute to inaccurate CO evaluations.

Another CO measurement technique displaying substantial percentage error, low concordance, consistent $iPATD_{CO}$ overestimation, and poor trending capacity was APWA. Several factors might have contributed to the heightened proportion of miscalculations seen with APWA. Lithium dilution serves as the preferred CO calibration method for the PulseCO algorithm, enabling beat-to-beat CO monitoring through a lithium-selective electrode sensor connected to a standard arterial line setup. Nondepolarizing muscle relaxants, however, can interact with the lithium sensor, leading to drift and calibration interference (60). Given that rocuronium bolus followed by constant rate infusion was administered throughout the study, its influence on $APWA_{CO}$ values cannot be disregarded. During hemodynamic fluctuations, recalibration for the LiDCO system is advised with major shifts (35). In our study,

recalibration was conducted only three times (before Steps 1, 3, and 4). We speculate that the PLR_M maneuver, particularly during hypovolemia, introduced significant hemodynamic shifts, evident in an $iPATD_{CO}$ increase exceeding 30%. This could potentially contribute to $APWA_{CO}$ errors. The PulseCO algorithm transforms the arterial pressure waveform into a volume-time waveform through autocorrelation and subsequently assesses the effective value using the root mean square approach. The "nominal stroke volume" is estimated during aortic ejection and equated with actual stroke volume through independent lithium dilution CO measurements (35, 61). An alternative scaling method entails employing a calibration factor based on a human nomogram derived from patient age, height, and weight. This accounts for vascular tree compliance specific to a given blood pressure (35, 62). However, direct application of this nomogram to veterinary species may not be appropriate. An inherent challenge of this method lies in the repeated lithium injections necessary for CO estimation, carrying a risk of lithium accumulation. It is worth noting that subpar performance of APWA has been reported in dogs (31, 63) and ponies (64) in previous studies.

Cardiac preload hinges upon the pressure gradient between mean systemic filling pressure and the right atrium, alongside vascular resistance. A considerable pressure gradient coupled with lower right atrial pressure corresponds to higher preload. Mean systemic filling pressure propels forward flow toward the right atrium, influenced by global blood volume and vascular compliance (9, 65). A specific resting fluid volume termed the "unstressed volume," occupies the vascular bed without exerting force on vessel walls or contributing to venous flow. By contrast, the "stressed volume" stretches vessel walls, exerting an outward force that facilitates fluid movement from vessels (9, 65). The Frank-Starling cardiac function curve stipulates that when ventricular preload increases, the interaction between actin and myosin filaments intensifies, bolstering intrinsic cardiac contractility and CO. However, if myofilaments stretch beyond their maximum length, increased cardiac preload has no impact on CO, defining the ventricles as "preload unresponsive" (2–5). At this juncture, a fluid challenge might escalate stressed volume and mean systemic filling pressure, albeit to a lesser extent than right atrial pressure. This scenario risks volume overload (65). The passive leg-raising test rapidly and temporarily redistributes fluids within the vasculature, without altering total vascular volume. This maneuver taps into part of the resting volume in the venous reservoir of the lower body, converting unstressed volume into stressed volume (17). As stressed volume increases, mean systemic filling pressure surges, subsequently elevating right ventricular preload. If the right ventricle is fluid responsive, CO on the right side and left ventricular filling witness an increase (2, 16, 17). Conversely, in cases of fluid nonresponsiveness, the "self-transfusion" effect of leg raising boosts right atrial pressure but fails to elevate cardiac preload and CO. A significant advantage over fluid challenges is that the "virtual" bolus effects of leg raising can be swiftly reversed by returning the legs to a horizontal position (2, 17). The transient and reversible nature of the PLR_M maneuver hemodynamic effects was also evident in our study. Following acute hemorrhage, when the legs and caudal abdomen were repositioned (Post-PLR_M), $iPATD_{CO}$ measurements and variables such as SVV, SDV, and PVV values reverted to those recorded prior to the maneuver (Pre-PLR_M).

The intensity of the hemodynamic response triggered by the passive leg raise test hinges on the extent to which unstressed volume from the lower body's venous reservoir is redirected toward the cardiac ventricles, manifesting as a significant rise in venous return and CO. In human patients, this test can be executed using two methods: (1) beginning from a 45° semirecumbent position, then lowering the head and upper torso to lie supine while simultaneously elevating the legs at a 45° angle; and (2) initiating from a supine (horizontal) position and elevating the legs to a 30° to 45° angle (15). Upon comparison, researchers found that the supine position recruited approximately 300 mL of unstressed blood volume, whereas the semirecumbent position recruited approximately 450–500 mL of unstressed volume (2, 15, 19). The semirecumbent-initiated leg raise led to significantly higher central venous pressure and CO values compared with the supine-initiated leg raise, indicating the starting effect of the position on the preload change. In the 45° semirecumbent position, this phenomenon can be attributed to the greater transfer of unstressed venous blood volume from both the legs and the splanchnic compartment due to simultaneous trunk lowering and leg raising (2, 19). The adaptation of the passive leg raise test to animals drew inspiration from these human findings, while also accounting for potential differences in limb conformation, size, and blood volume distribution between humans and quadrupeds. Although the exact volume autotransfused by the PLR_M maneuver in pigs (21) and dogs (22) is undisclosed, the substantial $iPATD_{CO}$ increase of ≈33% observed in our study during hypovolemia corroborates: (1) significant recruitment of unstressed blood volume from the pelvic limb and caudal abdomen venous reservoirs; (2) substantial conversion of unstressed blood to stressed blood by PLR_M; and (3) preload responsiveness exhibited by both ventricles. The angle of inclination used for the PLR_M maneuver in our study was consistent with the established standard in dogs (22). In accordance with extensive human literature, it is recommended to assess the response to the passive leg raise within 90 s of test initiation due to its short-term circulatory effects; extending leg elevation does not preserve these effects (2, 16, 17). Data acquisition times (immediately before and 5 min after PLR_M, and 5 min after returning the pelvic limbs and abdomen to their original positions) were aligned with the canine study, which demonstrated key hemodynamic changes within this timeframe. Continuous measurement of cardiovascular variables such as stroke distance, SDV, PVV, SVV, and EC_{CO} was maintained throughout the 5-min period. Based on data evaluation, we believe that the PLR_M maneuver induces a stable hemodynamic state lasting at least 5 min, although it remains unclear whether, after this period, the heart gradually adjusts to the new volume status or the effects start to diminish, potentially complicating their capture.

In the context of fluid administration decision-making, a pivotal question arises: does preload responsiveness invariably correlate with fluid resuscitation, while nonresponsiveness mandates fluid avoidance? Changes in cardiac contractility and afterload not only shift the Frank-Starling curve but also impact cardiac performance for a given preload. As a result, the ventricle does not operate on a single Frank-Starling curve; rather, a family of curves exists, characterized by inotropy and afterload (2, 5). Clinically, during acute absolute hypovolemia, a positive CO response to a fluid challenge can be anticipated, with the patient's ventricles operating on the steeper portion of the Frank-Starling curve. However, fluid responsiveness does not always signify hypovolemia, and such patients may not require volume expansion. This concept was demonstrated in earlier

canine studies (66, 67), where CO increased post-volume resuscitation in euvolemic, nonhypotensive, anesthetized dogs. Fluids augment the stressed venous volume, and considering the higher vascular capacitance of the venous system relative to the arterial system, a positive response to fluids that augment CO might be a normal physiological reaction. While the body is equipped to counter hypovolemia through homeostatic mechanisms, managing volume overload poses greater challenges. The absolute necessity for volume infusion must be assessed alongside the risks of fluid administration. The juxtaposition of the Frank-Starling curve and the Marik-Philips curve underscores the need to evaluate the effect of increasing preload and CO on extravascular lung water in fluid responders and nonresponders (8, 9). As a patient's capacity to respond to fluids diminishes, extravascular lung water increases significantly due to elevated cardiac filling pressures and transmitted hydrostatic pressures (4).

Several factors may influence the response to the PLR_M maneuver, as indicated by human studies investigating the passive leg raise test (2, 12–15). Pain, autonomic stimulation, and vasoactive medications could alter the maneuver's response. Patients with elevated intra-abdominal pressure might not be suitable candidates for the test, as PLR_M could exacerbate intra-abdominal hypertension and yield false results by interrupting caudal vena cava flow. Additionally, splanchnic blood volume recruited by the test could decrease in the presence of intra-abdominal hypertension (5, 16, 17). While keeping the thorax in the horizontal plane during PLR_M might reduce the risk of gastro-esophageal reflux, this requires further investigation. Furthermore, due to positional differences between PLR_M in our study and passive leg raise test in humans, it's worth exploring whether PLR_M minimally affects intracerebral pressure and is safe to perform during head trauma. Considering that handling stress and anxiety can trigger sympathetic stimulation, utilizing PLR_M might not be feasible in awake canine patients, necessitating an examination of anesthetic and sedative influences on the test. Patients with pelvic and hindlimb fractures and hindleg amputations should not undergo PLR_M. The response to the maneuver could also be altered during vasodilation and vasoconstriction due to variations in unstressed blood volume relative to stressed volume, as well as the availability of blood in the venous reservoir (2, 17). Executing PLR_M in the operating theater or during imaging procedures might not be practical for diagnosing FR. This simple, valuable, and cost-effective assessment tool could prove diagnostically valuable in clinical scenarios involving canine patients that are spontaneously breathing or mechanically ventilated, devoid of intra-abdominal hypertension, and experiencing: (1) arrhythmias; (2) hemodynamic collapse due to trauma; (3) absolute hypovolemia; (4) sepsis; or (5) admission to intensive care units, enabling repeated FR assessment without the risk of inducing pulmonary edema or cor pulmonale in potential fluid nonresponders.

Our study has several limitations. The small sample size is a notable constraint. The stepwise approach for acute blood volume manipulation was not randomized; its fixed sequence was crucial for detecting FR by PLR_M and the responsiveness of the tested CO methods. If hypervolemia preceded hypovolemia, crossover effects would significantly affect hemodynamics and our study data. The minimally invasive or noninvasive CO measurement techniques (EC, APWA, TEE, and ED) were selected based on current literature on CO monitoring in canines. It is acknowledged that while these techniques are less invasive and easy to learn, they may be costly for clinical practices and not universally available. Hence, other CO monitoring methods such as transpulmonary thermodilution, bioreactance, transpulmonary ultrasound dilution, and partial carbon dioxide rebreathing should be evaluated during PLR_M for their potential applicability in clinical settings. While integrating EC, ED, and APWA into veterinary species, careful scrutiny is needed regarding the mathematical models' application based on human data for animals. The study involved healthy canines weighing approximately 10 kg placed in dorsal recumbency. Further clinical exploration is imperative to demonstrate the application of these CO measurement techniques during PLR_M in critically ill canine patients, encompassing different sizes, breeds, limb conformations, relative hypovolemia, and septic shock.

5. Conclusion

This study represents one of the first exploratory efforts to assess minimally invasive or noninvasive CO measurement techniques potentially substituting the invasive gold standard iPATD during PLR_M response evaluation in anesthetized healthy dogs undergoing acute blood volume manipulation. TEE, EC, and ED effectively diagnosed FR in hypovolemic dogs during this maneuver by detecting CO increases of >15%. Percentage error for TEE, ED, and EC fell within acceptable ranges, whereas it exceeded 55% for APWA. Moreover, TEE, EC, and iPATD exhibited good agreement, suggesting potential clinical applicability. Also, TEE_{CO}, EC_{CO}, and ED_{CO} displayed a satisfactory trending pattern across the range of CO values in our study dogs. Lin's concordance was the highest for TEE and EC, followed by ED, and lowest for APWA. Further studies are essential to validate the constancy of TEE, EC, and ED performance across diverse clinical canine populations when applied during this maneuver.

Data availability statement

The original contributions presented in the study are included in the article/supplementary material, further inquiries can be directed to the corresponding author.

Ethics statement

The animal study was approved by Virginia Tech University-Institutional Animal Care and Use Committee (protocol number 20-235). The study was conducted in accordance with the local legislation and institutional requirements.

Author contributions

VP: conception and study design, funding acquisition, execution and supervision of the study, animal care and management, training for the selected cardiac output techniques, data collection, data

interpretation, original manuscript draft preparation, and artwork. NH-G and GM: data collection, review, and editing during manuscript preparation. SS: statistical analysis, data interpretation, review and editing during manuscript preparation, and figures for data presentation. All authors contributed to the article and approved the submitted version.

Funding

This study was funded by the Virginia-Maryland College of Veterinary Medicine-Veterinary Memorial Fund (grant no. 446641) and Virginia Polytechnic Institute and State University (fund no. 178592).

Acknowledgments

We thank Andre C. Shih and Fernando Garcia-Pereira for contributing to early study planning, Hyeon Jeong for helping with data collection, and Jordi Mauragis for assistance with creating graphical artwork. We would also like to thank Markus Osypka (ICON monitor; Osypka Medical Inc., CA, USA), Andy Mears (CardioQ-EDMV+ esophageal Doppler monitor; Deltex Medical, West Sussex, UK), and Janet K. Tate (LiDCOplus monitor; LiDCO Ltd., Cambridge, UK) for providing expertise and training for the equipment utilized in this study.

Conflict of interest

The authors declare that the research was conducted in the absence of any commercial or financial relationships that could be construed as a potential conflict of interest.

Publisher's note

References

1. Hall K, Drobatz K. Volume resuscitation in the acutely hemorrhaging patient: historic use to current applications. *Front Vet Sci*. (2021) 8:638104. doi: 10.3389/fvets.2021.638104

2. Monnet X, Shi R, Teboul JL. Prediction of fluid responsiveness. What's new? *Ann Intensive Care*. (2022) 12:46. doi: 10.1186/s13613-022-01022-8

3. Cherpanath TG, Geerts BF, Lagrand WK, Schultz MJ, Groeneveld AB. Basic concepts of fluid responsiveness. *Neth Heart J*. (2013) 21:530–6. doi: 10.1007/s12471-013-0487-7

4. Marik PE, Lemson J. Fluid responsiveness: an evolution of our understanding. *Br J Anaesth*. (2014) 112:617–20. doi: 10.1093/bja/aet590

5. Marik PE, Monnet X, Teboul JL. Hemodynamic parameters to guide fluid therapy. *Ann Intensive Care*. (2011) 1:1. doi: 10.1186/2110-5820-1-1

6. Osman D, Ridel C, Ray P, Monnet X, Anguel N, Richard C, et al. Cardiac filling pressures are not appropriate to predict hemodynamic response to volume challenge. *Crit Care Med*. (2007) 35:64–8. doi: 10.1097/01.CCM.0000249851.94101.4F

7. Marik PE, Cavallazzi R. Does the central venous pressure predict fluid responsiveness? An updated meta-analysis and a plea for some common sense. *Crit Care Med*. (2013) 41:1774–81. doi: 10.1097/CCM.0b013e31828a25fd

8. Araos J, Kenny JS, Rousseau-Blass F, Pang DS. Dynamic prediction of fluid responsiveness during positive pressure ventilation: a review of the physiology underlying heart-lung interactions and a critical interpretation. *Vet Anaesth Analg*. (2020) 47:3–14. doi: 10.1016/j.vaa.2019.08.004

9. Boysen SR, Gommeren K. Assessment of volume status and fluid responsiveness in small animals. *Front Vet Sci*. (2021) 8:630643. doi: 10.3389/fvets.2021.630643

10. Marik PE, Cavallazzi R, Vasu T, Hirani A. Dynamic changes in arterial waveform derived variables and fluid responsiveness in mechanically ventilated patients: a systematic review of the literature. *Crit Care Med*. (2009) 37:2642–7. doi: 10.1097/CCM.0b013e3181a590da

11. Michard F, Chemla D, Teboul JL. Applicability of pulse pressure variation: how many shades of grey? *Crit Care*. (2015) 19:144. doi: 10.1186/s13054-015-0869-x

12. Cavallaro F, Sandroni C, Marano C, La Torre G, Mannocci A, De Waure C, et al. Diagnostic accuracy of passive leg raising for prediction of fluid responsiveness in adults: systematic review and meta-analysis of clinical studies. *Intensive Care Med*. (2010) 36:1475–83. doi: 10.1007/s00134-010-1929-y

13. Cherpanath TG, Hirsch A, Geerts BF, Lagrand WK, Leeflang MM, Schultz MJ, et al. Predicting fluid responsiveness by passive leg raising: a systematic review and meta-analysis of 23 clinical trials. *Crit Care Med*. (2016) 44:981–91. doi: 10.1097/CCM.0000000000001556

14. Monnet X, Marik P, Teboul JL. Passive leg raising for predicting fluid responsiveness: a systematic review and meta-analysis. *Intensive Care Med*. (2016) 42:1935–47. doi: 10.1007/s00134-015-4134-1

15. Pickett JD, Bridges E, Kritek PA, Whitney JD. Passive leg-raising and prediction of fluid responsiveness: systematic review. *Crit Care Nurse*. (2017) 37:32–47. doi: 10.4037/ccn2017205

16. Monnet X, Teboul JL. Passive leg raising: five rules, not a drop of fluid! *Crit Care*. (2015) 19:18. doi: 10.1186/s13054-014-0708-5

17. Monnet X, Teboul JL. Passive leg raising. *Intensive Care Med*. (2008) 34:659–63. doi: 10.1007/s00134-008-0994-y

18. Rutlen DL, Wackers FJ, Zaret BL. Radionuclide assessment of peripheral intravascular capacity: a technique to measure intravascular volume changes in the capacitance circulation in man. *Circulation*. (1981) 64:146–52. doi: 10.1161/01.cir.64.1.146

19. Jabot J, Teboul JL, Richard C, Monnet X. Passive leg raising for predicting fluid responsiveness: importance of the postural change. *Intensive Care Med*. (2009) 35:85–90. doi: 10.1007/s00134-008-1293-3

20. Dragoumanos V, Iacovidou N, Chalkias A, Lelovas P, Koutsovasilis A, Papalois A, et al. Passive leg raising during cardiopulmonary resuscitation results in improved neurological outcome in a swine model of prolonged ventricular fibrillation. *Am J Emerg Med*. (2012) 30:1935–42. doi: 10.1016/j.ajem.2012.04.014

21. Paranjape VV, Shih AC, Garcia-Pereira FL. Use of a modified passive leg-raising maneuver to predict fluid responsiveness during experimental induction and correction of hypovolemia in healthy isoflurane-anesthetized pigs. *Am J Vet Res*. (2019) 80:24–32. doi: 10.2460/ajvr.80.1.24

22. Paranjape VV, Henao-Guerrero N, Menciotti G, Saksena S. Volumetric evaluation of fluid responsiveness using a modified passive leg raise maneuver during experimental induction and correction of hypovolemia in anesthetized dogs. *Vet Anaesth Analg*. (2023) 50:211–9. doi: 10.1016/j.vaa.2023.02.009

23. Garofalo NA, Teixeira-Neto FJ, Rodrigues JC, Cerejo SA, Aguiar AJ, Becerra-Velásquez DR. Comparison of transpulmonary thermodilution and calibrated pulse contour analysis with pulmonary artery thermodilution cardiac output measurements in anesthetized dogs. *J Vet Intern Med*. (2016) 30:941–50. doi: 10.1111/jvim.13984

24. Paranjape VV, Shih AC, Garcia-Pereira FL, Saksena S. Transpulmonary ultrasound dilution is an acceptable technique for cardiac output measurement in anesthetized pigs. *Am J Vet Res*. (2022) 83:83. doi: 10.2460/ajvr.21.11.0189

25. Paranjape VV, Henao-Guerrero N, Menciotti G, Saksena S. Esophageal doppler-derived indices and arterial load variables provide useful hemodynamic information during assessment of fluid responsiveness in anesthetized dogs undergoing acute changes in blood volume. *Am J Vet Res*. (2023) 84:84. doi: 10.2460/ajvr.22.11.0198

26. Evans DC, Doraiswamy VA, Prosciak MP, Silviera M, Seamon MJ, Rodriguez Funes V, et al. Complications associated with pulmonary artery catheters: a comprehensive clinical review. *Scand J Surg*. (2009) 98:199–208. doi: 10.1177/145749690909800402

27. Sasaki K, Mutoh T, Mutoh T, Kawashima R, Tsubone H. Electrical velocimetry for noninvasive cardiac output and stroke volume variation measurements in dogs undergoing cardiovascular surgery. *Vet Anaesth Analg*. (2017) 44:7–16. doi: 10.1111/vaa.12380

28. Osthaus WA, Huber D, Beck C, Winterhalter M, Boethig D, Wessel A, et al. Comparison of electrical velocimetry and transpulmonary thermodilution for measuring cardiac output in piglets. *Paediatr Anaesth*. (2007) 17:749–55. doi: 10.1111/j.1460-9592.2007.02210.x

29. Paranjape VV, Henao-Guerrero N, Menciotti G, Saksena S, Agostinho M. Agreement between electrical cardiometry and pulmonary artery thermodilution for measuring cardiac output in isoflurane-anesthetized dogs. *Animals (Basel)*. (2023) 13:1420. doi: 10.3390/ani13081420

30. Valverde A, Gianotti G, Rioja E, Hathway A. Comparison of cardiac output determined by arterial pulse pressure waveform analysis method (Flotrac/Vigileo) versus lithium dilution method in anesthetized dogs. *J Vet Emerg Crit Care (San Antonio)*. (2011) 21:328–34. doi: 10.1111/j.1476-4431.2011.00650.x

31. Cooper ES, Muir WW. Continuous cardiac output monitoring via arterial pressure waveform analysis following severe hemorrhagic shock in dogs. *Crit Care Med*. (2007) 35:1724–9. doi: 10.1097/01.CCM.0000266590.25109.F2

32. Linton RA, Band DM, Haire KM. A new method of measuring cardiac output in man using lithium dilution. *Br J Anaesth*. (1993) 71:262–6. doi: 10.1093/bja/71.2.262

33. Chen HC, Sinclair MD, Dyson DH, McDonell WN, Sears WC. Comparison of arterial pressure waveform analysis with the lithium dilution technique to monitor cardiac output in anesthetized dogs. *Am J Vet Res*. (2005) 66:1430–6. doi: 10.2460/ajvr.2005.66.1430

34. Rhodes A, Sunderland R. *Editors. Arterial pulse power analysis: The LiDCOM plus system*. Berlin, Heidelberg: Springer Berlin Heidelberg (2005).

35. Montenij LJ, de Waal EE, Buhre WF. Arterial waveform analysis in anesthesia and critical care. *Curr Opin Anaesthesiol*. (2011) 24:651–6. doi: 10.1097/ACO.0b013e32834cd2d9

36. Puchalski MD, Lui GK, Miller-Hance WC, Brook MM, Young LT, Bhat A, et al. Guidelines for performing a comprehensive transesophageal echocardiographic: examination in children and all patients with congenital heart disease: recommendations from the American Society of Echocardiography. *J Am Soc Echocardiogr*. (2019) 32:173–215. doi: 10.1016/j.echo.2018.08.016

37. Domenech O, Oliveira P. Transoesophageal echocardiography in the dog. *Vet J*. (2013) 198:329–38. doi: 10.1016/j.tvjl.2013.08.014

38. Porter TR, Shillcutt SK, Adams MS, Desjardins G, Glas KE, Olson JJ, et al. Guidelines for the use of echocardiography as a monitor for therapeutic intervention in adults: a report from the American Society of Echocardiography. *J Am Soc Echocardiogr*. (2015) 28:40–56. doi: 10.1016/j.echo.2014.09.009

39. Canfrán S, Cediel R, Sández I, Caro-Vadillo A, Gómez de Segura IA. Evaluation of an oesophageal Doppler device for monitoring cardiac output in anaesthetised healthy normotensive dogs. *J Small Anim Pract*. (2015) 56:450–5. doi: 10.1111/jsap.12362

40. Critchley LA, Critchley JA. A meta-analysis of studies using bias and precision statistics to compare cardiac output measurement techniques. *J Clin Monit Comput*. (1999) 15:85–91. doi: 10.1023/a:1009982611386

41. Lin LI. A concordance correlation coefficient to evaluate reproducibility. *Biometrics*. (1989) 45:255–68. doi: 10.2307/2532051

42. Bland JM, Altman DG. Statistical methods for assessing agreement between two methods of clinical measurement. *Lancet*. (1986) 47:931–6. doi: 10.1016/j.ijnurstu.2009.10.001

43. Critchley LA, Lee A, Ho AM. A critical review of the ability of continuous cardiac output monitors to measure trends in cardiac output. *Anesth Analg*. (2010) 111:1180–92. doi: 10.1213/ANE.0b013e3181f08a5b

44. Critchley LA, Yang XX, Lee A. Assessment of trending ability of cardiac output monitors by polar plot methodology. *J Cardiothorac Vasc Anesth*. (2011) 25:536–46. doi: 10.1053/j.jvca.2011.01.003

45. Evans L, Rhodes A, Alhazzani W, Antonelli M, Coopersmith CM, French C, et al. Surviving sepsis campaign: international guidelines for management of sepsis and septic shock 2021. *Crit Care Med*. (2021) 49:e1063–143. doi: 10.1097/CCM.0000000000005337

46. Hasanin A, Mostafa M. Evaluation of fluid responsiveness during Covid-19 pandemic: what are the remaining choices? *J Anesth*. (2020) 34:758–64. doi: 10.1007/s00540-020-02801-y

47. Van de Bovenkamp AA, Wijkstra N, Oosterveer FPT, Vonk Noordegraaf A, Bogaard HJ, van Rossum AC, et al. The value of passive leg raise during right heart catheterization in diagnosing heart failure with preserved ejection fraction. *Circ Heart Fail*. (2022) 15:e008935. doi: 10.1161/CIRCHEARTFAILURE.121.008935

48. Sasaki K, Mutoh T, Mutoh T, Taki Y, Kawashima R. Noninvasive stroke volume variation using electrical velocimetry for predicting fluid responsiveness in dogs undergoing cardiac surgery. *Vet Anaesth Analg*. (2017) 44:719–26. doi: 10.1016/j.vaa.2016.11.001

49. Sasaki K, Mutoh T, Yamamoto S, Taki Y, Kawashima R. Utility of electrical velocimetry-based noninvasive stroke volume variation in predicting fluid responsiveness under different ventilation modes in anaesthetized dogs. *Clin Exp Pharmacol Physiol*. (2018) 45:983–8. doi: 10.1111/1440-1681.12968

50. Sasaki K, Yamamoto S, Mutoh T. Noninvasive assessment of fluid responsiveness for emergency abdominal surgery in dogs with pulmonary hypertension: insights into high-risk companion animal anesthesia. *PLoS One*. (2020) 15:e0241234. doi: 10.1371/journal.pone.0241234

51. Vignon P, Repessé X, Bégot E, Léger J, Jacob C, Bouferrache K, et al. Comparison of echocardiographic indices used to predict fluid responsiveness in ventilated patients. *Am J Respir Crit Care Med*. (2017) 195:1022–32. doi: 10.1164/rccm.201604-0844OC

52. Paranjape VV, Pereira FLG, Menciotti G, Saksena S, Guerrero NH, Pereira CHR. Agreement of cardiac output measurements by esophageal Doppler and transesophageal echocardiography with intermittent pulmonary artery thermodilution during pharmacologic manipulation of hemodynamics in anesthetized dogs. *Am J Vet Res*. (2023) 84:1–11. doi: 10.2460/ajvr.23.05.0101

53. Labib H, Hussien R, Salem Y. Monitoring the correlation between passive leg-raising maneuver and fluid challenge in pediatric cardiac surgery patients using impedance cardiography. *Egypt J Cardiothorac Anesth*. (2016) 10:17. doi: 10.4103/1687-9090.183222

54. Li L, Ai Y, Huang L, Ai M, Peng Q, Zhang L. Can bioimpedance cardiography assess hemodynamic response to passive leg raising in critically ill patients: a strobe-compliant study. *Med (Baltim)*. (2020) 99:e23764. doi: 10.1097/MD.0000000000023764

55. Bernstein D, Osypka M. Apparatus and method for determining an approximation of the stroke volume and the cardiac output of the heart. U.S. Patent, 6,511,438 B2. (2003). Available at: https://patents.google.com/patent/EP1247487A1/en (Accessed 24 February, 2023)

56. Osypka M. An introduction to electrical cardiometry. Electrical Cardiometry (2009) 46:1. Available at: https://www.osypka-asia.com/pdf/technique.pdf

57. Schober P, Loer SA, Schwarte LA. Perioperative hemodynamic monitoring with transesophageal Doppler technology. *Anesth Analg*. (2009) 109:340–53. doi: 10.1213/ane.0b013e3181aa0af3

58. Singer M. Oesophageal Doppler. *Curr Opin Crit Care*. (2009) 15:244–8. doi: 10.1097/MCC.0b013e32832b7083

59. Cholley BP, Singer M. Esophageal Doppler: noninvasive cardiac output monitor. *Echocardiography*. (2003) 20:763–9. doi: 10.1111/j.0742-2822.2003.03033.x

60. Sangkum L, Liu GL, Yu L, Yan H, Kaye AD, Liu H. Minimally invasive or noninvasive cardiac output measurement: an update. *J Anesth*. (2016) 30:461–80. doi: 10.1007/s00540-016-2154-9

61. Hendy A, Bubenek Ş. Pulse waveform hemodynamic monitoring devices: recent advances and the place in goal-directed therapy in cardiac surgical patients. *Rom J Anaesth Intensive Care*. (2016) 23:55–65. doi: 10.21454/rjaic.7518.231.wvf

62. Teboul JL, Saugel B, Cecconi M, De Backer D, Hofer CK, Monnet X, et al. Less invasive hemodynamic monitoring in critically ill patients. *Intensive Care Med*. (2016) 42:1350–9. doi: 10.1007/s00134-016-4375-7

63. Duffy AL, Butler AL, Radecki SV, Campbell VL. Comparison of continuous arterial pressure waveform analysis with the lithium dilution technique to monitor cardiac output in conscious dogs with systemic inflammatory response syndrome. *Am J Vet Res*. (2009) 70:1365–73. doi: 10.2460/ajvr.70.11.1365

64. Schauvliege S, Van den Eede A, Duchateau L, Pille F, Vlaminck L, Gasthuys F. Comparison between lithium dilution and pulse contour analysis techniques for cardiac output measurement in isoflurane anaesthetized ponies: influence of different inotropic drugs. *Vet Anaesth Analg*. (2009) 36:197–208. doi: 10.1111/j.1467-2995.2009.00446.x

65. Persichini R, Lai C, Teboul JL, Adda I, Guérin L, Monnet X. Venous return and mean systemic filling pressure: physiology and clinical applications. *Crit Care*. (2022) 26:150. doi: 10.1186/s13054-022-04024-x

66. Muir WW 3rd, Kijtawornrat A, Ueyama Y, Radecki SV, Hamlin RL. Effects of intravenous administration of lactated Ringer's solution on hematologic, serum biochemical, rheological, hemodynamic, and renal measurements in healthy isoflurane-anesthetized dogs. *J Am Vet Med Assoc*. (2011) 239:630–7. doi: 10.2460/javma.239.5.630

67. Muir WW, Ueyama Y, Pedraza-Toscano A, Vargas-Pinto P, Delrio CL, George RS, et al. Arterial blood pressure as a predictor of the response to fluid administration in euvolemic nonhypotensive or hypotensive isoflurane-anesthetized dogs. *J Am Vet Med Assoc*. (2014) 245:1021–7. doi: 10.2460/javma.245.9.1021

frontiers | Frontiers in Veterinary Science

TYPE Original Research
PUBLISHED 22 September 2023
DOI 10.3389/fvets.2023.1227009

OPEN ACCESS

EDITED BY
Mindaugas Tamosiunas,
University of Latvia, Latvia

REVIEWED BY
Roberts Kadikis,
Institute of Electronics and Computer Science, Latvia
Vykintas Samaitis,
Kaunas University of Technology, Lithuania

*CORRESPONDENCE
Tommaso Banzato
✉ tommaso.banzato@unipd.it

RECEIVED 22 May 2023
ACCEPTED 12 September 2023
PUBLISHED 22 September 2023

CITATION
Valente C, Wodzinski M, Guglielmini C, Poser H, Chiavegato D, Zotti A, Venturini R and Banzato T (2023) Development of an artificial intelligence-based method for the diagnosis of the severity of myxomatous mitral valve disease from canine chest radiographs.
Front. Vet. Sci. 10:1227009.
doi: 10.3389/fvets.2023.1227009

Development of an artificial intelligence-based method for the diagnosis of the severity of myxomatous mitral valve disease from canine chest radiographs

Carlotta Valente[1], Marek Wodzinski[2,3], Carlo Guglielmini[1], Helen Poser[1], David Chiavegato[4], Alessandro Zotti[1], Roberto Venturini[4] and Tommaso Banzato[1]*

[1]Department of Animal Medicine, Production and Health, University of Padua, Padua, Italy, [2]Department of Measurement and Electronics, AGH University of Science and Technology, Krakow, Poland, [3]Information Systems Institute, University of Applied Sciences—Western Switzerland (HES-SO Valais), Sierre, Switzerland, [4]AniCura Clinica Veterinaria Arcella, Padua, Italy

An algorithm based on artificial intelligence (AI) was developed and tested to classify different stages of myxomatous mitral valve disease (MMVD) from canine thoracic radiographs. The radiographs were selected from the medical databases of two different institutions, considering dogs over 6years of age that had undergone chest X-ray and echocardiographic examination. Only radiographs clearly showing the cardiac silhouette were considered. The convolutional neural network (CNN) was trained on both the right and left lateral and/or ventro-dorsal or dorso-ventral views. Each dog was classified according to the American College of Veterinary Internal Medicine (ACVIM) guidelines as stage B1, B2 or C+D. ResNet18 CNN was used as a classification network, and the results were evaluated using confusion matrices, receiver operating characteristic curves, and t-SNE and UMAP projections. The area under the curve (AUC) showed good heart-CNN performance in determining the MMVD stage from the lateral views with an AUC of 0.87, 0.77, and 0.88 for stages B1, B2, and C+D, respectively. The high accuracy of the algorithm in predicting the MMVD stage suggests that it could stand as a useful support tool in the interpretation of canine thoracic radiographs.

KEYWORDS

dog, heart, artificial intelligence, myxomatous mitral valve disease, radiology

1. Introduction

Myxomatous mitral valve disease (MMVD) is the most common acquired cardiac disease in small to medium-sized adult dogs. Myxomatous mitral valve disease is potentially a serious threat to canine health because in its final stages it can lead to congestive heart failure (CHF). According to the *American College of Veterinary Internal Medicine* (ACVIM), MMVD can be classified as: preclinical (referred to as stages B1 and B2) when structural cardiac abnormalities associated with MMVD, but no clinical signs of heart failure (HF), are evident or decompensated (stages C and D) when current or past signs of HF are reported (1). Early identification of MMVD can help both to delay the onset and to efficiently manage decompensated HF (2).

Chest radiographs should always be performed as part of the routine clinical evaluation of patients with suspected cardiac disease to detect concurrent lung disease (e.g., interstitial lung

disease, bronchial disease, etc). Furthermore, the correct evaluation of the cardiac silhouette on thoracic radiographs, in particular the screening for left atrial and left ventricular enlargement, carinal elevation, presence of an alveolar and/or venous pulmonary pattern, can aid in staging the severity of MMVD (3). However, such an interpretation can be challenging and requires the presence of an experienced radiologist and/or cardiologist in the clinic. Furthermore, echocardiography is the gold-standard imaging technique for the detection and staging of heart disease. Unfortunately, it is time-consuming and requires trained operators and specific equipment. For the above reasons, it is not always easy to perform in general practice.

In recent years, several tools based on artificial intelligence (AI) have been released to support clinicians in their day-to-day medical routine, both for human and veterinary medicine. Along with this expanding development, the use of AI-based tools for cardiovascular imaging has also increased (4, 5). In humans, these techniques were developed to predict heart disease, to improve image interpretation, and, lastly to increase the quality of patient care (6). Recently, a deep learning (DL)-based model for the diagnosis of mitral regurgitation from thoracic radiographs has been developed in humans (7).

In veterinary medicine, AI-based algorithms has been developed for the detection of some radiographic findings, such as pneumothorax, pulmonary masses or pleural effusion (8–10). Furthermore, some articles proposing tools for the automatic evaluation of cardiac silhouette from canine thoracic radiographs have been published. Detection of cardiomegaly has been investigated in both dogs and cats (9, 11–13). In addition, AI-based tools have been proposed in assessing cardiogenic pulmonary edema secondary to MMVD and in identifying left atrium (LA) dilation on canine thoracic radiographs (14, 15). However, radiographs in the above studies were classified according to: the radiographic appearance of the cardiac silhouette (9); or the echocardiographic evaluation of LA dilation (13, 14). The ACVIM guidelines for patient classification were never used in the above studies. Therefore, the aim of this study was to develop and test a convolutional neural network (CNN) for classifying, from canine thoracic radiographs, the different stages of MMVD as set out in the ACVIM guidelines.

2. Materials and methods

2.1. Study design and database creation

In this retrospective multicentric study, data were collected from the Veterinary Teaching Hospital of the University of Padua and from the AniCura Arcella Veterinary Clinic (Padua). Dogs over 6 years of age with concomitant thoracic radiographs and echocardiographic examination were extracted from the medical database of the two centres. Cases admitted between July 2012 and December 2022 were included. The animals were classified to the ACVIM guidelines (2019) (1), as described below: asymptomatic dogs with no signs of radiographic or echocardiographic cardiac remodelling (e.g., left atrial and ventricular enlargement) were classified as B1; dogs were classified as B2 if cardiomegaly with left atrial and ventricular enlargement was evident; animals with at least one episode of pulmonary edema and/or pleural effusion due to CHF were considered stage C; symptomatic dogs refractory to standard cardiac treatment were classed as stage D. Lastly, if no abnormalities were found in clinical examination, echocardiographies or thoracic radiographs, the dogs were classified as healthy. Dogs affected by other heart or systemic diseases were excluded.

2.2. Radiographic and echocardiographic findings

Right or left lateral (RL or LL) and/or a dorso-ventral (DV) or ventro-dorsal (VD) projections were obtained for each dog. All radiographs in which the cardiac silhouette was not perfectly visible due to a severe abnormal pulmonary pattern were discarded, and only radiographs with a clearly defined cardiac silhouette was clearly defined were included in the final database.

Experienced operators (CG, HP, and DC) performed transthoracic echocardiographic examination in the right and left parasternal windows using standard views (16) and by means of commercially available ultrasound scanners (CX50, Philips, Eindhoven, The Netherlands; Philips Affiniti 50, Italy).

Echocardiographic assessment of cardiomegaly was based on left atrium (LA) and left ventricle (LV) dimensions. Early diastolic LA diameter and aortic root diameter (Ao) were measured from the short-axis view at the heart base level in the right parasternal window. The left atrium to aortic root ratio (LA/Ao) was calculated and LA dilation was considered when LA/Ao $\geq$ **1.6** (17).

Left ventricular internal diastolic diameter (LVIDd) was measured in the right parasternal window from the M-mode short axis view at the level of the cordae tendinae; this was then normalised for body weight (LVIDd-N). Values of LVIDd-N $\geq$ **1.7** were representative of LV dilation (18).

2.3. Image analysis

The radiographic images were stored in DICOM format and then converted to mha format for analysis. All images were resampled at a 224×224 resolution, and the intensity range was normalised to (0–1). CNN ResNet18 was used as a classification network due to the relatively small dataset size (compared to other computer vision datasets) and the lack of improvement compared to larger networks (ResNet50, EfficientNet, Vision Transformer). ResNet18 was fine-tuned from ImageNet pre-trained weights by unfreezing all layers. Fine-tuning only the last layer was suboptimal because the low-level radiographic features differ substantially from the ImageNet features.

The training was performed using five-fold cross-validation, separately, for the lateral and DV or VD projections. Each fold was trained for the same number of epochs (3000), and the state of the model from the last training epoch was utilised for further evaluation. The number of epochs was chosen experimentally until convergence. The number of epochs was relatively high due to heavy data augmentation and small epoch size. The validation set was not used to make any decisions during the training procedure. The objective function was the cross-entropy loss, the optimiser was the AdamW algorithm, and the learning rate scheduler was based on exponential decay. The training set was online augmented by random: (i) horizontal and vertical flipping, (ii) affine transformations, (iii) elastic transformations, (iv) contrast changes, (v) Gaussian blur, (vi) pixel dropout, (vii) random sharpening, using the Albumentations library.

The class imbalance was addressed by oversampling the minority classes for the training cases to achieve balance in the training batches. All experiments were implemented using the PyTorch library and performed on a single NVIDIA A100 GPU. The results were evaluated using confusion matrices, receiver operating characteristic (ROC) curves, t-distributed stochastic neighbour embedding (t-SNE) and uniform manifold approximation and projection (UMAP).

3. Results

3.1. Database

The database consisted of 1,242 (793 from the Veterinary Teaching Hospital and 449 from the Arcella Veterinary Clinic) radiographs in total, including 728 (58.6%) (381 from the Veterinary Teaching Hospital and 347 from the Arcella Veterinary Clinic lateral and 514 (41.4%) (412 from the Veterinary Teaching Hospital and 102 from the Arcella Veterinary Clinic) DV or VD projections.

Due to the relatively low number of healthy control cases (84 and 53 lateral and DV/VD radiographic views, respectively), these were not included in the database for the final analysis. Similarly, since only a few radiographs were classified as stage D (27 and 15 lateral and DV/VD radiographic views, respectively) dogs classified as stage C or D were merged in the database and named as the C + D group.

The lateral and DV or VD views were analysed separately. Two hundred and thirty-three (32%) lateral radiographs were classified as B1, 165 (22.7%) as B2, and 330 (45.3%) as C + D. One hundred and seventy-nine (34.8%) DV or VD radiographs were classed as B1, 127 (24.7%) were classified as B2, and 208 (40.5%) as C + D.

3.2. Classification results

3.2.1. ROC curve

The confusion matrices for classifying the lateral and DV or VD radiographs are reported in Tables 1, 2, respectively. The ROC curves are reported in Figures 1, 2 for the lateral and DV or VD views, respectively. The area under the curve (AUC) showed a good performance of the developed algorithm in determining MMVD stages from lateral radiographic views, with an AUC of 0.87, 0.77, and 0.88 for the B1, B2, and C + D groups, respectively. Instead, the AUCs for the DV or VD images were 0.80, 0.70 and 0.81 for the B1, B2, and C + D groups, respectively.

The overall precision in classifying the lateral radiographs was 71%, with a precision of 73, 51% and 80% for B1, B2, and C + D, respectively. The macro average and the weighted average were 68% and 71%, respectively.

A lower accuracy was obtained for DV or VD radiographs, with an overall accuracy of 65% and a precision of 66%, 52%, and 74% for the B1, B2, and C + D groups, respectively. The macro average and weighted average were 64% and 66%, respectively.

3.2.2. Reduction in dimensionality

Latent spaces are present after dimensionality reduction using t-SNE and UMAP in Figures 3, 4 for the right and left lateral projections, and in Figures 5, 6 for the DV or VD projections. A latent space is a set of the features describing the input images after an automatic feature extraction by the deep neural network. The

TABLE 1 Confusion matrix of right and left lateral radiographic views.

		Predicted labels		
		B1 group	B2 group	C + D group
Real labels	B1 group	167	38	28
	B2 group	39	88	38
	C + D group	22	46	262

TABLE 2 Confusion matrix of dorso-ventral or ventro-dorsal radiographic views.

		Predicted labels		
		B1 group	B2 group	C + D group
Real labels	B1 group	125	29	25
	B2 group	32	69	26
	C + D group	31	35	142

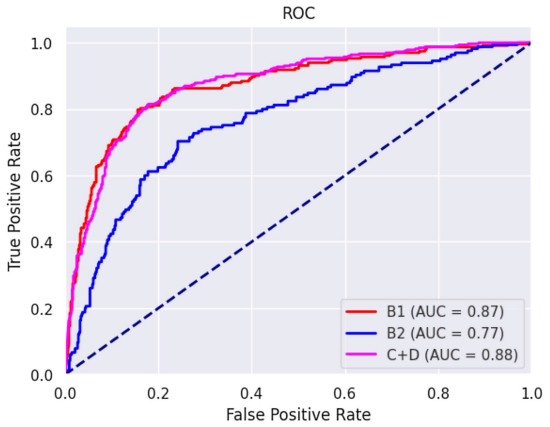

FIGURE 1
Receiver operating characteristic curve of right and left lateral radiographic views. The area under the curve was 0.87, 0.77, and 0.88 for B1, B2, and C + D, respectively.

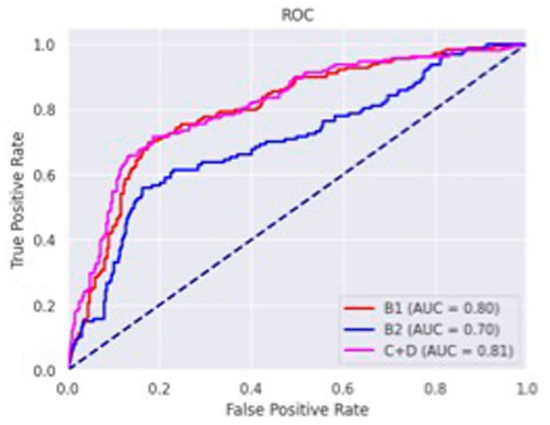

FIGURE 2
Receiver operating characteristics curve of dorso-ventral or ventro-dorsal radiographic views. The area under the curve was 0.80, 0.70 and 0.81 for B1, B2, and C + D, respectively.

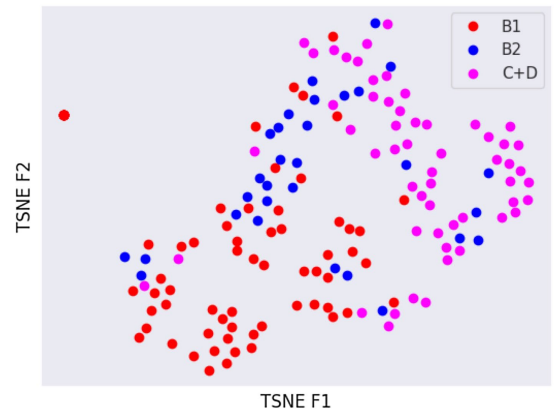

FIGURE 3
Visual distribution of latent spaces using t-SNE graph of right and left lateral radiographic views.

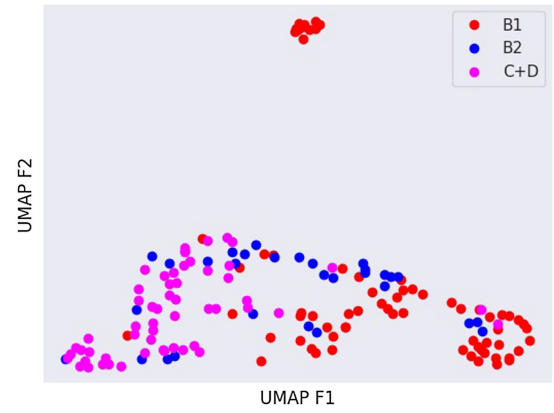

FIGURE 4
Visual distribution of latent spaces using UMAP graph of dorso-ventral or ventro-dorsal radiographic views.

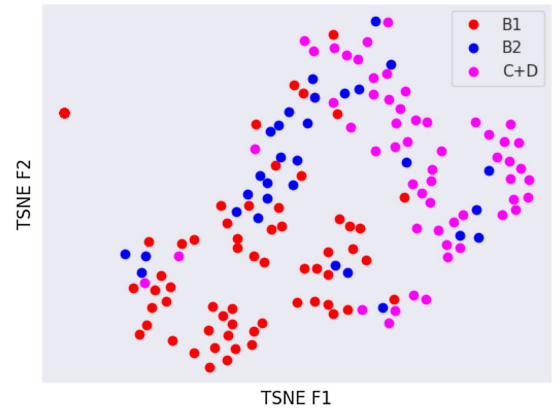

FIGURE 5
Visual distribution of latent spaces using t-SNE graph of right and left lateral radiographic views.

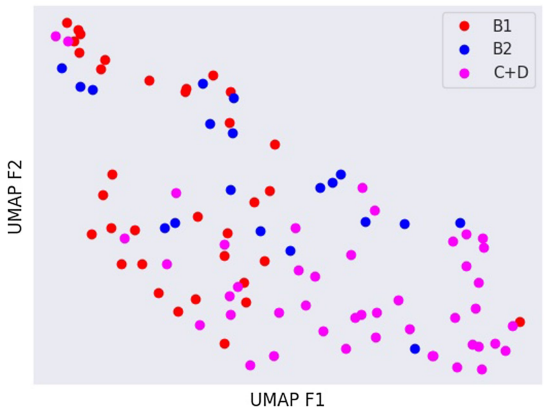

FIGURE 6
Visual distribution of latent spaces using UMAP graph of dorso-ventral or ventro-dorsal radiographic views.

dimensionality of the latent space may be further reduced by dimensionality reduction algorithms such as principal component analysis (PCA), t-SNE or UMAP, while preserving as much variance as possible. In practice, nonlinear learning-based methods such as t-SNE or UMAP are superior compared to PCA. These algorithms enable intuitive visualisation of the features distribution in low-dimensional space (e.g., 2D or 3D). Figures 3–6 illustrate that the classification features are distributed in a way that places the B2 cases between the B1 and C + D cases, even though the ground truth was not annotated using the radiography images. This confirms that the features learned by the network are indeed connected with disease severity and are not dominated by bias related to confounders caused by radiographs acqusition. Cases classed the same ACVIM group are shown close to each other. The same behaviour is achieved using both t-SNE and UMAP dimensionality reduction.

4. Discussion

In this study, an AI-based algorithm is proposed to predict the stage of MMVD from canine thoracic radiographs. The high accuracy of the algorithm in predicting the MMVD stage suggests that it could potentially support general practitioners in the interpretation of canine thoracic radiographs, possibly suggesting the need for further cardiological studies, such as an echocardiographic examination.

The vertebral heart score (VHS) is the most widely used system for assessing cardiomegaly on canine thoracic radiographs (19). However, it can be influenced by the canine morphotype considered. For istance, the reference intervals for some canine breeds (e.g., Cavalier King Charles Spaniel or Chihuahua) (20–22) are different from those of the general canine population. Furthermore, body structure, the respiratory phase and the recumbency side used during the radiography all influence VHS (23). In such a scenario, the interpretation of thoracic X-rays, especially when evaluating the cardiac silhouette, can be challenging. For the above reasons, some of the potential advantages of deploying the proposed model are to overcome interobserver variability and to standardise thoracic radiographs evaluation among veterinarians.

Interestingly, our model performed better in identifying stage B1 and C + D dogs than stage B2 dogs. A straightforward comparison with the literature is not possible because the cases were classified using different parameters in previous studies. In fact, Li et al. (14) report a high precision (accuracy of 82.7%) in the identification by CNN of LA enlargement. The study cases were classed only according to the presence or absence of LA enlargement as classified by echocardiography, while ACVIM stage was not considered. In Banzato et al. (12), a very high accuracy (AUC = 0.965) in the detection of cardiomegaly is reported. However, in this latter study, the dogs were classified only considering the size of the cardiac silhouette evaluated from thoracic radiographs.

Even if the overall accuracy of the developed system for the B2 and C + D stages was adequate a significant number of B2 (23.6%) and C + D (6.7%) cases was this misclassified as B1 potentially classifying deseased dogs as healthy. The authors believe that the lower overall precision in the case classification resulting in the present study (71%) is related to different factors. Firstly, the cases were divided into three groups, whereas a binary case classification was used in the previous studies. The intrinsic differences between dogs classed as B1, B2 or C + D are smaller compared to the differences existing between dogs showing/not showing cardiomegaly. In the current study, the sample was more homogeneous because only elderly dogs were included and, since MMVD is age-related, it is also possible that this factor may have played a role in the classification results generated by the CNNs developed by the other authors. Lastly, this was a multicentric study, whereas all the previous studies were carried out in a single centre, and differences in image quality might lower CNN accuracy. On the other hand, CNNs created using data from multiple institutions tend to have a higher generalisation ability (24).

Not surprisingly, the worst classification results were obtained for the B2 stage dogs. This can be explained, among other factors, by the greater variability that exists between animals classified in this stage of the disease and animals classified as B1 or C + D. In fact, they range from having a slightly enlarged cardiac silhouette to having a severe cardiomegaly with signs of cardiac remodelling. This aspect was also confirmed by the visual distribution of the cases in the t-SNE graph (Figures 3, 5); in fact, we can immediately perceive the variability of stage B2 dogs from the wide distribution of the dots representing this group.

Lastly, the developed heart CNN had a high accuracy in detecting stage C + D dogs. This aspect of the results is similar to that of a previous study evaluating to what extent AI software could identify canine pulmonary oedema (15). Furthermore, high precision in classifying alveolar and/or interstitial pattern was also previously documented in dogs and cats (9, 11).

In human medicine, Ueda et al. (7) proposed a model based on DL for the diagnosis of mitral regurgitation based on chest radiographs. In addition, a visualisation technique was used to check and confirm that the features learned by the AI algorithm were specifically related to cardiac morphological changes due to disease severity. Furthermore, they found that the sensitivity of the model rose as the severity of mitral regurgitation increased. A direct comparison between the previous study and our results was not straightforward due to the different system of heart disease classification.

In the present study, radiographs from both institutions involved were included in the database and used for algorithm training and testing. Another approach could have been to use the radiographs from one institution as a training and validation set and the radiographs from the other institution as a test set. We chose to mix the two databases because the overall number of radiographs was limited and the size of the two databases was markedly different. Furthermore, CNN performance is also influenced by disease prevalence in the different databases. One of the main problems is what is known as overfitting; models often show very high accuracy in internal tests but fail to generalise when exposed to external data. One of the strategies that can be adopted to overcome overfitting, at least partially, is to use data acquired from multiple institutions for the training (24). Further studies, possibly involving a higher number of veterianary clinics are required to assess the real generalisation ability of the network.

This study does have some limitations. Its retrospective nature did not allow us to establish a more rigorous collection of data. The relatively small size of the database, compared to human studies on similar topics (7), also acted as a limiting factor. On this aspect, we would like to point out that the database size was comparable to other studies developing similar CNNs in dogs (9, 13, 14) and cats (11). Lastly, many stage C dogs were receiving diuretic therapy when the radiographs were taken. Even if cardiomegaly was evident, it could be associated with a normal pulmonary pattern. This factor may have led to misclassification of dogs in the C + D group. Further studies selecting only dogs with acute or chronic decompensated HF should be considered.

5. Conclusion

An AI-based algorithm for the automatic staging of dogs affected by MMVD was proposed based on canine thoracic radiographs. This method showed a high accuracy in identifying dogs belonging to stage B1 or C + D stage and a moderate accuracy in the identification of stage B2 dogs. Potentially, the use of a larger dataset could provide greater result accuracy. The heart CNN could stand as a useful support tool for general practitioners when interpreting canine chest radiographs. Nonetheless, more studies with a larger sample size would provide a better insight into the performance of the heart-CNN.

Data availability statement

The raw data supporting the conclusions of this article will be made available by the authors, without undue reservation.

Ethics statement

This study was conducted respecting Italian Legislative Decree No. 26/2014 (transposing EU directive 2010/63/EU). As the data used in this study were part of routine clinical activity, no ethical committee approval was needed. Informed consent regarding the treatment of personal data was obtained from owners.

Author contributions

TB, AZ, CG, HP, and CV conceived the study, performed echocardiographic and radiographic examinations, and drafted the manuscript. MW developed the CNN and drafted the manuscript. DC performed echocardiographic examinations and drafted the manuscript. RV drafted the manuscript. All authors contributed to the article and approved the submitted version.

Funding

The present paper was part of a project funded by a research grant from the Department of Animal Medicine, Production and Health – MAPS, University of Padua, Italy: SID- Banzato 2023 (€20.000).

Conflict of interest

The authors declare that the research was conducted in the absence of any commercial or financial relationships that could be construed as a potential conflict of interest.

Publisher's note

References

1. Keene BW, Atkins CE, Bonagura JD, Fox PR, Häggström J, Fuentes VL, et al. ACVIM consensus guidelines for the diagnosis and treatment of myxomatous mitral valve disease in dogs. *J Vet Intern Med*. (2019) 33:1127–40. doi: 10.1111/jvim.15488

2. Boswood A, Häggström J, Gordon SG, Wess G, Stepien RL, Oyama MA, et al. Effect of pimobendan in dogs with preclinical myxomatous mitral valve disease and cardiomegaly: the EPIC study-a randomized clinical trial. *J Vet Intern Med*. (2016) 30:1765–79. doi: 10.1111/jvim.14586

3. Ettinger SJ, Feldman EC, Coté E eds. *Textbook of veterinary internal medicine. 8th* ed. St Louis, MO: Elservier (2017).

4. Rouzrokh P, Khosravi B, Vahdati S, Moassefi M, Faghani S, Mahmoudi E, et al. Machine learning in cardiovascular imaging: a scoping review of published literature. *Curr Radiol Rep*. (2023) 11:34–45. doi: 10.1007/s40134-022-00407-8

5. Seetharam K, Brito D, Farjo PD, Sengupta PP. The role of artificial intelligence in cardiovascular imaging: state of the art review. *Front Cardiovasc Med*. (2020) 7:618849. doi: 10.3389/fcvm.2020.618849

6. Esteva A, Robicquet A, Ramsundar B, Kuleshov V, DePristo M, Chou K, et al. A guide to deep learning in healthcare. *Nat Med*. (2019) 25:24–9. doi: 10.1038/s41591-018-0316-z

7. Ueda D, Ehara S, Yamamoto A, Iwata S, Abo K, Walston SL, et al. Development and validation of artificial intelligence-based method for diagnosis of mitral regurgitation from chest radiographs. *Radiol Artif Intell*. (2022) 4:e210221. doi: 10.1148/ryai.210221

8. Boissady E, de La Comble A, Zhu X, Hespel AM. Artificial intelligence evaluating primary thoracic lesions has an overall lower error rate compared to veterinarians or veterinarians in conjunction with the artificial intelligence. *Vet Radiol Ultrasound*. (2020) 61:619–27. doi: 10.1111/vru.12912

9. Banzato T, Wodzinski M, Burti S, Osti VL, Rossoni V, Atzori M, et al. Automatic classification of canine thoracic radiographs using deep learning. *Sci Rep*. (2021) 11:3964. doi: 10.1038/s41598-021-83515-3

10. Müller TR, Solano M, Tsunemi MH. Accuracy of artificial intelligence software for the detection of confirmed pleural effusion in thoracic radiographs in dogs. *Vet Radiol Ultrasound*. (2022) 63:573–9. doi: 10.1111/vru.13089

11. Banzato T, Wodzinski M, Tauceri F, Donà C, Scavazza F, Müller H, et al. An AI-based algorithm for the automatic classification of thoracic radiographs in cats. *Front Vet Sci*. (2021) 8:731936. doi: 10.3389/fvets.2021.731936

12. Burti S, Longhin Osti V, Zotti A, Banzato T. Use of deep learning to detect cardiomegaly on thoracic radiographs in dogs. *Vet J*. (2020) 262:105505. doi: 10.1016/j.tvjl.2020.105505

13. Jeong Y, Sung J. An automated deep learning method and novel cardiac index to detect canine cardiomegaly from simple radiography. *Sci Rep*. (2022) 12:14494. doi: 10.1038/s41598-022-18822-4

14. Li S, Wang Z, Visser LC, Wisner ER, Cheng H. Pilot study: application of artificial intelligence for detecting left atrial enlargement on canine thoracic radiographs. *Vet Radiol Ultrasound*. (2020) 61:611–8. doi: 10.1111/vru.12901

15. Kim E, Fischetti AJ, Sreetharan P, Weltman JG, Fox PR. Comparison of artificial intelligence to the veterinary radiologist's diagnosis of canine cardiogenic pulmonary edema. *Vet Radiol Ultrasound*. (2022) 63:292–7. doi: 10.1111/vru.13062

16. Thomas WP, Gaber CE, Jacobs GJ, Kaplan PM, Lombard CW, Moise NS, et al. Recommendations for standards in transthoracic two-dimensional echocardiography in the dog and cat. *J Vet Intern Med*. (1993) 7:247–52. doi: 10.1111/j.1939-1676.1993.tb01015.x

17. Rishniw M, Erb HN. Evaluation of four 2-dimensional echocardiographic methods of assessing left atrial size in dogs. *J Vet Intern Med*. (2000) 14:429–35. doi: 10.1892/0891-6640(2000)014<0429:eofemo>2.3.co;2

18. Cornell CC, Kittleson MD, Della Torre P, Häggström J, Lombard CW, Pedersen HD, et al. Allometric scaling of M-mode cardiac measurements in normal adult dogs. *J Vet Intern Med*. (2004) 18:311–21. doi: 10.1892/0891-6640(2004)18<311:asomcm>2.0

19. Buchanan JW, Bücheler J. Vertebral scale system to measure canine heart size in radiographs. *J Am Vet Med Assoc*. (1995) 206:194–9.

20. Bagardi M, Locatelli C, Manfredi M, Bassi J, Spediacci C, Ghilardi S, et al. Breed-specific vertebral heart score, vertebral left atrial size, and radiographic left atrial dimension in Cavalier King Charles Spaniels: reference interval study. *Vet Radiol Ultrasound*. (2022) 63:156–63. doi: 10.1111/vru.13036

21. Puccinelli C, Citi S, Vezzosi T, Garibaldi S, Tognetti R. A radiographic study of breed-specific vertebral heart score and vertebral left atrial size in Chihuahuas. *Vet Radiol Ultrasound*. (2021) 62:20–6. doi: 10.1111/vru.12919

22. Baisan RA, Vulpe V. Vertebral heart size and vertebral left atrial size reference ranges in healthy Maltese dogs. *Vet Radiol Ultrasound*. (2022) 63:18–22. doi: 10.1111/vru.13027

23. Greco A, Meomartino L, Raiano V, Fatone G, Brunetti A. Effect of left vs. right recumbency on the vertebral heart score in normal dogs. *Vet Radiol Ultrasound*. (2008) 49:454–5. doi: 10.1111/j.1740-8261.2008.00406.x

24. Zech JR, Badgeley MA, Liu M, Costa AB, Titano JJ, Oermann EK. Variable generalization performance of a deep learning model to detect pneumonia in chest radiographs: a cross-sectional study. *PLoS Med*. (2018) 15:e1002683. doi: 10.1371/journal.pmed.1002683

frontiers | Frontiers in Veterinary Science

TYPE Original Research
PUBLISHED 04 January 2024
DOI 10.3389/fvets.2023.1307938

OPEN ACCESS

EDITED BY
Mindaugas Tamosiunas,
University of Latvia, Latvia

REVIEWED BY
Jole Mariella,
University of Bologna, Italy
Martynas Maciulevicius,
Vytautas Magnus University, Lithuania

*CORRESPONDENCE
Jean-Yin Tan
✉ jeanyin.tan@ucalgary.ca

RECEIVED 05 October 2023
ACCEPTED 11 December 2023
PUBLISHED 04 January 2024

CITATION
Haardt H, Romero AE, Boysen SR and Tan JY (2024) Comparison of transrectal and transabdominal transducers for use in fast localized abdominal sonography of horses presenting with colic.
Front. Vet. Sci. 10:1307938.
doi: 10.3389/fvets.2023.1307938

Comparison of transrectal and transabdominal transducers for use in fast localized abdominal sonography of horses presenting with colic

Hanna Haardt[1,2], Alfredo E. Romero[1], Søren R. Boysen[1] and Jean-Yin Tan[1]*

[1]Faculty of Veterinary Medicine, University of Calgary, Calgary, AB, Canada, [2]Department of Large Animal Surgery, Anaesthesia and Orthopaedics, Ghent University, Merelbeke, Belgium

Abdominal ultrasonography is valuable in the diagnosis of equine colic. Fast localized abdominal sonography of horses (FLASH) enables practitioners with limited experience to perform ultrasonography in emergency settings. However, many practitioners only possess rectal format linear array transducers (RFLT). The hypotheses are: (a) A low frequency curvilinear transducer (LFCT) and RFLT will detect free abdominal fluid and abnormal small intestinal loops with similar frequency during FLASH, and (b) there will be a difference between the transducers for detection of gastric abnormalities and nephrosplenic entrapment. The objective is to compare transcutaneous abdominal ultrasonographic detection of abnormalities in horses presenting with colic using a LFCT and RFLT. Twenty-four horses requiring FLASH for investigation of colic were enrolled. Horses that were too painful to undergo transcutaneous abdominal ultrasonographic examination were excluded. A single investigator performed FLASH on all horses using a RFLT, while one of three other clinicians simultaneously performed FLASH using a LFCT. Comparison of abnormal findings between the two transducers was performed using Chi square, Fisher's exact or Wilcoxon tests. The incidence of identification of abnormal findings was similar between the two transducers for all comparisons except the visibility of the left kidney and stomach (kidney LFCT 81.25% vs. RFLT 22.92%, stomach LFCT 87.5% vs. RFLT 62.5%). While there are limitations to using a RFLT to identify nephrosplenic entrapment of the colon and detection of the stomach, it reliably detects other common abnormalities, including peritoneal effusion, lesions of the small intestine, and changes to the wall of the large colon and cecum.

KEYWORDS

ultrasound, probe, abdomen, diagnostic imaging, rectal

1 Introduction

Abdominal ultrasonography is an important diagnostic modality in the assessment of the equine colic patient (1–3). Due to technical advancements ultrasound image quality has improved throughout the years and ultrasonography has become an integral part of a colic workup in many clinics and practices (4–7). Traditionally ultrasonographic

examination of the abdomen is performed using a 2–5 MHz low frequency curvilinear transducer (abdominal transducer) (2, 8). While first-opinion equine veterinarians commonly possess 5–10 MHz rectal format linear array transducers (transrectal transducer), only 8% of ultrasound machines purchased in equine configurations in Canada over the last 5 years from an international company include an abdominal transducer.[1] In a previous study, the authors established that a transrectal transducer produces ultrasonographic images of sufficient quality to allow incidence of organ identification similar to that of an abdominal transducer except for the left kidney, left liver, and stomach, when performing transcutaneous equine abdominal ultrasonography (9). The difference in detection of abnormalities between transducers was believed to be due to the depth limitation of the transrectal transducer compared to the abdominal transducer (the transrectal transducer used in that study operated at 8–13 MHz, and the abdominal transducer at 3.0–3.8 MHz) (9). A thick haircoat and horses with increased abdominal fat were discussed as possible factors influencing the ability to detect abdominal structures, but this data was not specifically collected and assessed in the previous study.

Ultrasonographic protocols, such as fast localized abdominal sonography of horses (FLASH), have proven to be effective in the emergency diagnosis of major abnormalities causing colic (6). Expedited diagnosis of key abnormalities such as excessive peritoneal effusion and small intestinal and colon pathology may ensure immediate referral for intensive medical or surgical intervention.

The objective of this prospective clinical study was to compare ultrasonographic detection of abnormalities between an abdominal and transrectal transducer in horses presenting for colic, using a transcutaneous abdominal scanning technique. A second objective was to determine if hair coat and body condition score (10) would influence ultrasonographic findings. We hypothesize that both transrectal and abdominal transducers will detect free abdominal fluid and abnormalities of small intestinal loops, such as distention, absent or decreased motility, and thickened wall, with similar frequency. We also hypothesize that there will be a difference between the transducers for detection of gastric conditions such as dilation, thickening of the wall, or masses, and left dorsal displacement of the colon.

2 Materials and methods

Animal ethics approval was obtained from University of Calgary Animal Care Committee (AC19-0116) and informed consent was obtained. Horses greater than 1 year of age that presented to a referral clinic[2] for colic and had transcutaneous abdominal ultrasonography requested by the attending clinician were enrolled. Horses clinically assessed as being in too much discomfort to complete the ultrasonographic examination (unable to stand in stocks despite sedation), and cases where the owner declined ultrasonography due to financial restrictions, were excluded from the study.

Based on availability during the study period of 2 months (December 1 2019 to January 31 2020) 24 horses were enrolled. Breed, body condition score, sex, body weight, and length of the hair coat was recorded at the time of presentation. Working diagnosis (final diagnosis if confirmed through surgery or post-mortem examination) and duration of the ultrasonographic examination were recorded. Horses were restrained in stocks for the duration of the ultrasonographic exam. Due to the time sensitivity of the procedure in evaluating colic emergencies, the haircoat was not clipped and 70% isopropyl alcohol was used as the coupling agent. Horses that were excessively soiled were brushed prior to performing ultrasound. Portable veterinary ultrasound machines were used (Mindray M5 vet, Shenzhen Mindray Bio-Medical Electronics Co., Ltd., Shen Zhen, China). The transrectal (linear) transducer was a 5–8 MHz frequency transducer (6LE5Vs Shenzhen Mindray Bio-Medical Electronics Co., Ltd., Shen Zhen, China) with a maximum depth setting of 30 cm, however, no image could be obtained beyond a depth of 12 cm at the lowest frequency in B-Mode (5 MHz). An initial depth setting of 12 cm and a frequency of 5 MHz was used for all examinations. These values were then adjusted based on operator preference during the examination. Using FLASH 7 areas were evaluated on each horse: Ventral abdomen, left cranial abdomen, caudal dorsal and ventral abdomen (left and right) and the right thorax (6). The standard abdominal transducer was a convex transducer of 2.5–6 MHz (3C5s Shenzhen Mindray Bio-Medical Electronics Co., Ltd., Shen Zhen, China). The initial settings for the abdominal transducer were 25 cm depth and 2.5 MHz, which were adjusted based on operator preference.

After the attending clinician completed the presenting physical examination, horses were placed in stocks. The working diagnosis was determined by the attending clinician based on clinical, rectal, and ultrasonographic examination and recorded following completion of the ultrasound examination. Horses were simultaneously examined bilaterally by two out of the four participating examiners, whom were veterinarians that had between 6 months and 5 years of clinical experience. All examiners involved in the study received standardized ultrasonographic training consisting of one full day of practical training in abdominal ultrasound and a 2-h theoretical lecture-based presentation. All examiners had equal experience with abdominal ultrasound. The examiner operating the abdominal transducer decided the side of the horse that they commenced the examination based on the location of the suspected clinically relevant lesion, while the examiner with the transrectal probe started on the opposite side of the abdomen. The same veterinarian (H.H.) with 1.5 years of experience completed all ultrasonographic examinations with the transrectal transducer, whereas one of three additional examiners performed the simultaneous ultrasonographic examination using the abdominal transducer. Each examiner completed a FLASH, recording results on a standardized FLASH score sheet (6). When the examiner using the abdominal transducer signaled completion of the examination on their side of the abdomen, the examination with the transrectal transducer was interrupted, irrespective of whether it had been completed or not. This was done to avoid any negative impact on patients enrolled in the study. The time taken to complete each exam, or time to interruption of the transrectal transducer exam, was recorded. At least one cine-loop of 5 s was

1 Walklate D. Heska Canada Limited (National Product Manager - Ultrasound and Advanced Imaging), Calgary, Canada (personal communication) 2021.

2 Moore Equine Veterinary Center, Balzac, Alberta, Canada.

10.3389/fvets.2023.1307938

recorded at each of the 7 sites included in the FLASH. Each examiner independently completed the FLASH score sheet. Cine-loops were redacted and randomized for blinding and retrospectively analyzed by two specialists 1 board-certified large animal internal medicine specialist with 14 years of experience [J.T., DVM, DACVIM (LAIM)], and 1 board-certified large animal surgeon with 14 years of experience [A.R., DVM, DACVS (LA)]. Upon review of the recorded Cine-loops, the experts completed a modified FLASH scoring sheet. Abnormalities were categorized according to the FLASH score sheets. The data of all score sheets was pooled for statistical analysis. Further treatment of the horses was at the discretion of the attending clinician, and included withholding food, intravenous or nasogastric fluids, laxatives, jogging, and or surgery.

All data was tested for normality using a Shapiro–Wilk test, and subsequently analyzed using parametric or non-parametric tests. A p value <0.05 was considered statistically significant. To determine any statistically significant difference between transducers for dichotomous data a Chi square test (when $n \geq 10$ in all cells of a 2×2 table) or Fisher's Exact Test ($n \leq 5$ in any cell of a 2×2 table) was used. To determine any difference in the mean (or median) between groups, a paired t-test or Wilcoxon matched-pairs signed rank test was used for data that passed or failed normalcy, respectively. A t-test or Mann Whitney test was used to compare differences between transducers for continuous variables that passed or failed normalcy, respectively. For haircoat length, numerical values from 1 to 4 were assigned with 1 designated as a clipped haircoat, 2 a light coat (horse was wearing a heavy rug or had been stabled indoors), 3 a winter coat, and 4 a heavy winter coat. Abnormal motility of the small intestine was defined as absence or reduction of peristaltic waves. Wall thickness was considered increased when it exceeded 0.3 cm for small intestine and 0.5 cm for colon. Graphpad prism (version 8.4.2, San Diego, CA, United States) was used to perform all statistical analysis. Mean and median age, body weight, and BCS (10) were calculated using Excel (Microsoft Office Professional 2019, Redmont, Washington, United States).

3 Results

Twenty-four horses of various breeds (10 Warmblood, 8 Quarter Horse, 4 Thoroughbred, 1 Fjord horse, and 1 Percheron cross) and sex (15 geldings, 8 mares, and 1 stallion) were enrolled between December 2019 and January 2020. Age ranged from 3 to 27 years (median 12), weight from 402 kg to 610 kg (median 500 kg), and the body condition score from 2 to 8 (median 6). A presumptive diagnosis was available in 22/24 horses: 5 horses presented with right dorsal displacement of the colon, 5 with primary impaction of the large colon with ingesta, 4 horses with left dorsal displacement of the colon out of which one was a nephrosplenic entrapment, 5 horses with tympany of the cecum or colon, 2 horses with colitis and 1 horse with a suspected gastroduodenojejunitis. Diagnoses were made by the attending clinician based on clinical examination including physical examination, bloodwork, rectal palpation, and ultrasonography. All patients were medically managed, thus there is no final diagnosis available. For two horses the authors could obtain a final diagnosis: one horse that had a 720-degree torsion of the colon, which underwent a ventral midline laparotomy and a pedunculated, strangulating, lipoma that was diagnosed on post-mortem examination in one horse that was euthanized. All other horses responded to medical management without confirmation of a definitive cause of colic.

Duration of the ultrasonographic examination ranged from 12 min to 42 min (median 18 min). The attending clinician was at liberty to capture additional images or to investigate additional locations during their ultrasound examination, which has caused longer examination times in some instances. Images taken in additional locations were not recorded. The transrectal transducer examination was discontinued before completion in one case (left side of the abdomen) as it exceeded the length of time to complete the FLASH exam using the abdominal probe.

There was no statistically significant difference in detection of abdominal or thoracic free fluid and of the small intestine and its abnormalities, such as distention/liquid content, wall thickness and motility (Table 1). Although the colon wall was found to be thickened

TABLE 1 Identification of pathologies and organs using the abdominal and transrectal transducers.

Abdominal structure/Abnormality	Abdominal Transducer Identification rate in %	Transrectal Transducer Identification rate in %	*P*-value
Free fluid abdomen	27.78	29.17	1.0000
Free fluid thorax	1.42	8.57	0.1156
Duodenum seen	81.94	68.06	0.0824
Duodenum abnormal motility	8.47	6.12	0.25
Duodenum liquid content/distention	5.08	14.29	0.75
Other small intestine (not duodenum) (OSI) thickened wall	9.72	8.33	1.0000
OSI seen	95.83	94.44	1.0000
OSI abnormal motility	27.54	19.12	>0.9999
OSI liquid content/distention	34.78	41.18	>0.9999
Colon thickened wall	1.39	5.56	0.3662
L Kidney detected by ultrasonographers	91.67	37.50	0.0005 *
L Kidney detected by experts	81.25	22.92	<0.0001*
Stomach seen	87.50	62.50	0.0005 *

Statistically significant differences between transrectal and abdominal transducers in identifying organs and pathologies are indicated with an asterisk (*) OSI = Other small intestine, that was not identified as duodenum, the visualization of the kidney was analyzed for experts and ultrasonographers separately in consistency with the previous study (9).

in 1.4% of the images captured with the abdominal transducer and in 5.6% of the images captured with the transrectal transducer, there was no statistically significant difference (Table 1). The detection of the left kidney was analyzed separately for the novices and experts and was found to be significantly different between the transducers for both novices and experts. The detection rate of the stomach was also significantly different between transducers with the stomach being seen in 88% of the images with the abdominal transducer, but only 63% of the images with the transrectal transducer. Detailed results can be found in Table 1. Due to the low identification rate of the stomach, comparative statistics between the two transducers for dilation of the stomach [identification of the stomach past the 15th ICS or its presence in more than 5 ICS (11)] was not performed.

Most horses had a BCS of 5 ($n = 7/24$) or 6 ($n = 8/24$), with only one horse having a BCS below 5 (BCS 2), and the remaining horses having BCS 7 ($n = 5/24$) and BCS 8 ($n = 3/24$). No statistically significant difference could be established in detection rate of abnormalities between the different BCS groups.

When comparing the effect of the haircoat score on both transducers, there was a statistically significant difference (values reported as median) between cases that had detectable free peritoneal fluid vs. cases that did not have detectable free peritoneal fluid (haircoat score 2 vs. 3, $p = 0.0261$) and ability to ultrasonographically identify the duodenum (haircoat score 2 vs. 3, $p = 0.0265$).

4 Discussion

To the authors' knowledge this is the first clinical study to compare the incidence of detecting abnormalities using a transrectal and abdominal transducer in equine abdominal ultrasonography. The results suggest that the transrectal transducer can be used to identify many of the ultrasonographic abnormalities included in FLASH, except for conditions that require identification of the stomach and left kidney.

Transabdominal ultrasonography is a common diagnostic tool for assessment of equine colic (4–6). It provides valuable information to help differentiate surgical from non-surgical causes of colic and plays a role in deciding if cases should be referred for specialist care (4, 6). Farrell et al. demonstrated abnormal ultrasound findings along with 5 other values in horses with colic are correlated with survival, and that 76% of non-survivors have ultrasonographically detected abnormalities (12). Equine ultrasonographic examination of colic should include location, wall thickness, motility, diameter and content of the intestine, as well as the presence of abdominal or thoracic fluid (4, 8). Beccati et al. established statistically significant correlations between ultrasonographic abnormalities and definitive diagnoses in horses with colic. These included small intestinal strangulations with amotile small intestinal loops and thickened walls in conjunction with free peritoneal fluid, as well as a failure to visualize the left kidney with nephrosplenic entrapment (13).

In the current study, the FLASH protocol was used to evaluate horses with colic as it has been validated for use by operators with minimal ultrasonographic experience, and evidence suggests it can diagnose the most common causes of colic in the emergency setting (6). An abbreviated ultrasound protocol was chosen as it is deemed to be most applicable to first-opinion practice, even though it may have underestimated the severity of conditions in some horses, or exacerbated differences between the two transducers by reducing the imaging time and locations (2, 6).

There was no statistically significant difference in detection of small intestines between the two transducers, with both identifying "other small intestine" (all small intestine that was not identified as duodenum) and duodenum in 94–98% of cases and 68–82% of cases. The presence of distended small intestinal loops [diameter > 7 cm (4)] can be associated with both nonsurgical lesions (e.g., ileus and smaller impactions of the ileum) and surgical lesions (e.g., strangulation of the small intestine). A recent study found that abnormal small intestinal findings in the ventral and left inguinal locations identified using the FLASH protocol were the best predictors for surgical intervention (14). Therefore, rapid diagnosis using a readily available transrectal probe and ultrasound machine under field conditions could lead to faster referral and improved survival rates. The transrectal transducer was consistently able to identify small intestinal loops in sufficient detail to appreciate abnormalities such as distention, increased wall thickness and absence of normal motility (Figure 1).

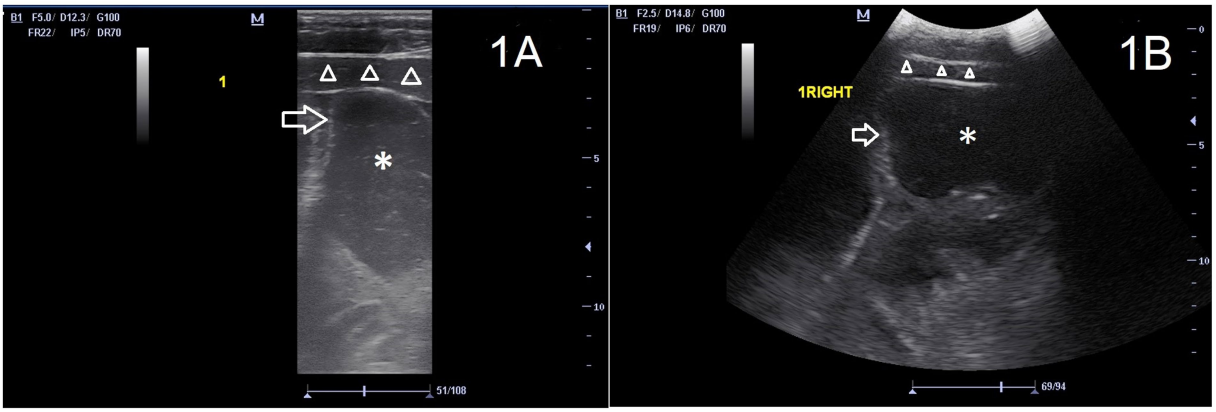

FIGURE 1
Images of the ventral abdomen (location 1) of the same horse, with a mildly distended loop of small intestine (asterisk) with wall of normal thickness (arrow). Ventral abdominal musculature (triangles) and subcutis are also visible in the near field. The left side of the image is cranial of the horse. **(A)** transrectal transducer, frequency 5 MHz, depth 12.3 cm. **(B)** abdominal transducer 2.5 MHz, depth 14.5 cm. Both transducers allow the ultrasonographer to identify the distention of the small intestine.

Increased intestinal wall thickness can be associated with inflammation (colitis/enteritis) and strangulating lesions such as volvulus or torsion of the small and large intestines (4, 15–17). While abdominal ultrasound is not imperative to diagnose colon torsions, a study has found a wall thickness of the colon of > or = 9 mm to be highly specific (100%) and moderately sensitive (67%) (15). Strangulating lesions are treated surgically or lead to euthanasia of the patient, while enteritis and colitis are often managed with intensive medical treatment. Recognition of both these disease processes is important for early referral of the patient to a facility with the option of hospitalization and intensive care. A colonic wall thickness > 0.5 cm is regarded as pathological, while the cutoff for the small intestine lies at 0.2–0.35 cm (15, 16, 18–20). There was no statistically significant difference in detection of increased intestinal wall thickness. Nevertheless, a thickened colonic wall was seen in 4 instances with the transrectal transducer: one horse with a left dorsal displacement of the colon, two with colon impaction, and one with colitis, and only 1 case with a secondary impaction in combination with a right dorsal displacement with the abdominal transducer. This difference may be explained by the low-depth penetration but high near-field resolution of the transrectal probe, which at a lower depth settings, allows for an enlarged colon wall on the ultrasound image and emphasizes near-field structures relative to the transrectal transducer. Subtle changes may therefore be more obvious to the examiner using a linear probe than images captured using a lower resolution abdominal transducer. There was no difference in detection of changes in motility or content between transducers (Figure 2). An ultrasonographic examination with the transrectal probe therefore has similar ability compared to the abdominal probe in aiding the differentiation between a strangulating and an inflammatory lesion of the small and large intestines.

In accordance with a previous study performed by the same authors, the detection rate of the left kidney was significantly lower with the transrectal transducer (25%) compared to the abdominal transducer (85%), likely due to the kidney being positioned deep to the 5–8 cm-thickness equine spleen (8). With the maximum depth at which the transrectal transducer delivers images being 12 cm, a kidney located more than 10 cm from the skin surface and deep to the spleen would be difficult to visualize (9). Detection of the left kidney during FLASH is important since failure to image the kidney is associated with a diagnosis of left dorsal displacement of the large colon, although this finding is not definite (3, 4). In our study 4 horses were suspected to have a left dorsal displacement of the large colon. This was based on rectal palpation in conjunction with ultrasonographic findings detected with the abdominal probe, such as inability to image the spleen due to obscuration with gas. A diagnosis of nephrosplenic entrapment was made in one horse in which the colon could be felt in the nephrosplenic space on rectal palpation and where the dorsal aspect of the spleen was obliterated by gas on ultrasonography, as described in the literature (21). The majority of these were not detected with the transrectal transducer, making it unsuitable for assessment of this condition. Medical treatment in these cases included IV fluids, jogging, and administration of phenylephrine at the clinician's discretion. Resolution of the left dorsal displacement or nephrosplenic entrapment was confirmed with rectal palpation, improvement of clinical signs, and in some cases repeat ultrasound.

The identification rate of the stomach using the transrectal transducer was lower than that with the abdominal transducer. This finding was consistent with the data of the previous study in which the stomach could be detected in 100% of horses using the abdominal probe, but in only 50% of cases using the transrectal transducer (9). Other equine studies report ultrasonographic variability in detecting the stomach of horses using an abdominal transducer. A study by Epstein et al. imaged the stomach in 7/9 ponies, Williams et al. excluded the stomach due to inconsistencies in ultrasonographically identifying it during their pilot work, while Freeman et al. state that the ability to ultrasonographically detect the stomach is inconsistent in normal horses (2, 17, 20). In the current study the detection rate of the stomach with the abdominal transducer was 87.5%. The relative inexperience of the veterinarian operating the ultrasound

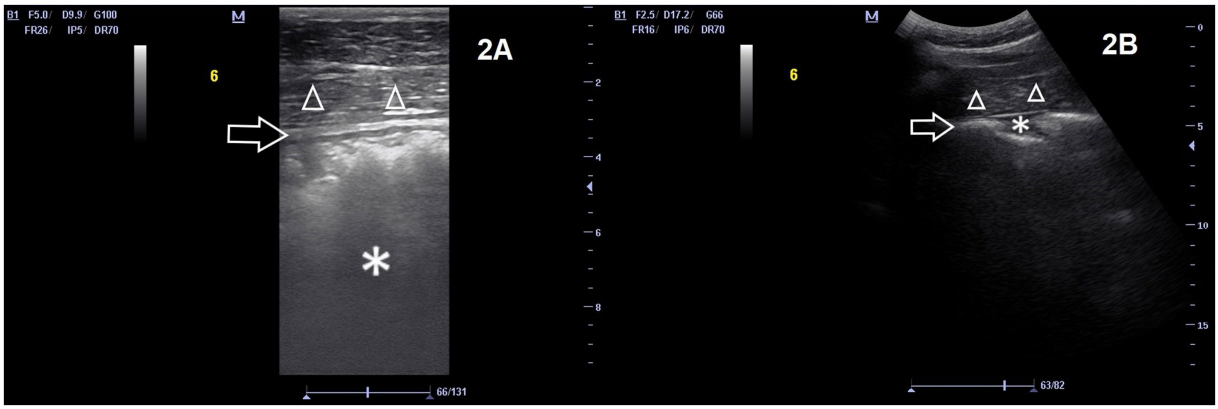

FIGURE 2
Images of the right lateral abdomen (location 6) of the same horse, with the numerous layers of the colon wall more distinct and visible in the near field (arrow). A small pocket of effusion is visible in **(B)** (asterisk). Body wall is also visible ventral to the colon (triangles). The left side of the image is cranial of the horse. **(A)** transrectal transducer, frequency 5 MHz, depth 9.9 cm. **(B)** abdominal transducer 2.5 MHz, depth 17.2 cm. Both images show a normal wall thickness, however, the magnification on the image taken with the rectal transducer allows an inexperienced ultrasonographer to measure the wall thickness with more ease.

machine may also have contributed to the lower detection rate seen in this study compared to the previous study by the same authors. The number of cases with stomach distention was too low to allow statistical analysis, and a study with a larger number of cases is needed to identify any difference between transducers.

Air trapped between the hair of horses can reflect ultrasound waves, which is why many authors recommend clipping horses prior to performing ultrasonographic examinations (3, 16). In the current study isopropyl alcohol was liberally applied to the hair coat of all horses without clipping. However, to examine the influence of the length of the horses' haircoat, horses were divided into four categories ranging from clipped to heavily coated. While there was no difference in detection rate of abnormalities seen, abdominal fluid detection and identification of the duodenum were seen more often in horses with a clipped or light coat with the transrectal transducer. Free fluid is most commonly detected at the lowest point of the abdomen. Often this is also where the horse's haircoat is the longest. The transrectal transducer may have thus been more affected by the long haircoat than the abdominal transducer. However, this does not explain the influence of the haircoat on the ability to detect the duodenum. A possible explanation could be the limited field in which the duodenum can be viewed, making it more unlikely to be detected than other organs due to reduced ability to recognize surrounding structures with characteristic proximity such as the right kidney, right dorsal colon, and liver that help to distinguish the duodenum (22). A statistically significant difference between detection of the stomach in lighter coated horses with the abdominal transducer vs. the linear transducer could not be established. The number of horses with a light haircoat may not have been sufficient to reach statistical significance for this value. Further studies are warranted to establish a possible association between thickness of haircoat and ability to identify abnormal structures on ultrasound.

This study found BCS did not influence the ability to detect abnormalities on FLASH between transducers. Therefore, a cutoff value for BCS and detection of abnormalities using the transrectal transducer could not be determined. This was likely caused by the relatively homogeneous distribution of BCS in our study population with BCS 5 and 6 being overrepresented (63% of the horses fell within these two BCS scores).

A main limitation of this study was that severely painful horses were excluded due to the clinical need for immediate surgery without ultrasonographic examination. This was done to ensure animal welfare and a high standard of care for the horses. A second limitation was that experts graded cine-loops captured by veterinarians with limited experience. The presence of a winter haircoat on the horses examined may have impacted the results of the study, yet this mimics the circumstances of evaluating horses in the field during time-sensitive colic evaluations. The relative inexperience of the veterinarians may have resulted in suboptimal image quality and artificially lowered detection rates of abnormalities and limited the findings of this study. However, this also likely correlates with the experience of field veterinarians that do not frequently perform abdominal ultrasound. Even though the veterinary examiners had various years of previous experience, all of them had introduced abdominal ultrasound into their daily practice at the same time, and thus similar experience in abdominal ultrasound of horses. The veterinarian (H.H.) operating the transrectal transducer had previously participated in the first study. This may have enhanced the quality of cine-loops captured by this examiner in comparison to the veterinarians operating the abdominal transducer. Finally, there were relative low numbers in the subcategories of the large and small intestine (motility and content) which may have led to a type 2 error.

5 Conclusion

In conclusion, the transrectal transducer achieves comparable identification rates with the abdominal transducer for all abnormalities included in the FLASH protocol in horses presenting for colic, except those affecting the left kidney and stomach. These findings were consistent with the previously published data in healthy horses (9).

Data availability statement

The original contributions presented in the study are included in the article/supplementary material, further inquiries can be directed to the corresponding author.

Ethics statement

The animal studies were approved by University of Calgary Animal Care Committee. The studies were conducted in accordance with the local legislation and institutional requirements. Written informed consent was obtained from the owners for the participation of their animals in this study.

Author contributions

HH: Conceptualization, Data curation, Investigation, Writing – original draft. AER: Conceptualization, Data curation, Investigation, Methodology, Supervision, Writing – review & editing. SRB: Conceptualization, Formal analysis, Supervision, Writing – review & editing. JYT: Conceptualization, Data curation, Investigation, Funding acquisition, Methodology, Project administration, Resources, Supervision, Writing – review & editing.

Funding

The author(s) declare financial support was received for the research, authorship, and/or publication of this article. This work was funded by the University of Calgary – Faculty of Veterinary Medicine Internship Research Fund.

Acknowledgments

The authors wish to thank Anika Lohnherr, Jamie Neufield, Merete Moller-Jensen, and Simon Bourassi for their contribution to the image collection.

Conflict of interest

The authors declare that the research was conducted in the absence of any commercial or financial relationships that could be construed as a potential conflict of interest.

The author(s) declared that they were an editorial board member of Frontiers, at the time of submission. This had no impact on the peer review process and the final decision.

Publisher's note

References

1. Cribb NC, Arroyo LG. Techniques and accuracy of abdominal ultrasound in gastrointestinal diseases of horses and foals. *Vet Clin North Am Equine Pract*. (2018) 34:25–38. doi: 10.1016/j.cveq.2017.11.001

2. Williams S, Cooper JD, Freeman SL. Evaluation of normal findings using a detailed and focused technique for transcutaneous abdominal ultrasonography in the horse. *BMC Vet Res*. (2014) 10:S5. doi: 10.1186/1746-6148-10-S1-S5

3. Scharner D, Rötting A, Gerlach K, Rasch K, Freeman DE. Ultrasonography of the abdomen in the horse with colic. *Clinic Tech Equine Pract*. (2001) 1:118–24. doi: 10.1053/ctep.2002.35579

4. Klohnen A, Vachon AM, Fischer AT Jr. Use of diagnostic ultrasonography in horses with signs of acute abdominal pain. *J Am Vet Med Assoc*. (1996) 209:1597–601.

5. Freeman S. Ultrasonography of the equine abdomen: findings in the colic patient. *In Pract*. (2002) 24:262–73. doi: 10.1136/inpract.24.5.262

6. Busoni V, De Busscher V, Lopez D, Verwilghen D, Cassart D. Evaluation of a protocol for fast localised abdominal sonography of horses (FLASH) admitted for colic. *Vet J*. (2011) 188:77–82. doi: 10.1016/j.tvjl.2010.02.017

7. Fischer AT Jr. Advances in diagnostic techniques for horses with colic. *Vet Clin North Am Equine Pract*. (1997) 13:203–19. doi: 10.1016/S0749-0739(17)30237-7

8. Reef VB. *Equine diagnostic ultrasound*. Philadelphia, PA: W.B. Saunders (1998).

9. Haardt H, Romero AE, Boysen SR, Lohnherr A, Tan J-Y. Incidence of superficial abdominal organ identification is similar using high-frequency linear (transrectal) and low-frequency curvilinear (abdominal) transducers in clinically healthy horses: a pilot study. *Vet Radiol Ultrasound*. (2022) 63:345–52. doi: 10.1111/vru.13060

10. HENNEKE DR, POTTER GD, KREIDER JL, YEATES BF. Relationship between condition score, physical measurements and body-fat percentage in mares. *Equine Vet J*. (1983) 15:371–2. doi: 10.1111/j.2042-3306.1983.tb01826.x

11. Epstein KL, Hall MD. Effect of nasogastric tube placement, manipulation, and fluid administration on transcutaneous ultrasound visualization and assessment of stomach position in healthy unfed and fed horses. *Animals*. (2022) 12:3433. doi: 10.3390/ani12233433

12. Farrell A, Kersh K, Liepman R, Dembek KA. Development of a colic scoring system to predict outcome in horses. *Front Vet Sci*. (2021) 8:697589. doi: 10.3389/fvets.2021.697589

13. Beccati F, Pepe M, Gialletti R, Cercone M, Bazzica C, Nannarone S. Is there a statistical correlation between ultrasonographic findings and definitive diagnosis in horses with acute abdominal pain? *Equine Vet J*. (2011) 43:98–105. doi: 10.1111/j.2042-3306.2011.00428.x

14. Lawson AL, Mair TS, Fairburn A, Sherlock CE, Archer DC, Carslake HB, et al. Evaluation of a protocol for a modified fast localised abdominal sonography of horses (FLASH) admitted for colic. *Equine Vet J*. (2021) 53:6. doi: 10.1111/evj.02_13492

15. Pease AP, Scrivani PV, Erb HN, Cook VL. Accuracy of increased large-intestine wall thickness during ultrasonography for diagnosing large-colon torsion in 42 horses. *Vet Radiol Ultrasound*. (2004) 45:220–4. doi: 10.1111/j.1740-8261.2004.04038.x

16. Jones SL, Davis J, Rowlingson K. Ultrasonographic findings in horses with right dorsal colitis: five cases (2000-2001). *J Am Vet Med Assoc*. (2003) 222:1248–51. doi: 10.2460/javma.2003.222.1248

17. Freeman SL. Diagnostic ultrasonography of the mature equine abdomen. *Equine Vet Educ*. (2003) 15:319–30. doi: 10.1111/j.2042-3292.2003.tb00257.x

18. Bithell S, Habershon-Butcher JL, Bowen IM, Hallowell GD. Repeatability and reproducibility of transabdominal ultrasonographic intestinal wall thickness measurements in thoroughbred horses. *Vet Radiol Ultrasound*. (2010) 51:647–51. doi: 10.1111/j.1740-8261.2010.01715.x

19. Hendrickson EH, Malone ED, Sage AM. Identification of normal parameters for ultrasonographic examination of the equine large colon and cecum. *Can Vet J*. (2007) 48:289–91.

20. Epstein K, Short D, Parente E, Reef VR, Southwood L. Gastrointestinal ultrasonography in normal adult ponies. *Vet Radiol Ultrasound*. (2008) 49:282–6. doi: 10.1111/j.1740-8261.2008.00367.x

21. Santschi EM, Slone DE Jr, Frank WM 2nd. Use of ultrasound in horses for diagnosis of left dorsal displacement of the large colon and monitoring its nonsurgical correction. *Vet Surg*. (1993) 22:281–4. doi: 10.1111/j.1532-950X.1993.tb00398.x

22. Henry BM. Understanding abdominal ultrasonography in horses: which way is up? *Compend Contin Educ Vet*. (2011) 33:E2.

frontiers | Frontiers in Bioengineering and Biotechnology

TYPE Original Research
PUBLISHED 27 February 2024
DOI 10.3389/fbioe.2024.1297675

OPEN ACCESS

EDITED BY
Blaz Cugmas,
University of Latvia, Latvia

REVIEWED BY
Won Bae,
University of California, San Diego,
United States
Lynn Griffin,
Colorado State University, United States

*CORRESPONDENCE
Jihye Choi,
imsono@snu.ac.kr

RECEIVED 20 September 2023
ACCEPTED 09 February 2024
PUBLISHED 27 February 2024

CITATION
Lee D, Kim E, Woo H, Jeon C-Y, Yoon J and Choi J (2024), Fast field echo resembling CT using restricted echo-spacing (FRACTURE) MR sequence can provide craniocervical region images comparable to a CT in dogs.
Front. Bioeng. Biotechnol. 12:1297675.
doi: 10.3389/fbioe.2024.1297675

Fast field echo resembling CT using restricted echo-spacing (FRACTURE) MR sequence can provide craniocervical region images comparable to a CT in dogs

Dongjae Lee[1], Eunjee Kim[1], Hyeonjae Woo[1], Chang-Yeop Jeon[2], Junghee Yoon[1] and Jihye Choi[1]*

[1]Department of Veterinary Medical Imaging, College of Veterinary Medicine, Seoul National University, Seoul, Republic of Korea, [2]National Primate Research Center, Korea Research Institute of Bioscience and Biotechnology, Cheongju, Republic of Korea

Magnetic resonance imaging (MRI) is essential for evaluating cerebellar compression in patients with craniocervical junction abnormalities (CJA). However, it is limited in depicting cortical bone because of its short T2 relaxation times, low proton density, and organized structure. Fast field echo resembling a computed tomography (CT) scan using restricted echo-spacing (FRACTURE) MRI, is a new technique that offers CT-like bone contrast without radiation. This study aimed to assess the feasibility of using FRACTURE MRI for craniocervical junction (CCJ) assessment compared with CT and conventional MRI, potentially reducing the need for multiple scans and radiation exposure, and simplifying procedures in veterinary medicine. CT and MRI of the CCJ were obtained from five healthy beagles. MRI was performed using three-dimensional (3D) T1-weighted, T2-weighted, proton density-weighted (PDW), single echo-FRACTURE (sFRACTURE), and multiple echo-FRACTURE (mFRACTURE) sequences. For qualitative assessment, cortical delineation, trabecular bone visibility, joint space visibility, vertebral canal definition, overall quality, and artifacts were evaluated for each sequence. The geometrical accuracy, signal-to-noise ratio (SNR), and contrast-to-noise ratio (CNR) were quantified. Both sFRACTURE and CT images provided significantly higher scores for cortical delineation and trabecular bone visibility than conventional MRI. Joint space visibility and vertebral canal definition were similar to those observed on CT images, regardless of the MR sequence. In the quantitative assessment, the distances measured on T2-weighted images differed significantly from those measured on CT. There were no significant differences between the distances taken using T1-weighted, PD-weighted, sFRACTURE, mFRACTURE and those taken using CT. T1-weighted and sFRACTURE had a higher SNR for trabecular bone than CT. The CNR between the cortical bone and muscle was high on CT and FRACTURE images. However, the CNR between the cortical and trabecular bones was low in mFRACTURE. Similar to CT, FRACTURE sequences showed higher cortical delineation and trabecular bone visibility than T2-weighted, T1-weighted, and PDW CCJ sequences. In particular, sFRACTURE provided a high signal-to-noise ratio (SNR) of the trabecular bone and a high CNR between the cortical bone and

muscle and between the cortical and trabecular bones. FRACTURE sequences can complement conventional MR sequences for bone assessment of the CCJ in dogs.

KEYWORDS

bone, canine, CT-like, MRI, vertebra

1 Introduction

Abnormalities of the craniocervical junction (CJA) are common in veterinary medicine. CJA is a general term used to describe malformations of the craniocervical region (CCJ), such as Chiari-like malformations, atlantooccipital instability, atlantoaxial instability, occipitoatlantoaxial malformations, atlantooccipital overlapping, and dens abnormalities in small-breed dogs. Magnetic resonance imaging (MRI) provides excellent assessment of soft tissues and medullary bone without ionizing radiation. Therefore, MRI is essential for evaluating cerebellar compression in patients with CJA. However, in diagnosing CJA, it is often difficult to determine which bone structures are involved in the abnormality and which areas are affected secondary to CJA. MRI is limited in depicting the cortical (including the subchondral) bone because of its very short T2 relaxation times, low proton density, and organized structure (Marino et al., 2012). Computed tomography (CT) is often performed in addition to MRI to determine the bone structures that cause neural tissue compression in human patients with CJAs and in veterinary medicine, because CT can visualize the bone structures in detail with high resolution (Goel et al., 1998; Botelho et al., 2007; Cerda-Gonzalez et al., 2009a; Marino et al., 2012; Stalin et al., 2015; Kiviranta et al., 2017; Planchamp et al., 2022). In addition, three-dimensional (3D) isotropic CT allows multiplanar and volumetric reconstruction to help depict bone and joint structures (Kwon et al., 2005; Griffith et al., 2007; Bishop et al., 2013; Chong et al., 2021). Despite these advantages, patient exposure to ionizing radiation is a primary concern in CT in humans. Moreover, additional CT scans after MRI require the complex process of moving the patient from the MR machine to the CT room while maintaining the correct position of the patient for the CT scans. Unlike humans, animals generally require anesthesia for MRI and CT scans. This process requires a long anesthesia time, and many personnel, which incur high examination costs.

With the improvement of MRI techniques, new MR sequences that can depict the cortical bone and provide CT-like bone contrast (CLBC) have been introduced in human medicine (Chong et al., 2021). There are various 3D MRI approaches for generating CLBC images, including the ultrashort echo time gradient echo (UTE) (Chang et al., 2015), zero echo time (ZTE) (Kwon et al., 2005; Griffith et al., 2007; Bishop et al., 2013), T1-weighted gradient-recalled echo(GRE) pulse sequences (Dremmen et al., 2017; Gersing et al., 2019), susceptibility-weighted imaging (SWI) pulse sequences (Böker et al., 2018; Böker et al., 2019; Böker et al., 2020; Haller et al., 2021), and deep learning methods (Han, 2017).

Fast field echo resembling a CT scan using restricted echo-spacing (FRACTURE) is a Cartesian 3D GRE-pulse sequence that generates CLBC 3D MRI with high spatial resolution. FRACTURE is a high-resolution 3D gradient-echo-based technique that uses multiple echoes with constant echo spacing and post-processing subtraction to provide CT-like image contrast. 3D gradient echo–based sequences have been shown to provide high bony contrast by providing images with low-signal bone contours compared to the surrounding high-signal fatty bone marrow and soft tissue. After acquisition, two additional post-processing steps are performed to produce images with more CT-like contrast. The first post-processing step consists of a summation of the magnitude of all the echoes. This increases the signal-to-noise ratio, which is inherently low due to the high resolution and receiver bandwidth. After summation, the images from the last echo are subtracted from the summed images. This inverts the grey scale and gives the bone CT-like contrast. The advantages of 3D Cartesian gradient echo-based sequences are that they are commonly available on MRI scanners from all vendors, have field strengths, permit high-spatial-resolution imaging, and use small flip angles for lower specific absorption rates (Johnson et al., 2021).

Based on previous human studies, we anticipated that CLBC 3D MR sequence could complement bone structure assessment after soft tissue evaluation using a FRACTURE MR scan instead of an additional CT scan. The use of CLBC images would simplify the examination of CJAs and reduce costs for patients for whom preoperative planning with MRI and CT is typically required (Chong et al., 2021). However, to the best of our knowledge, there have been no published clinical studies on CCJ evaluation using FRACTURE sequence MRI in dogs. We hypothesized that FRACTURE MR can provide similar resolution images to CT images of the cortical bone of the CCJ in dogs. This study aimed to describe the MR features of the CCJ in normal dogs using 3.0-T MRI and assess the feasibility of FRACTURE sequences for CCJ evaluation by comparing them with CT and conventional MR images in dogs.

2 Materials and methods

2.1 Selection and description of subjects

In this prospective method comparison pilot study, five clinically healthy purpose-bred beagles (three neutered males and two intact females) were used (mean body weight: 13 kg (range: 9.9–15.5 kg); mean age: 3 years (range: 2–5 years). The sample size was determined using convenience sampling. The dogs were housed individually and provided commercial dry food and tap water *ad libitum*. All dogs were clinically healthy based on a physical examination, complete blood count, serum biochemistry, electrolytes, cranial nerve examination, and thoracic and abdominal radiography. The CCJs of all dogs were determined to be normal based on CT findings. All procedures performed in this study were approved by the Seoul National University Institutional Animal Care and Use Committee (SNU IACUC-230726-2).

TABLE 1 MRI parameters and sequences.

Parameter	MR sequences				
	3D FRACTURE multi-echo	3D FRACTURE single-echo	3D PDW	3D T1W	3D T2W
Number of In phase echo	4	1			
TR (ms)	16	5.4	1,100	350	1,500
TE (ms)	In phase (2.3) Echo-spacing (2.3)	In phase (2.3)	34	19	100
Flip angle	12	8	90	90	90
Slice interval	0.6	0.6	0.6	0.6	0.6
FOV (mm)	160 × 160 × 60	160 × 160 × 60	160 × 160 × 60	160 × 160 × 60	160 × 160 × 60
Matrix	268 × 266	268 × 266	268 × 266	268 × 266	268 × 235
Reconstruction Matrix	320	288	320	320	320
NEX	1	1	1	1	1
Acquisition time (min:sec)	7:01	4:51	12:57	11:55	13:31

MR, magnetic resonance image; CT, computed tomography; mFRACTURE, Fast field Echo Resembling a CT Using Restricted Echo-spacing- multiple echoes; sFRACTURE, Fast field Echo Resembling a CT Using Restricted Echo-spacing- single echo; PDW, Proton density-weighted; T2W, T2-weighted; and T1W, T1-weighted image; TR, repeated time; TE, echo time; FOV, field of view; NEX, number of excitation.

2.2 Anesthesia and schedule

In each dog, MRI and CT scans were performed in random order at 7–9-day intervals using the same anesthesia procedure. After each dog had been fasted for 12 h, a 24-gauge catheter was placed in the cephalic vein to induce anesthesia. After premedication with medetomidine (0.01 mg/kg IM, Domitor, Zoetis, Finland), anesthesia was induced with alfaxalone (2.0 m/kg IV, Alfaxan, Jurox Pty Ltd., Australia) and maintained with isoflurane (Ifran, Hana Pharm, South Korea) in oxygen. For CT and MRI, noninvasive blood pressure, oxygen saturation, heart rate, respiratory rate, and body temperature were monitored during the induction and maintenance of anesthesia.

The general condition and anesthesia-related side effects, such as respiratory signs, vomiting, depression, and anorexia, of each dog were monitored for 5 days postoperatively.

2.3 MRI examinations

In all dogs, MR of the head and neck was performed using a 3.0-T MRI scanner (Achieva, Philips Healthcare, Netherlands) with a 32-channel cardiac coil. All dogs were positioned in sternal recumbency with both forelegs pulled back and head-first. T1-weighted (T1W) images were obtained as localizers in three orthogonal planes using 3D turbo field-echo (TFE) scans. The field of view (FOV) was set to include the CCJ from the olfactory bulb to the axial level in all planes (Deininger-Czermak et al., 2021). The following were then obtained from each dog: 1) T2-weighted (T2W) images using 3D turbo spin-echo (TSE) sequences, 2) T1-weighted (T1W) images using 3D TSE sequences, 3) proton density-weighted (PDW) images using 3D TSE sequences, 4) 3D fast-field echo sequences using sFRACTURE, and 5) 3D fast-field echo sequences using mFRACTURE. In this study, mFRACTURE was created by summation of four in-phase echo images. On the other hand, sFRACTURE used only one in-phase echo image to obtain an unsummated image with a lower signal to noise than mFRACTURE. Table 1 shows the parameters and their sequences. In 3D acquisition sequences, sagittal images were acquired, and transverse and dorsal images were reconstructed. The total scan and image acquisition times for each sequence were measured automatically (Deininger-Czermak et al., 2021).

2.4 CT examinations

After placing the dog in sternal recumbency, a CT scan of the CCJ was performed using a 160 multi-slice CT scanner (Aquilion Lightning 160, Canon Medical Systems, Japan) with the following parameters; 120 kVp with a tube current of 200 mA, slice thickness of 0.5 mm, and tube rotation time of 1.0 s. The image dataset was reconstructed at a slice thickness of 0.6 mm and an increment of 0.4 mm, using a medium-frequency algorithm for soft tissue and a high-frequency algorithm for bone structures in the transverse and sagittal planes. The FOV was set to include the region from the nose to the cervical vertebrae. A maximum FOV of 200 × 200 mm^2 with a matrix of 512 × 512 mm^2 was used.

2.5 Image analyses

All MR and CT images were sent to a picture archiving and communication system (Infinitt PACS; Infinitt Healthcare, Seoul, South Korea). Qualitative and quantitative assessments of MRI and CT images were performed individually by two observers (D.J.L. and E.J.K.), each with 1–2 years of radiology experience, in random order under the supervision of a radiologist (J.H.C.) at the Korean College of Veterinary Medical Imaging. All CT images were evaluated using a bone window with a window level of 500 Hounsfield Units (HU) and a window width of 2000 HU.

Images were assessed at three evaluation sites: the occipital bone, the first cervical vertebra (C1), and the second cervical vertebra (C2).

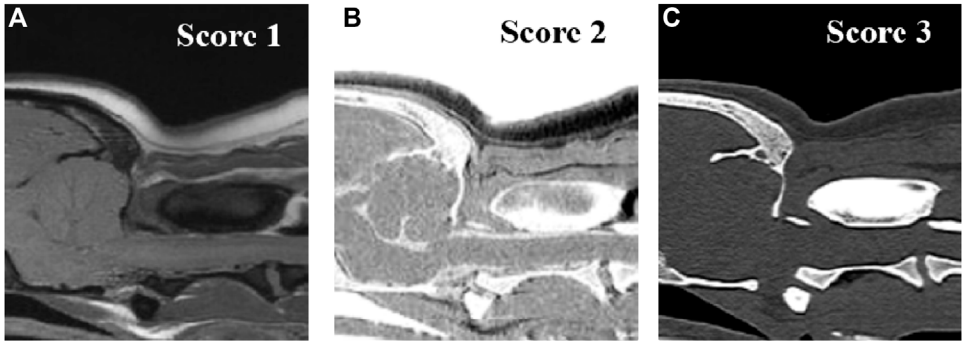

FIGURE 1
Qualitative evaluation of the image qualities on T1-weighted **(A)**, single echo-FRACTURE **(B)**, CT **(C)** images of craniocervical region in a beagle. 1 = Artifacts present, affecting the images; 2 = Artifacts were present but minimal, not affecting the images; and 3 = Artifacts were absent.

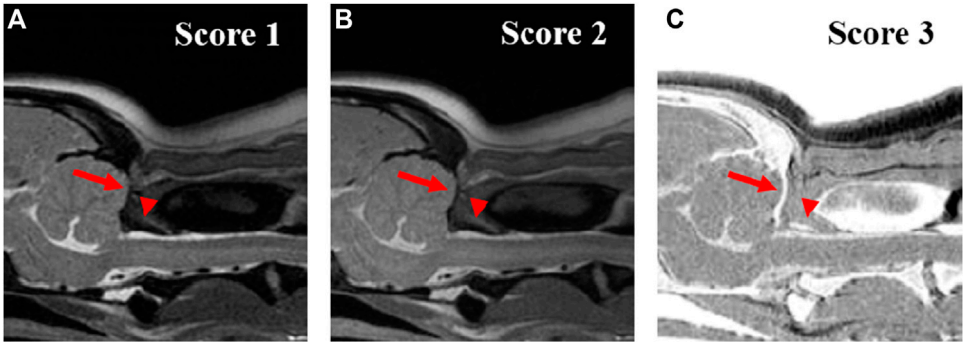

FIGURE 2
Qualitative evaluation of the visuality of the cortical delineation of occipital region (arrow) and dorsal arch of atlas (arrow-head) on T2-weighted **(A)**, Proton density-weighted **(B)**, single echo-FRACTURE **(C)** images of the craniocervical region in a beagle. 1 = The border of the cortical bone was too blurry to be distinguished from the surrounding soft tissue; 2 = Most cortical bones were well distinguished, but there were some blurry parts; and 3 = The cortical bone was clearly distinguishable from the surrounding soft tissue.

For image assessment, both CT images of the bone window and MRI images were interpreted by scrolling through all images. For the qualitative assessment, the image quality and artifacts of the overall images (Figure 1), visualization of the cortical delineation (Figure 2), clarity of the trabecular bone (Figure 3), conspicuity of the joint spaces, and delineation of the vertebral canal of the evaluation sites were evaluated. Only the delineation of the vertebral canal image was evaluated in the transverse plane, and all others were evaluated in the sagittal plane. The main evaluation site of the occipital bone was the occiput; both the dorsal and ventral arches were evaluated in C1, and the ventral body was the main evaluation site in C2. For image quality, motion, partial volume, and chemical shift artifacts were evaluated separately using a three-point scale: 1 = Artifacts present, affecting the images; 2 = Artifacts were present but minimal, not affecting the images; and 3 = Artifacts were absent. Visualization of cortical delineation was assessed using a three-point scale based on whether the cortical bone and surrounding soft tissue were well distinguished. 1 = The border of the cortical bone was too blurry to be distinguished from the surrounding soft tissue; 2 = Most cortical bones were well distinguished, but there were some blurry parts; 3 = The cortical bone was clearly distinguishable from the surrounding soft tissue. The clarity of the trabecular bone was assessed using a three-point scale based on its differentiation from the cortical bone and visualization of trabecular patterns. 1 = The trabecular bone appeared homogeneous overall, and there were no visible trabecular patterns; 2 = The trabecular pattern was visible but not clear; 3 = The trabecular and cortical bones were well distinguished, and the trabecular pattern was visible. The conspicuity of the joint spaces was assessed using a three-point scale based on the distinction between the joint space and the articulating bones. 1 = It was difficult to distinguish between the parts that comprised the joint and the boundary of the joint; 2 = The bone and joint space were easily distinguished from each other, but there were ambiguous parts; and 3 = The bones forming the joint and the space between them were clearly visible. Delineation of the vertebral canal was assessed using a three-point scale based on the definition of the spinal cord and bones. 1 = The border between the spinal cord and bone was blurred and an accurate distinction was difficult; 2 = The

FIGURE 3
Qualitative evaluation of the clarity of trabecular bone of occipital region (arrow) and axis (arrow head) on T2-weighted **(A)**, single echo-FRACTURE **(B)**, CT **(C)** images of craniocervical region in a beagle. 1 = The trabecular bone appeared homogeneous overall, and there were no visible trabecular patterns; 2 = The trabecular pattern was visible but not clear; 3 = The trabecular and cortical bones were well distinguished, and the trabecular pattern was visible.

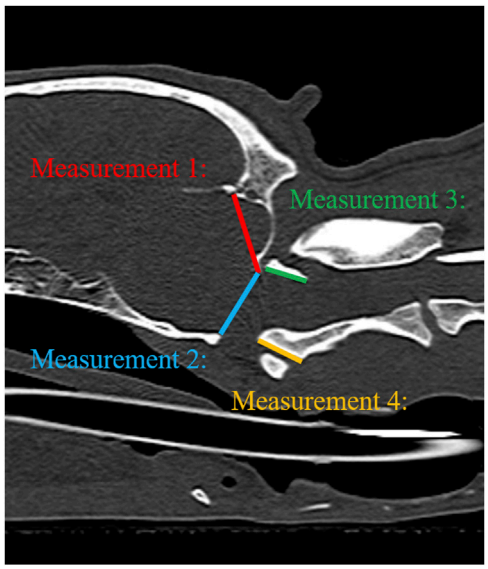

FIGURE 4
Illustration of measurements 1–4 to evaluate geometric accuracy on CT sagittal images. Measurement 1: Occipital bone length measured from the occipital protuberance to the ventral surface of the occipital bone (opisthion). Measurement 2: Caudal height of the foramen magnum measured from the inside of the basion to the inside of the opisthion. Measurement 3: Length of the dorsal arch of the atlas measured from the ventral line. Measurement 4: Maximum length of the dens measured from the ventral line.

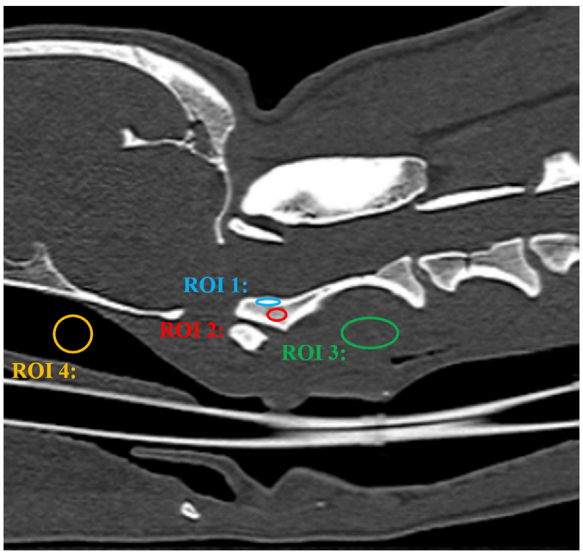

FIGURE 5
CT image of a craniocervical region in the sagittal plane. The signal intensity of the cortical bone was measured by placing a oval region of interest (ROI) over the cortical bone of axis (ROI 1). The signal intensity of the trabecular bone was measured by placing a oval region of interest (ROI) over the trabecular bone of axis (ROI 2). The signal intensity of the surrounding muscle was measured by placing a circular or oval ROI over the muscle adjacent to the axis (ROI 3). Background noise was measured by placing a circular or oval ROI in the air of the nasopharynx (ROI 4).

border was slightly blurry but distinguishable; 3 = The spinal cord and surrounding bones were clearly visible.

For a quantitative evaluation, the geometric accuracy, signal-to-noise ratio (SNR), and contrast-to-noise ratio (CNR) were measured. To evaluate the geometric accuracy between MRI and CT images, two observers manually measured four distances twice on each randomly aligned MRI and CT image using an electronic digital caliper on the monitor at four sites (Figure 4); 1) occipital bone length-measured from the occipital protuberance to the ventral surface of the occipital bone (opisthion), 2) caudal height of the foramen magnum-measured from the inside of the basion to the inside of the opisthion, 3) length of the dorsal arch of the atlas-measured from the ventral line, and 4) maximum length of the dens measured from the ventral line. All measurements were performed in the sagittal plane and included two sections from the occipital bone and one section each from C1 and C2. Measurements of the occipital bone length, caudal height of the

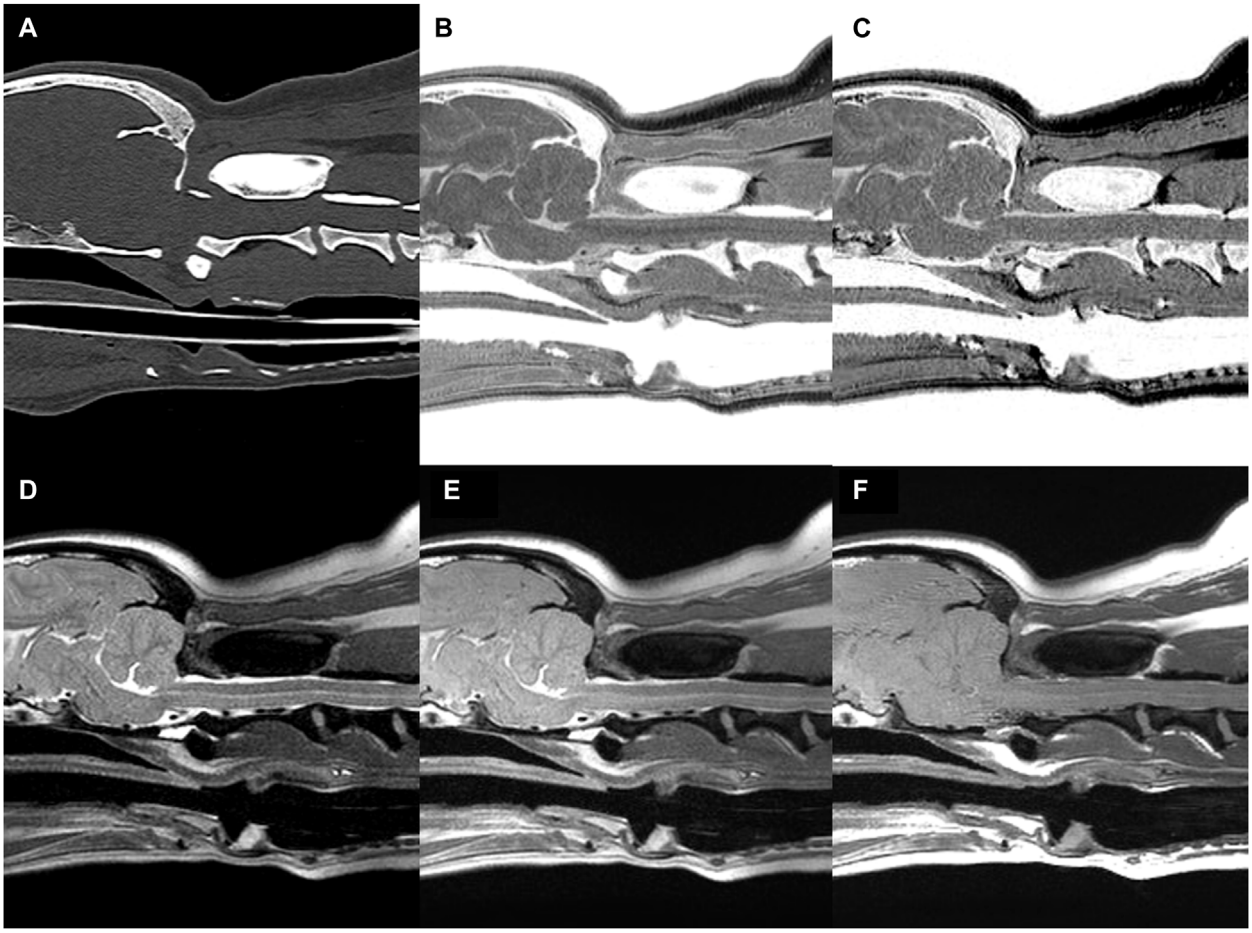

FIGURE 6
CT **(A)** and MR **(B–F)** images of the craniocervical junction (CCJ) in a beagle. Multiple echo-FRACTURE **(B)** and single echo-FRACTURE **(C)** showed higher cortical delineation and trabecular bone visibility than T2-weighted **(D)**, proton density-weighted **(E)**, and T1-weighted **(F)** images of CCJ, similar to that observed on CT images.

foramen magnum, and length of the dorsal arch of the atlas were taken from the same cross-section as the most aligned atlanto-occipital joint, and the maximum length of the dens was measured from the cross-section with the maximum dens length.

The SNR and CNR were calculated to evaluate the quality of MRI and CT images. The SNR of the cortical and trabecular bones, CNR of the cortical and trabecular bones, and CNR of the cortical bone and surrounding muscle (longus colli muscle) were measured in the largest dimensioned slice, where the vertebral body and spinous process of C2 were visible. For this purpose, the signal intensity (SI) of a 5–10 mm^2 region of interest (ROI) was measured in C2 (cortical bone, trabecular bone) and muscle. The ROI was drawn to be as large as possible, with the exclusion of blood vessels and artifacts. Background noise was measured by placing a circular or oval ROI in the air of the nasopharynx (Figure 5). All measurements were repeated three times, and the average values were used to calculate the SNR and CNR (Usamentiaga et al., 2018). SNR and CNR were calculated as follows:

$$SNR\,cortical\,bone = \frac{SI\ (cortical\,bone)}{SD\ (air)}$$

$$SNR\,trabecular\,bone = \frac{SI\ (trabecular\,bone)}{SD\ (air)}$$

$$CNR\,cortical\,bone, muscle = \frac{SI\,(cortical\,bone) - SI\,(muscle)}{SD\ (air)}$$

$$CNR\,cortical\,bone, trabecular\,bone = \frac{SI\,(cortical\,bone) - SI\,(trabecular\,bone)}{SD\ (air)}$$

2.6 Statistical analyses

Statistical analysis was performed by a statistician (J.Y.P.) using commercially available software (SPSS statistical program, IBM SPSS Statistics 27.0, IBC Corporation, NY). The non-parametric Wald–Wolfowitz test was used to measure the likelihood of measurement of five dogs with the same expression distribution (Wald and Wolfowitz, 1943). Differences in qualitative assessment (image quality and artifacts, visualization of cortical delineation, clarity of the trabecular bone, conspicuity of the joint spaces, and delineation of the vertebral canal), SNR of the cortical bone, SNR of

TABLE 2 Scores of several parameters of magnetic resonance imaging (MRI) and computed tomography (CT).

Item	Level	CT	mFRACTURE	sFRACTURE	PDW	T1W	T2W
Image quality and artifacts		2.80 ± 0.45[a]	2.80 ± 0.45[b,c]	2.20 ± 0.45[d]	2.00 ± 0.71[b,e]	1.00 ± 00[a,c,d,f]	2.20 ± 0.45[e,f]
Visualization of cortical delineation	Occipital	3.00 ± 0.00	3.00 ± 0.00	3.00 ± 0.00	2.60 ± 0.55	2.20 ± 0.84	1.60 ± 0.89
	C1	3.00 ± 0.00	3.00 ± 0.00	3.00 ± 0.00	2.40 ± 0.55	2.20 ± 0.84	1.80 ± 0.84
	C2	3.00 ± 0.00[a,b]	3.00 ± 0.00[c,d]	3.00 ± 0.00[e,f]	2.40 ± 0.55	2.20 ± 0.45[a,c,e]	2.00 ± 0.00[b,d,f]
Clarity of trabecular bone	Occipital	3.00 ± 0.00[a,b,c]	1.80 ± 0.45[a,d]	3.00 ± 0.00[d]	2.20 ± 0.45[b]	2.00 ± 0.71	1.80 ± 0.45[c]
	C1	2.60 ± 0.55	1.60 ± 0.89	2.80 ± 0.45[a,b,c]	1.60 ± 0.55[a]	1.60 ± 0.55[b]	1.20 ± 0.45[c]
	C2	3.00 ± 0.00[a,b,c,d]	1.60 ± 0.55[a,e]	3.00 ± 0.00[e,f,g,h]	2.00 ± 0.00[b,f]	2.00 ± 0.00[c,g]	1.80 ± 0.45[d,h]
Conspicuity of joint margin	Occipital	3.00 ± 0.00[a]	3.00 ± 0.00[b]	3.00 ± 0.00[c]	2.60 ± 0.55[d]	1.80 ± 0.45[a,b,c,d]	2.20 ± 0.84
	C1	3.00 ± 0.00[a]	3.00 ± 0.00[b]	3.00 ± 0.00[c]	2.40 ± 0.55	1.80 ± 0.84	1.80 ± 0.45[a,b,c]
	C2	3.00 ± 0.00[a,b,c]	3.00 ± 0.00[d,e,f]	3.00 ± 0.00[g,h,i]	2.00 ± 0.00[a,d,g]	1.80 ± 0.45[b,e,h]	1.60 ± 0.55[c,f,i]
Delineation of vertebral canal	C1	3.00 ± 0.00	3.00 ± 0.00	3.00 ± 0.00	2.60 ± 0.55	2.00 ± 0.71	2.40 ± 0.55
	C2	3.00 ± 0.00	3.00 ± 0.00	3.00 ± 0.00	2.60 ± 0.55	2.00 ± 0.71	2.40 ± 0.55

All data are presented as mean ± standard deviation.

[a-i] Within a row, the same superscript indicated statistically significant differences between two groups using a Wilcoxon signed rank test. (significance level of *p*-value and< 0.05).

mFRACTURE, Fast field Echo Resembling a CT Using Restricted Echo-spacing- multiple echoes; sFRACTURE, Fast field Echo Resembling a CT Using Restricted Echo-spacing- single echo; PDW, Proton density-weighted; T2W, T2-weighted; and T1W, T1-weighted image; C1, the first cervical vertebrae; C2, the second vertebrae.

10.3389/fbioe.2024.1297675

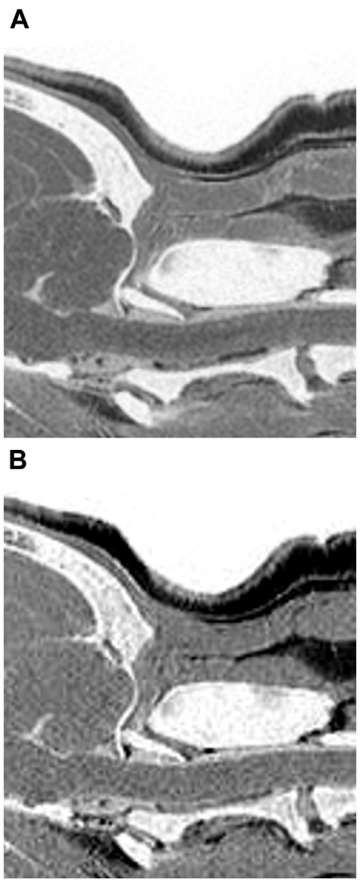

FIGURE 7
Multiple echo-FRACTURE **(A)** and single echo-FRACTURE **(B)** images of the craniocervical junction (CCJ) in a beagle. Single echo-FRACTURE showed higher trabecular bone visibility than multiple echo-FRACTURE.

the trabecular bone, CNR of the cortical bone-muscle, CNR of the cortical bone-trabecular bone, and geometrical measurements were analyzed using the Wilcoxon signed-rank test. To assess geometrical accuracy, the limits of agreement between MRI and CT were calculated for each of the four distances measured using Bland-Altman plot. The interrater agreement between the two observers for the MRI and CT images was evaluated using the interclass correlation coefficient (ICC) test (Landis and Koch, 1977): ICC <.4, poor agreement; ICC .41–.6, moderate agreement; ICC .61–.8, good agreement; ICC >.8, excellent agreement. All data are presented as mean ± standard deviation, and $p < 0.05$ was considered significant.

3 Results

MR and CT images of the CCJ were obtained successfully in all dogs, using FRACTURE sequences, without any complications (Figure 6). The image acquisition times for each MRI sequence are listed in Table 1.

The mean and standard deviation (SD) values for each evaluation factor used in the qualitative evaluation are presented in Table 2. The ICC results for all qualitative evaluation factors were >.8, showing excellent agreement. The image qualities of mFRACTURE and T2W were significantly higher than those of the other sequences, including sFRACTURE. However, T1W had the lowest image quality score, similar to that of PDW. There were no significant differences in visualization of cortical delineation between any of the sequences at the occipital bone and C1 level, whereas sFRACTURE, mFRACTURE, and CT had significantly higher scores than T1W and T2W at C2. The clarity of the trabecular bone had a high score with sFRACTURE and CT at all evaluation sites. In particular, sFRACTURE scored significantly higher than mFRACTURE, PDW, and T2W at the occipital bone (Figure 7). CT also scored significantly higher than all other sequences, except for sFRACTURE. At the C1 level, T2W had the lowest score which was significantly worse than those of sFRACTURE, mFRACTURE, and CT. At the C2 level, CT was not significantly different from sFRACTURE or mFRACTURE. The conspicuity of the joint margin was found to be lower at the level of the occipital bone, with a mean of 1.8 T1W, which was significantly worse than that of all other sequences. At C1, T2W had a mean of 1.8, and scored significantly lower than all sequences except T1W. At C2, sFRACTURE, mFRACTURE, and CT scores were significantly higher than those for PDW, T1W, and T2W. Vertebral canal delineation showed mean scores above 2.0, with no significant difference between sequences at either the C1 or C2 levels (Figure 8). The mean and SD values for the qualitative assessment are shown in Table 2. The ICC results of the qualitative evaluation were all >.8, showing excellent agreement.

The mean and SD of the values obtained in the quantitative assessment are listed in Table 3. For all measured distances, geometrical agreement using Bland-Altman plot between MRI and CT was considered good to excellent, based on the limits of agreement (Table 4). The ICC results showed excellent agreement of > .8 for all measurements, except for the caudal height of the foramen magnum. In addition, among the values measured in the T2W images, all except the dens length showed a significant difference from those of CT. There were no significant differences between the distances measured using mFRACTURE, sFRACTURE, and T1W and those measured using CT.

The means and SDs of the SNRs and CNRs are shown in Table 5. The ICC results showed excellent agreement, with all >.8. The SNR of the cortical bone was higher with CT, showing a significant difference compared with all other MRI sequences with a mean of 29.40 (Figure 9A). By contrast, the muscle SNR was higher for MRI than for CT (Figure 9B). The SNR of the trabecular bone was higher with T1W, showing a significant difference compared with all other sequences except sFRACTURE, and sFRACTURE showing a significant difference compared with mFRACTURE (Figure 9C). The CNR of the cortical bone-trabecular bone was shown to have a low score, with both mFRACTURE and T2W averages below 10.0. No significant differences were found between the CT and MRI sequences, except for the mFRACTURE and T2W sequences, and a significant difference was observed between sFRACTURE and mFRACTURE sequences (Figure 10A). The CNR of the cortical bone-muscle showed no significant differences between CT, sFRACTURE, and mFRACTURE, and showed significant differences between CT and PDW, T1W, and T2W, with CT showing the highest contrast (Figure 10B).

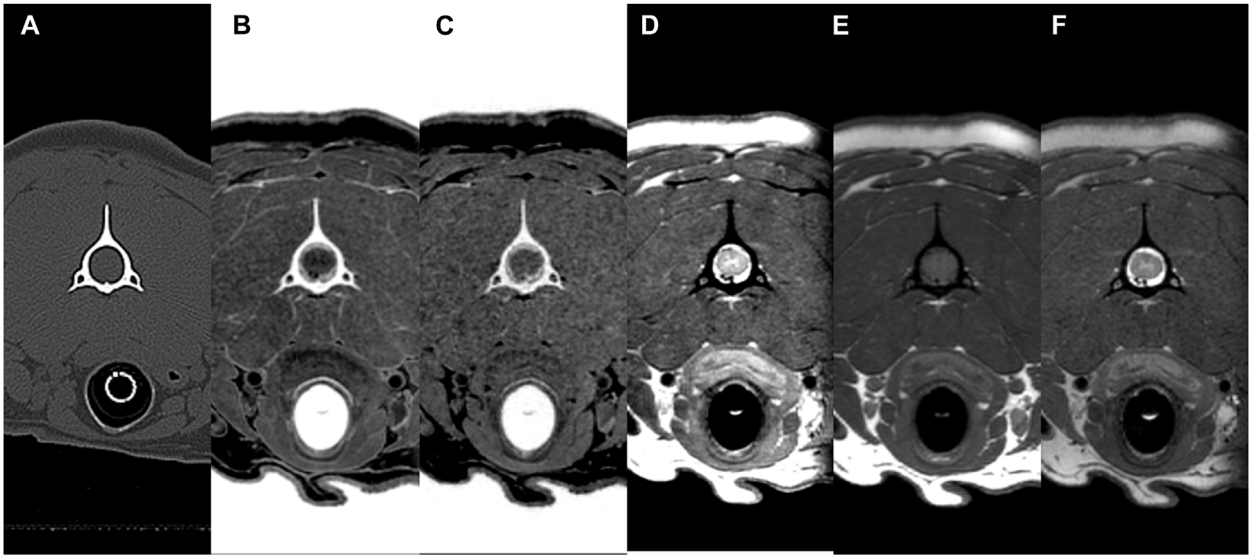

FIGURE 8
CT **(A)** and MR **(B–F)** transverse images of the vertebral canal at C2 (axis) in a beagle. All sequences (CT, multiple echo-FRACTURE **(B)**, single echo-FRACTURE **(C)**, proton density-weighted **(D)**, T1-weighted **(E)**, and T2-weighted **(F)** had high scores for the evaluation of vertebral canal delineation.

4 Discussion

This study assessed the feasibility of evaluating the CCJ in dogs using the FRACTURE MRI sequence compared with CT and conventional MRI. Qualitative evaluation revealed that both the sFRACTURE and CT scores were significantly higher than those obtained with conventional MRI for cortical delineation and trabecular visibility. sFRACTURE and mFRACTURE scored highly for joint margin clarity and spinal canal clarity, as did the CT images. In the quantitative evaluation, distances measured on T2W images were significantly different from those measured on CT images, whereas there were no significant differences between the measurements taken using the other MRI sequences and those taken from CT images. T1W and sFRACTURE had higher SNRs than CT for trabecular bone. The CNR between the cortical bone and muscle was high for CT, sFRACTURE, and mFRACTURE, whereas that between the cortical bone and trabecular bone was low for mFRACTURE.

Because the dogs were scanned under anesthesia, there were very few motion artifacts to disturb the overall image quality, providing an optimal study environment for a thorough image quality comparison. Except in T1W, the other imaging types showed good image quality with an average score >2.0. In particular, the image quality obtained using mFRACTURE was high, and was significantly higher than that of PDW and T1W, showing that mFRACTURE is suitable for use for diagnostic purposes.

By contrast, sFRACTURE and CT had high scores for trabecular bone clarity, whereas mFRACTURE had low scores. This was attributed to the relatively narrow coverage of the trabecular bone in the cervical spine and high attenuation of the trabecular bone by the summation of MRI signals from five consecutive echo times in a sequence (Held et al., 2001; Deininger-Czermak et al., 2021). However, analysis of single- and multi-echo FRACTURE sequences together could facilitate a more comprehensive assessment, as mFRACTURE provides a higher CNR between the cortical and trabecular bones, joint margin, and cortical delineation, and a higher image quality than sFRACTURE. The acquisition time was 4 min 51 s for a single echo and 7 min 1 s for multiple echoes. Both sequences could be acquired faster than conventional 3D sequences. This result is in disagreement with human studies, in which FRACTURE sequences had a longer reconstruction time than conventional sequences because of the algebraic algorithm used to construct a CT-like image (Deininger-Czermak et al., 2021). However, in this study, sFRACTURE and mFRACTURE were obtained using 3D sequences with short acquisition times, and the combined time for both FRACTURE sequences was comparable to that of conventional sequences.

The conspicuity of the joint margins in the occipital bone was significantly lower on T2W than in all other sequence types. This could be due to the low image quality of T2W images or areas of high signal intensity on T2W, showing, for example, synovial fluid between the joint surfaces, which may be poorly visible on T2W, resulting in blurred boundaries that were difficult to assess.

In this study, we also found that the visualization of cortical boundaries was significantly better using sFRACTURE and mFRACTURE sequences, even though some conventional MRI images were assessable (Samim et al., 2019; Jans et al., 2021). Therefore, we concluded that FRACTURE helps assess cortical boundaries. In support of this, the CNR between the cortical bone and muscle was also higher in the FRACTURE sequences.

To the best of our knowledge, this is the first report of FRACTURE MRI of the CCJ in dogs. In humans, various types of MRI sequences such as UTE, ZTE, and bone MRI have been used to examine the skull, spine, shoulder, hip, and long bones (Bishop et al., 2013; Rathnayaka et al., 2013; Eley et al., 2014; Wiesinger et al., 2016; Stillwater et al., 2017; Breighner et al., 2019; de Mello et al.,

TABLE 3 Overview of geometrical measurements by two observers for four anatomical distances. Measurement 1: Occipital bone length measured from the occipital protuberance to the ventral surface of the occipital bone (opisthion). Measurement 2: Caudal height of the foramen magnum measured from the inside of the basion to the inside of the opisthion. Measurement 3: Length of the dorsal arch of the atlas measured from the ventral line. Measurement 4: Maximum length of the dens measured from the ventral line.

Measurement	CT	mFRACTURE	sFRACTURE	PDW	T1W	T2W
1	21.23 ± 1.14[a]	20.97 ± 1.89	21.18 ± 1.95	21.96 ± 1.49	21.77 ± 1.47	22.55 ± 1.53[a]
2	14.74 ± 0.41[a,b]	14.72 ± 1.28	14.53 ± 1.04	13.78 ± 0.50a	14.08 ± 0.68	13.68 ± 0.89[b]
3	11.02 ± 1.16[a]	11.72 ± 0.87	11.53 ± 0.79	11.91 ± 0.79	11.±0.98	12.10 ± 0.68[a]
4	10.74 ± 1.16[a]	10.43 ± 1.80	10.51 ± 1.28	11.13 ± 1.39	10.65 ± 1.39	10.74 ± 1.29[a]

All data are presented as mean ± standard deviation.
[a, b] Within a row, the same superscript indicated statistically significant differences between two groups using a Wilcoxon signed rank test. (significance level of *p*-value and< 0.05).
mFRACTURE, Fast field Echo Resembling a CT Using Restricted Echo-spacing- multiple echoes; sFRACTURE, Fast field Echo Resembling a CT Using Restricted Echo-spacing- single echo; PDW, Proton density-weighted; T2W, T2-weighted; and T1W, T1-weighted image; C1, the first cervical vertebrae; C2, the second vertebrae.

TABLE 4 Limits of agreement between CT of geometrical measurements for four anatomical distances. Measurement 1: Occipital bone length measured from the occipital protuberance to the ventral surface of the occipital bone (opisthion). Measurement 2: Caudal height of the foramen magnum measured from the inside of the basion to the inside of the opisthion. Measurement 3: Length of the dorsal arch of the atlas measured from the ventral line. Measurement 4: Maximum length of the dens measured from the ventral line.

Measurement	mFRACTURE	sFRACTURE	PDW	T1W	T2W
1	[-2.56; 2.05]	[-2.42; 2.32]	[-1.01; 2.47]	[-0.93; 2.01]	[-0.32; 2.96]
2	[-1.78; 1.74]	[-1.66; 1.24]	[-1.64; −0.28]	[-1.62; 0.30]	[-2.58; 0.47]
3	[-0.75; 2.14]	[-0.63; 1.66]	[0.00; 1.78]	[-0.44; 1.95]	[-0.36; 2.52]
4	[-1.68; 1.06]	[-0.75; 0.28]	[-0.37; 1.14]	[-0.91, 0.73]	[-0.66; 0.65]

mFRACTURE, Fast field Echo Resembling a CT Using Restricted Echo-spacing- multiple echoes; sFRACTURE, Fast field Echo Resembling a CT Using Restricted Echo-spacing- single echo; PDW, Proton density-weighted; T2W, T2-weighted; and T1W, T1-weighted image; C1, the first cervical vertebrae; C2, the second vertebrae.

TABLE 5 Comparison of magnetic resonance (MR) sequences and computed tomography (CT) for signal-to-noise ratio (SNR) and contrast-to-noise ratio (CNR).

Item	CT	mFRACTURE	sFRACTURE	PDW	T1W	T2W
SNR cortical bone	29.40 ± 4.35[a,b,c,d,e]	3.99 ± 0.89[a,f,g,h]	2.62 ± 0.65[b,f]	2.52 ± 0.56[c,g]	2.82 ± 0.92[d]	1.52 ± 0.83[e,h]
SNR muscle	0.93 ± 0.24[a,b,c,d,e]	35.74 ± 5.41[a,f,g,h]	30.92 ± 5.97[b,i,j,k]	21.48 ± 5.25[c,f,i,l,m]	24.10 ± 5.25[d,g,j,l,n]	14.02 ± 2.94[e,h,k,m,n]
SNR trabecular bone	8.22 ± 2.18[a]	13.93 ± 5.02[b,c]	18.14 ± 6.54[b]	14.81 ± 5.37[d,e]	17.68 ± 4.79[a,c,d,f]	9.58 ± 4.27[e,f]
CNR cortical bone-muscle	28.47 ± 4.15[a,b,c]	31.75 ± 4.64[d,e,f]	28.31 ± 5.47[g,h,i]	18.95 ± 4.03[a,d,g]	21.28 ± 4.69[b,e,h,j]	12.51 ± 2.26[c,f,i,j]
CNR cortical bone-trabecular bone	21.18 ± 4.27[a,b]	9.94 ± 4.34[a,c,d]	15.53 ± 6.21[c]	12.28 ± 4.84[e,f]	14.86 ± 4.61[d,e,g]	8.06 ± 3.85[b,f,g]

All data are presented as mean ± standard deviation.
[a-n] Within a row, the same superscript indicated statistically significant differences between two groups using a Wilcoxon signed rank test. (significance level of *p*-value and< 0.05).
mFRACTURE, Fast field Echo Resembling a CT Using Restricted Echo-spacing- multiple echoes; sFRACTURE, Fast field Echo Resembling a CT Using Restricted Echo-spacing- single echo; PDW, Proton density-weighted; T2W, T2-weighted; and T1W, T1-weighted image.

2020; Stephen et al., 2021). Bone MRI, sCT, is a deep learning-based technique that performs 3D MRI-to-CT mapping to produce CT-like images (Florkow et al., 2020; Jans et al., 2021; Florkow et al., 2022). This technique has already been validated in the pelvis, sacroiliac joints, lumbar spine, cervical spine, and hip for radiotherapy and orthopedic and neurosurgical treatment planning by learning from paired MRI and CT data (Florkow et al., 2020; Jans et al., 2021; Morbée et al., 2021; Morbée et al., 2022). Based on the results of a previous human study comparing sCT and CT, a tendency to reduce fine details in the trabecular bone was observed in sCT, possibly because of the limited variety of images used to train the network, which would limit the identification of certain pathologies, such as intravertebral bone attachments. In contrast, the sFRACTURE sequence in our study showed that the trabecular bone could be visualized at a level similar to that on CT.

Conventional MRI sequences have an echo time (TE) of more than 1 ms, which results in little or no detectable signal from the cortical bone. However, nominal TEs of less than 200 μs can be achieved using half-synchronized radio frequency (RF) pulses or short hard pulses, radial or spiral mapping of K-space, and other techniques. The UTE pulse sequence uses short RF pulses for signal excitation and collects data as the readout gradient increases (TE 8–50 μs). Consequently, UTE pulse sequences can detect signals in the cortical bone and directly image and quantify T1, T2*, and water concentrations in bone tissue. In humans, several studies have

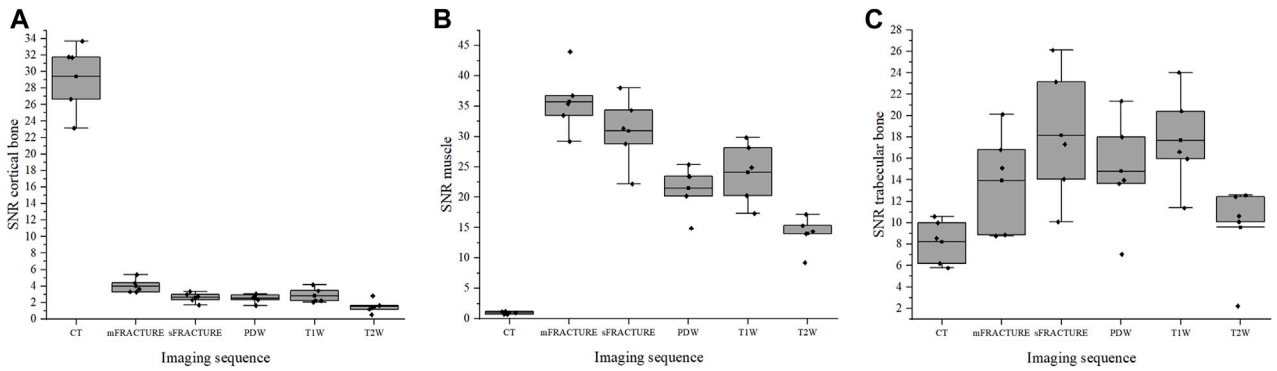

FIGURE 9
The signal-to-noise ratio (SNR) of cortical bone **(A)**, muscle **(B)**, and trabecular bone **(C)** for all evaluating methods (CT; computed tomography, mFRACTURE; fast field echo resembling CT using restricted echo-spacing- multiple echo, sFRACTURE; fast field echo resembling CT using restricted echo-spacing- single echo, PDW; proton density-weighted, T2W; T2-weighted, and T1W; T1-weighted images).

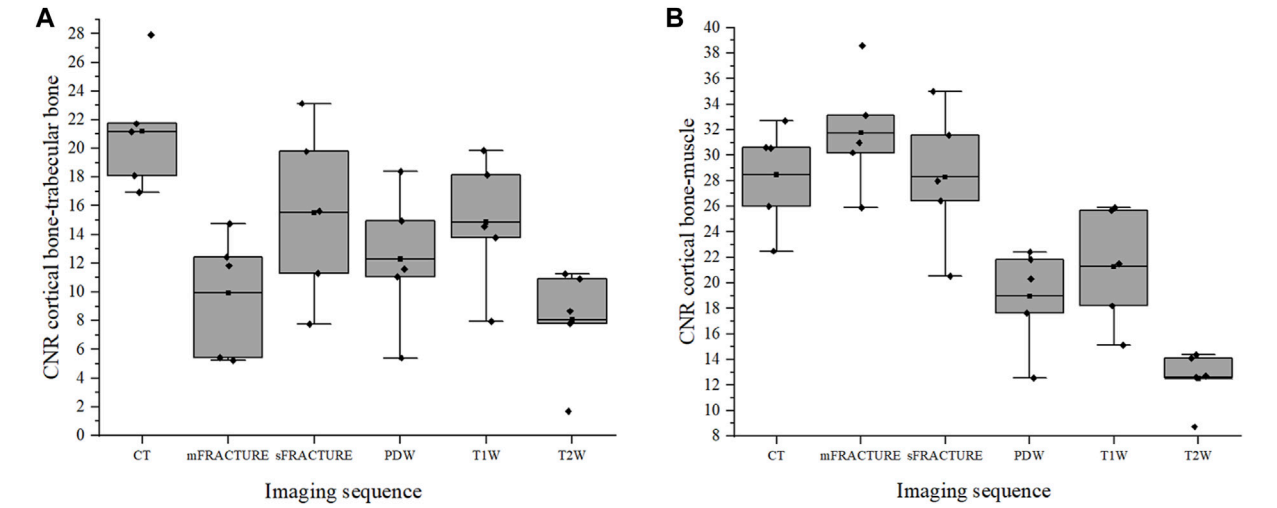

FIGURE 10
The contrast-to-noise ratio (CNR) of the cortical bone-trabecular bone **(A)** and cortical bone-muscle **(B)** for all evaluating methods. (CT; computed tomography, mFRACTURE; fast field echo resembling CT using restricted echo-spacing- multiple echo, sFRACTURE; fast field echo resembling CT using restricted echo-spacing- single echo, PDW; proton density-weighted, T2W; T2-weighted, and T1W; T1-weighted images).

evaluated the ability of CLBC 3D UTE to characterize and delineate bone structures and have reported its strong performance in shoulder and cervical spine imaging (Chang et al., 2015; Larson et al., 2016; Deininger-Czermak et al., 2021). The qualitative scores for UTE showed more similarity to CT than to FRACTURE, and there was no difference in the geometric measurements between UTE and FRACTURE(25). However, the hardware and software requirements for UTE and ZTE acquisition include fast transmission and receive switching, precise RF waveform transmission, high-gradient performance, tilt compensation, and no commercially available pulse sequences, which limit the number of MRI scanners capable of performing UTE and ZTE acquisition in practice.

In this study, as in previous ones (Rathnayaka et al., 2013; Wiesinger et al., 2016), most lengths measured using FRACTURE were not significantly different from those measured on CT. Regarding the quantitative assessment of all modalities, CT and FRACTURE were able to measure lengths in as similar a cross section as possible, as CT and FRACTURE are 3D techniques that use isotropic voxels, allowing for accurate midsagittal plane correction. However, the lengths measured on T2W images were significantly different from those measured on CT images. This suggests that T2W may not be accurate enough to measure the distance between bone margins on MRI images. This may also suggest that additional visual information about the surrounding soft tissue and fluid structures influences the assessment of distance on MRI in humans. The occipital bone length, length of the dorsal arch of the atlas, and maximum length of the dens showed excellent ICC agreement, and the caudal height of the foramen magnum showed poor ICC agreement, which may be due to the small number of patients; however, it is possible that the length of the foramen magnum is more affected by posture than we expected.

In veterinary medicine, various studies have used CT and MRI to diagnose abnormalities of the CCJ in dogs (Lu et al., 2003; García-Real et al., 2004; Cerda-Gonzalez et al., 2009a; Cerda-Gonzalez et al., 2009b; Carrera et al., 2009; Schmidt et al., 2009; Parry et al., 2010; Marino et al., 2012; Stalin et al., 2015; Kiviranta et al., 2017; Planchamp et al., 2022). CT has been used mainly for morphologic evaluation of the bones. One study evaluated the morphological variation between dogs with and without atlantoaxial subluxation using CT (Parry et al., 2010). Two studies assessed the shape and volume of the cranial cavity and caudal fossa using CT (García-Real et al., 2004; Schmidt et al., 2009). MRI studies have primarily been used to determine the presence of spinal cord pathology and disorders of cerebrospinal fluid flow (Lu et al., 2003; Cerda-Gonzalez et al., 2009b). However, because of the limitations of using MRI alone to assess osseous structures, a number of studies have combined both CT and MRI (Cerda-Gonzalez et al., 2009a; Marino et al., 2012; Stalin et al., 2015; Kiviranta et al., 2017; Planchamp et al., 2022). In one study of atlanto-occipital overlapping, CT was used to assess the position of the atlas and occipital bones, and MRI was used to assess medullary kinking, compression of the cerebellum, and ventriculomegaly (Cerda-Gonzalez et al., 2009a). The combination of the conventional MRI with the FRACTURE sequence, which is useful for evaluating osseous structures, will allow MRI to be used to evaluate bone morphology and nerve injury at the one time, reducing complexity.

Our study has some limitations. First, in post-processing, inverting the greyscale makes areas that were identified as dark with low signal in the MRI image appear brighter. Therefore, areas such as air, which are not bones, may appear bright when inverted due to lack of signal, so when viewing FRACTURE images, it is important to refer to anatomical structures and other MRI sequences to avoid misinterpretation and consult a radiologist if necessary. Second, all examinations were performed on a small number of healthy dogs of the same body size. Therefore, the images may not be the same as those of diseased dogs. Further studies on the application of FRACTURE MRI in large populations of healthy dogs of various body sizes and dogs with craniocervical diseases are necessary. Furthermore, there was no comparison between FRACTURE and other MRI sequences that provide CLBC images; therefore, it is difficult to determine the differences between the imaging types.

Despite these limitations, the FRACTURE MRI sequences showed higher cortical delineation and trabecular bone visibility than T2-weighted, T1-weighted, and PDW images of the CCJ, as did CT. The CNR between the cortical bone and muscle was high, similar to that on CT, and sFRACTURE showed a high SNR of the trabecular bone and a high CNR between the cortical and trabecular bone. In conclusion, FRACTURE sequences can be used as an adjunct to conventional MR sequences for evaluating CCJ bones in dogs (Weiger et al., 2013; Weiger et al., 2011).

Data availability statement

The original contributions presented in the study are included in the article/Supplementary Material, further inquiries can be directed to the corresponding author.

Ethics statement

The animal study was approved by The procedures performed in this study were approved by the Seoul National University Institutional Animal Care and Use Committees (SNU IACUC-230726-2). The study was conducted in accordance with the local legislation and institutional requirements.

Author contributions

DL: Conceptualization, Data curation, Formal Analysis, Investigation, Methodology, Writing–original draft. EK: Writing–review and editing, Formal Analysis, Methodology. HW: Investigation, Methodology, Writing–review and editing. C-YJ: Methodology, Software, Visualization, Writing–review and editing. JY: Validation, Writing–review and editing. JC: Conceptualization, Funding acquisition, Project administration, Resources, Supervision, Validation, Writing–review and editing.

Funding

The author(s) declare financial support was received for the research, authorship, and/or publication of this article. This research was supported by Basic Science Research Program through the National Research Foundation of Korea (NRF) funded by the Ministry of Science, ICT and Future Planning (NRF-2021R1A2C200573011).

Conflict of interest

The authors declare that the research was conducted in the absence of any commercial or financial relationships that could be construed as a potential conflict of interest.

Publisher's note

Supplementary material

The Supplementary Material for this article can be found online at: https://www.frontiersin.org/articles/10.3389/fbioe.2024.1297675/full#supplementary-material

References

Bishop, J. Y., Jones, G. L., Rerko, M. A., Donaldson, C., Miller, B., Cox, C., et al. (2013). 3-D CT is the most reliable imaging modality when quantifying glenoid bone loss. *Clin. Orthop. Relat. Res.* 471 (4), 1251–1256. doi:10.1007/s11999-012-2607-x

Böker, S. M., Adams, L. C., Bender, Y. Y., Fahlenkamp, U. L., Wagner, M., Hamm, B., et al. (2019). Differentiation of predominantly osteoblastic and osteolytic spine metastases by using susceptibility-weighted MRI. *Radiology* 290 (1), 146–154. doi:10.1148/radiol.2018172727

Böker, S. M., Adams, L. C., Bender, Y. Y., Wagner, M., Diekhoff, T., Fallenberg, E., et al. (2018). Evaluation of vertebral body fractures using susceptibility-weighted magnetic resonance imaging. *Eur. Radiol.* 28 (5), 2228–2235. doi:10.1007/s00330-017-5195-z

Böker, S. M., Adams, L. C., Fahlenkamp, U. L., Diederichs, G., Hamm, B., and Makowski, M. R. (2020). Value of susceptibility-weighted imaging for the assessment of angle measurements reflecting hip morphology. *Sci. Rep.* 10 (1), 20899. doi:10.1038/s41598-020-77671-1

Botelho, R. V., Neto, E. B., Patriota, G. C., Daniel, J. W., Dumont, P. A. S., and Rotta, J. M. (2007). Basilar invagination: craniocervical instability treated with cervical traction and occipitocervical fixation: case report. *J. Neurosurg. Spine.* 7, 444–449. doi:10.3171/spi-07/10/444

Breighner, R. E., Bogner, E. A., Lee, S. C., Koff, M. F., and Potter, H. G. (2019). Evaluation of osseous morphology of the hip using zero echo time magnetic resonance imaging. *Ame J. Sports Med.* 47 (14), 3460–3468. doi:10.1177/0363546519878170

Carrera, I., Dennis, R., Mellor, D. J., Penderis, J., and Sullivan, M. (2009). Use of magnetic resonance imaging for morphometric analysis of the caudal cranial fossa in Cavalier King Charles Spaniels. *Am. J. Vet. Res.* 70 (3), 340–345. doi:10.2460/ajvr.70.3.340

Cerda-Gonzalez, S., Dewey, C. W., Scrivani, P. V., and Kline, K. L. (2009a). Imaging features of atlanto-occipital overlapping in dogs. *Vet. Radiol. Ultrasound* 50 (3), 264–268. doi:10.1111/j.1740-8261.2009.01531.x

Cerda-Gonzalez, S., Olby, N. J., Broadstone, R., McCullough, S., and Osborne, J. A. (2009b). Characteristics of cerebrospinal fluid flow in cavalier king charles spaniels analyzed using phase velocity cine magnetic resonance imaging. *Vet. Radiol. Ultrasound* 50 (5), 467–476. doi:10.1111/j.1740-8261.2009.01571.x

Chang, E. Y., Du, J., and Chung, C. B. (2015). UTE imaging in the musculoskeletal system. *J. Magn. Reson Imaging* 41 (4), 870–883. doi:10.1002/jmri.24713

Chong, L. R., Lee, K., and Sim, F. Y. (2021). 3D MRI with CT-like bone contrast – an overview of current approaches and practical clinical implementation. *Eur J. Radiol.* 143. Elsevier Ireland Ltd. doi:10.1016/j.ejrad.2021.109915

Deininger-Czermak, E., Villefort, C., von Knebel Doeberitz, N., Franckenberg, S., Kälin, P., Kenkel, D., et al. (2021). Comparison of MR ultrashort echo time and optimized 3D-multiecho in-phase sequence to computed tomography for assessment of the osseous craniocervical junction. *J. Magn. Reson Imaging* 53 (4), 1029–1039. doi:10.1002/jmri.27478

de Mello, R. A. F., Ma, Y. jun, Ashir, A., Jerban, S., Hoenecke, H., Carl, M., et al. (2020). Three-dimensional zero echo time magnetic resonance imaging versus 3-dimensional computed tomography for glenoid bone assessment. *Arthroscopy* 36 (9), 2391–2400. doi:10.1016/j.arthro.2020.05.042

Dremmen, M. H. G., Wagner, M. W., Bosemani, T., Tekes, A., Agostino, D., Day, E., et al. (2017). Does the addition of a "black bone" sequence to a fast multisequence trauma mr protocol allow MRI to replace ct after traumatic brain injury in children? *Am. J. Neuroradiol.* 38 (11), 2187–2192. doi:10.3174/ajnr.a5405

Eley, K. A., Watt-Smith, S. R., Sheerin, F., and Golding, S. J. (2014). "Black Bone" MRI: a potential alternative to CT with three-dimensional reconstruction of the craniofacial skeleton in the diagnosis of craniosynostosis. *Eur. Radiol.* 24 (10), 2417–2426. doi:10.1007/s00330-014-3286-7

Florkow, M. C., Willemsen, K., Zijlstra, F., Foppen, W., van der Wal, B. C. H., van der Voort van Zyp, J. R. N., et al. (2022). MRI-based synthetic CT shows equivalence to conventional CT for the morphological assessment of the hip joint. *J. Orthop. Res.* 40 (4), 954–964. doi:10.1002/jor.25127

Florkow, M. C., Zijlstra, F., Willemsen, K., Maspero, M., van den Berg, C. A. T., Kerkmeijer, L. G. W., et al. (2020). Deep learning–based MR-to-CT synthesis: the influence of varying gradient echo–based MR images as input channels. *Magn. Reson Med.* 83 (4), 1429–1441. doi:10.1002/mrm.28008

García-Real, I., Kass, P. H., Sturges, B. K., and Wisner, E. R. (2004). Morphometric analysis of the cranial cavity and caudal cranial fossa in the dog: a computerized tomographic study. *Vet. Radiol. Ultrasound* 45 (1), 38–45. doi:10.1111/j.1740-8261.2004.04006.x

Gersing, A. S., Pfeiffer, D., Kopp, F. K., Schwaiger, B. J., Knebel, C., Haller, B., et al. (2019). Evaluation of MR-derived CT-like images and simulated radiographs compared to conventional radiography in patients with benign and malignant bone tumors. *Eur. Radiol.* 29 (1), 13–21. doi:10.1007/s00330-018-5450-y

Goel, A., Bhatjiwale, M., and Desai, K. (1998). Basilar invagination: a study based on 190 surgically treated patients. *J. Neurosurg.* 88 (6), 962–968. doi:10.3171/jns.1998.88.6.0962

Griffith, J. F., Yung, P. S. H., Antonio, G. E., Tsang, P. H., Ahuja, A. T., and Kai, M. C. (2007). CT compared with arthroscopy in quantifying glenoid bone loss. *Am J Roentgenol* 189 (6), 1490–1493. doi:10.2214/ajr.07.2473

Haller, S., Haacke, E. M., Thurnher, M. M., and Barkhof, F. (2021). Susceptibility-weighted imaging: technical essentials and clinical neurologic applications. *Radiology* 299, 3–26. Radiological Society of North America Inc. doi:10.1148/radiol.2021203071

Han, X. (2017). MR-based synthetic CT generation using a deep convolutional neural network method. *Med. Phys.* 44 (4), 1408–1419. doi:10.1002/mp.12155

Held, P., Seitz, J., Nitz, W., Lenhart, M., and Geissler, A. (2001). Comparison of two-dimensional gradient echo, turbo spin echo and two-dimensional turbo gradient spin echo sequences in MRI of the cervical spinal cord anatomy. *Eur J Radiol* 38, 64–71. doi:10.1016/s0720-048x(00)00253-9

Jans, L. B. O., Chen, M., Elewaut, D., Van den Bosch, F., Carron, P., Jacques, P., et al. (2021). MRI-Based synthetic CT in the detection of structural lesions in patients with suspected sacroiliitis: comparison with MRI. *Radiology* 298 (2), 343–349. doi:10.1148/radiol.2020201537

Johnson, B., Alizai, H., and Dempsey, M. (2021). Fast field echo resembling a CT using restricted echo-spacing (FRACTURE): a novel MRI technique with superior bone contrast. *Skelet. Radiol.* 50 (8), 1705–1713. doi:10.1007/s00256-020-03659-7

Kiviranta, A. M., Rusbridge, C., Laitinen-Vapaavuori, O., Hielm-Björkman, A., Lappalainen, A. K., Knowler, S. P., et al. (2017). Syringomyelia and craniocervical junction abnormalities in chihuahuas. *J. Vet. Intern Med.* 31 (6), 1771–1781. doi:10.1111/jvim.14826

Kwon, Y. W., Powell, K. A., Yum, J. K., Brems, J. J., and Iannotti, J. P. (2005). Use of three-dimensional computed tomography for the analysis of the glenoid anatomy. *J. Shoulder Elb. Surg.* 14 (1), 85–90. doi:10.1016/j.jse.2004.04.011

Landis, J. R., and Koch, G. G. (1977). The measurement of observer agreement for categorical data. *Biometrics* 33, 159. doi:10.2307/2529310

Larson, P. E. Z., Han, M., Krug, R., Jakary, A., Nelson, S. J., Vigneron, D. B., et al. (2016). Ultrashort echo time and zero echo time MRI at 7T. *Biol. Med.* 29 (3), 359–370. doi:10.1007/s10334-015-0509-0

Lu, D., Lamb, C. R., Pfeiffer, D. U., and Targett, M. P. (2003). Neurological signs and results of magnetic resonance imaging in 40 cavalier King Charles spaniels with Chiari type 1-like malformations. *Vet. Rec.* 153 (9), 260–263. doi:10.1136/vr.153.9.260

Marino, D. J., Loughin, C. A., Dewey, C. W., Marino, L. J., Sackman, J. J., Lesser, M. L., et al. (2012). Morphometric features of the craniocervical junction region in dogs with suspected Chiari-like malformation determined by combined use of magnetic resonance imaging and computed tomography. *Am. J. Vet. Res.* 73 (1), 105–111. doi:10.2460/ajvr.73.1.105

Morbée, L., Chen, M., Herregods, N., Pullens, P., and Jans, L. B. O. (2021). MRI-based synthetic CT of the lumbar spine: geometric measurements for surgery planning in comparison with CT. *Eur. J. Radiol.*, 144. doi:10.1016/j.ejrad.2021.109999

Morbée, L., Chen, M., Van Den Berghe, T., Schiettecatte, E., Gosselin, R., Herregods, N., et al. (2022). MRI-based synthetic CT of the hip: can it be an alternative to conventional CT in the evaluation of osseous morphology? *Eur. Radiol.* 32 (5), 3112–3120. doi:10.1007/s00330-021-08442-3

Parry, A. T., Upjohn, M. M., Schlegl, K., Kneissl, S., and Lamb, C. R. (2010). Computed tomography variations in morphology of the canine atlas in dogs with and without atlantoaxial subluxation. *Vet. Radiol. Ultrasound* 51 (6), 596–600. doi:10.1111/j.1740-8261.2010.01711.x

Planchamp, B., Forterre, F., Vidondo, B., Hernandez-Guerra, A. M., Plessas, I. N., Schmidt, M. J., et al. (2022). Determination of cutoff values on computed tomography and magnetic resonance images for the diagnosis of atlantoaxial instability in small-breed dogs. *Vet. Surg.* 51 (4), 620–630. doi:10.1111/vsu.13799

Rathnayaka, K., Cowin, G., Schuetz, M. A., Sahama, T., and Schmutz, B. (2013). Correction of step artefact associated with MRI scanning of long bones. *Med. Eng. Phys.* 35 (7), 988–993. doi:10.1016/j.medengphy.2012.09.010

Samim, M., Eftekhary, N., Vigdorchik, J. M., Elbuluk, A., Davidovitch, R., Youm, T., et al. (2019). 3D-MRI versus 3D-CT in the evaluation of osseous anatomy in femoroacetabular impingement using Dixon 3D FLASH sequence. *Skelet. Radiol.* 48 (3), 429–436. doi:10.1007/s00256-018-3049-7

Schmidt, M. J., Biel, M., Klumpp, S., Schneider, M., and Kramer, M. (2009). Evaluation of the volumes of cranial cavities in Cavalier King Charles Spaniels with Chiari-like malformation and other brachycephalic dogs as measured via computed tomography. *Am. J. Vet. Res.* 70 (4), 508–512. doi:10.2460/ajvr.70.4.508

Stalin, C., Gutierrez-Quintana, R., Faller, K., Guevar, J., Yeamans, C., and Penderis, J. (2015). A review of canine atlantoaxial joint subluxation. *Vet. Comp. Orthop. Traumatol.* 28, 1–8. doi:10.3415/vcot-14-05-0064

Stephen, J. M., Calder, J. D. F., Williams, A., and El Daou, H. (2021). Comparative accuracy of lower limb bone geometry determined using MRI, CT, and direct bone 3D models. *J. Orthop. Res.* 39 (9), 1870–1876. doi:10.1002/jor.24923

Stillwater, L., Koenig, J., Maycher, B., and Davidson, M. (2017). 3D-MR vs. 3D-CT of the shoulder in patients with glenohumeral instability. *Skelet. Radiol.* 46 (3), 325–331. doi:10.1007/s00256-016-2559-4

Usamentiaga, R., Ibarra-Castanedo, C., and Maldague, X. (2018). More than fifty shades of grey: quantitative characterization of defects and interpretation using SNR and CNR. *J. Nondestr Eval.* 37 (2), 25. doi:10.1007/s10921-018-0479-z

Wald, A., and Wolfowitz, J. (1943). An exact test for randomness in the non-parametric case based on serial correlation. *Ann. Math. Stat.* 14 (4), 378–388. doi:10.1214/aoms/1177731358

Weiger, M., Brunner, D. O., Dietrich, B. E., Müller, C. F., and Pruessmann, K. P. (2013). ZTE imaging in humans. *Magn. Reson Med.* 70 (2), 328–332. doi:10.1002/mrm.24816

Weiger, M., Pruessmann, K. P., and Hennel, F. (2011). MRI with zero echo time: hard versus sweep pulse excitation. *Magn. Reson Med.* 66 (2), 379–389. doi:10.1002/mrm.22799

Wiesinger, F., Sacolick, L. I., Menini, A., Kaushik, S. S., Ahn, S., Veit-Haibach, P., et al. (2016). Zero TE MR bone imaging in the head. *Magn. Reson Med.* 75 (1), 107–114. doi:10.1002/mrm.25545

frontiers | Frontiers in Veterinary Science

TYPE Original Research
PUBLISHED 11 April 2024
DOI 10.3389/fvets.2024.1386425

OPEN ACCESS

EDITED BY
Blaz Cugmas,
University of Latvia, Latvia

REVIEWED BY
Ismael Hernández Avalos,
National Autonomous University of Mexico, Mexico
Adriana Domínguez-Oliva,
Metropolitan Autonomous University, Mexico

*CORRESPONDENCE
Ryou Tanaka
✉ fu0253@go.tuat.ac.jp

RECEIVED 15 February 2024
ACCEPTED 02 April 2024
PUBLISHED 11 April 2024

CITATION
Hasegawa M, Sasaki M, Umemoto Y, Hayashi R, Hatanaka A, Hosoki M, Farag A, Matsuura K, Yoshida T, Shimada K, Hamabe L, Takahashi K and Tanaka R (2024) Exploring sleep heart rate variability: linear, nonlinear, and circadian rhythm perspectives. *Front. Vet. Sci.* 11:1386425. doi: 10.3389/fvets.2024.1386425

Exploring sleep heart rate variability: linear, nonlinear, and circadian rhythm perspectives

Mizuki Hasegawa[1,2], Mayuko Sasaki[1], Yui Umemoto[1], Rio Hayashi[1], Akari Hatanaka[1], Marino Hosoki[1], Ahmed Farag[1], Katsuhiro Matsuura[3], Tomohiko Yoshida[4], Kazumi Shimada[1], Lina Hamabe[1], Ken Takahashi[5] and Ryou Tanaka[1]*

[1]Department of Veterinary Surgery, Tokyo University of Agriculture and Technology, Tokyo, Japan, [2]Yokohama Isogo Animal Hospital, Yokohama, Kanagawa, Japan, [3]Department of Small Animal Clinical Sciences, College of Veterinary Medicine University of Florida, Gainesville, FL, United States, [4]Department of Small Animal Medical Center, Obihiro University of Agriculture and Veterinary Medicine, Obihiro, Hokkaido, Japan, [5]Department of Pediatrics, Juntendo University, Urayasu Hospital, Chiba, Japan

Background: Heart rate variability (HRV) is believed to possess the potential for disease detection. However, early identification of heart disease remains challenging, as HRV analysis in dogs primarily reflects the advanced stages of the disease.

Hypothesis/objective: The aim of this study is to compare 24-h HRV with sleep HRV to assess the potential utility of sleep HRV analysis.

Animals: Thirty healthy dogs with no echocardiographic abnormalities were included in the study, comprising 23 females and 7 males ranging in age from 2 months to 8 years (mean [standard deviation], 1.4 [1.6]).

Methods: This study employed a cross-sectional study. 24-h HRV and sleep HRV were measured from 48-h Holter recordings. Both linear analysis, a traditional method of heart rate variability analysis, and nonlinear analysis, a novel approach, were conducted. Additionally, circadian rhythm parameters were assessed.

Results: In frequency analysis of linear analysis, the parasympathetic index nHF was significantly higher during sleep compared to the mean 24-h period (mean sleep HRV [standard deviation] vs. mean 24 h [standard deviation], 95% confidence interval, *p* value, r-family: 0.24 [0.057] vs. 0.23 [0.045], 0.006–0.031, $p = 0.005$, $r = 0.49$). Regarding time domain analysis, the parasympathetic indices SDNN and RMSSD were also significantly higher during sleep (SDNN: 179.7 [66.9] vs. 156.6 [53.2], 14.5–31.7, $p < 0.001$, $r = 0.71$ RMSSD: 187.0 [74.0] vs. 165.4 [62.2], 13.2–30.0, $p < 0.001$, $r = 0.70$). In a geometric method of nonlinear analysis, the parasympathetic indices SD1 and SD2 showed significantly higher values during sleep (SD1: 132.4 [52.4] vs. 117.1 [44.0], 9.3–21.1, $p < 0.001$, $r = 0.70$ SD2: 215.0 [80.5] vs. 185.9 [62.0], 17.6–40.6, $p < 0.001$, $r = 0.69$). Furthermore, the circadian rhythm items of the parasympathetic indices SDNN, RMSSD, SD1, and SD2 exhibited positive peaks during sleep.

Conclusion: The findings suggest that focusing on HRV during sleep can provide a more accurate representation of parasympathetic activity, as it captures the peak circadian rhythm items.

KEYWORDS

autonomic balance, parasympathetic nerves, sympathetic nerves, early detection, daytime activities

1 Introduction

Heart rate variability (HRV) refers to the variation in time between successive heartbeats, or RR intervals, caused by the changes in autonomic nerve stimulation to the sinus node (1). HRV analysis in human medicine has emerged as a valuable analytical tool for early disease detection and prognostic prediction across various conditions. For example, in COVID-19, a decrease in HRV has been observed to predict cardiac injury earlier than myocardial markers, suggesting that its early detection could potentially enhance patient prognosis (2). In the context of cardiovascular abnormalities, studies have suggested that decreased resting HRV in children conceived through assisted reproduction techniques may predispose them to premature cardiovascular aging (3). Abnormal HRV parameters have also been suggested to be associated with the development of congestive heart failure in asymptomatic individuals (4). On the other hand, recent findings in dogs suggest that combination therapy involving pimobendan, furosemide, and enalapril restores normal autonomic nervous system activity in dogs with myxomatous mitral valve degeneration (MMVD) stage C (5). It has been reported that both sympathetic and parasympathetic tone are altered in dogs with mitral valve disease before clinical signs appear, as demonstrated by the using of short-term HRV analysis (6). Some reports have also evaluated the influence of the dog-owner relationship on emotional reactivity in dogs and whether medication can positively affect stress indicators (7, 8). In dogs, it has been utilized to assess cardiac autonomic balance in therapy, disease assessment, and behavioral research (5–7). Other have been reported in a variety of areas, such as assessing stress levels related to animal welfare, evaluating intraoperative analgesia and nociceptive balance, and assessing intraoperative pain to improve postoperative care (9–11). In all of this cases there is a predominant sympathetic tone and a consequent endocrine response that directly influences heart rate and, therefore, HRV (12–15).

Several reports aiming early detection of cardiac disease in dogs have shown that sympathetic indices of HRV parameters increase as heart disease progresses (16). Respiratory arrhythmias, characterized by variations in the heart rate that are synchronized with the respiratory cycle, commonly occur during parasympathetic (vagal) tone. Particularly in the presence of heart disease, these respiratory arrhythmias can be a factor in assessing the progression of the condition, as they may diminish or become less prominent as the disease progresses (17). On the other hand, canine respiratory arrhythmias can complicate HRV analysis. Normal RR interval variability in dogs during sleep and rest can reach as high as 77%, while extrasystoles have been observed to exhibit variability ranging from 50 to 60%. This variability can make them challenging to distinguish in conventional linear analysis, which may result in the exclusion of data that could potentially contain valuable information for disease identification (16, 18, 19). Therefore, some reports indicate that HRV analysis in dogs may only reflect only advanced disease, posing challenges for its use in early detection and prognosis prediction unlike in human medicine (11). Additionally, in humans, daytime activity is also a factor that disrupts heart rate variability (20). Even in the same individual, unrestricted activity can vary from day to day, unpredictably affecting 24-h HRV (21). In recent years, sleep has been proposed as a time-efficient measure of HRV that is less susceptible to environmental factors than daytime measurements (22). Although the relationship between sleep HRV and cardiovascular events in humans is emerging, there is limited data specifically on sleep HRV in dogs.

Based on the above, we hypothesized that there is a difference between sleep HRV and 24-h HRV in dogs. We focused on the sleep period, during which the parasympathetic nervous system is dominant, and respiratory arrhythmia is high, unaffected by daytime activities. The aim of this study is to compare 24-h HRV with sleep HRV to assess the potential utility of sleep HRV analysis. A comparison between 24-h HRV and sleep HRV was conducted using both conventional analysis method, such as linear analysis, and a novel analysis method, nonlinear analysis, which has been shown to be an indicator with high specificity, sensitivity, and diagnostic accuracy for identifying dogs at risk of death (23).

2 Materials and methods

This is a cross-sectional study.

2.1 Animals

Dogs for the study were selected from those brought to the Department of Dog & Cat Pediatric Hospital in Tokyo, Japan. Healthy dogs were chosen from among those admitted to the hospital for pet boarding or temporary dog care. Additionally, experimental Beagle dogs from our laboratory at Kitayama Labes in Nagano, Japan, were enrolled between August 2018 and January 2023. G*Power (The G*Power Team, G*Power 3.1.9.7 version, Germany) was used to calculate sample sizes. To adapt a paired *t*-test, we set $\alpha = 0.05$, $1\text{-}\beta = 0.8$, and effect size (d-family) = 0.5. The sample size was calculated to require at least 34 cases, so efforts were made to collect dogs for the study as a target value. Healthy dogs with normal physical examination and echocardiography were selected as the test subjects for this study. Dogs with obvious pain on physical examination were excluded. Puppies weighing less than 1.0 kg and too small to be fitted with a Holter electrocardiograph were also excluded from the study. All dog owners provided their consent for their pets to participate in the study. Experimental dogs were handled according to the guidelines established by the Institutional Animal Care and Use Committee of the TUAT (Approval number: R05-140).

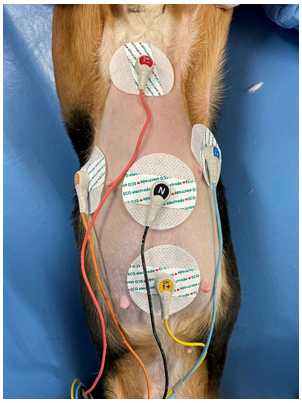

FIGURE 1
The M-X induction method and the R-L induction method. CH1- (red) electrodes placed on the manubrium of the sternum, CH1+ (yellow) on the xiphoid process, CH2- (orange) on the right 5th ~ 6th intercostal space, CH2+ (blue) on the left 5th ~ 6th intercostal space, and a ground electrode (black) in the middle.

FIGURE 2
A vest to secure the Holter recorder and leads to the dog.

2.2 Holter monitoring

The Holter electrocardiograph used in this study was manufactured by NIHON KOHDEN CORPORATION (RAC-5203, Japan). Prior to electrode placement, the dogs' thoraxes were shaved vertically from the sternal scape to the xiphoid process and horizontally around the fifth and sixth intercostal spaces and cleaned with alcohol. Disposable ECG electrodes (XUNDA BRAND, China) were positioned using the M-X induction method and the R-L induction method, which is perpendicular to the M-X method. Subsequently, the induction cords were attached to the electrodes, CH1- (red) electrodes placed on the manubrium of the sternum, CH1+ (yellow) on the xiphoid process, CH2- (orange) on the right 5th ~ 6th intercostal space, CH2+ (blue) on the left 5th ~ 6th intercostal space, and a ground electrode (black) in the middle (24) (Figure 1). Both M-X and R-L leads were recorded. To secure the Holter recorder and leads to the dog, an elastic bandage and a vest utilized (Figure 2). Holter electrocardiogram (ECG) measurements were conducted by veterinarians and clinical laboratory technicians in the TUAT laboratory for 48 h period, during which the animals were allowed free movement within the enclosure.

2.3 Heart rate variability

For the 48-h Holter ECG measurements, the period from 12 p.m. on the first night to 12 a.m. on the second night was designated for 24-h HRV, while the period from 12 p.m. on the first night to 8 a.m. on the second day was earmarked for analysis as sleep HRV. HRV analysis was conducted using the Juntendo University algorithm with MATLAB (MathWorks, R2022a, United States). Both traditional linear analysis and a newer nonlinear analysis method were employed under the following conditions.

2.3.1 Linear heart rate variability

HRV variables for frequency analysis include total power (TP, 0–0.4 Hz), ultra low frequency (ULF, 0–0.00333 Hz), very low frequency (VLF, 0.00333–0.04 Hz), low frequency (LF, 0.04–0.15 Hz), and high frequency (HF, 0.15–0.4 Hz). The parameters utilized in this study were normalized high frequency (nHF) and LF/HF ratio. Normalization eliminates much of the significant within-subject and between-subject variation, resulting in increased reproducibility. Therefore, HF and LF were normalized using the equations nHF = HF / (LF + HF) and normalized low frequency (nLF) = LF / (LF + HF) (25). Regarding time domain analysis in linear analysis, standard deviation on NN intervals (SDNN) and root mean squared of successive RR intervals (RMSSD) were employed. SDANN, SDNN index and pNN50 were not included in the analysis for the following reasons (26). (1) SDANN is correlated with SDNN and is generally considered redundant. (2) SDNN index only estimates variability due to factors affecting HRV within a 5 min period. (3) RMSSD typically provides a better assessment of respiratory sinus arrhythmia (RSA) and most researchers prefer it over pNN50.

2.3.2 Nonlinear heart rate variability

For the nonlinear analysis, both geometric and fractal analyses were employed. Geometric analysis involved plotting a Poincaré plot by graphing every RR interval against the prior interval, thus creating a scatter plot. This plot can be analyzed by fitting an ellipse to the plotted points. The standard deviation of the distance of each point from the y = x axis was measured as SD1 (width of ellipse), While the standard deviation of the distance of each point from y = x + mean R-R interval was measured as SD2 (length of ellipse) (26–31). The ratio SD1/SD2 was measured to assess autonomic balance. Since the healthy heartbeat interval are complex and variable, detrended fluctuation analysis (DFA) was utilized for fractal analysis. DFA quantifies the correlative properties in non-stationary physiological series by examining correlations between consecutive RR intervals (32, 33).

2.3.3 Circadian rhythm

Circadian rhythms were measured to identify the maximum peak for each item. The entire 24-h normal beat RR interval data were divided into 5-min segments for circadian rhythm analysis. HRV circadian rhythm items were fitted to a cosine periodic function and

measured (34). These measurements included nHF, LF/HF, SDNN, RMSSD, SD1, SD2, SD1/SD2, and DFA.

2.4 Statistical analysis

Statistical analyses were conducted using R software (R Development Core Team, version 4.1.0, New zealand). The significance level set at $p < 0.05$. A difference test was adapted to examine the difference between 24-h HRV and sleep HRV. Normality was confirmed using the Shapiro–Wilk test. If the distribution followed a normal distribution, a paired t-test was used. Conversely, if the distribution did not follow a normal distribution, the Wilcoxon signed-rank sum test was applied. Parametric data are presented as means and standard deviations, with 95% confidence intervals also calculated. Nonparametric data are presented as median and interquartile range. The effect size was calculated using R-family. HRV circadian rhythm times were quantified.

3 Results

3.1 Animals

A total of 30 dogs were included in the present study, comprising 23 females and 7 males, with ages ranging from 2 months to 8 years (mean [standard deviation], 1.4 [1.6]), and weights ranging from 1.7 to 9.3 kg (5.6 [2.9]). The breeds included Beagles ($n = 16$), Chihuahuas ($n = 4$), Miniature Schnauzers ($N = 2$), Mongrels ($n = 3$), Miniature Pinscher ($n = 1$), Yorkshire Terrier ($n = 1$), Maltese ($n = 1$), Border Collie ($n = 1$), and Miniature Dachshund ($n = 1$). No abnormal rhythm findings that would affect HRV were detected on the Holter ECG.

3.2 Linear heart rate variability

Linear HRV data were summarized in Table 1. Frequency analysis nHF was significantly higher in sleep HRV compared to in 24-h HRV (mean [standard deviation], 95% confidence interval, p value, r-family: 0.24 [0.057] vs. 0.23 [0.045], 0.006–0.031, $p = 0.005$, $r = 0.49$). Meanwhile, there was no statistically significant difference in LF/HF between 24-h HRV and sleep HRV (0.87 [0.38] vs. 0.84 [0.49], −0.11-0.15, $p = 0.72$, $r = 0.067$). In time domain analysis, both SDNN and RMSSD were significantly higher in sleep HRV than in 24-h HRV (SDNN: 179.7 [66.9] vs. 156.6 [53.2], 14.5–31.7, $p < 0.001$, $r = 0.71$) (RMSSD: 187.0 [74.0] vs. 165.4 [62.2], 13.2–30.0, $p < 0.001$, $r = 0.70$).

3.3 Nonlinear heart rate variability

Nonlinear HRV data were summarized in Table 1. In the geometric analysis, both SD1 and SD2 were significantly higher sleep HRV than 24-h HRV (SD1: 132.4 [52.4] vs. 117.1 [44.0], 9.3–21.1, $p < 0.001$, $r = 0.70$) (SD2: 215.0 [80.5] vs. 185.9 [62.0], 17.6–40.6, $p < 0.001$, $r = 0.69$). However, there was no significant difference in SD1/SD2 between 24-h HRV and sleep HRV (median [interquartile range], 0.63 [0.59–0.66] vs. 0.60 [0.54–0.65], $p = 0.43$, $r = 0.041$). Additionally, DFA in fractal analysis showed no statistically significant difference between 24-h HRV and sleep HRV (0.71 [0.11] vs. 0.71[0.12], −0.024-0.040, $p = 0.62$, $r = 0.092$).

3.4 Circadian rhythm

An average example of circadian rhythm elements for HRV indicators is shown in Figure 3, while a representative example is illustrated in Figure 4. The parasympathetic indicators SDNN (mean [standard deviation]: 6.42 [5.07]), RMSSD (7.45 [6.41]), SD1 (7.45 [6.41]), and SD2 (5.8 [3.82]) exhibited positive peaks during sleep HRV. However, the positive peak for nHF (9.92 [8.06]), a parasympathetic index, was observed to fall outside the range defined as sleep HRV.

4 Discussion

4.1 Brief summary

One of the main objectives of the present study was to compare 24-h HRV with sleep HRV to delineate the differences. The findings

TABLE 1 Heart rate variability variables during 24 h and sleep in 30 dogs.

Indices	Units	24 h HRV		Sleep HRV		95% Confidence interval	*p* value	r-family
		Mean (SD)	Median (range)	Mean (SD)	Median (range)			
nHF	ms^2	0.23 (0.045)	–	0.24 (0.057)	–	0.006–0.031	0.005*	0.49
LF/HF	ms^2	0.87 (0.38)	–	0.84 (0.49)	–	−0.11 - 0.15	0.72	0.067
SDNN	ms	156.6 (53.2)	–	179.7 (66.9)	–	14.5–31.7	< 0.001*	0.71
RMSSD	ms	165.4 (62.2)	–	187.0 (74.0)	–	13.2–30.0	< 0.001*	0.7
SD1	ms	117.1 (44.0)	–	132.4 (52.4)	–	9.3–21.2	< 0.001*	0.7
SD2	ms	185.9 (62.0)	–	215.0 (80.5)	–	17.6–40.6	< 0.001*	0.69
SD1/SD2	%	–	0.63 (0.59–0.66)	–	0.60 (0.54–0.65)	–	0.43	0.041
DFA		0.71 (0.11)	–	0.71 (0.12)	–	−0.024–0.040	0.62	0.092

Data are expressed as mean, standard deviation, and median, range. Asterisks (*) are used to compare significance between 24 h HRV and sleep HRV (*$p < 0.05$). nHF, SDNN, RMSSD, SD1, and SD2 were significantly higher for sleep HRV. For abbreviations of HRV variables, nHF, normalized high frequency; LF, low frequency; SDNN, Standard deviation of NN intervals; RMSSD, Root mean square of successive RR interval differences; SD1, Poincaré plot standard deviation perpendicular the line of identity; SD2, Poincaré plot standard deviation along the line of identity; DFA, Detrended fluctuation analysis.

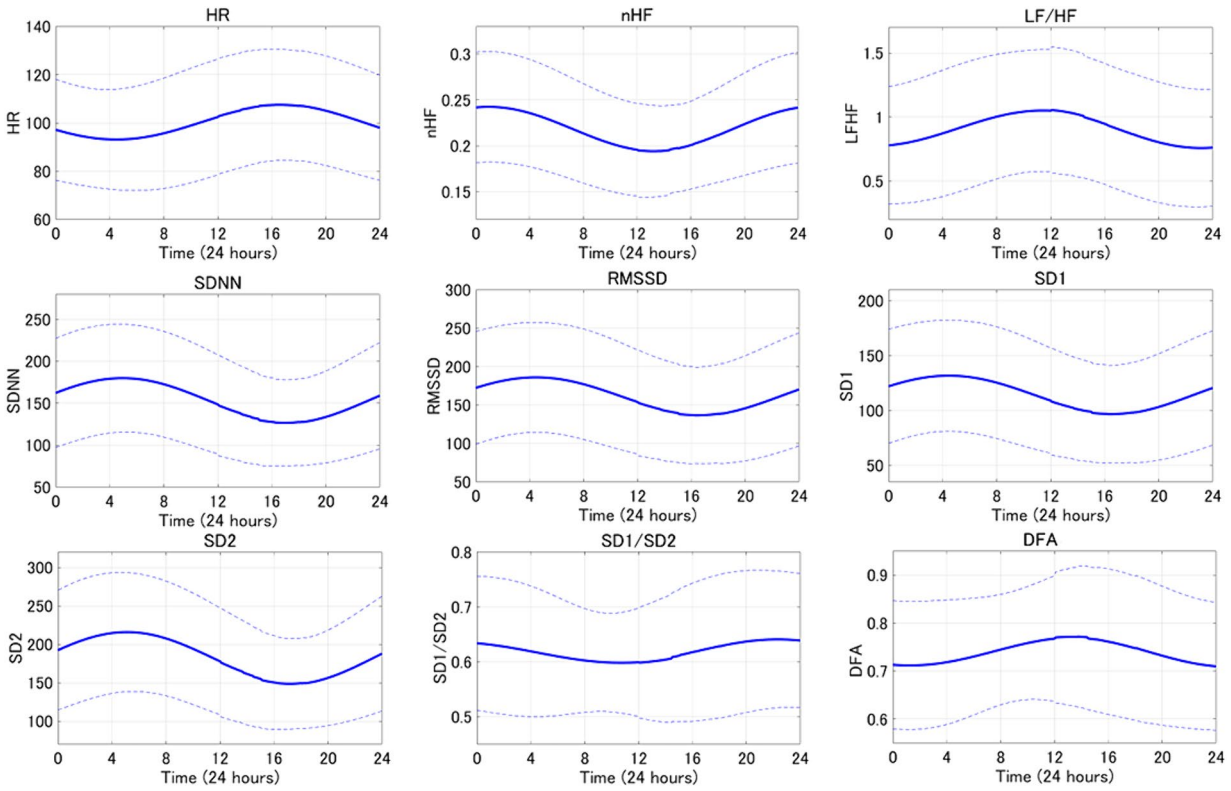

FIGURE 3
The averaged circadian rhythm averaging curve for the 24-h HRV index is shown. Bold lines indicate mean curves and dotted lines indicate standard deviations.

of the present study suggest that the parasympathetic indices nHF, SDNN, RMSSD, SD1, and SD2 predominantly reflect parasympathetic activity during sleep. Moreover, as the positive peaks of the circadian rhythm elements of the parasympathetic indices fall within the range defined as HRV during sleep, HRV during sleep can serve as an indicator of the peak parasympathetic activity during the day. These results support the hypothesis that differences exist between 24 h HRV and sleep HRV.

4.2 Comparison with previous studies

Previous studies in humans have suggested that parasympathetic activity increases during the night with the circadian rhythm components of the HRV parasympathetic index exhibiting a positive peak during nighttime (34). The data presented in the present study suggest that sleep HRV may be useful metric in dogs, as a valuable analytical tool for early detection and prognosis of various diseases, as they exhibit similar changes to those observed in humans. This study distinguishes itself from previous studies by utilizing circadian rhythms to identify the maximum peak of circadian rhythm elements of parasympathetic indices within a 24-h period focusing specifically on the measurement range of sleep HRV. Rasmussen et al. (35) defined sleep HRV as the period starting from 30 min after the dog enters sleep and extending to 6 h. Blake et al. (28) also defined resting HRV as the period from 0:00 to 6:00 and activity HRV as the period from 12:00 to 18:00. Since both measurements are based on activity records, the measurement times are back and forth. Therefore, it would enhance the external validity of the results if the peak time of the HRV circadian rhythm item could be utilized as a reference when evaluating the HRV index.

4.3 Possible explanation and implications

The nHF observed in the frequency analysis was consistent with expectations, showing high values during HRV in sleep. However, the circadian rhythm item of the parasympathetic index deviated from expectations by falling outside the range defined in this study as HRV during sleep. Identifying the peak time of parasympathetic activity proves challenging even when utilizing circadian rhythms due to significant individual variation in nHF and the discrepancy between the average peak derived from each case and the peak calculated from the average curve. nHF demonstrates respiratory variability due to interference from the respiratory center and reflexive input from the periphery, which is transmitted to the sinus node to become HF. Therefore, it is plausible that nHF may not be considered a pure indicator of the cardiac vagus nerve activity (20, 36). SDNN in time domain analysis is known to be influenced by the duration of analysis. In short-term recordings, the primary source of SDNN variability is parasympathetically mediated RSA, whereas in 24-h recordings, sympathetic nerves contribute significantly to SDNN (20, 31). Therefore, it is expected that the difference in analysis time between 24-h HRV and 1-h sleep HRV would impact SDNN values. RMSSD is

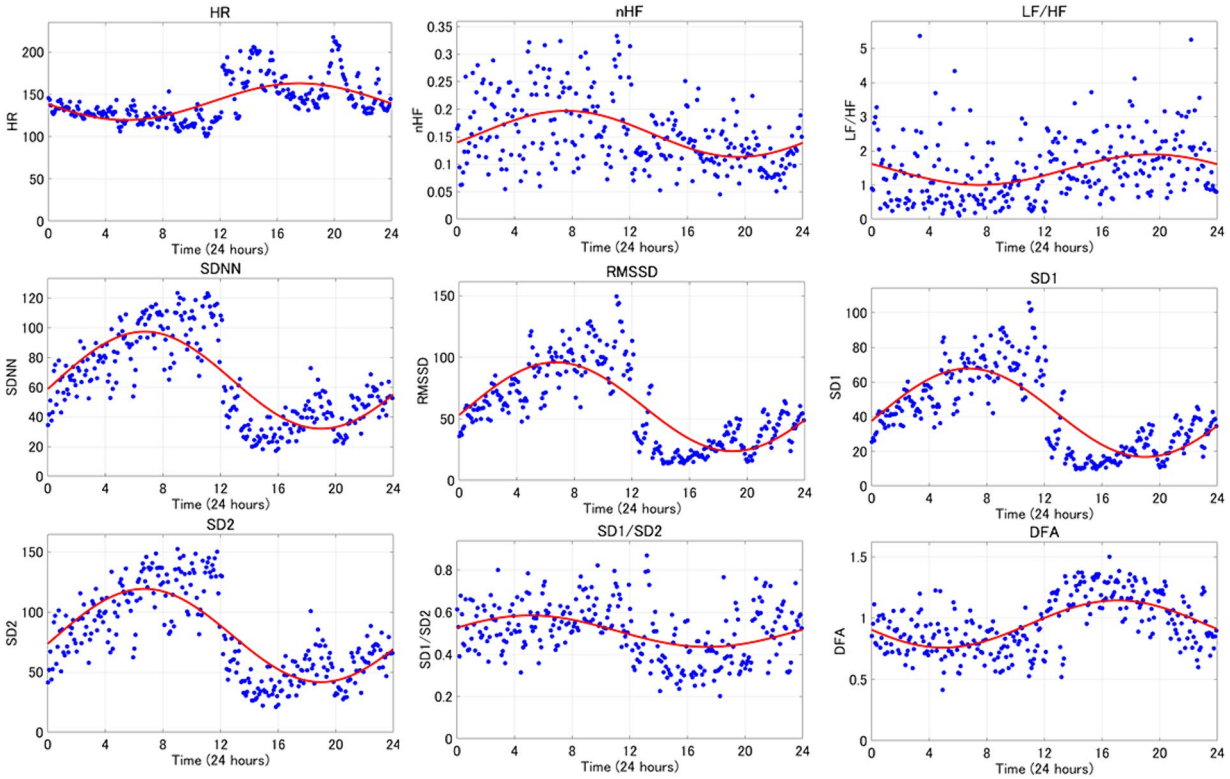

FIGURE 4
The circadian rhythm items of the 24-h HRV index are shown. This is one representative example. The red curve represents the circadian rhythm and the blue dots represent the 5-min readings for each indicator.

considered a superior indicator of parasympathetic activity compared to SDNN. However, RMSSD is less affected by respiration than SDNN, but more influenced by RSA (37). RSA also depend on a number of control mechanisms due to interference from cardiovascular centers in the medulla oblongata, the degree of lung distension, and reflexive input from right atrial wall distension (38). Therefore, interpretations other than cardiac vagal activity must be considered, but this potential influence is rarely taken into account in linear analysis methods (39). Consequently, it was hypothesized that dogs with physiological respiratory arrhythmias might be affected by this phenomenon. Linear analysis of HRV during sleep in dogs may be susceptible to several biases, including those related to respiration, duration, and respiratory arrhythmia. Therefore, utilizing linear analysis for HRV measurement in dogs may not be an appropriate analytical method.

On the contrary, nonlinear analysis is an analytical method that circumvents the drawbacks associated with linear analysis. While linear analysis entails examining the time series of RR intervals obtained. Life is inherently nonlinear, meaning that the relationship between variables cannot be plotted as a straight line. Nonlinear analysis serves as a method of assessing the unpredictability of a time series and reveals correlations when the complexity arises from the same underlying process (26). In humans, nonlinear analysis has attracted attention due to its potential to predict the onset of heart failure (4). Additionally, HRV measurement during sleep, which is less susceptible to environmental factors compared to daytime measurements, has been proposed (22). Therefore, considering that SD1 and SD2 in this study were nonlinear analyses and showed significant increases during sleep compared to the 24-h period, and that the maximum peak of circadian rhythm items occurred during sleep, we believe that future investigations into heart disease in dogs utilizing sleep HRV and nonlinear analyses could be advantageous for early detection of heart disease mirroring approaches used in humans.

4.4 Limitations

One limitation of this study is the lack of consideration for breed differences, as well as the wide age range of the subjects, spanning from 2 months to 8 years. In humans, studies such as those by Bonnemeier et al. (40) have shown that HRV indices experience the most significant decline between the ages of 20 and 30. Additionally, Almeida-Santos et al. also reported that RMSSD decreases between the ages of 40 and 60, followed by an increase after the age of 70 (41). Therefore, age may have influenced the findings of the present study. As a perspective for future studies to clarify the effects of breed and age on HRV in dogs, it may be necessary to equalize breeds or differentiate between small, medium, and large dogs, or to conduct HRV studies by age stratification. Another limitation is the inclusion of brachycephalic breeds. It has been suggested that brachycephalic breeds may exhibit higher cardiac vagal activity compared to non-brachycephalic breeds (42). Furthermore, the heterogeneity of the rearing environment of the experimental animals is another limitation. If future studies are conducted with domestic dogs living in human households, the circadian rhythm may be influenced by the human life rhythm, potentially impacting HRV measurements. In practice, we are investigating the early detection of

doxorubicin-induced myocardial damage. If myocardial damage is detected before irreversibility, it can be treated. Sleep HRV may detect smaller myocardial changes.

5 Conclusion

In conclusion, SDNN, RMSSD, SD1, and SD2 significantly reflected parasympathetic activity during sleep. Focusing on HRV during sleep enables us to capture the maximum peak of the circadian rhythm items of the parasympathetic index of HRV and more accurately represents parasympathetic activity than 24-h HRV.

Data availability statement

The original contributions presented in the study are included in the article/supplementary material, further inquiries can be directed to the corresponding author.

Ethics statement

The animal studies were approved by the Institutional Animal Care and Use Committee of the TUAT. The studies were conducted in accordance with the local legislation and institutional requirements. Written informed consent was obtained from the owners for the participation of their animals in this study.

Author contributions

MHa: Conceptualization, Data curation, Formal analysis, Investigation, Methodology, Project administration, Validation, Visualization, Writing – original draft, Writing – review & editing. MS: Data curation, Project administration, Writing – review & editing. YU: Writing – review & editing, Data curation. RH: Writing – review & editing, Data curation. AH: Writing – review & editing, Data curation. MHo: Writing – review & editing, Data curation. AF: Writing – review & editing, Data curation. KM: Writing – review & editing. TY: Writing – review & editing. KS: Writing – review & editing. LH: Writing – review & editing. KT: Conceptualization, Investigation, Methodology, Software, Visualization, Writing – review & editing. RT: Conceptualization, Investigation, Methodology, Project administration, Supervision, Validation, Writing – review & editing.

Funding

The author(s) declare that no financial support was received for the research, authorship, and/or publication of this article.

Acknowledgments

The authors would like to thank the Department of Dog & Cat Pediatric Hospital (Tokyo, Japan) for their extensive contributions to this study.

Conflict of interest

The authors declare that the research was conducted in the absence of any commercial or financial relationships that could be construed as a potential conflict of interest.

Publisher's note

References

1. Santilli RA, Moise NS, Pariaut R, Perego M. *Electrocardiography of the dog and cat*. Milano: Edra S.p.A (2018). 77 p.

2. Chengfen Y, Jianguo L, Zhiyong W, Yongle Z, Lei X. Decreased heart rate variability in COVID-19. *Intensive Care Res*. (2023) 3:87–91. doi: 10.1007/s44231-022-00024-1

3. Ikram M, Morten AVL, Ann VL, Louise LA, Niels-Henrik H-R, Gorm G. Cardiovascular autonomic nervous function in children conceived by assisted reproductive technology with frozen or fresh embryo transfer. *Am J Physiol Heart Circ Physiol*. (2024) 326:H216–22. doi: 10.1152/ajpheart.00680.2023

4. Vaiibhav NP, Brian RP, Rohan KB, David LB, Diane GI, Phyllis KS. Association of holter-derived heart rate variability parameters with the development of congestive heart failure in the cardiovascular health study. JACC. *Heart Failure*. (2017) 5:424–31. doi: 10.1016/j.jchf.2016.12.015

5. Prapawadee P, Nakkawee S, Pakit B, Robert LH, Anusak K. Impact of a combination of pimobendan, furosemide, and enalapril on heart rate variability in naturally occurring, symptomatic, myxomatous mitral valve degeneration dogs. *BMC Vet Res*. (2023) 19:201. doi: 10.1186/s12917-023-03770-6

6. Mathieu B, Vincent P, Geoffroy S, Pedro MV, José HR, Peter V, et al. Association between nocturnal heart rate variability and incident cardiovascular disease events: the HypnoLaus population-based study. *Heart Rhythm*. (2022) 19:632–9. doi: 10.1016/j.hrthm.2021.11.033

7. Sanni S, Heini T, Aija K, Antti V, Veikko S, Outi V, et al. Dog–owner relationship, owner interpretations and dog personality are connected with the emotional reactivity of dogs. *Animals*. (2022) 12:1338. doi: 10.3390/ani12111338

8. Alysia BGH, Hannah EF, Darren WL, Tammie K. A single dose of cannabidiol (CBD) positively influences measure of stress in dogs during separation and car travel. *Front Vet Sci*. (2023) 10:1112604. doi: 10.3389/fvets.2023.1112604

9. Turini L, Bonelli F, Lanata A, Vitale V, Nocera I, Sgorbini M, et al. Validation of a new smart textiles biotechnology for heart rate variability monitoring in sheep. *Front Vet Sci*. (2022) 22:1018213. doi: 10.3389/fvets.2022.1018213

10. Mansour C, Merlin T, Bonnet-Garin JM, Chaaya R, Mocci R, Ruiz CC, et al. Evaluation of the parasympathetic tone activity (PTA) index to assess the analgesia/nociception balance in anaesthetized dogs. *Res Vet Sci*. (2017) 115:271–7. doi: 10.1016/j.rvsc.2017.05.009

11. Hernández-Avalos I, Valverde A, Ibancovichi-Camari JA, Sanchez-Aparicio P, Recillas-Morales S, Rodríguez-Velázquez D, et al. Clinical use of the parasympathetic tone activity index as a measurement of postoperative analgesia in dogs undergoing ovariohysterectomy. *J Vet Res*. (2021) 65:117–23. doi: 10.2478/jvetres-2021-0004

12. Eberhard VB, Jan L, Gérard D, Sven H, Le C, Jeremy M, et al. Heart rate variability as a measure of autonomic regulation of cardiac activity for assessing stress and welfare in farm animals — a review. *Physiol Behav*. (2007) 92:293–316. doi: 10.1016/j.physbeh.2007.01.007

13. Hernández-Avalos I, Mota-Rojas D, Mendoza-Flores JE, Casas-Alvarado A, Flores-Padilla K, Miranda-Cortes AE, et al. Nociceptive pain and anxiety in equines: physiological and behavioral alterations. *Vet World*. (2021) 14:2984–95. doi: 10.14202/vetworld.2021.2984-2995

14. Nancy G, Zuzanna Z, Annabel W, Ross H, Valeria M. Heart rate variability (HRV) as a way to understand associations between the autonomic nervous system (ANS) and

affective states: a critical review of the literature. *Int J Psychophysiol*. (2023) 192:35–42. doi: 10.1016/j.ijpsycho.2023.08.001

15. Gaidica M, Dantzer B. Quantifying the autonomic response to stressors—one way to expand the definition of "stress" in animals. *ICB*. (2020) 60:113–25. doi: 10.1093/icb/icaa009

16. Oliveira MS, Muzzi RAL, Araújo RB, Muzzi LAL, Ferreira DF, Nogueira R, et al. Heart rate variability parameters of myxomatous mitral valve disease in dogs with and without heart failure obtained using 24-hour Holter electrocardiography. *Vet Rec*. (2012) 170:622. doi: 10.1136/vr.100202

17. Clay AC. Heart rate variability. *J Small Anim Pract*. (1998) 28:1409–27. doi: 10.1016/S0195-5616(98)50129-5

18. Clay AC, Michelle W, Clay A. Effect of severity of myocardial failure on heart rate variability in Doberman pinschers with and without echocardiographic evidence of dilated cardiomyopathy. *JAVMA*. (2001) 219:1084–8. doi: 10.2460/javma.2001.219.1084

19. Alan WS, Kathryn MM. Assessment of heart rate variability in boxers with arrhythmogenic right ventricular cardiomyopathy. *JAVMA*. (2004) 224:534–7. doi: 10.2460/javma.2004.224.534

20. David AG, Nick D. Heart rate variability during exercise: a comparison of artefact correction methods. *J Strength Cond Res*. (2018) 32:726–35. doi: 10.1519/JSC.0000000000001800

21. Bernardi L, Valle F, Coco M, Calciati A, Sleight P. Physical activity influences heart rate variability and very-low-frequency components in Holter electrocardio grams. *Cardiovasc Res*. (1996) 32:234–7. doi: 10.1016/0008-6363(96)00081-8

22. David H, Prisca E, Ximena O, Robert R, Matthias W, Peter A. Reproducibility of heart rate variability is parameter and sleep stage dependent. *Front Physiol*. (2018) 10:1100. doi: 10.3389/fphys.2017.01100

23. Martinello L, Romão FG, Godoy MF, Machado LHA, Tsunemi MH, Lourenço MLG. Study of autonomic modulation by non-linear analysis of heart rate variability in different age groups and analysis of health status, disease and risk of death in dogs. *Pol J Vet Sci*. (2023) 26:581–90. doi: 10.24425/pjvs.2023.148278

24. Uchino T. About long-term ECG recording methods in dogs (in Japanese). *Jpn J Electrocardiology*. (2001) 21:45–51. doi: 10.5105/jse.21.Suppl1_45

25. Robert LB. Interpretation of normalized spectral heart rate variability indices in sleep research: a critical review. *Sleep*. (2007) 30:913–9. doi: 10.1093/sleep/30.7.913

26. Shaffer F, Ginsberg JP. An overview of heart rate variability metrics and norms. *Front Public Health*. (2017) 28:258. doi: 10.3389/fpubh.2017.00258

27. Moïse NS, Gladuli A, Hemsley SA, Otani NF. "Zone of avoidance": RR interval distribution in tachograms, histograms, and Poincaré plots of a boxer dog. *J Vet Cardiol*. (2010) 12:191–6. doi: 10.1016/j.jvc.2010.07.001

28. Blake RR, Shaw DJ, Culshaw GJ, Martinez-Pereira Y. Poincare´ plots as a measure of heart rate variability in healthy dogs. *J Vet Cardiol*. (2018) 20:20–32. doi: 10.1016/j.jvc.2017.10.006

29. Moïse NS, Brewer FC, Flanders WH, Kornreicha BG, Otani NF. Insights into sinus arrhythmia of the dog: acetylcholine perfusion of canine right atrium results in beat-to-beat patterns that mimic sinus arrhythmia supporting exit block in the sinoatrial conduction pathways. *Vet J*. (2021) 272:105651. doi: 10.1016/j.tvjl.2021.105651

30. Giovanni R, Carlo G, Helen P, Marco BT. Lorenz plot analysis in dogs with sinus rhythm and Tachyarrhythmias. *Animals*. (2021) 11:1645. doi: 10.3390/ani11061645

31. Flanders WH, Moïse NS, Pariaut R, Sargent J. The next heartbeat: creating dynamic and histographic Poincaré plots for the assessment of cardiac rhythms. *J Vet Cardiol*. (2022) 42:1–13. doi: 10.1016/j.jvc.2022.04.003

32. Peng CK, Havlin S, Stanley HE, Goldberger AL. Quantification of scaling exponents and crossover phenomena in nonstationary heartbeat time series. *Chaos*. (1995) 5:82–7. doi: 10.1063/1.166141

33. Peng CK, Havlin S, Hausdorff JM, Mietus J, Stanley HE, Goldberger AL. Fractal mechanisms and heart rate dynamics: long-range correlations and their breakdown with disease. *J Electrocardiol*. (1996) 28:59–65. doi: 10.1016/s0022-0736(95)80017-4

34. Xian L, Michele LS, Sol RC, Fan H, Deborah LW, Peter AJ, et al. The circadian pattern of cardiac autonomic modulation in a middle-aged population. *Clin Auton Res*. (2011) 21:143–50. doi: 10.1007/s10286-010-0112-4

35. Rasmussen CE, Falk T, Zois NE, Moesgaard SG, Haggstrom J, Pedersen HD, et al. Heart rate, heart rate variability, and arrhythmias in dogs with myxomatous mitral valve disease. *J Vet Intern Med*. (2012) 26:76–84. doi: 10.1111/j.1939-1676.2011.00842.x

36. Paul G, Edwin WT. Toward understanding respiratory sinus arrhythmia: relations to cardiac vagal tone, evolution and biobehavioral functions. *Biol Psychol*. (2007) 74:263–85. doi: 10.1016/j.biopsycho.2005.11.014

37. Shaffer F, McCraty R, Zerr CL. A healthy heart is not a metronome: an integrative review of the heart's anatomy and heart rate variability. *Front Psychol*. (2014) 5:1040. doi: 10.3389/fpsyg.2014.01040

38. Moise NS. From cell to cageside: autonomic influences on cardiac rhythms in the dogs. *J Small Anim Pract*. (1998) 39:460–8. doi: 10.1111/j.1748-5827.1998.tb03680.x

39. Ritz T. Putting back respiration into respiratory sinus arrhythmia or high-frequency heart rate variability: implication for interpretation, respiratory rhythmicity and health. *Biol Phychol*. (2014) 185:108728. doi: 10.1016/j.biopsycho.2023.108728

40. Bonnemeier H, Wiegand UKH, Brandes A, Kluge N, Katus HA, Richardt G, et al. Circadian profile of cardiac autonomic nervous modulation in healthy subjects: differing effects of aging and gender on heart rate variability. *J Cardiovasc Electrophysiol*. (2003) 14:791–9. doi: 10.1046/j.1540-8167.2003.03078.x

41. Almeida-Santos MA, Barreto-Filho JA, Oliveira JL, Reis FP, da Cunha Oliveira CC, Sousa ACS. Aging, heart rate variability and patterns of autonomic regulation of the heart. *Arch Gerontol Geriatr*. (2016) 63:1–8. doi: 10.1016/j.archger.2015.11.011

42. Doxey S, Boswood A. Differences between breeds of dog in a measure of heart rate variability. *Vet Rec*. (2004) 154:713–7. doi: 10.1136/vr.154.23.713

frontiers | Frontiers in Veterinary Science

TYPE Original Research
PUBLISHED 06 June 2024
DOI 10.3389/fvets.2024.1374890

OPEN ACCESS

EDITED BY
Blaz Cugmas,
University of Latvia, Latvia

REVIEWED BY
Juan Claudio Gutierrez,
University of California, Davis,
United States
Martin Ceballos,
University of Buenos Aires, Argentina

*CORRESPONDENCE
Eric J. Snider
✉ eric.j.snider3.civ@health.mil

RECEIVED 23 January 2024
ACCEPTED 20 May 2024
PUBLISHED 06 June 2024

CITATION
Hernandez Torres SI, Holland L, Edwards TH, Venn EC and Snider EJ (2024) Deep learning models for interpretation of point of care ultrasound in military working dogs.
Front. Vet. Sci. 11:1374890.
doi: 10.3389/fvets.2024.1374890

Deep learning models for interpretation of point of care ultrasound in military working dogs

Sofia I. Hernandez Torres[1], Lawrence Holland[1], Thomas H. Edwards[2,3], Emilee C. Venn[4] and Eric J. Snider[1]*

[1]Organ Support and Automation Technologies Group, U.S. Army Institute of Surgical Research, JBSA Fort Sam Houston, San Antonio, TX, United States, [2]Hemorrhage Control and Vascular Dysfunction Group, U.S. Army Institute of Surgical Research, JBSA Fort Sam Houston, San Antonio, TX, United States, [3]Texas A&M University, School of Veterinary Medicine, College Station, TX, United States, [4]Veterinary Support Group, U.S. Army Institute of Surgical Research, JBSA Fort Sam Houston, San Antonio, TX, United States

Introduction: Military working dogs (MWDs) are essential for military operations in a wide range of missions. With this pivotal role, MWDs can become casualties requiring specialized veterinary care that may not always be available far forward on the battlefield. Some injuries such as pneumothorax, hemothorax, or abdominal hemorrhage can be diagnosed using point of care ultrasound (POCUS) such as the Global FAST® exam. This presents a unique opportunity for artificial intelligence (AI) to aid in the interpretation of ultrasound images. In this article, deep learning classification neural networks were developed for POCUS assessment in MWDs.

Methods: Images were collected in five MWDs under general anesthesia or deep sedation for all scan points in the Global FAST® exam. For representative injuries, a cadaver model was used from which positive and negative injury images were captured. A total of 327 ultrasound clips were captured and split across scan points for training three different AI network architectures: MobileNetV2, DarkNet-19, and ShrapML. Gradient class activation mapping (GradCAM) overlays were generated for representative images to better explain AI predictions.

Results: Performance of AI models reached over 82% accuracy for all scan points. The model with the highest performance was trained with the MobileNetV2 network for the cystocolic scan point achieving 99.8% accuracy. Across all trained networks the diaphragmatic hepatorenal scan point had the best overall performance. However, GradCAM overlays showed that the models with highest accuracy, like MobileNetV2, were not always identifying relevant features. Conversely, the GradCAM heatmaps for ShrapML show general agreement with regions most indicative of fluid accumulation.

Discussion: Overall, the AI models developed can automate POCUS predictions in MWDs. Preliminarily, ShrapML had the strongest performance and prediction rate paired with accurately tracking fluid accumulation sites, making it the most suitable option for eventual real-time deployment with ultrasound systems. Further integration of this technology with imaging technologies will expand use of POCUS-based triage of MWDs.

KEYWORDS

ultrasound imaging, military medicine, canine, deep learning, triage, abdominal hemorrhage, pneumothorax, hemothorax

1 Introduction

Ultrasound is commonly used in canines with suspected abdominal or thoracic injuries following trauma, to identify free fluid which may require surgical intervention. Different standardized exams are used in veterinary medicine such as the abdominal focused assessment with sonography for trauma (AFAST®), thoracic FAST (TFAST®), or the Veterinary Bedside Lung Ultrasound Exam (Vet BLUE®) (1–3). These are often performed together and referred to as GlobalFAST® which can be used for civilian trauma cases, but also for working dog casualties (4). Working dogs cover a wide range of occupations including military working dogs (MWDs) which go anywhere soldiers are deployed and aid with a wide range of tasks (5). The ever increasing high risk mission that MWDs share with their handlers puts them at risk for similar injuries as their Service member counterparts (6, 7). Unfortunately, in the early roles of care, where MWD casualties are first managed, veterinary expertise may not be present to properly acquire ultrasound images and to interpret images making GlobalFAST® inaccessible for treatment of MWDs at these early stages of care (8).

This is further complicated on the future battlefield where medical evacuation will be limited and more medical care and triage will need to be provided in theater, at early roles of care (9). In fact, this is already being experienced with the Ukraine-Russia conflict, where limited medical evacuation opportunities arise due to challenged airspace, which is requiring far forward surgical teams to treat and manage a larger number of casualties for up to 72 h in theater (10). This is further complicated by precise long-range weaponry minimizing the relative safety of CASEVAC even at distances above 500 km away from enemy lines. In addition, more than 70% of Ukraine casualties stem from more advanced rocket or artillery injuries, which often result in complex polytrauma to multiple organ systems (10). Thus, as we look towards the future battlefield, it is even more imperative to have accurate triage procedures for prioritizing injured warfighters for access to limited evacuation opportunities.

Towards addressing this critical capability gap for canine and human casualties on the future battlefield, artificial intelligence (AI) can be utilized to automate medical triage image interpretation (11, 12). AI for image interpretation often relies on deep convolutional neural network models containing millions of trainable parameters to extract features from images for making categorical predictions (13, 14). For medical applications, AI has been widely used for tumor detection (15, 16), COVID-19 diagnosis (17, 18), and obstetric ultrasound applications (19, 20). In addition, AI has been applied to interpret radiographs in thoracic (21, 22), cardiac (23, 24), and orthopedic (25) settings. Our research team has previously developed an ultrasound image AI interpretation model for detecting shrapnel in tissue, termed ShrapML (26, 27). We have recently expanded this work to the enhanced FAST (eFAST) exam commonly used for human emergency triage applications (28). This application resulted in different AI models for detecting pneumothorax, hemothorax, and abdominal hemorrhage injuries in tissue phantom image sets. In this presented work, we hypothesize if AI image interpretation models are trained on canine image datasets, they will be able to automatically identify injuries at each POCUS scan point. By doing so, the skill threshold for POCUS interpretation will be lowered so that this critical triage task can be available at early echelons of care where emergency intervention is most needed for MWDs.

2 Materials and methods

2.1 Imaging protocol

Research was conducted in compliance with the Animal Welfare Act, implementing Animal Welfare regulations, and the principles of the Guide for the Care and Use for Laboratory Animals. The Institutional Animal Care and Use Committee at the Department of Defense Military Working Dog Veterinary Services approved all research conducted in this study. The facility where this research was conducted is fully accredited by the AAALAC International. The POCUS protocol used mirrored the GlobalFAST® procedure in a total of five (1.5 to 10 years old) healthy canine subjects (20 to 55 kgs weight) under general anesthesia or deep sedation for other medical procedures, as prescribed by the attending veterinarian. Ultrasound (US) clips were collected in 8 scan points (Table 1) using a C11 transducer (Fujifilm, Bothell, WA, United States) with a Sonosite Edge ultrasound system (Fujifilm, Bothell, WA, United States). The subject was positioned in right lateral, left lateral, sternal or dorsal recumbency for ease of access to each scan point. A minimum of three 15 s clips were collected at each scan point with the probe orientation held in the coronal plane for the first 6 s and then rotated to the transverse plane for the remainder of each clip. All clips collected from the live subjects were used as baseline (negative for injury) data. The same scanning protocol was used to obtain US imaging data from a cadaver canine model. A total of five frozen cadavers (Skulls Unlimited, Oklahoma City, OK, United States) were received and stored at −20°C until ready for use. Once thawed, an endotracheal tube (McKesson Medical-Surgical, Irving, TX, United States) was placed into the trachea of each subject and secured to a bag valve mask (EMS Safety Services, Eugene, OR, United States) for ventilation. At this time

TABLE 1 Scan point description for the POCUS imaging protocol.

Scan point	Abbreviation	Description
Bilateral Chest Tube Site	CTS	Longitudinal plane on both sides of the chest perpendicular to the ribs at the 7th to 9th intercostal space.
Bilateral Pericardial Site	PCS	Longitudinal and transverse planes on each side of the chest between the 5th and 6th intercostal spaces over the heart.
Diaphragmatic Hepatic	DH	Subxiphoid view for visualization of the pleural and pericardial spaces beyond the diaphragm to evaluate hepatodiaphragmatic interface, gallbladder region, and pericardial sac.
Splenorenal	SR	Left flank view to assess the splenorenal interface and areas between the spleen and body wall
Cystocolic	CC	Midline view to assess the apex of the bladder
Hepatorenal	HR	Right flank view to assess the hepatorenal interface and areas between the spleen and body wall

thoracic and abdominal CT scans (Toshiba Aquilion CT Scanner, Cannon Medical Systems, Tustin, CA, United States) were collected to identify any pre-existing injuries. Then, data was collected at each scan point, using the same protocol as the live subjects. After collecting the first round of data, if the subject was positive for any injury, e.g., a pneumothorax, a needle decompression was performed to remove air and obtain a negative scan. Another round of data was collected with the scan points that were negative for injury. Next, controlled injuries were performed by adding blood or saline to the pleural space (up to 300 mL) or the abdomen (up to 400 mL) for a final round of positive injury image collection in the cadaver subjects.

2.2 Preprocessing images

All clips were exported from the US machine as MP4 format and then renamed to reflect the scan point, subject ID, and recumbency of each subject. Frames were extracted from each clip using ffmpeg tool, via a Ruby script, and then sorted by positive or negative for injury by scan point. Each frame was then cropped to remove the user interface information from the US system and the images were resized to 512 × 512 pixels. Additional steps were taken with images collected at the chest tube site, to recreate M-mode images. Briefly, clips were processed to extract a pixel-wide image over time for visualizing the lung-pleura interface movement. These custom-M-mode images were then cropped and resized to 512 × 512 as well.

Before images were ready for training, they were augmented to prevent model overfitting and improve performance. While data augmentation is useful to prevent overfitting, it can result in poor model performance and more computationally intensive training if not setup optimally for the application (29). A representative image was chosen from each scan point, including M-mode reconstructions, to match histogram values across all the other images using "imhistmatch" function by MATLAB (MathWorks, Natick, MA, United States). Then, contrast and brightness were randomly adjusted by ±20% to add training noise using the "jitterColorHSV" function by MATLAB. Both MATLAB functions were applied to all images for every scan point using Image Batch Processor on MATLAB. Augmented US images were imported at a 512 × 512 × 3 image size and were randomly assigned to training, validation or testing datasets at a 70:15:15 ratio. Image sets were set up so that an even number of positive or negative images were selected in each dataset for each split. Next, training images were augmented randomly by affine transformations: random scaling, random X and Y reflections, random rotation, random X and Y shear, and random X and Y translation. However, for the CTS M-mode scan point only X reflection and translation affine transformations were applied given how these images were constructed. Due to DH scan point images being unable to train with all augmentations (data not shown), only reflection and translation augmentations were applied for both the X and Y direction.

2.3 Training AI models

Three different AI models were evaluated for this application that have previously been used for ultrasound image interpretation successfully – MobileNetV2 (30), DarkNet-19 (31), and ShrapML (26). MobileNetV2 has 53 convolutional layers, 3.5 million parameters, and was optimized for use on mobile devices. We have previously shown this architecture to perform at the highest accuracy for identifying shrapnel in a custom tissue phantom. The second-best performing architecture, DarkNet-19, has 19 convolutional layers, 20.8 million parameters, and utilizes global average pooling for making predictions. The last model used, ShrapML, was purpose built and Bayesian optimized for identifying shrapnel in ultrasound images at a high accuracy and much more rapid than conventional models. In addition, we have shown it to be successful at identifying pneumothorax, hemothorax, and abdominal hemorrhage injuries in eFAST images captured in human tissue phantom models (28). ShrapML consists of 8 convolutional layers with only 430,000 trainable parameters.

Training for all scan points consisted of a learning rate of 0.001 with a batch size of 32 images and RMSprop (root mean squared propagation) as the optimizer. A maximum of 100 epochs was allowed for training with a validation patience of 5 epochs if the overall validation loss did not improve. The model with the lowest validation loss was selected for use with blind predictions. All training was performed using MATLAB R2022b run on a Microsoft Windows workstation with a NVIDIA GeForce RTX 3090 Ti 24Gb VRAM graphics card, Intel i9-12900k and 64 GB RAM.

2.4 Performance metrics

Testing image sets were used to assess blind performance in multiple ways. First, confusion matrices were generated to categorize prediction as either true positive (TP), true negative (TN), false positive (FP), or false negative (FN) results. These results were used to generate performance metrics for accuracy Eq. 1, precision Eq. 2, recall Eq. 3, specificity Eq. 4, and F1 scores Eq. 5 using commonly used formulas for each.

$$Accuracy = \frac{(TP + TN)}{(TP + TN + FP + FN)} \quad (1)$$

$$Precision = \frac{TP}{TP + FP} \quad (2)$$

$$Recall = \frac{TP}{TP + FN} \quad (3)$$

$$Specificity = \frac{TN}{TN + FP} \quad (4)$$

$$F1\,score = \frac{2 \times Precision \times Recall}{Precision + Recall} \quad (5)$$

Then, we constructed receiver operating characteristic (ROC) plots to further classify performance for a number of confidence thresholds for the predictions. ROC plots were used to calculate the area under the ROC curve or AUROC, which tells you how well the model differentiates between categories. Next, inference time for test image predictions were quantified for each trained model to assess differences in computational efficiency of the three different AI models used. Lastly, Gradient-weighted Class Activation Mapping (GradCAM) overlays were generated for test predictions to highlight the regions of images where the AI predictions were focused (32). These were used as an explainable-AI methodology to verify the AI models were accurately tracking the image regions where injury differences were present (16, 33, 34).

3 Results

3.1 MobileNetV2

MobileNetV2 was successfully trained for each POCUS scan point, with an average accuracy across all locations of 98.8% (Table 2). In addition, strong performance was evident for other conventional metrics across each POCUS scan point. However, upon closer inspection using GradCAM mask overlays, the MobileNetV2 trained model was not always properly tracking the injury site, but instead was focused on image artifacts that will likely not be consistent for additional canine subjects not included in the current datasets (Figure 1). CTS scan sites for both M- and B-mode were accurately tracking injuries, other scan sites such as HR, DH, and SR were not tracking correctly. Average inference times across all MobileNetV2 scan site models was 6.21 ms per prediction.

3.2 DarkNet-19

The DarkNet-19 models had similar inference speeds compared to MobileNetV2 at 5.93 ms per prediction, but overall performance was reduced for a number of the scan sites, resulting in an average accuracy across all scan points of 86.4% (Table 3). Certain scan points like chest-tube M-mode images resulted only in predictions of negative (TN or FN) and the GradCAM overlays identified no obvious tracked features in the image (Figure 2). While this was the worst performing dataset trained against, the Cystocolic scan site was also only at 69.2% accuracy. While performance was reduced compared to MobileNetV2 across nearly all metrics, the GradCAM overlays were more accurately tracking image features consistent with locations where free fluid was or could be identified. These results indicated that while performance was overall reduced for DarkNet-19, the predictions were more often tracking the proper image features. More images and subject variability may improve on training performance.

3.3 ShrapML

The last model evaluated was ShrapML, which resulted in an accuracy across all scan sites of 93.4% (Table 4). Unlike DarkNet-19, no trained model resulted in an instance of 100% positive or negative guesses. However, performance metrics were consistently worse than MobileNetV2. Given the smaller model size of ShrapML, the inference times were much quicker compared to the other models with prediction rates at an average of 3.43 ms per image. GradCAM overlays more closely resembled DarkNet-19 in that many of the heat map intensity points were focused on regions where free fluid was likely to be found or near organs present in the ultrasound scan (Figure 3), except for the HR site. Overall, ShrapML was successful at performing similarly well to these large network structures for this GlobalFAST application, model overfitting was less evident in the results, and overall prediction speed outperformed the other models tested.

A summary table of average performance metrics for each scan site across all three model architectures is shown in Table 5.

4 Discussion

Medical imaging-based triage is critical for both human and veterinary emergency medicine to identify issues early on and ensure resources are properly distributed. In remote or military medicine situations, the lack of skilled personnel makes imaging based-triage less relied upon, but AI prediction models can simplify this for the end user. Here, we focus on the POCUS procedure GlobalFAST®, a widely used triage exam to look for abdominal or thoracic free fluid in injured dogs. The AI models shown in this work can automate predictions for ultrasound results if properly tuned for the application.

Three different AI architectures were evaluated to see which was capable of being trained to distinguish positive injury cases from baseline images. While all models were generally successful at being trained for these applications, strong test performance may not indicate properly trained models. For instance, MobileNetV2 had

TABLE 2 Summary of performance metrics for MobileNetV2.

Metric	CTS	CTS M-mode	PCS	DH	SR	CC	HR	Average
Accuracy	0.987	0.997	0.985	0.986	0.979	0.998	0.987	0.988
Precision	0.986	0.994	0.995	0.998	0.999	1.000	0.982	0.995
Recall	0.987	1.000	0.976	0.973	0.960	0.996	0.992	0.980
Specificity	0.986	0.994	0.995	0.998	0.999	1.000	0.982	0.995
F1 Score	0.987	0.997	0.985	0.985	0.979	0.998	0.987	0.987
AUROC	0.999	1.000	1.000	1.000	0.999	1.000	0.999	1.000
Inference Time (ms/image)	6.22	7.67	5.59	5.58	6.64	6.06	6.57	6.21

10.3389/fvets.2024.1374890

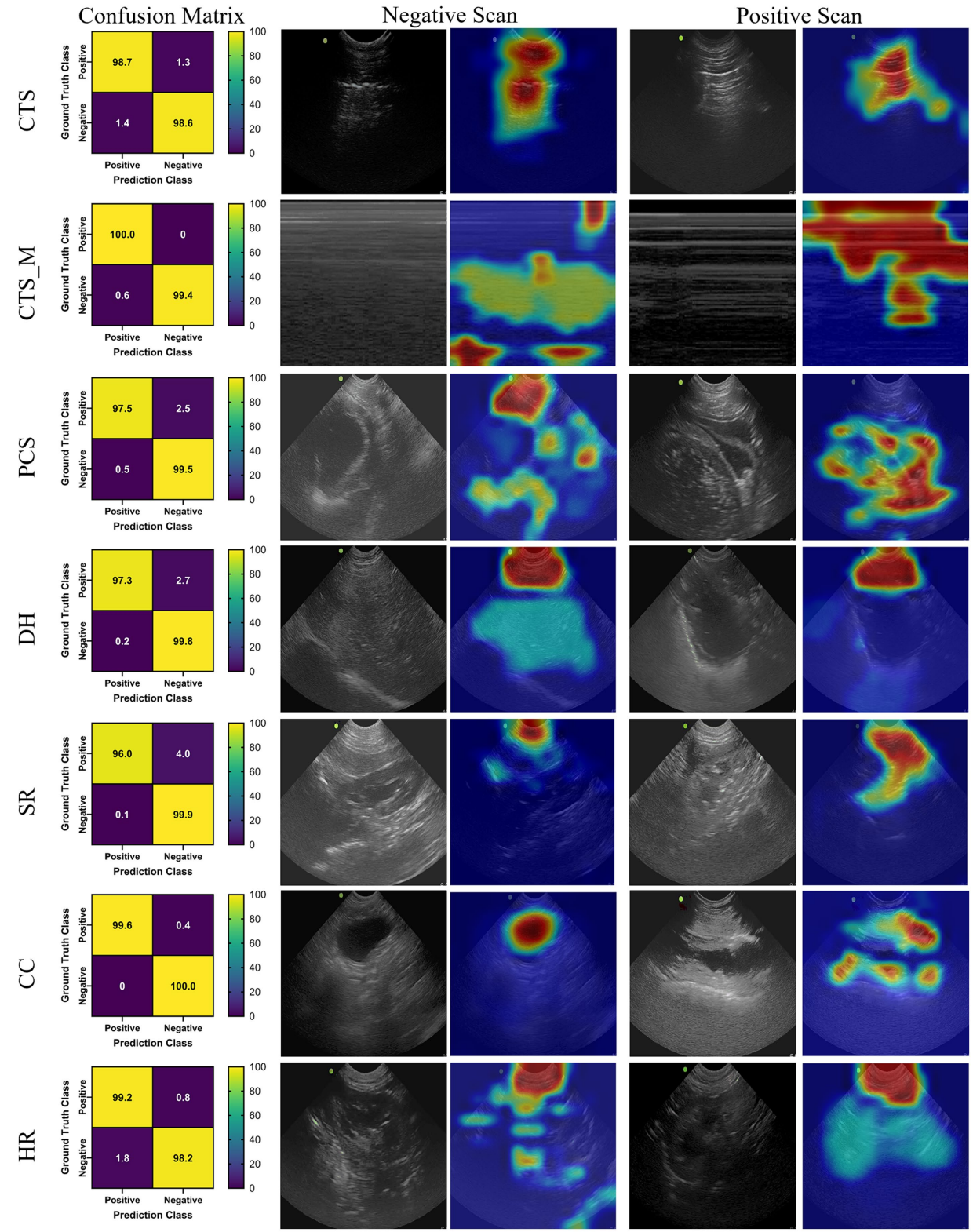

FIGURE 1
Prediction results by scan point for MobileNetV2. Results for each scan site showing (column 1) confusion matrix test prediction results, (column 2–3) negative and (column 4–5) positive representative images without and with the GradCAM overlay. Regions in the images with high relevance to model predictions have red-yellow overlays, while those of lower relevance have blue-green overlays.

TABLE 3 Summary of performance metrics for DarkNet-19.

Metric	CTS	CTS M-mode	PCS	DH	SR	CC	HR	Average
Accuracy	0.933	0.500	0.930	0.967	0.878	0.692	0.919	0.864
Precision	0.954		0.993	1.000	0.865	0.636	0.873	0.844
Recall	0.911	0.000	0.867	0.933	0.896	0.895	0.979	0.926
Specificity	0.956	1.000	0.994	1.000	0.860	0.488	0.858	0.801
F1 Score	0.932		0.926	0.966	0.880	0.744	0.923	0.878
AUROC	0.984	0.575	0.992	0.999	0.953	0.737	0.988	0.92
Inference Time (ms/image)	6.32	8.73	5.53	5.61	5.86	6.17	6.07	5.93

TABLE 4 Summary of performance metrics for ShrapML.

Metric	CTS	CTS M-mode	PCS	DH	SR	CC	HR	Average
Accuracy	0.900	0.966	0.908	0.989	0.861	0.965	0.950	0.934
Precision	0.901	0.994	0.917	0.993	0.806	0.967	0.977	0.936
Recall	0.898	0.938	0.897	0.984	0.950	0.963	0.921	0.936
Specificity	0.901	0.994	0.919	0.993	0.772	0.967	0.978	0.932
F1 Score	0.900	0.965	0.907	0.988	0.872	0.965	0.948	0.935
AUROC	0.961	0.998	0.97	0.999	0.928	0.995	0.988	0.977
Inference Time (ms/image)	5.72	3.78	2.63	2.68	3.31	2.83	3.05	3.43

TABLE 5 Summary of performance metrics for each POCUS site.

	CTS	CTS M-Mode	PCS	DH	SR	CC	HR
Accuracy	93.98%	82.11%	94.12%	98.02%	90.61%	88.49%	95.18%
Precision	94.69%	99.42%	96.83%	99.69%	89.00%	86.76%	94.42%
Recall	93.19%	64.60%	91.32%	96.35%	93.52%	95.15%	96.41%
Specificity	94.77%	99.62%	96.92%	99.70%	87.69%	81.82%	93.95%
F1 Score	93.92%	98.11%	93.93%	97.98%	91.04%	90.22%	95.29%
Number of Training Images	23,305	1,652	16,380	11,340	9,455	10,080	9,455

the highest accuracy, but heat map overlays indicating where the AI was focused were not tracking proper image locations. Model overfit was combatted with the various image augmentation techniques used for the training, but this was insufficient to mimic proper subject variability to create a more robust model for this architecture. This issue was less evident for the other two model architectures, highlighting the importance of AI model selection and validation on ultrasound image applications such as this. However, without more subjects and the variability that those bring, it is hard to fully verify if the developed DarkNet-19 or ShrapML models are suitable. Preliminarily, ShrapML had the strongest performance and prediction rate, making it the most suitable going forward as well as eventual integration for real-time deployment with ultrasound machines.

Focusing on the various scan points in the used POCUS exam, there were obvious differences in the AI model training. Training image sets were not equally sized, but that did not correlate to what scan sites performed the best. The DH site was the overall strongest performing site across all performance metrics. However, this could be due to this scan site having the largest difference between live and cadaveric tissue resulting in a well-trained model. In addition, less augmentation steps were used for this site due to training issues using all affine transformations. More images are needed to address this issue from a wider range of subjects. CTS and HR views also performed well across the three models trained. Worst performing was the M-mode reconstructed chest tube images which could be influenced by the minimal training data used for this model, and thus may be improved with more training data. The CC site was also a lower performing scan site even though more than 10,000 images were used in the training dataset. However, this is mostly influenced by DarkNet-19 having lower performance for this scan site while the other two models had accuracies greater than 96%. Overall, each scan site for this POCUS application was successful as an input for an injury prediction model.

5 Conclusion

Artificial intelligence has the potential to simplify triage and injury diagnosis for emergency veterinary medicine. The results

10.3389/fvets.2024.1374890

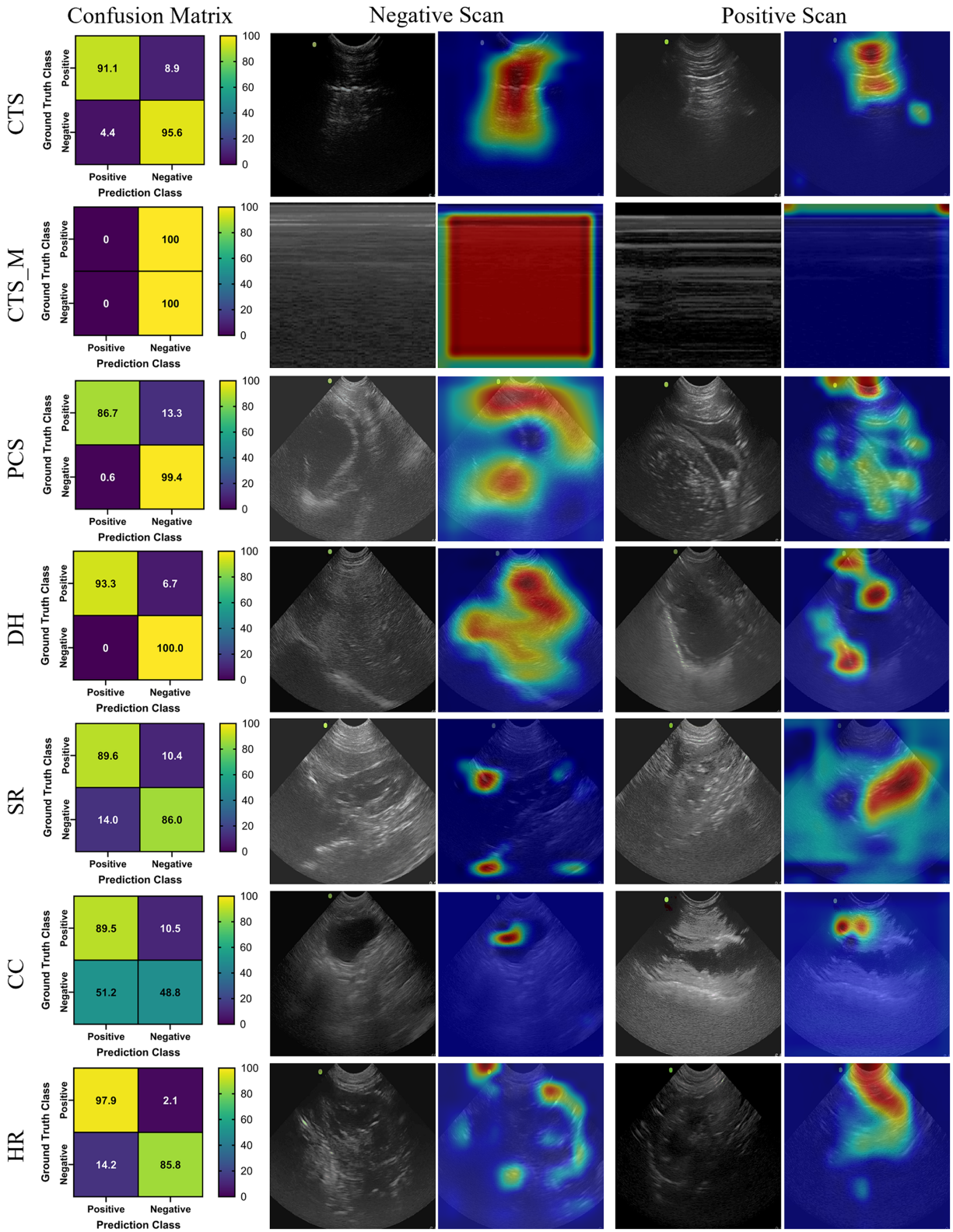

FIGURE 2
Prediction results by scan point for DarkNet-19. Results for each scan site showing (column 1) confusion matrix test prediction results, (column 2–3) negative and (column 4–5) positive representative images without and with the GradCAM overlay. Regions in the images with high relevance to model predictions have red-yellow overlays, while those of lower relevance have blue-green overlays.

10.3389/fvets.2024.1374890

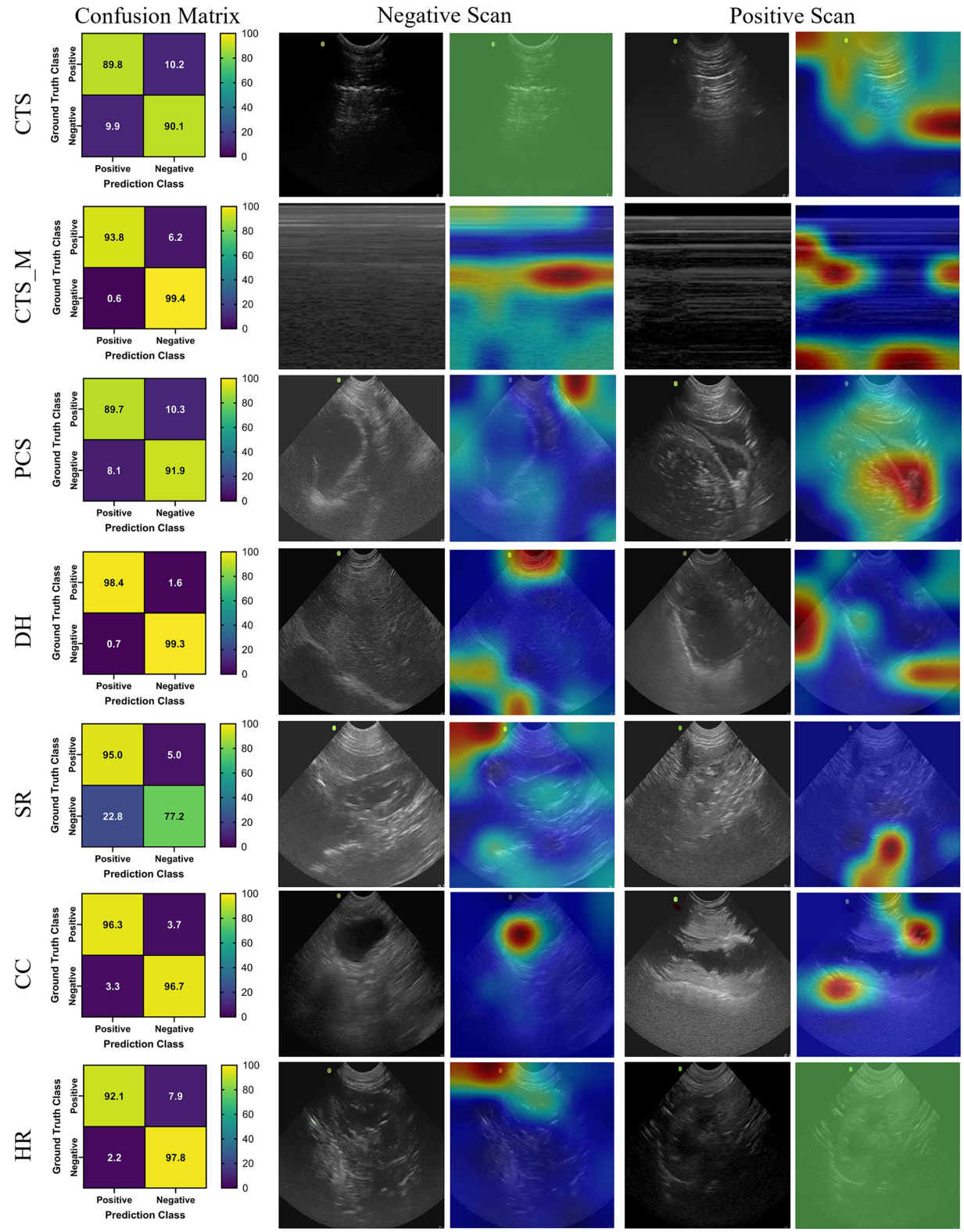

FIGURE 3
Prediction results by scan point for ShrapML. Results for each scan site showing (column 1) confusion matrix test prediction results, (column 2–3) negative and (column 4–5) positive representative images without and with the GradCAM overlay. Regions in the images with high relevance to model predictions have red-yellow overlays, while those of lower relevance have blue-green overlays.

shown in this work highlight how AI can be used for automating US detection of intrabdominal and intrathoracic injury detection for veterinary applications. Each scan point reached greater than 80% injury detection accuracy, with most surpassing 90% accuracy. However, more data is still needed to be able to ensure that the AI models are not overfitting the training data and can accurately predict for new subject data. Next steps for this work will expand training datasets so that blind subject testing is possible for confirming generalized models are developed. With more data, these models can be set up for real-time integration with ultrasound devices allowing for early detection of thoracic and abdominal injuries for military working dogs and other canine trauma situations. This will lower the skill threshold for medical imaging-based triage so that these techniques can be more widely used.

Data availability statement

The datasets presented in this article are not readily available because they have been collected and maintained in a government-controlled database that is located at the US Army Institute of Surgical Research. As such, this data can be made available through the development of a Cooperative Research & Development Agreement (CRADA) with the corresponding author. Requests to access the datasets should be directed to ES, eric.j.snider3.civ@health.mil.

Ethics statement

The animal study was approved by Research was conducted in compliance with the Animal Welfare Act, the implementing Animal Welfare regulations, and the principles of the Guide for the Care and Use for Laboratory Animals. The Institutional Animal Care and Use Committee at the Department of Defense Military Working Dog Veterinary Services approved all research conducted in this study. The facility where this research was conducted is fully accredited by the AAALAC International. The study was conducted in accordance with the local legislation and institutional requirements.

Author contributions

SH: Conceptualization, Data curation, Formal analysis, Methodology, Visualization, Writing – original draft, Writing – review & editing. LH: Data curation, Formal analysis, Methodology, Software, Writing – review & editing. TE: Funding acquisition, Writing – review & editing. EV: Writing – original draft, Methodology, Funding acquisition, Data curation, Conceptualization. ES: Conceptualization, Data curation, Formal analysis, Methodology, Writing – original draft, Writing – review & editing.

Funding

The author(s) declare that financial support was received for the research, authorship, and/or publication of this article. This work was funded through the Restoral program by the Defense Health Agency. This project was supported in part by an appointment to the Science Education Programs at National Institutes of Health (NIH), administered by ORAU through the U.S. Department of Energy Oak Ridge Institute for Science and Education (LH).

Acknowledgments

The authors would like to acknowledge Dr. Joanna Hourani, MAJ (Dr.) Richard Brooksby, and MAJ (Dr.) Erin Hennessey for their assistance with image capture in Military Working Dogs.

Conflict of interest

The authors declare that the research was conducted in the absence of any commercial or financial relationships that could be construed as a potential conflict of interest.

Publisher's note

Author disclaimer

The views expressed in this article are those of the authors and do not reflect the official policy or position of the U.S. Army Medical Department, Department of the Army, DOD, or the U.S. Government.

References

1. Boysen SR, Lisciandro GR. The use of ultrasound for dogs and cats in the emergency room: AFAST and TFAST. *Vet Clin North Am Small Anim Pract*. (2013) 43:773–97. doi: 10.1016/j.cvsm.2013.03.011

2. Cole L, Pivetta M, Humm K. Diagnostic accuracy of a lung ultrasound protocol (vet BLUE) for detection of pleural fluid, pneumothorax and lung pathology in dogs and cats. *J Small Anim Pract*. (2021) 62:178–86. doi: 10.1111/jsap.13271

3. Boatright K. (2020). Up your imaging game: The power of AFAST 52. Available at: https://www.dvm360.com/view/up-your-imaging-game-the-power-of-afast (Accessed January 5, 2024).

4. Lisciandro GR, Lisciandro SC. Global FAST for patient monitoring and staging in dogs and cats. *Vet Clin North Am Small Anim Pract*. (2021) 51:1315–33. doi: 10.1016/j.cvsm.2021.07.011

5. Green R. (2021). What do military working dogs do? *Am. Kennel Club* Available at: https://www.akc.org/expert-advice/news/what-are-military-working-dogs/ (Accessed January 5, 2024).

6. Edwards T, Scott LLF, Gonyeau KE, Howard EH, Parker JS, Hall K. Comparison of trauma sustained by civilian dogs and deployed military working dogs. *J Vet Emerg Crit Care (San Antonio)*. (2021) 31:498–507. doi: 10.1111/vec.13064

7. McGraw AL, Thomas TM. Military working dogs: an overview of veterinary Care of these Formidable Assets. *Vet Clin North Am Small Anim Pract*. (2021) 51:933–44. doi: 10.1016/j.cvsm.2021.04.010

8. Lagutchik M, Baker J, Balser J, Burghardt W, Enroth M, Flournoy S, et al. Trauma Management of Military Working Dogs. *Mil Med*. (2018) 183:180–9. doi: 10.1093/milmed/usy119

9. Townsend S, Lasher W. *The U.S. Army in multi-domain operations 2028*. Arlington, VA, USA: U.S. Army (2018).

10. Epstein A, Lim R, Johannigman J, Fox CJ, Inaba K, Vercruysse GA, et al. Putting medical boots on the ground: lessons from the war in Ukraine and applications for future conflict with near-peer adversaries. *J Am Coll Surg*. (2023) 237:364–73. doi: 10.1097/XCS.0000000000000707

11. Latif J., Xiao C., Imran A., Tu S. (2019). Medical imaging using machine learning and deep learning algorithms: a review, in 2019 2nd international conference on computing, mathematics and engineering technologies (iCoMET), (IEEE), 1–5.

12. Liu R, Rong Y, Peng Z. A review of medical artificial intelligence. *Glob Health J*. (2020) 4:42–5. doi: 10.1016/j.glohj.2020.04.002

13. Komatsu M, Sakai A, Dozen A, Shozu K, Yasutomi S, Machino H, et al. Towards clinical application of artificial intelligence in ultrasound imaging. *Biomedicines*. (2021) 9:720. doi: 10.3390/biomedicines9070720

14. Liu S, Wang Y, Yang X, Lei B, Liu L, Li SX, et al. Deep learning in medical ultrasound analysis: a review. *Engineering*. (2019) 5:261–75. doi: 10.1016/j.eng.2018.11.020

15. Chiang T-C, Huang Y-S, Chen R-T, Huang C-S, Chang R-F. Tumor detection in automated breast ultrasound using 3-D CNN and prioritized candidate aggregation. *IEEE Trans Med Imaging*. (2019) 38:240–9. doi: 10.1109/TMI.2018.2860257

16. Song D, Yao J, Jiang Y, Shi S, Cui C, Wang L, et al. A new xAI framework with feature explainability for tumors decision-making in ultrasound data: comparing with grad-CAM. *Comput Methods Prog Biomed*. (2023) 235:107527. doi: 10.1016/j.cmpb.2023.107527

17. Diaz-Escobar J, Ordóñez-Guillén NE, Villarreal-Reyes S, Galaviz-Mosqueda A, Kober V, Rivera-Rodriguez R, et al. Deep-learning based detection of COVID-19 using lung ultrasound imagery. *PLoS One*. (2021) 16:e0255886. doi: 10.1371/journal.pone.0255886

18. Gil-Rodríguez J, Pérez de Rojas J, Aranda-Laserna P, Benavente-Fernández A, Martos-Ruiz M, Peregrina-Rivas J-A, et al. Ultrasound findings of lung ultrasonography in COVID-19: a systematic review. *Eur J Radiol*. (2022) 148:110156. doi: 10.1016/j.ejrad.2022.110156

19. Baumgartner CF, Kamnitsas K, Matthew J, Fletcher TP, Smith S, Koch LM, et al. SonoNet: real-time detection and localisation of Fetal standard scan planes in freehand ultrasound. *IEEE Trans Med Imaging*. (2017) 36:2204–15. doi: 10.1109/TMI.2017.2712367

20. Iriani Sapitri A, Nurmaini S, Naufal Rachmatullah M, Tutuko B, Darmawahyuni A, Firdaus F, et al. Deep learning-based real time detection for cardiac objects with fetal ultrasound video. *Inform Med Unlocked*. (2023) 36:101150. doi: 10.1016/j.imu.2022.101150

21. Banzato T, Wodzinski M, Burti S, Osti VL, Rossoni V, Atzori M, et al. Automatic classification of canine thoracic radiographs using deep learning. *Sci Rep*. (2021) 11:3964. doi: 10.1038/s41598-021-83515-3

22. Müller TR, Solano M, Tsunemi MH. Accuracy of artificial intelligence software for the detection of confirmed pleural effusion in thoracic radiographs in dogs. *Vet Radiol Ultrasound*. (2022) 63:573–9. doi: 10.1111/vru.13089

23. Kim E, Fischetti AJ, Sreetharan P, Weltman JG, Fox PR. Comparison of artificial intelligence to the veterinary radiologist's diagnosis of canine cardiogenic pulmonary edema. *Vet Radiol Ultrasound*. (2022) 63:292–7. doi: 10.1111/vru.13062

24. Li S, Wang Z, Visser LC, Wisner ER, Cheng H. Pilot study: application of artificial intelligence for detecting left atrial enlargement on canine thoracic radiographs. *Vet Radiol Ultrasound*. (2020) 61:611–8. doi: 10.1111/vru.12901

25. McEvoy FJ, Proschowsky HF, Müller AV, Moorman L, Bender-Koch J, Svalastoga EL, et al. Deep transfer learning can be used for the detection of hip joints in pelvis radiographs and the classification of their hip dysplasia status. *Vet Radiol Ultrasound*. (2021) 62:387–93. doi: 10.1111/vru.12968

26. Boice EN, Hernandez-Torres SI, Snider EJ. Comparison of ultrasound image classifier deep learning algorithms for shrapnel detection. *J Imaging*. (2022) 8:140. doi: 10.3390/jimaging8050140

27. Snider EJ, Hernandez-Torres SI, Boice EN. An image classification deep-learning algorithm for shrapnel detection from ultrasound images. *Sci Rep*. (2022) 12:8427. doi: 10.1038/s41598-022-12367-2

28. Hernandez-Torres SI, Bedolla C, Berard D, Snider EJ. An extended focused assessment with sonography in trauma ultrasound tissue-mimicking phantom for developing automated diagnostic technologies. *Front Bioeng Biotechnol*. (2023) 11:1244616. doi: 10.3389/fbioe.2023.1244616

29. Xu Y., Noy A., Lin M., Qian Q., Li H., Jin R. (2020). Wemix: How to better utilize data augmentation. *arXiv preprint*. arXiv:2010.01267. Available at: https://arxiv.org/abs/2010.01267

30. Sandler M., Howard A., Zhu M., Zhmoginov A., Chen LC. (2018). Mobilenetv2: Inverted residuals and linear bottlenecks. In: *Proceedings of the IEEE conference on computer vision and pattern recognition*. IEEE publisher. 4510–4520. Available at: https://ieeexplore.ieee.org/abstract/document/8578572

31. Redmon J., Farhadi A. (2016). YOLO9000: Better, Faster, Stronger. *ArXiv161208242 Cs*. Available at: http://arxiv.org/abs/1612.08242 (Accessed April 22, 2022).

32. Selvaraju R. R., Cogswell M., Das A., Vedantam R., Parikh D., Batra D. (2017). Grad-cam: visual explanations from deep networks via gradient-based localization, in Proceedings of the IEEE international conference on computer vision, 618–626.

33. Hsu S-T, Su Y-J, Hung C-H, Chen M-J, Lu C-H, Kuo C-E. Automatic ovarian tumors recognition system based on ensemble convolutional neural network with ultrasound imaging. *BMC Med Inform Decis Mak*. (2022) 22:298. doi: 10.1186/s12911-022-02047-6

34. Yang J, Shi X, Wang B, Qiu W, Tian G, Wang X, et al. Ultrasound image classification of thyroid nodules based on deep learning. *Front Oncol*. (2022) 12:905955. doi: 10.3389/fonc.2022.905955

frontiers | Frontiers in Veterinary Science

TYPE Case Report
PUBLISHED 14 June 2024
DOI 10.3389/fvets.2024.1357626

OPEN ACCESS

EDITED BY
Mindaugas Tamosiunas,
University of Latvia, Latvia

REVIEWED BY
Ziwei Zhang,
Northeast Agricultural University, China
Xueyuan Hu,
Qingdao Agricultural University, China
Martin Ceballos,
University of Buenos Aires, Argentina

*CORRESPONDENCE
Tiezhu Chen
✉ cctzcd@126.com
Guangliang Shi
✉ shiguangliang@neau.edu.cn

†These authors have contributed equally to this work and share first authorship

RECEIVED 18 December 2023
ACCEPTED 16 May 2024
PUBLISHED 14 June 2024

CITATION
Shao B, Liu Y, Tai T, Liu Z, Han T, Yang Y, Fei S, Wang S, Wang H, Chen T and Shi G (2024) Case report: Diagnosis and surgical treatment of delayed traumatic diaphragmatic hernia with hepatothorax and enterothorax in a small dog.
Front. Vet. Sci. 11:1357626.
doi: 10.3389/fvets.2024.1357626

Case report: Diagnosis and surgical treatment of delayed traumatic diaphragmatic hernia with hepatothorax and enterothorax in a small dog

Bing Shao[1†], Yiding Liu[1†], Tiange Tai[1], Zhaoyang Liu[1], Tianyu Han[1], Yu Yang[1], Shanshan Fei[1], Shu Wang[1], Haibin Wang[1], Tiezhu Chen[2,3]* and Guangliang Shi[1]*

[1]Heilongjiang Northeast Agricultural University Animal Hospital Company Limited, College of Veterinary Medicine, Northeast Agricultural University, Harbin, China, [2]Sichuan Academy of Chinese Medicine Sciences, Chengdu, China, [3]Sichuan Provincial Key Laboratory of Quality and Innovation Research of Chinese Materia Medica, Chengdu, China

An 8-year-old castrated male teddy bear dog presented to our clinic with a persistent cough. The sick dog suffered from vehicular trauma 6 months prior to the visit and had imaging and exploratory laparotomy. Imaging and exploratory laparotomy at the time showed no significant damage. We performed contrast radiography (barium gavage) on the sick dog. Based on the results of a complete contrast radiography (barium gavage), tubular shadows in the thoracic cavity were identified as the small intestine and cecum, and delayed traumatic diaphragmatic hernia with hepatothorax and enterothorax was confirmed with radiographs. Accordingly, the sick dog underwent general anesthesia, manual ventilation and diaphragmatic herniorrhaphy by standard ventral midline abdominal approach. Postoperatively, the dog was given analgesia and antibacterial treatment, and the liver biochemical indexes were monitored to prevent endotoxin. Postoperative radiographs revealed clear contours of thoracic and abdominal organs. The dog moved, ate, and urinated normally within 10 days of the surgery. This case provides a reference for a complete barium meal imaging procedure that clearly shows the position of the organs in the thoracoabdominal cavity after the occurrence of a delayed traumatic diaphragmatic hernia. This paper provides a practical reference for the diagnosis of delayed traumatic diaphragmatic hernia with hepatothorax and enterothorax.

KEYWORDS

dog, delayed diaphragmatic hernia, X-ray, ultrasound examination, case report

1 Introduction

Diaphragmatic hernias, common in cats and dogs, can be congenital or traumatic. Congenital diaphragmatic hernia is characterized by a musculoskeletal defect, manifested as cracks in the diaphragm tendon or muscle portion, allowing abdominal organs to enter the chest cavity (1). This hernia is difficult to diagnose because small animals with congenital diaphragmatic hernia have almost no clinical symptoms, most often being an incidental finding during necropsy or diagnostic imaging (2). Traumatic diaphragmatic

hernias occur following blunt force trauma to the abdomen causing increased abdominal pressure. When this force is combined with an open glottis, the air-filled lungs deflate, causing an increased pressure gradient across the diaphragm. This sudden pressure change across the diaphragm causes it to rupture (3). Vehicular trauma are the most common cause of traumatic diaphragmatic hernia, which presents through varied clinical signs, with dyspnea being the most common (4).

Delayed diaphragmatic hernia is a long-term complication of an undetected diaphragmatic injury that occurs weeks or even years after an injury and is not accompanied by diaphragmatic hernia manifestations in the acute phase (5, 6). Delayed diaphragmatic hernia is less common and can present with varied symptoms, including cough, dyspnea, abdominal pain, diarrhea, vomiting, and in severe cases, respiratory failure or cardiopulmonary failure (7). Hepatothorax is the displacement of the liver into the thorax due to a traumatic rupture of the right diaphragm. The main clinical presentation is usually dyspnea and abdominal pain, but may also include cyanosis, arrhythmia, and hypotension. Surgical repair is the standard treatment for diaphragmatic hernia (8). The current standard treatment for diaphragmatic hernia repair in small animals is laparotomy and thoracotomy. The approach depended on the hemodynamic stability of the patients, and the preference and skills of the surgeon (9). In addition, when delayed diaphragmatic hernia occurs, if adhesions between visceras and chest is suspected, thoracotomy or combined thoracic-abdominal approach is preferred.

This report describes the clinical examination, imaging results, and surgical procedure for delayed traumatic diaphragmatic hernia with hepatothorax and enterothorax in an 8-year-old dog. The case underwent a comprehensive barium meal imaging examination, and for the first time the specific condition of the gastrointestinal tract in the thoracoabdominal cavity after the occurrence of delayed diaphragmatic hernia was carefully documented. The aim of this case report is to provide a reference for identifying and treating similar cases.

2 Case description

Teddy bear dog, a male (de-sexed), 8-year-old dog weighing 3.9 kg, was involved in a vehicular trauma 6 months prior to his presentation to our facility. The dog had undergone exploratory laparotomy at the time, and no apparent visceral damage was observed. Before coming to our hospital for treatment, the dog exhibited a severe cough for 1 month. The coughing was only temporarily relieved with azithromycin, but occasional coughing was still present.

The sick dog was in good mental condition, rectal temperature was 38.6°C, the heart rate was 104 beats/min, both forelimbs dilated outward, the chest was exposed, and the chest was sensitive to palpation and showed signs of pain. Blood routine examination showed no obvious abnormality. The platelet count was 541 10^9/L, which was beyond the normal range (the reference ranges: 117–490 10^9/L), indicative of chronic infection. Blood biochemical tests (Supplementary Figure S1) revealed that alkaline phosphatase (ALKP) was 317 U/L (the reference ranges: 20–150 U/L), which was more than twice the normal level, and alanine aminotransferase (ALT) was 1,012 U/L (the reference ranges: 10–118 U/L), which was nearly nine times the normal level, suggestive of liver damage.

Radiographs revealed a low-density tubular shadow in the thoracic cavity with a well-defined wall (Figures 1A,B). We chose the barium sulfate powder provided by the manufacturer, which was mixed with water to prepare a 60% w/v barium sulfate suspension (Barium Sulfate (Type II) for Suspension, Shandong Shengli Pharmaceutical Co., Ltd., China). The suspension was administered via an orogastric tube at a dose of 15 mL/kg (10). After 30 minutes, the dogs was examined by X-ray again, radiograph revealed that the tubular shadow in the chest cavity contains a large amount of barium sulfate suspension (Figures 1C,D). The sick dog was diagnosed with diaphragmatic hernia, and the small intestine entered the thoracic cavity through the hernia hole. Radiographs were taken 2 hours and 30 minutes after the oral gavages with barium, and barium deposits were seen in the cecum, which was located in the thoracic cavity, confirming the herniation of the cecum into the thoracic cavity (Figures 1E,F). At 4 hours and 30 minutes after the oral gavages with barium, radiographs of the chest of the sick dog in the dorsal, right and left positions was performed, and a small portion of the barium was observed in the cecum, but not the thoracic cavity. Furthermore, most of the barium went into the colon and rectum, which was located in the abdominal cavity (Figures 1G–I). Radiographs of the dorsal, right lateral and left lateral positions of the chest of the sick dog were taken 21 hours and 30 minutes after oral gavages with barium. The results showed that all the barium had moved to the colon and rectum, both of which were in the abdominal cavity (Figures 1J–L).

An ultrasound examination of the ventral side of the heart revealed soft tissue in the right hepatic lobe with myocardial diastolic obstruction and a small area of fluid between the myocardium and the soft tissue image, which further increased the suspicion of diaphragmatic hernia (Figure 2).

Since no abnormality was found 6 months prior when the dog was involved in an accident, a delayed traumatic diaphragmatic hernia was initially considered. Based on the clinical signs of the sick dog, combined with blood routine examination, blood biochemical examination, ultrasonic examination, and contrast radiography was performed. The results showed small intestine and cecum in the thoracic cavity, and ultrasound showed liver and fluid area on the ventral side of the heart. A further comprehensive analysis confirmed the presence of delayed traumatic diaphragmatic hernia with hepatothorax and enterothorax, and the contents of the hernia were the small intestine, cecum and liver.

Meloxicam (0.2 mg/kg SC, Metacam, Boehringer Ingelheim/Rhein Germany) and ceftiofur sodium (7 mg/kg IV, Woruite, YUANZHNG/China) were administered prior to surgery. Stabilization was initialized with oxygen supplementation by mask with a flow rate of 2 L/min. After induction with propofol (4 mg/kg IV, Propofol Injection, JIABO/China, 10 mg/mL), the patient was intubated with an endotracheal tube and maintained with

Abbreviations: ALT, Alanine aminotransferase; ALKP, Alkaline phosphatase; CREA, Creatinine; GGT, Gamma-glutamyltransferase.

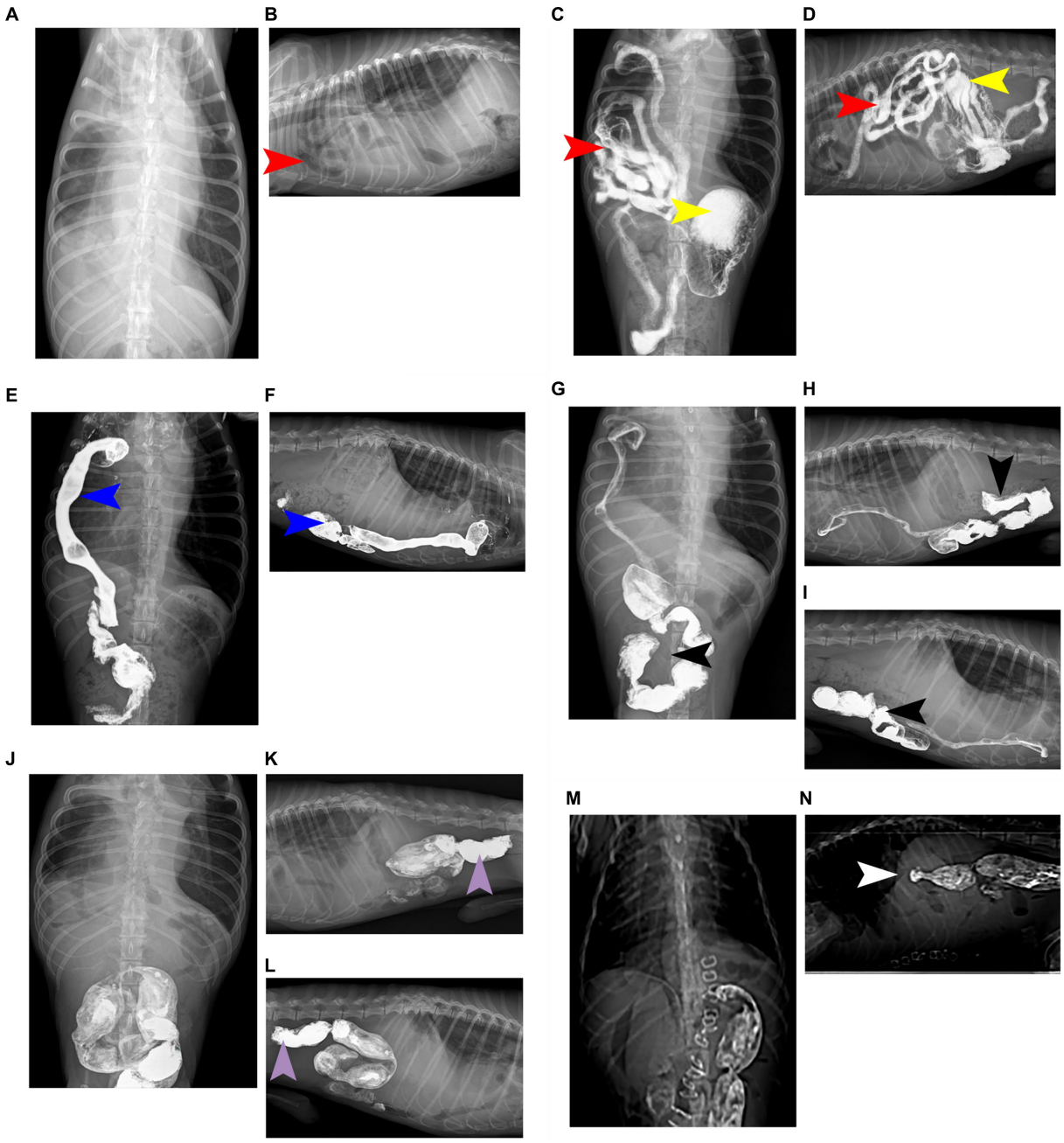

FIGURE 1
Complete barium meal contrast procedure. **(A)** Oral barium preprandial chest and abdominal dorsal radiographs showed abnormal shadows with uneven density and air-containing cavities in the chest. **(B)** Oral barium prepristine chest right position radiograph, showing a low-density tubular shadow in the chest cavity and a clear contour of the tube wall. **(C)** 30 minutes after oral barium meal, a chest and abdominal dorsum X-ray shows a large amount of barium meal deposition in the stomach, with some barium meal entering the small intestine, which is located in the right chest cavity. **(D)** 30 minutes after oral barium meal, the right chest X-ray shows the appearance of small intestine in the chest cavity, with barium meal deposition and high-density imaging. **(E)** After 2 hours and 30 minutes of oral barium meal, a chest abdominal and dorsal X-ray shows that the barium meal enters the cecum and is located in the right chest cavity, presenting high-density imaging. **(F)** On the right chest X-ray 2 hours and 30 minutes after oral barium meal, it can be seen that the barium meal enters the cecum and is located in the chest cavity, showing a high-density effect. **(G)** 4 hours and 30 minutes after oral barium meal, there is a small amount of barium meal located in the cecum, and most of the barium meal enters the colon and is located in the abdominal cavity, presenting high-density imaging. **(H)** On the right chest X-ray 4 hours and 30 minutes after oral barium meal, a large amount of barium meal can be seen entering the colon and located in the abdominal cavity. **(I)** On the left chest X-ray 4 hours and 30 minutes after oral barium meal, a large amount of barium meal can be seen entering the colon and located in the abdominal cavity. **(J)** 21 hours and 30 minutes after oral barium meal, there is no residual barium meal in the chest and intestines, and barium meal enters the colon and rectum, presenting high-density imaging. **(K)** 21 hours and 30 minutes after oral barium meal, on the right chest X-ray, it can be seen that there is no residual barium meal in the intestinal tract of the chest. The barium meal enters the colon and rectum, located in the abdominal cavity. **(L)** On the left chest X-ray 21 hours and 30 minutes after oral barium meal, it can be seen that there is no residual barium meal in the thoracic intestine. The barium meal enters the colon and rectum, located in the abdominal cavity. **(M)** Postoperative chest and abdominal dorsal radiograph, it can be seen that the chest cavity and abdominal organs have clear contours and obvious diaphragm. **(N)** Postoperative chest right radiograph, the chest cavity and abdominal organs are clearly contoured and the diaphragm line is obvious. The organ indicated by the red arrow is the small intestine; the organ indicated by the yellow arrow is the stomach; the organ indicated by the blue arrow is the cecum; the organ indicated by the black arrow is the colon; the organ indicated by the purple arrow is the rectum; and the part indicated by the white arrow is the diaphragm line.

isoflurane (Isoflurane, Ringpu/China) in oxygen. Lactated Ringer's solution was administered (10 mL/kg/h, IV) throughout anesthesia. The dog was moved to the operating room, positioned in dorsal recumbency, and connected to an anesthetic machine. The sick dog was mechanically ventilated by use of a respirator operated. The respiratory rate was adjusted to maintain an $ETCO_2$ of 35–45 mm Hg. Initial vaporizer setting was 1.5% isoflurane. Median expired isoflurane concentration was 1.2% during the surgery. Intermittent positive pressure ventilation was started. Minute ventilation was continuously monitored throughout anesthesia. A skin incision of approximately 8–10 cm was made along the midline of the abdomen posterior to the xiphoid prominence, and the subcutaneous tissue was separated to expose the abdominal cavity. Part of the liver and intestine could be seen, and an abnormal intestinal course was seen by running down the intestine. Further exploration revealed that part of the small intestine and liver lobe had entered the thoracic cavity, and a hernia hole were seen on the right diaphragm (Figure 3A). The abdominal wall retractor was used to prop up the abdominal cavity and expand the field of view. First, the intestine that had entered the thoracic cavity was slowly removed and retracted outside the body, followed by the move out of the liver. The liver lobe in the thoracic cavity was purplish-red, the hernia hole was visible at this stage (Figure 3B), and the diaphragm had a circular tear hole. A small amount of milky fluid was found in the thoracic cavity, which was absorbed with gauze. The thoracic cavity was flushed with warm saline, and the saline residue was aspirated with gauze. The thoracic and abdominal organs were examined for ischemia or other injuries. Each organ was intact before the hernia hole was closed and the ruptured diaphragm hole was repaired. Starting from the sternum, the hernia hole was closed with SIS (simple interrupted suture), and after the last stitch, a slit was left to insert an extension tube. The surgical assistant used a syringe to extract the residual liquid and gas in the chest cavity to restore the negative pressure in this cavity to prevent the occurrence of postoperative complications similar to pulmonary atelectasis and pulmonary atrophy. The intestine and liver were reset, and the abdominal cavity was closed. Postoperative chest plain radiograph results showed good diaphragm continuity, and no abdominal organs, such as the intestine and liver, were seen in the thoracic cavity (Figures 1M,N). Care was focused on protecting the liver, replenishing energy, protein, and electrolytes, maintaining acid–base balance in the body, preventing antibacterial infection, pain relief, and modulating inflammation. Postoperatively, the dog was treated with intravenous maintenance fluids (2 mL/kg/h; NaCl 0.9%, Braun). Postoperative analgesia was provided with a constant rate infusion of lidocaine (2 mg/kg/h, Lidor, Richter Pharma) IV. Meloxicam 0.1 mg/kg SC q24h (Metacam, Boehringer Ingelheim), and ceftiofur sodium (7 mg/kg IV q8h, Woruite, YUANZHNG/China) were administered during recovery.

After 4 days of continuous administration (include analgesia and antimicrobial therapy), the dog fed normally and had normal bowel movements and normal urination. There was a painful reaction during deep palpation in the sick dog. PLR test was positive. However, the dog was in good mental condition on day 10 after the operation and moved, ate, and urinated normally.

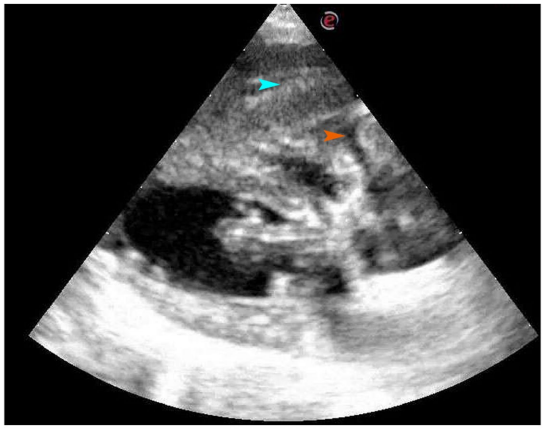

FIGURE 2
Four-chamber view of long axis of right sternum. On the ventral side of the heart, there is a soft tissue mass, which is the right liver lobe, and a small amount of liquid area can be seen between the myocardium and the soft tissue image. The organ indicated by the blue arrow is the liver, while the part indicated by the orange arrow is fluid accumulation.

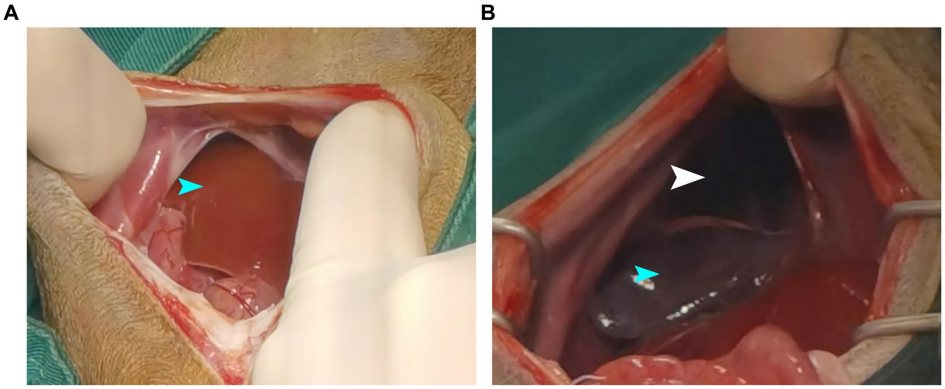

FIGURE 3
Showing intraoperative findings. **(A)** Liver and intestinal herniation into the chest cavity. **(B)** The liver lobes are purplish-red and hernia holes are visible. The organ indicated by the blue arrow is the liver, while the part indicated by the white arrow is the hernia.

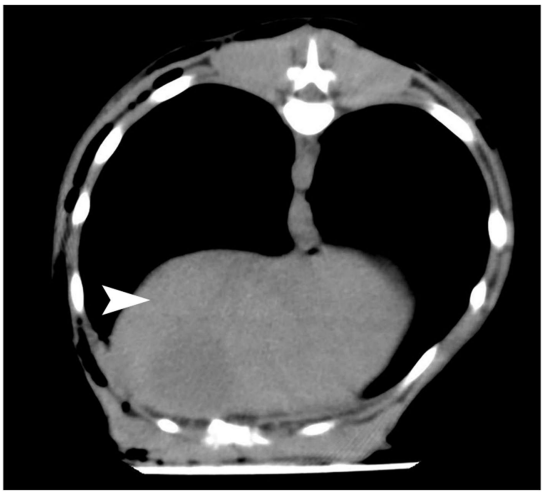

FIGURE 4
CT results after a vehicular trauma in October 2022.The diaphragm was seen to be in good continuity from the CT images with no obvious damage. The part indicated by the white arrow is the diaphragm.

3 Discussion

The present case report presents a case of a diaphragmatic hernia in a dog after a vehicular trauma. Diaphragmatic hernia is most commonly seen in the pleural and refers to the protrusion of abdominal visceral organs into the thoracic cavity through a natural or traumatic diaphragmatic fissure. The clinical manifestations of delayed diaphragmatic hernia are not specific (11), but include (1) delayed rupture of the diaphragm, partial rupture of the diaphragm in the acute phase, or complete rupture of the diaphragm due to pressure difference in the thoracoabdominal cavity or local infection of the diaphragm; (2) chronic diaphragmatic hernias: the rupture in the diaphragm is small, and the abdominal organs herniate gradually and slowly; (3) missed diagnosis of diaphragmatic rupture arising from lack of consultation in the acute phase, lack of imaging examination, or missing out on no abnormalities in imaging findings (12). The last scenario is what was witnessed in this report, in which no obvious diaphragmatic rupture was ever seen in the chest CT examination after a vehicular trauma (Figure 4). It was not until 6 months later that the dog began to cough frequently, but there were no other clinical symptoms. It has been suggested that in traumatic diaphragmatic hernia, the site of diaphragmatic hernia is more common on the left side for the following reasons: firstly, the left side of the diaphragm is relatively weaker than the right side, and this is related to the good fusion of the right diaphragm during embryonic development; secondly, the right diaphragm is cushioned by the liver during external impact (13), which minimizes the risk of tear. Thus, the location of diaphragmatic rupture is related to both the location of the external impact and the position of the dog at the time of impact (14). The organs that herniate depend on the location of the diaphragm rupture, and the herniation varies with the organs involved. Right-sided diaphragm rupture often results in the herniation of the small intestine and pancreas, while left-sided diaphragm rupture often results in the herniation of the stomach, small intestine, and spleen (15). The clinical symptoms of traumatic diaphragmatic hernia are mainly related to the displacement of internal organs and manifest in three areas: the lung, heart, and gastrointestinal tract. Furthermore, they mainly involve, dyspnea, pain in the abdomen, and cyanosis of the conjunctiva, mouth, and tongue. In the case of delayed diaphragmatic hernia, the most important thing is to confirm the diagnosis as early as possible and perform the surgery in time, which will help in the postoperative recovery (16).

Diagnosis of diaphragmatic hernia is mainly performed by conventional X-ray, contrast radiography (barium gavage) and ultrasonography (17). Chest radiograph may show the disappearance of the diaphragmatic outline, fluid or air-filled organs in the thoracic cavity, as well as the disappearance of normal lung fields, and an abdominal radiograph may show the absence of abdominal organs (15). In the present case, X-ray and echocardiography were used to confirm the diagnosis. The sick dog underwent a 24-h contrast radiography (barium gavage) examination, which fully and clearly displayed the gastrointestinal condition of the sick dog. Before administration of barium sulfate suspension through orogastric tube, chest radiograph showed low-density tubular shadows in the chest cavity. In order to further diagnose and understand the patient's condition in detail, a contrast radiography (barium gavage) examination was performed. The results showed that some small intestine and cecum entered the chest cavity, which was consistent with the X-ray examination of the above diaphragmatic hernia. The echocardiographic findings showed soft tissue images and a small amount of fluid on the ventral side of the heart, while laboratory findings showed elevated ALT, which is mainly secreted hepatocytes. Damage to hepatocytes or a change in the permeability of hepatocytes' membranes due to liver disease causes an increase in the blood ALT level, and the level of ALT increase is proportional to the liver damage (18). Thus, a high ALT level is a specific indicator for hepatocyte damage. Based on the normal CT examination results of the dog after the vehicular trauma last year, the comprehensive diagnosis is delayed right diaphragmatic rupture in the dog. The normal physiological functions of the lungs and heart are affected by the compression of the liver and intestines, resulting in respiratory symptoms, including the inability of the heart to fully dilate, resulting in reduced blood supply, exercise intolerance, and decreased stamina. In the present study, the right lobe of liver entered the thoracic cavity through a hernia. The right lobe of liver had a right hepatic vein on it, affecting blood circulation. However, no other liver abnormality indices were explored. Combined with the purplish-red coloration of the right inner lobe of the liver, the elevated ALT was considered to be caused by blood circulation disorders, and the liver function had to be monitored at a later stage to prevent the production of endotoxins (19). Slight congestion due to blood circulation disorders was observed in the intestines. In the clinical field of small animals, barium sulfate has always been considered an important tool for diagnosing gastrointestinal diseases. Barium sulfate should be avoided in certain diseases, such as gastrointestinal perforation (20). If the integrity of the gastrointestinal tract is poor, it can lead to barium peritonitis. Its clinical symptoms include abdominal palpation pain, vomiting, anorexia, drowsiness, hypotension, shortness of breath, and abdominal distension. And it can lead to some special complications, such as hypovolemia, hypoalbuminemia, severe peritonitis, multiple abdominal adhesions and granulomas, increasing the mortality rate of secondary diffuse hemorrhagic peritonitis. Barium peritonitis has a poor prognosis and a higher mortality rate than systemic sepsis

peritonitis. In experimental studies, once barium sulfate is mixed with gastrointestinal contents in the abdominal cavity, the mortality rate within 24 h is 100% (21). In this case, during the clinical examination of the sick dog, no gastrointestinal symptoms such as abdominal pain or vomiting were observed, and no fluid accumulation was found on the abdominal ultrasound examination. Therefore, the possibility of gastrointestinal perforation can be ruled out. Therefore, we consider using contrast radiography (barium gavage) for clinical examination.

Treatment modalities for diaphragmatic hernia mainly include conservative and surgical treatments. Some studies have shown that surgery is mostly considered for young dogs, while most dogs considered for conservative treatment are usually not fit for surgery due to lack of obvious clinical manifestations or suffering from other diseases (22). The main accesses for diaphragmatic rupture repair include laparotomy, thoracotomy, combined thoracic-abdominal approach, and single paracostal approach. Most diaphragmatic hernias are corrected through laparotomy, which does not require consideration of the location of the diaphragmatic tear and the need for a wider field of view. The single paracostal approach is more difficult but is suitable for exposing the field of view of the dorsal diaphragmatic tear (14). The case was treated with laparotomy for diaphragmatic hernia. Therefore, the sick dog need preoperative oxygenation to improve blood oxygen concentration and ensure cardiopulmonary function. During surgery, attention should be paid to the heartbeat and blood oxygen concentration. Maintaining good mechanical ventilation and oxygenation, avoiding hypercapnia, preventing reexpansion pulmonary edema (23), and replenishing fluids and energy intravenously are recommended. The liver should be handled carefully because it is brittle and easily damaged. Before closing the hernia hole, the gas in the thoracic cavity should be aspirated with an extension tube connected to a syringe to restore the negative pressure in the thoracic cavity.

In conclusion, we reported a case of a dog with a delayed traumatic diaphragmatic hernia. According to the timeline (Supplementary Figure S2), no significant abnormality had been detected through imaging after a vehicular trauma, but the dog developed frequent coughing 6 months later. The hernia presenting with hepatothorax and enterothorax was detected through ultrasonography, X-ray, and contrast radiography (barium gavage). The hernia was corrected by suturing the ruptured diaphragm. The dog received excellent postoperative care and eventually recovered. This study provides complete contrast radiography (barium gavage) results and provides a valuable reference for the diagnosis and treatment of delayed traumatic diaphragmatic hernia.

Data availability statement

The original contributions presented in the study are included in the article/Supplementary material, further inquiries can be directed to the corresponding authors.

Ethics statement

Ethical approval was not required for the studies involving animals in accordance with the local legislation and institutional requirements because ethical approval was not required for the study because the case report is a description of a clinical case. Written informed consent was obtained from the owners for the participation of their animals in this study.

Author contributions

BS: Writing – original draft, Writing – review & editing, Methodology, Conceptualization. YL: Writing – review & editing, Writing – original draft, Software, Methodology, Formal analysis, Data curation, Conceptualization. TT: Writing – original draft, Conceptualization. ZL: Writing – original draft, Conceptualization. TH: Writing – original draft, Methodology. YY: Writing – original draft, Data curation. SF: Writing – original draft, Software. SW: Writing – original draft, Methodology. HW: Writing – original draft, Conceptualization. TC: Writing – review & editing, Writing – original draft, Conceptualization. GS: Methodology, Conceptualization, Writing – review & editing, Writing – original draft.

Funding

The author(s) declare that financial support was received for the research, authorship, and/or publication of this article. This research was funded by the "Academic Backbone" Project of Northeast Agricultural University (20XG32), Sichuan Provincial Key Laboratory of Quality and Innovation Research of Chinese Materia Medica (Z-2023N-6), and Preclinical Substitution of Veterinary Chinese Herbal Medicine Huanglian Joint Research and Development (FKHT-202308–0004).

Conflict of interest

The authors declare that the research was conducted in the absence of any commercial or financial relationships that could be construed as a potential conflict of interest.

The reviewer ZZ declared a shared affiliation with the authors BS, YL, TT, ZL, TH, YY, SF, SW, HW, and GS to the handling editor at the time of review.

Publisher's note

Supplementary material

The Supplementary material for this article can be found online at: https://www.frontiersin.org/articles/10.3389/fvets.2024.1357626/full#supplementary-material

References

1. Tăbăran AF, Nagy AL, Cătoi C, Morar I, Tăbăran A, Mihaiu M, et al. Congenital diaphragmatic hernia with concurrent aplasia of the pericardium in a foal. *BMC Vet Res*. (2015) 11:309. doi: 10.1186/s12917-015-0623-2

2. Bai T. X-ray diagnosis of 6 cases of diaphragmatic hernia in dogs. *Chin J Vet Med*. (2013) 49:65–6.

3. Xiao YY, Teng T, Liu LK, Xu MY, Wang H, Li GH, et al. Diagnosis and treatment of a case of traumatic diaphragmatic hernia in a dog. *J Anim Sci Vet Med*. (2021) 40:86–9.

4. Legallet C, Thieman Mankin K, Selmic LE. Prognostic indicators for perioperative survival after diaphragmatic herniorrhaphy in cats and dogs: 96 cases (2001-2013). *BMC Vet Res*. (2017) 13:16. doi: 10.1186/s12917-016-0926-y

5. Zhang YL, Su ZY, Jiang TS, Xin Z. Treatment of delayed traumatic diaphragmatic hernia and review of the literature. *Chin J Thorac Cardiovasc Surg*. (2017) 24:324–6.

6. Abdellatif W, Chow B, Hamid S, Khorshed D, Khosa F, Nicolaou S, et al. Unravelling the mysteries of traumatic diaphragmatic injury: an up-to-date review. *Can Assoc Radiol J*. (2020) 71:313–21. doi: 10.1177/0846537120905133

7. Song IH. Tension gastrothorax in late-onset congenital diaphragmatic hernia, a rare but life-threatening condition: a case report. *Medicine*. (2021) 100:e24815. doi: 10.1097/MD.0000000000024815

8. Guner A, Bekar Y, Kece C, Kahraman I, Sezer C, Reis E. Delayed enterothorax and hepatothorax due to missed right-sided traumatic diaphragmatic rupture. *Am J Emerg Med*. (2012) 30:263.e7–263.e10. doi: 10.1016/j.ajem.2010.11.016

9. Furák J, Athanassiadi K. Diaphragm and transdiaphragmatic injuries. *J Thorac Dis*. (2019) 11:S152–7. doi: 10.21037/jtd.2018.10.76

10. Shaikh L, Sharma A, Secrest S. Imaging diagnosis–duodenobiliary reflux of barium sulfate during esophagogastrography in a dog. *Vet Radiol Ultrasound*. (2015) 56:E36–9. doi: 10.1111/vru.12190

11. Alsuwayj AH, Al Nasser AH, Al Dehailan AM, Alburayman AZ, Alhuwaiji KA, Binsifran KF, et al. Giant traumatic diaphragmatic hernia: a report of delayed presentation. *Cureus*. (2021) 13:e20315. doi: 10.7759/cureus.20315

12. Yang JG, Li ZP, Yang T. A case of giant delayed diaphragmatic hernia. *J Rare Uncom Dis*. (2016) 23:23+9.

13. Feng SM, Chen HL. A case of traumatic delayed diaphragmatic hernia forensically identified. *Med Jurisprud*. (2020) 12:92–3.

14. O'Byrne KL, Smalle T, Ryan SD. Repair of a delayed, traumatic dorsal diaphragmatic hernia using a single paracostal approach in a dog. *N Z Vet J*. (2021) 70:55–62. doi: 10.1080/00480169.2021.1963873

15. Hoddinott K. Traumatic diaphragmatic hernia in a 5-month-old boxer dog. *Can Vet J*. (2013) 54:507–9.

16. Ban CP, Cheng R, Zhang XQ, Huang YQ, Li XM, Liang GQ, et al. Diagnosis and treatment of a case of diaphragmatic hernia in a dog. *J Anhui Agric Sci*. (2019) 47:98–100. doi: 10.1017/9781108668736.023

17. Campanile D, Cafaro M, Paci S, Panarese M, Sparapano G, Masi M, et al. Evidence of pneumopericardium after elective ovariectomy in a peritoneopericardial diaphragmatic hernia-affected dog: a case report. *Animals*. (2024) 14:633–42. doi: 10.3390/ani14040633

18. Wang AQ. *Establishment of canine liver injury model and ultrasonic imaging in the evaluation research of liver damage*. [Master's thesis]. Yanbian: Yanbian University (2022).

19. Zhang ZY, He MY, Xie Y, Peng X. Diagnosis and treatment of a case of chronic diaphragmatic hernia in a dog. *Anim Poult Indust*. (2020) 31:125–6.

20. Czajkowski PS, Fryer KJ. Colonic torsion in 4 great Danes. *Vet Emerg Crit Care*. (2020) 30:581–6. doi: 10.1111/vec.12986

21. Ko JJ, Mann FA. Barium peritonitis in small animals. *Vet Med Sci*. (2014) 76:621–8. doi: 10.1292/jvms.13-0220

22. Morgan KRS, Singh A, Giuffrida MA, Balsa IM, Hayes G, Chu ML, et al. Outcome after surgical and conservative treatments of canine peritoneopericardial diaphragmatic hernia: a multi-institutional study of 128 dogs. *Vet Surg*. (2020) 49:138–45. doi: 10.1111/vsu.13360

23. Melis SM, de Rooster H, Waelbers T, Polis I. Anesthesia case of the month. Diaphragmatic herniation. *J Am Vet Med Assoc*. (2014) 245:1230–4. doi: 10.2460/javma.245.11.1230

frontiers | Frontiers in Veterinary Science

TYPE Original Research
PUBLISHED 31 July 2024
DOI 10.3389/fvets.2024.1392504

OPEN ACCESS

EDITED BY
Sibylle Maria Kneissl,
University of Veterinary Medicine Vienna, Austria

REVIEWED BY
Floryne Ottilie Buishand,
Royal Veterinary College (RVC), United Kingdom
Carlos Alberto Antunes Viegas,
University of Trás-os-Montes and Alto Douro, Portugal

*CORRESPONDENCE
Michelle L. Oblak
✉ moblak@uoguelph.ca

RECEIVED 27 February 2024
ACCEPTED 11 July 2024
PUBLISHED 31 July 2024

CITATION
Ram AS, Matuszewska K, McKenna C, Petrik J and Oblak ML (2024) Validation of a semi-quantitative scoring system and workflow for analysis of fluorescence quantification in companion animals. *Front. Vet. Sci.* 11:1392504. doi: 10.3389/fvets.2024.1392504

Validation of a semi-quantitative scoring system and workflow for analysis of fluorescence quantification in companion animals

Ann S. Ram[1], Kathy Matuszewska[1], Charly McKenna[2], Jim Petrik[1] and Michelle L. Oblak[2]*

[1]Department of Biomedical Sciences, University of Guelph, Guelph, ON, Canada, [2]Department of Clinical Studies, University of Guelph, Guelph, ON, Canada

Significance: Many commercially available near-infrared (NIR) fluorescence imaging systems lack algorithms for real-time quantifiable fluorescence data. Creation of a workflow for clinical assessment and *post hoc* analysis may provide clinical researchers with a method for intraoperative fluorescence quantification to improve objective outcome measures.

Aim: Scoring systems and verified image analysis are employed to determine the amount and intensity of fluorescence within surgical specimens both intra and postoperatively.

Approach: Lymph nodes from canine cancer patients were obtained during lymph node extirpation following peritumoral injection of indocyanine green (ICG). First, a semi-quantitative assessment of surface fluorescence was evaluated. Images obtained with a NIR exoscope were analysed to determine fluorescence thresholds and measure fluorescence amount and intensity.

Results: *Post hoc* fluorescence quantification (threshold of Hue = 165–180, Intensity = 30–255) displayed strong agreement with semi-quantitative scoring ($k = 0.9734$, $p < 0.0001$). Fluorescence intensity with either threshold of 35–255 or 45–255 were significant predictors of fluorescence and had high sensitivity and specificity ($p < 0.05$). Fluorescence intensity and quantification had a strong association ($p < 0.001$).

Conclusion: The validation of the semi-quantitative scoring system by image analysis provides a method for objective *in situ* observation of tissue fluorescence. The utilization of thresholding for ICG fluorescence intensity allows *post hoc* quantification of fluorescence when not built into the imaging system.

KEYWORDS

indocyanine green, fluorescence-guided surgery, NIR imaging, canine cancer, sentinel lymph node (SLN) mapping

1 Introduction

Indocyanine green (ICG) is a frequently reported fluorescent agent utilized for intraoperative sentinel lymph node (SLN) mapping and tumor bed imaging (1–3) due to its high signal-to-background ratio (SBR), low autofluorescence in tissue, nontoxicity, and accessibility (4, 5). With an excitation peak of 780 nm and an emission peak of 820 nm, ICG is a fluorescent near-infrared (NIR) tracer within the NIR spectrum (4–6). This tracer is non-specific and, when injected intravenously, binds readily to intravascular plasma proteins (4, 7), whereas peritumorally injected ICG will interact with proteins in the lymph (8). Near-infrared fluorescence imaging with ICG provides improved resolution in SLN mapping procedures compared to radioisotopes, blue dyes or the combination of radiocolloids and visible dyes traditionally used in veterinary medicine (4, 9). While ICG is commonly used in human medicine, ICG-NIR is viewed as an emerging technology in veterinary medicine, gaining traction in companion animal patients for oncologic surgeries as well as many other applications.

Various NIR imaging systems are used in tandem with ICG, each resulting in differing NIR light depth of penetration (3, 4, 10–16). A limited number of clinically approved imaging systems have built-in fluorescence quantification algorithms and processing with arbitrary units, including SPY Elite (Novadaq Technologies, Waterloo, Canada), EleVision IR (Medtronic, Dublin, Ireland) and IC-View (Pulsion Medical Systems AG, Munich, Germany) (17–20). Other approved open-surgery imaging systems including Photodynamic Eye or PDE Neo (PDE, Hamamatsu Photonics K. K., Honshu, Japan), FLARE (Curadel, Massachusetts, United States), Fluobeam (Fluoptics, Grenoble, France), and VITOM II ICG (Karl Storz, Tuttlingen, Germany); do not have the ability to quantify fluorescence *in situ* or *ex vivo* (17). The challenge in fluorescence-guided surgery is the lack of built-in fluorescence quantification or intensity algorithms as this limits the ability to objectively compare fluorescence intensity between procedures and therefore hinders a researcher's ability to efficiently compare surgical techniques, accurately assess fluorophores and develop protocols for clinical research and practice (21). Therefore, there is a need to provide imaging procedures with standardized methods for the quantification of fluorescence in order to advance future research (21–23). Furthermore, researchers and clinicians lack methods for real-time quantification of fluorescence and resort to subjective reporting of the presence or absence of fluorescence (24–28) which impairs the ability to make strong scientific conclusions (21). Image analysis protocols for fluorescence are also catered towards fixed tissues and cells that utilize standard immunofluorescence and microscopy (29, 30). Currently, reporting standards for fluorescence-guided surgical specimens recommend SBR to quantify fluorescence (21), however, protocols vary depending on imaging system, tracer and specimen type. Additionally, with the commonality of equipment in human and veterinary medicine and the similarity of naturally occurring diseases between species, there is cross-over potential in applying these analysis methods. Therefore, it is important to provide defined protocols when assessing fluorescence to limit bias and increase reproducibility (21).

This study aims to provide a simple, validated intraoperative semi-quantitative method to evaluate fluorescence. We hypothesize that a scoring system would benefit researchers and clinicians when built-in quantification algorithms or post-hoc analysis are unavailable. This study also depicts optimized parameters within image analysis to assess fluorescence amount and intensity in lymph nodes. We postulate that this will assist in the standardization of the analysis process when evaluating whole tissue specimens.

2 Materials and methods

Lymph nodes were obtained prospectively from 17 canine patients with naturally occurring cancer enrolled in a study involving complete regional lymph node bed extirpation for comparison with ICG SLN mapping techniques at the Ontario Veterinary College Health Sciences Centre from 2018 to 2019 (AUP 3606-008R). For each patient, pharmaceutical grade ICG (IC-Green, NDC 17478–701-02, Akorn, Illinois, United States) was reconstituted according to label instructions. All dogs had a 1 mL (0.25 mg/mL) ICG solution injected peritumorally. All lymph nodes in the basin, positive or negative for fluorescence, were removed during routine regional lymph node extirpation.

2.1 Proposal of a semi-quantitative scoring system for lymph node imaging

The VITOM II ICG system ($\lambda_{excitation} = 805$ nm, $\lambda_{emission} = 835$ nm) consists of a telescope connected to a SPIES 3-chip high-definition IMAGE1 S camera head with Karl Storz NIR/ICG camera (27, 28). Using the VITOM II ICG system, fluorescence appears as blue on the monitor. The imaging system was fixed above a table with an articulating stand positioned perpendicular focal distance of 20 cm from the specimen. Fluorescence scores were assigned as follows: 0 = no fluorescence, 1+ = 1–25% of the node surface fluorescent, 2+ = 26–50% fluorescent, 3+ = 51–75% fluorescent, and 4+ = 76–100% fluorescent. Lymph nodes were imaged in a standardized manner using a white background and consistent height parameters (26). Images from the VITOM II ICG were formatted with pseudo-colored blue fluorescence and raw images (grayscale) were not available from this system. Scoring was performed intraoperatively and 1-h after lymph node extirpation. The surgeon (MO) determined visual fluorescence status (positive or negative) and assigned a score immediately following removal of the lymph node. Within 1 h of extirpation, all lymph nodes, whether positive or negative, were assessed by a blinded investigator (SR) and assigned an *ex vivo* fluorescence score using the same scoring system. At the same time as scoring (28), still fluorescent images were obtained of both sides of each lymph node and saved for future assessment. The postoperative *ex vivo* score was given to both sides of the lymph node by a blinded investigator and the scored side with the clearest visible fluorescence and minimum fat tissue was used for analysis.

2.2 Validation of semi-quantitative scoring system

Intraoperative scores and blinded postoperative scores were evaluated for further analysis of agreement at least 4 weeks following surgery to assess scoring based on *ex vivo* images. Images of each lymph node were assigned a number and randomized for evaluation

and image analysis. Each image was assigned into 4 groups of 21, consisting of 83 images analyzed in total, which was done with a random set generator (GraphPad Randomizer, California, United States). One of the groups has only 20 images due to the uneven number of total images analyzed. Two investigators, blinded to the original findings, then assessed the amount of surface fluorescence in each image and assigned a score as described above.

2.3 Verification of image analysis method

The image analysis process was verified with positive and negative controls. Negative controls ($n = 5$) were lymph nodes with no exposure to ICG, previously collected from canine patients. Positive controls ($n = 18$) were lymph nodes that scored 4+ on the semiquantitative scale. These controls were used to set the hue and intensity histogram in an image analysis software (MetaMorph®) (31). The set of lymph nodes used as positive controls for fluorescence was based on the totality of the fluorescence signal on the surface of the lymph node and brightness depicting unambiguous results. Using principles from fluorescence microscopy analysis, rigor and reproducibility were introduced into the analysis process (32). Controls for autofluorescence were accounted for by using clean white backgrounds and thresholding strictly (31, 32). To avoid introducing bias and subjectivity, saturation was not adjusted for the intensity and surface fluorescence analysis. Surface area of fluorescence was modeled after SBR where fluorescence signal is divided against background signal (32, 33). Signal acquisition was validated by color thresholding that distinguished the fluorescent area from the non-fluorescent areas of the lymph node. Signals outside the specified threshold were excluded from the analysis. Average fluorescence intensity (FI), the amount of light emitted, was automatically calculated by the image analysis software based on set threshold parameters. Typically, FI measures account for background noise; however, the standardized imaging conditions prevented any background signal. This was validated in image analysis where background FI was consistently 0 across all images and compared to max intensity (33).

2.4 Quantification of surface fluorescence signal using image analysis

Randomized images of the clearest visible fluorescence and minimum fat tissue were processed and analyzed in MetaMorph (Molecular Devices, California, United States). Images were cropped and a Median Filter was applied. A Region of Interest (ROI) was drawn manually around the whole lymph node. Using the "Color Threshold" function, two threshold settings (A and B) were applied to every image. The hue and intensity of pixels were measured with a range of 0 to 255. Threshold A performed analysis using the following settings: Hue = 165–180 and Intensity = 30–255. Threshold B performed analysis using the following settings: Hue = 165–180 and Intensity = 45–255. Saturation was not altered in any of the images. The area of the lymph node ROI and the area of the detected signal in the measure of pixels were generated by the program. A percentage of the threshold signal in the ROI was used to measure the amount of fluorescence detected and calculated automatically by the software depicted by Eq. (1).

$$Amount\ of\ surface\ fluorescence = \frac{area\ of\ signal\ detected}{area\ of\ lymph\ node} \times 100 \quad (1)$$

2.5 Quantification of fluorescence intensity using image analysis

Images the clearest visible fluorescence and minimum fat tissue were analyzed in tandem with the previous analysis (2.4). As previously described, a ROI of the surface image of one side of the lymph node was generated. For the background ROI, a uniform circle near the lymph node was used. The same circle (area = 5,806 pixels) was used for all images. The "Color Threshold" function was used and three threshold settings (1–3) were applied for intensity. Hue was kept consistent for all three threshold settings at 165–180. Threshold 1 intensity was 30–255, Threshold 2 intensity was 35–255, and Threshold 3 intensity was 45–255. Since 24-bit color images were analyzed, the output was configured to a "Blue" color channel and "threshold for intensity measurements" was selected to only include the gray value intensities within the specified threshold range. For each ROI, the average FI was obtained as a grayscale value (arbitrary units, AU) and calculated by the software using Eq. (2). Intensity measurement terms are used to describe and quantify grayscale intensity (pixel brightness) values.

$$Average\ fluorescence intensity = \left(\frac{\sum Gray\ value}{Number\ of\ pixels}\right) - Background\ signal \quad (2)$$

2.6 Statistical analysis

Statistical analyses were completed using commercially available software SAS 9.4 (SAS Institute Inc., Cary, NC) by a biostatistician (G.M.) who was blinded to the specimen collection and assessment process. The percentage of fluorescence on the surface of the lymph nodes was not normally distributed, therefore a non-parametric Wilcoxan-Mann–Whitney was used to compare the differences between the values from Threshold A and Threshold B. Cohen's weighted kappa and simple kappa (k) statistics were used to assess the concordance of semi-quantitative scoring, surface fluorescence analysis, fluorescence status, and inter- and intraobserver agreement. Weighted kappa and simple kappa coefficients with 95% confidence intervals (CI) were calculated to determine the strength of agreement. Kappa coefficients that fell within 0.21–0.40 were interpreted as fair agreement, 0.41–0.60 as moderate agreement, 0.61–0.80 as substantial agreement, and 0.81–1 as almost perfect agreement (34). A non-parametric Friedman test was applied to compare the average intensity values for Threshold 1, 2, and 3. Logistic regressions were used to generate the empirical receiver operating curve (ROC) of sensitivity and 1-specificity for all three FI thresholds in the data set. The ROC provided an optimal predicted probability cut-off for these intensity thresholds. The area under the ROC curve (AUC) is the average sensitivity of the thresholds over the range of specificities to

represent the overall performance of the continuous threshold variable. Spearman rank-order correlation was used to measure the strength of monotonic relationship between average FI and surface amount of fluorescence. The r^2 value in this test indicates the strength of a relationship between two sets of data; as r^2 values become closer to 1, the stronger the relationship. Statistical significance was set at a two-sided *p*-value less than 0.05.

3 Results

A total of 87 lymph nodes were collected from 17 dogs with naturally occurring cancer and included in the analysis (Supplementary Table S1). Four specimens were excluded due to poor image quality or the small size of the lymph node, resulting in 83 standardized images with complete scoring and analysis using Threshold A for the amount of surface fluorescence and both Threshold 2 and 3 for fluorescence intensity (Figure 1A). Threshold B for the amount of surface fluorescence and Threshold 1 for fluorescence were omitted from the workflow due to poor significance and agreement. Most lymph nodes (58%; 48/83) were identified *in situ* as fluorescence positive, falling into 1+ (23%; 11/48), 2+ (10%; 5/48), 3+ (29%; 14/48), and 4+ (38%; 18/48) scoring categories. The remainder of the lymph nodes (42%; 35/83) were fluorescence negative. Image analysis was successfully performed for all lymph node images using MetaMorph for intensity and surface fluorescence (Figure 1B). Analysis of negative controls picked up 0% surface amount of fluorescence and FI of 0 AU (Supplementary Table S2).

The mean difference of agreement between Threshold A and Threshold B for surface fluorescence analysis was statistically significant ($p = <0.0001$). Threshold B, in comparison, had lower agreement values in all tested settings and types of scoring

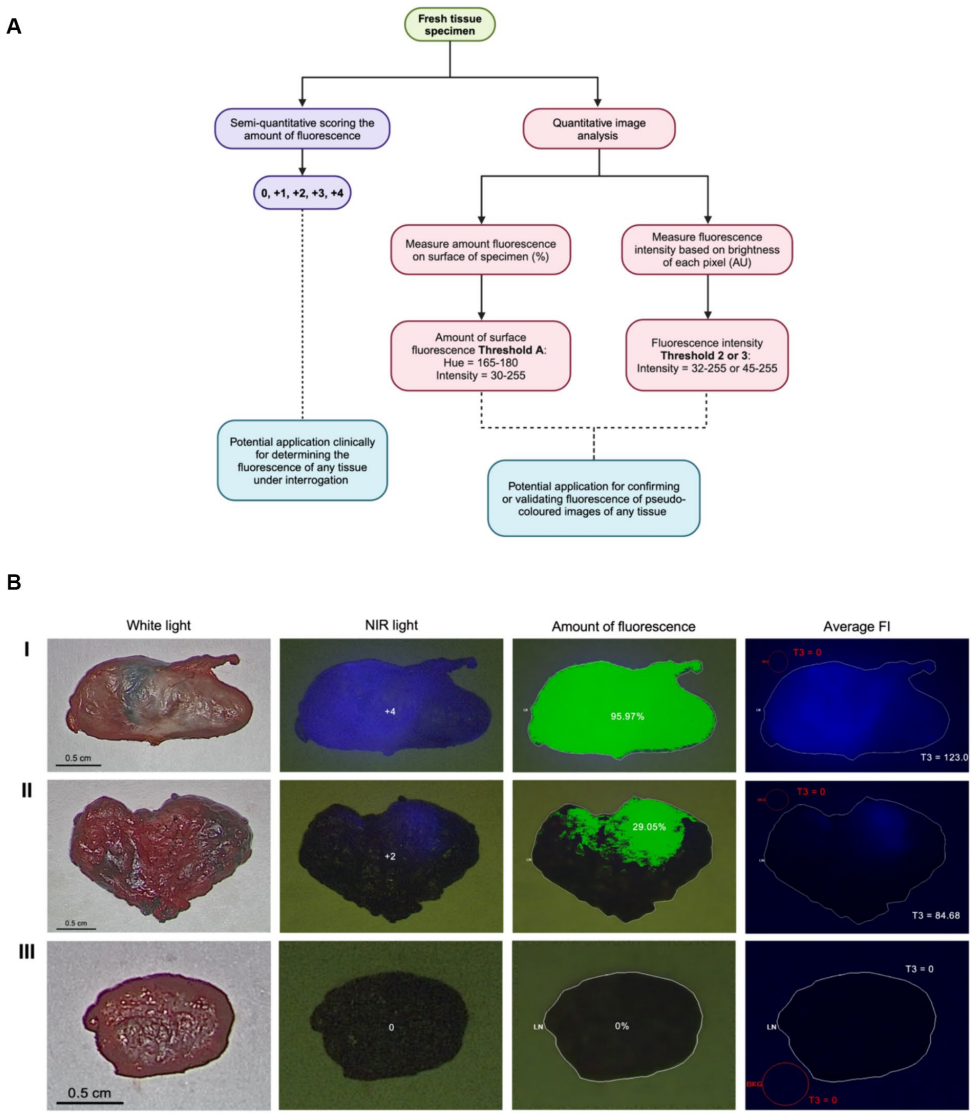

FIGURE 1
Visual assessment and image analysis workflow and outcomes. **(A)** Workflow for quantifying ICG fluorescence semi-quantitatively and through image analysis. **(B)** Imaging methods, score and analysis of highly fluorescent node (I), slightly fluorescent node (II) and true negative node (III) using Threshold A for the amount of fluorescence and Threshold 3 (T3) for FI.

(Supplementary Table S3A), resulting in the disuse of this analysis parameter to quantify the amount of fluorescence. There was an almost perfect concordance between *ex vivo* scores and fluorescence status (positive or negative) against analysis using Threshold A ($k = 0.9734$ [0.95–1], $p < 0.0001$ and $k = 0.9752$ [0.93–1], $p < 0.0001$, respectively) (Table 1). A strong intraobserver and interobserver agreement was found for visual scores designated by the two investigators ($k = 0.9732$ [0.95–1], $p < 0.0001$ and $k = 0.8900$ [0.84–0.94], $p < 0.0001$, respectively) and almost perfect agreement in assessing fluorescence status between ($k = 0.9267$ [0.85–1], $p < 0.0001$). When comparing different investigator lymph node fluorescence scores to image analysis, there was an excellent agreement for Threshold A analysis (Table 1). Lastly, there was perfect agreement between scores obtained intraoperatively and postoperatively ($k = 0.9267$ [0.88–0.97], $p < 0.000$). In addition, when Threshold A was compared against intraoperative scoring, Threshold A had excellent agreement (Table 1).

For each lymph node image, the average FI was assessed (Figure 2A). The average FI between Thresholds 1 and 2 and Thresholds 1 and 3 were significantly different ($Z = -2.79701$, $p = 0.0052$) and ($Z = -3.71327$, $p = 0.0002$), while the average FI between Thresholds 2 and 3 was not significantly different ($Z = -0.91626$, $p = 0.3595$).

Logistic regression demonstrated that the average FI values could predict the probability of negative or positive status for fluorescence from visual scoring and gold standard (fluorescence amount analysis) with significance for all intensity thresholds compared to dichotomous visual status. This resulted in all tested threshold settings being good predictors of nodal fluorescence for positive or negative status (Table 2). Specifically, for every Threshold 1 average FI gray unit increase, there was a 2.486 (CI 1.279–4.831) chance of the node being fluorescent based on visual assessment. The Threshold 1 setting produced an 87.6% sensitivity and 97.1% specificity with an intensity cut-point value of 39.95. For every Threshold 2 average FI unit increase there was 1.415 (CI 1.005–2.553) odds of the node being fluorescent. Threshold 2 modelled a sensitivity of 91.7% and specificity of 97.1% with an intensity cut-point of 44.56. For every Threshold 3 average FI unit increase there was a 1.073 (CI 1.042–1.105) chance of the node being fluorescent, therefore Threshold 3 resulted in an 89.6% sensitivity and 94.3% specificity with an intensity cut-point of 48. However, for every FI unit increase using Threshold 3, there was a 1.085 (CI 2.042–1.129) chance of the lymph node being fluorescent in the gold standard assessment (Table 3). This modeled an 89.8% sensitivity and 97.1% specificity with a cut-point of 48 (Table 4). Lastly, there was an almost perfect association between average FI values of all threshold settings and amount of fluorescence from Threshold A due to coefficients (Table 5).

4 Discussion

In this study, a semi-quantitative scoring system was developed and further validated through image analysis to measure fluorescence. The visual scoring was based on the amount of fluorescence on the surface of the lymph node. Semi-quantitative scoring was assessed against two different image analysis thresholds to compare the stringency between the analysis settings. Data demonstrated that both thresholds had concordance against scores observed *ex vivo* and subjective positive/negative fluorescence status. However, data using Threshold A had almost perfect agreement with scoring and visual status assessment compared to subpar agreement of Threshold B. This finding resulted from the cut-off point used in Threshold A where Intensity set at 30–255 allowed pixels that are a dark blue fluorescent hue to be included in the measurement. In contrast, Threshold B did not include these dull or faint fluorescent values which illustrates the limitations of this threshold and the subsequent disuse for further analyses. The semi-quantitative scoring system is adapted from immunohistochemistry (IHC) and immunofluorescence principles, which is the gold standard performed at the microscopic level for tissue and cellular staining (35, 36). Due to prominent ICG visualization on the surface of surgical specimens, IHC scoring methods can be applied to create semi-quantitative information about the visible fluorescence.

The developed ICG scoring system had substantial intra and interobserver agreement. The lack of variability between the two observers shows that this assessment system can be done by different investigators and still yield the same score for a given sample. Variability in scores between observers occurred when fluorescence was faint and a dark blue hue, which can be due to ambient light, poor perfusion or obstructed visibility by fat tissue. When visual fluorescence status was compared between observers there was also perfect concordance, illustrating that there is very low bias and variance between observers in assessing fluorescence at a visual level. This concordance verifies that the observers have a similar understanding of what is deemed positive or negative fluorescence, making identifications of false positives or negatives negligible. When comparing individual observer scores to the Threshold A settings, Threshold A strongly agreed with scores from different observers. This

TABLE 1 Agreement values and kappa coefficients comparing scoring, analysis and scoring settings.

	Percentage agreement	Weighted kappa (95% CI)	Two-sided *p*-value
Score vs. Threshold A	95.2%	0.9734 (0.95–0.1)	<0.0001
Visual fluorescence status vs. Threshold A	98.8%	0.9752 (0.93–1)	<0.0001
Intraobserver	95.2%	0.9732 (0.95–0.1)	<0.0001
Interobserver	80.7%	0.8900 (0.84–0.94)	<0.0001
Observer 1 vs. Threshold A	90.4%	0.9469 (0.91–0.98)	<0.0001
Observer 2 vs. Threshold A	73.5%	0.8508 (0.80–0.90)	<0.0001
Intraoperative vs. postoperative	87.9%	0.9254 (0.88–0.97)	<0.0001
Intraoperative vs. Threshold A	83.1%	0.8994 (0.85–0.95)	<0.0001

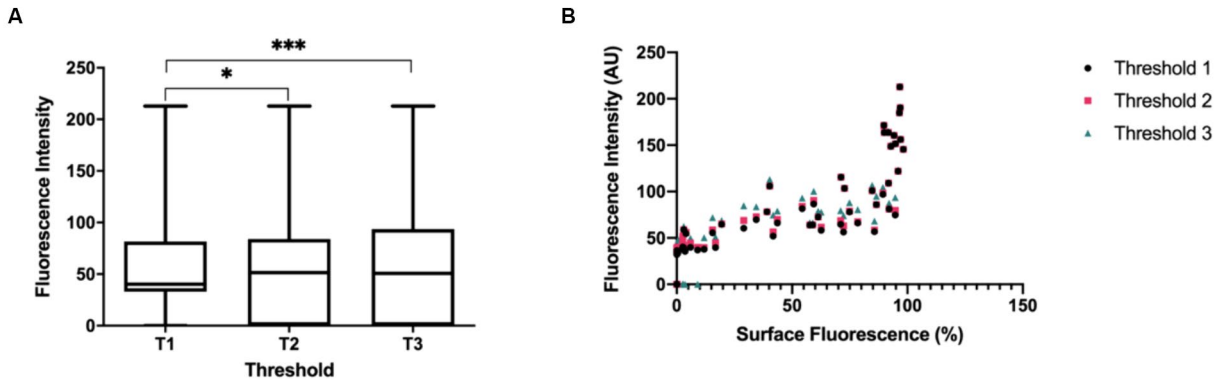

FIGURE 2
(A) Boxplots depicting the comparison of average FI (output measurement of the image analysis program) between Threshold 1 (T1), Threshold 2 (T2) and Threshold 3 (T3). Average FI between T1 ($S = 143.5$, $Mdn = 40.3$) vs. T2 ($S = 172.5$, $Mdn = 51.6$), T1 vs. T3 ($S = 182.0$, $Mdn = 50.8$), and T2 vs. T3. Asterisk denotes statistical significance. $N = 83$ **(B)** Relationship between average FI and surface fluorescence amount (Threshold A) on lymph node specimens. The boxplots and statistical tests report the medians of the output measurements collectively.

TABLE 2 Analysis of maximum likelihood and odds ratio estimates for FI predicting visual negative or positive fluorescence status.

	Maximum likelihood estimate					Odds ratio estimates	
Intensity setting	df	Estimate	*s*	Wald c^2	Pr > c^2	Point estimates	Wald 95% CI limits
Threshold 1	1	0.9106	0.3390	7.2151	0.0072	2.486	1.279–4.831
Threshold 2	1	0.4712	0.2378	3.9282	0.0475	1.602	1.005–2.553
Threshold 3	1	0.0702	0.0150	21.8892	<0.0001	1.073	1.042–1.105

s, standard deviation.

TABLE 3 Analysis of maximum likelihood and odds ratio estimates for FI predicting gold standard negative or positive fluorescence status.

	Maximum likelihood estimate					Odds ratio estimates	
Intensity setting	df	Estimate	*s*	Wald c^2	Pr > c^2	Point estimates	Wald 95% CI limits
Threshold 1	1	2.0849	1.1691	3.1802	0.0745	-	-
Threshold 2	1	1.4555	0.8698	2.8000	0.0943	-	-
Threshold 3	1	0.0813	0.0203	16.0793	<0.0001	1.085	1.042–1.129

s, standard deviation; -, not reported due insignificant *p*-value.

observation further solidifies that when the gold standard uses parameters such as Threshold A, it does not eliminate potential lymph nodes that have dull fluorescence or nodes with a small amount of fluorescence. Finally, high fidelity between intraoperative and postoperative scoring shows the reproducibility of the scoring system *in situ*. This reproducibility can be helpful for clinicians and researchers who are evaluating fluorescence in real-time, without consultation from analysis programs. When Threshold A was compared to intraoperative scoring, there was strong concordance between the intraoperative scores and Threshold A. This concordance confirms that image analysis using software strongly agrees with scoring *in situ*. This illustrates the potential usage of a semi-quantitative scoring system to assess fluorescence when imaging systems fail to quantify fluorescence.

Normally, studies that use scoring systems for clinical assessment of surgical fluorescence resort to methods that are subjective and descriptive (24, 25, 37). Terms are often based on how visible the fluorescence is, for example "moderate fluorescence," "hardly visible," or "weak contrast" (25, 38). Despite these being clinically accessible forms of assessment, there are limitations to the reproducibility and standardization of subjective scoring methods. Subjective scoring with descriptor words heavily relies on the observer's perception of the images and more than one observer is necessary to prevent observer bias and variability that could impinge on the reproducibility of the scoring system (24, 35). Even though the studies by Poellinger et al. (24) and Yokoyama et al. (25) established attempts to standardize the scoring system, they fail to justify the scores with a gold standard or quantification system, leaving room for further study (35).

The impact of threshold parameters on FI measurements was evaluated via the average FI of each lymph node image. Average fluorescence intensities between Threshold 1 vs. 2 and Threshold 1 vs. 3 produced significantly different values, demonstrating that the

TABLE 4 Classification table for predictors of fluorescence status.

Intensity setting	Sensitivity	Specificity	Cut-point
Visual fluorescence positive/negative status			
Threshold 1	87.6	97.1	39.95
Threshold 2	91.7	97.1	44.56
Threshold 3	89.6	94.3	48
Gold standard fluorescence positive/negative status			
Threshold 3	89.8	97.1	48

TABLE 5 Correlation coefficients and r-squared variance based on the association of intensity threshold settings to surface fluorescence amount analysis.

Threshold A		
Intensity setting	r^2	*p*-value
Threshold 1	0.91 (91%)	<0.0001
Threshold 2	0.89 (89%)	<0.0001
Threshold 3	0.85 (85%)	<0.0001

N = 83.

threshold settings, even a few units apart, influence the FI detected and, therefore, should be carefully chosen to minimize bias. Typically, during image analysis, users will choose thresholds based on a group of pictures and observe which threshold fits best (31). To evaluate the optimal threshold, for both intensity and amount of fluorescence, the pixel intensity histograms provided by the analysis software was used in this study to find a cumulative threshold that could be applied confidently to a batch of images (31). The overall threshold provided an estimate of the fraction of thresholding intervals to use, and which ones are statistically representative. Moreover, based on the pixel intensity histograms, three thresholds were further verified for significance through statistical tests that were then assessed for clinical research applicability.

To decide which threshold is optimal to quantify ICG fluorescence intensity, average FI values from each threshold were compared to fluorescence status based on visual observation and image analysis. Scores and the amount of fluorescence were transformed to positive (1) and negative (0) fluorescence status to fit the statistical model. Based on the results, the most practical and clinically applicable threshold parameter was Thresholds 2 and 3 where Intensity was set at 35–255 and 45–255, respectively. Threshold 1 was a significant predictor of fluorescence when tested against the visual status assessment, however it resulted in lower sensitivity and specificity compared to the other thresholds, resulting in false positives and negatives. Thresholds 1 and 2 were not found to be significant predictors of the gold standard fluorescence status test. However, this outcome is not indicative of the performance of these thresholds since the gold standard assessment is less inclusive and has higher detection of fluorescent pixels than the visual assessment. Therefore, this result does not reflect a clinician's evaluation of surgical tissue specimens. Threshold 1 possessed more inclusivity and leniency that potentially measured non-fluorescent signals such as reflections of light from the exoscope and operating environment and background non-fluorescent tissue. Conversely, Thresholds 2 and 3 are optimal settings to predict fluorescence and measure FI based on their high sensitivity and specificity in detecting fluorescent nodes. As it is more clinically relevant when FI measurements include more false positives than omit them, the higher the specificity the more useful the test (39). Additionally, the statistical test produced an intensity cut-point value for future data to gauge at which intensity level a lymph node is deemed to have significant fluorescent intensity. Threshold 2 produced an intensity cut-point of 44.56 AU, while Threshold 3 produced a cut-point of 48 AU. Due to the strictness of image analysis in determining the status of fluorescence, a statistically significant cut-point based on this, such as 48 AU, potentially disregards dull fluorescence in lymph nodes, increasing the chances of false negatives. The cut-point of 44.56 AU limits false positives while maintaining fidelity, making it the simplest and clinically applicable predictor of true ICG FI in lymph nodes. Measuring FI via image analysis software is the gold standard for fluorescence microscopy. The rationale for comparing between FI image analysis protocol to visual fluorescence assessments would be to determine what is clinically relevant to the surgeon. Intensity measurements in image-guided surgery depend on what the surgeon can see *in situ*, therefore a visual status of fluorescence is a good indicator of sensitivity on the intensity measure.

Finally, the relationship between average FI and surface amount of fluorescence was evaluated and a strong association between average FI for all threshold settings and the amount of fluorescence on the surface of the node was found (Figure 2B). This implies a monotonically increasing relationship wherein a high amount of fluorescence measured on the lymph node correlates with high intensity FI values. This signifies that both average FI and surface amount of fluorescence influence the degree of fluorescence visualization, thus either can be chosen as a reporting measure when researching or collecting data in SLN mapping. However, FI measures are recommended since this is more translatable amongst different fluorescent imaging agents and imaging systems (21).

A strength of this study was the high degree of agreement and significance found in the results that allows the sample size to be sufficient. Additionally, there was an almost equal distribution of positive and negative lymph node samples (48 positive SLNs and 35 negative SLNs). The study also contained rigorous protocols to assess fluorescence. For example, the standardized nature of *ex vivo* imaging and the rigidity of the MetaMorph program caused background signals to be void. In addition, the protocol evaluated different threshold cut points that fine-tuned the analysis process for both FI and surface amount of fluorescence. Specifically, for FI the "Blue" channel was selected because it allows the MetaMorph program to focus intensity measures in the "Blue" channel of the RGB image, disregarding "Green" and "Red" intensity signals which do not correspond to the fluorescence in the image. A limitation in this study is the use of pseudo-colored images instead of raw fluorescence images since the VITOM II ICG does not provide raw images. Using pseudo-colored images prevents the analysis program from defining the lowest possible fluorescence signal and instead separates the lowest detectable fluorescence signal within the white light photographic image. This also limits the dynamic range of the signal between 0 and 255. It is recommended in the literature to use raw fluorescence images, if possible, to promote further precision and avoid color separation using hue (40). Another limitation of this study was the lack of automation to further the objectivity of the analysis process. An automated method for creating ROIs would

be efficient and robust, however lymph nodes vary in size and shape which make it challenging to tailor specific macros for ROI creation. There are also no standardized methods for ROI selection available (21). The MetaMorph program allows for distinct ROI creation and minute ROI modifications to increase the accurate representation of the measured lymph node area. Additionally, due to standardized backgrounds and strict thresholding, ROIs adjacent to the lymph node area did not detect false background signals. Selection bias is avoided due to ROIs being a representative sample of the whole lymph node specimen (41). Another potential limitation is that residual bias may still exist in choosing thresholds, unlike an automated macro (42). Since our method is based on the SBR principle to quantify fluorescence in terms of amount and intensity, it was important to measure the background fluorescence that the threshold may detect (21). However, due to the standardized nature of our study, there was zero background fluorescence detected when the threshold was applied to every lymph node image, eliminating the need to use the SBR. This potentially decreases any human bias in threshold selection.

Our method for calculating the amount of fluorescence provides information about the amount of fluorescence on the surface of a lymph node that can be seen visually and through analysis. This information aids studies evaluating the uptake of fluorophores in tissue intraoperatively or *ex vivo*. The semi-quantitative assessment, in tandem with image analysis, allows a clinically accessible quantification system to classify lymph nodes during SLN mapping more objectively, straying away from the usual subjective terms (43, 44). Though this study uses whole specimen lymph nodes to evaluate our workflow, this can be extended as a general algorithm to apply to any whole tissue under interrogation that uses fluorescence. Additionally, the potential to implement more semi-quantitative assessments during surgery when not available through the imaging system may promote the advancement of the fluorescence-guided surgical technique to advanced stage trials, where there is a required criteria for determining positive fluorescence (43). Our study also describes a standardized method evaluating ICG FI and one that can easily be translatable to other fluorescent dyes. Currently, SPY-Q is able to quantify FI at the same scale as our method, where SPY-Q analyzes fluorescence imaging video sequences for FI in gray scale of 256 (AU) (45). Future research aims to compare our analysis method to systems, such as SPY-Q, that can quantify fluorescence. Imaging systems with quantification algorithms utilize comparable FI scales to those available in MetaMorph for lymph node images (AU of 255). This similarity implies that our system of measuring ICG fluorescence can be congruent to the quantification provided by commercially available imaging systems. More research is required to evaluate the application of our method in fluorescence-guided surgery using other systems, like VITOM II ICG, that lack built-in quantification.

5 Conclusion

In conclusion, we developed a standardized visual assessment and analytic system to quantify fluorescence by surface amount and intensity when imaging systems cannot provide this information during SLN mapping with fluorescence-guided surgeries (ICG and similar). The semi-quantitative scoring system had strong agreement with the analysis when Hue and Intesity were set at 165–180 and 30–255, respectively. In addition, Intensity set at 35–255 and 45–255 provide robust FI measures of fluorescent lymph nodes. The strong association between FI and the amount of fluorescence on a lymph node depicts the potential to use both measures interchangeably to quantify fluorescence. This assessment and analysis workflow provides the foundation for development of a system to quantify ICG visually and digitally, which may allow for standardized reporting of clinical research to improve comparability and consistency of results in SLN mapping of various cancers and tissue types utilizing ICG with different imaging systems. Future directions include the correlation of ICG distribution within lymph nodes to the localization of metastasis and morphological changes in lymph nodes as well as the impact on patient outcomes.

Data availability statement

The datasets presented in this article are not readily available because NA. Requests to access the datasets should be directed to MO, moblak@uoguelph.ca.

Ethics statement

Ethical approval was not required for the studies involving animals in accordance with the local legislation and institutional requirements because lymph nodes were collected as part of another study where approval/consent was collected or part of standard of care (negative controls). Written informed consent was not obtained from the owners for the participation of their animals in this study because this project centers around sample analysis once tissues have been excised.

Author contributions

AR: Conceptualization, Data curation, Formal analysis, Investigation, Methodology, Validation, Writing – original draft, Writing – review & editing. KM: Conceptualization, Supervision, Writing – original draft, Writing – review & editing. CM: Writing – original draft, Writing – review & editing. JP: Supervision, Writing – original draft, Writing – review & editing. MO: Conceptualization, Data curation, Supervision, Writing – original draft, Writing – review & editing.

Funding

The author(s) declare that financial support was received for the research, authorship, and/or publication of this article. This work was supported by Ontario Veterinary College (OVC) Pet Trust.

Acknowledgments

We would like to thank Gabrielle Monteith (University of Guelph) for assisting with the statistics used in this report.

Conflict of interest

The authors declare that the research was conducted in the absence of any commercial or financial relationships that could be construed as a potential conflict of interest.

Publisher's note

All claims expressed in this article are solely those of the authors and do not necessarily represent those of their affiliated organizations, or those of the publisher, the editors and the reviewers. Any product that may be evaluated in this article, or claim that may be made by its manufacturer, is not guaranteed or endorsed by the publisher.

Supplementary material

The Supplementary material for this article can be found online at: https://www.frontiersin.org/articles/10.3389/fvets.2024.1392504/full#supplementary-material

References

1. Vahrmeijer AL, Hutteman M, van der Vorst JR, van de Velde CJ, Frangioni JV. Image-guided cancer surgery using near-infrared fluorescence. *Nat Rev Clin Oncol*. (2013) 10:507–18. doi: 10.1038/nrclinonc.2013.123

2. Pogue BW. Perspective review of what is needed for molecular-specific fluorescence-guided surgery. *J Biomed Opt*. (2018) 23:1. doi: 10.1117/1.JBO.23.10.100601

3. Gao RW, Teraphongphom NT, van den Berg NS, Martin BA, Oberhelman NJ, Divi V, et al. Determination of tumor margins with surgical specimen mapping using near-infrared fluorescence. *Cancer Res*. (2018) 78:5144–54. doi: 10.1158/0008-5472.CAN-18-0878

4. Schaafsma BE, Mieog JSD, Hutteman M, van der Vorst JR, Kuppen PJK, Löwik CWGM, et al. The clinical use of indocyanine green as a near-infrared fluorescent contrast agent for image-guided oncologic surgery. *J Surg Oncol*. (2011) 104:323–32. doi: 10.1002/jso.21943

5. Alander JT, Kaartinen I, Laakso A, Pätilä T, Spillmann T, Tuchin VV, et al. A review of Indocyanine green fluorescent imaging in surgery. *Int J Biomed Imaging*. (2012) 2012:1–26. doi: 10.1155/2012/940585

6. Egloff-Juras C, Bezdetnaya L, Dolivet G, Lassalle HP. NIR fluorescence-guided tumor surgery: new strategies for the use of indocyanine green. *Int J Nanomed*. (2019) 14:7823–38. doi: 10.2147/IJN.S207486

7. Mordon S, Devoisselle JM, Soulie-Begu S, Desmettre T. Indocyanine green: physicochemical factors affecting its Fluorescencein vivo. *Microvasc Res*. (1998) 55:146–52. doi: 10.1006/mvre.1998.2068

8. Swartz MA, Lund AW. Lymphatic and interstitial flow in the tumour microenvironment: linking mechanobiology with immunity. *Nat Rev Cancer*. (2012) 12:210–9. doi: 10.1038/nrc3186

9. Papadia A, Gasparri ML, Buda A, Mueller MD. Sentinel lymph node mapping in endometrial cancer: comparison of fluorescence dye with traditional radiocolloid and blue. *J Cancer Res Clin Oncol*. (2017) 143:2039–48. doi: 10.1007/s00432-017-2501-8

10. Hirche C, Engel H, Kolios L, Cognie J, Hünerbein M, Lehnhardt M, et al. An experimental study to evaluate the Fluobeam 800 imaging system for fluorescence-guided lymphatic imaging and sentinel node biopsy. *Surg Innov*. (2013) 20:516–23. doi: 10.1177/1553350612468962

11. Marshall MV, Rasmussen JC, Tan IC, Aldrich MB, Adams KE, Wang X, et al. Near-infrared fluorescence imaging in humans with indocyanine green: a review and update. *Open Surg Oncol J*. (2010) 2:12–25. doi: 10.2174/1876504101002010012

12. Nakamura T, Kogashiwa Y, Nagafuji H, Yamauchi K, Kohno N. Validity of sentinel lymph node biopsy by ICG fluorescence for early head and neck cancer. *Anticancer Res*. (2015) 35:1669–74.

13. Pleijhuis RG, Langhout GC, Helfrich W, Themelis G, Sarantopoulos A, Crane LMA, et al. Near-infrared fluorescence (NIRF) imaging in breast-conserving surgery: assessing intraoperative techniques in tissue-simulating breast phantoms. *Eur J Surg Oncol*. (2011) 37:32–9. doi: 10.1016/j.ejso.2010.10.006

14. Townsend KL, Milovancev M, Bracha S. Feasibility of near-infrared fluorescence imaging for sentinel lymph node evaluation of the oral cavity in healthy dogs. *Am J Vet Res*. (2018) 79:995–1000. doi: 10.2460/ajvr.79.9.995

15. Starosolski Z, Bhavane R, Ghaghada KB, Vasudevan SA, Kaay A, Annapragada A. Indocyanine green fluorescence in second near-infrared (NIR-II) window. *PLoS One*. (2017) 12:e0187563. doi: 10.1371/journal.pone.0187563

16. van der Vorst JR, Schaafsma BE, Verbeek FPR, Keereweer S, Jansen JC, van der Velden LA, et al. Near-infrared fluorescence sentinel lymph node mapping of the oral cavity in head and neck cancer patients. *Oral Oncol*. (2013) 49:15–9. doi: 10.1016/j.oraloncology.2012.07.017

17. DSouza AV, Lin H, Henderson ER, Samkoe KS, Pogue BW. Review of fluorescence guided surgery systems: identification of key performance capabilities beyond indocyanine green imaging. *J Biomed Opt*. (2016) 21:080901. doi: 10.1117/1.JBO.21.8.080901

18. Newman MI, Jack MC, Samson MC. SPY-Q analysis toolkit values potentially predict mastectomy flap necrosis. *Ann Plast Surg*. (2013) 70:595–8. doi: 10.1097/SAP.0b013e3182650b4e

19. Griffiths M, Chae MP, Rozen WM. Indocyanine green-based fluorescent angiography in breast reconstruction. *Gland Surg*. (2016) 5:133–49. doi: 10.3978/j.issn.2227-684X.2016.02.01

20. Dalli J, Jindal A, Gallagher G, Epperlein JP, Hardy NP, Malallah R, et al. Evaluating clinical near-infrared surgical camera systems with a view to optimizing operator and computational signal analysis. *J Biomed Opt*. (2023) 28:35002–3. doi: 10.1117/1.JBO.28.3.035002

21. Hoogstins C, Burggraaf JJ, Koller M, Handgraaf H, Boogerd L, van Dam G, et al. Setting standards for reporting and quantification in fluorescence-guided surgery. *Mol Imaging Biol*. (2018) 21:11–8. doi: 10.1007/s11307-018-1220-0

22. Snoeks TJA, van Driel PBAA, Keereweer S, Aime S, Brindle KM, van Dam GM, et al. Towards a successful clinical implementation of fluorescence-guided surgery. *Mol Imaging Biol*. (2014) 16:147–51. doi: 10.1007/s11307-013-0707-y

23. Rosenthal EL, Warram JM, de Boer E, Basilion JP, Biel MA, Bogyo M, et al. Successful translation of fluorescence navigation during oncologic surgery: a consensus report. *J Nucl Med*. (2016) 57:144–50. doi: 10.2967/jnumed.115.158915

24. Poellinger A, Burock S, Grosenick D, Hagen A, Lüdemann L, Diekmann F, et al. Breast Cancer: early- and late-fluorescence near-infrared imaging with Indocyanine green—a preliminary study. *Radiology*. (2011) 258:409–16. doi: 10.1148/radiol.10100258

25. Yokoyama J, Fujimaki M, Ohba S, Anzai T, Yoshii R, Ito S, et al. A feasibility study of NIR fluorescent image-guided surgery in head and neck cancer based on the assessment of optimum surgical time as revealed through dynamic imaging. *Onco Targets Ther*. (2013) 6:325–30. doi: 10.2147/OTT.S42006

26. Manny TB, Krane LS, Hemal AK. Indocyanine green cannot predict malignancy in partial nephrectomy: histopathologic correlation with fluorescence pattern in 100 patients. *J Endourol*. (2013) 27:918–21. doi: 10.1089/end.2012.0756

27. Payton S. Small renal masses: indocyanine green cannot predict malignancy. *Nat Rev Urol*. (2013) 10:250. doi: 10.1038/nrurol.2013.51

28. Veys I, Pop CF, Barbieux R, Moreau M, Noterman D, de Neubourg F, et al. ICG fluorescence imaging as a new tool for optimization of pathological evaluation in breast cancer tumors after neoadjuvant chemotherapy. *PLoS One*. (2018) 13:e0197857. doi: 10.1371/journal.pone.0197857

29. Hirashima T, Adachi T. Procedures for the quantification of whole-tissue immunofluorescence images obtained at single-cell resolution during murine tubular organ development. *PLoS One*. (2015) 10:e0135343. doi: 10.1371/journal.pone.0135343

30. Ljosa V, Carpenter AE. Introduction to the quantitative analysis of two-dimensional fluorescence microscopy images for cell-based screening. *PLoS Comput Biol*. (2009) 5:e1000603. doi: 10.1371/journal.pcbi.1000603

31. Johnson SJ, Walker FR. Strategies to improve quantitative assessment of immunohistochemical and immunofluorescent labelling. *Sci Rep*. (2015) 5:1–4. doi: 10.1038/srep10607

32. Lee J-Y, Kitaoka M. A beginner's guide to rigor and reproducibility in fluorescence imaging experiments. *Mol Biol Cell*. (2018) 29:1519–25. doi: 10.1091/mbc.E17-05-0276

33. Tummers WS, Warram JM, van den Berg NS, Miller SE, Swijnenburg RJ, Vahrmeijer AL, et al. Recommendations for reporting on emerging optical imaging agents to promote clinical approval. *Theranostics*. (2018) 8:5336–47. doi: 10.7150/thno.27384

34. Cohen J. Weighted kappa: nominal scale agreement provision for scaled disagreement or partial credit. *Psychol Bull*. (1968) 70:213–20. doi: 10.1037/h0026256

35. Meyerholz DK, Beck AP. Principles and approaches for reproducible scoring of tissue stains in research. *Lab Investig*. (2018) 98:844–55. doi: 10.1038/s41374-018-0057-0

36. Gibson-Corley KN, Olivier AK, Meyerholz DK. Principles for valid histopathologic scoring in research. *Vet Pathol*. (2013) 50:1007–15. doi: 10.1177/0300985813485099

37. Hachey KJ, Gilmore DM, Armstrong KW, Harris SE, Hornick JL, Colson YL, et al. Safety and feasibility of near-infrared image-guided lymphatic mapping of regional

lymph nodes in esophageal cancer. *J Thorac Cardiovasc Surg*. (2016) 152:546–54. doi: 10.1016/j.jtcvs.2016.04.025

38. Rosenthal EL, Warram JM, Bland KI, Zinn KR. The status of contemporary image-guided modalities in oncologic surgery. *Ann Surg*. (2015) 261:46–55. doi: 10.1097/SLA.0000000000000622

39. Trevethan R. Sensitivity, specificity, and predictive values: foundations, Pliabilities, and pitfalls in research and practice. *Front Public Health*. (2017) 5:307. doi: 10.3389/fpubh.2017.00307

40. Waters JC. Accuracy and precision in quantitative fluorescence microscopy. *J Cell Biol*. (2009) 185:1135–48. doi: 10.1083/jcb.200903097

41. Jensen EC. Quantitative analysis of histological staining and fluorescence using ImageJ. *Anat Rec*. (2013) 296:378–81. doi: 10.1002/ar.22641

42. Guirado R, Carceller H, Castillo-Gómez E, Castrén E, Nacher J. Automated analysis of images for molecular quantification in immunohistochemistry. *Heliyon*. (2018) 4:e00669. doi: 10.1016/j.heliyon.2018.e00669

43. Warram JM, de Boer E, van Dam GM, Moore LS, Bevans SL, Walsh EM, et al. Fluorescence imaging to localize head and neck squamous cell carcinoma for enhanced pathological assessment. *J Pathol Clin Res*. (2016) 2:104–12. doi: 10.1002/cjp2.40

44. van Dam G, Themelis G, Crane LM, Harlaar NJ, Pleijhuis RG, Kelder W, et al. Intraoperative tumor-specific fluorescence imaging in ovarian cancer by folate receptor-α targeting: first in-human results. *Nat Med*. (2011) 17:1315–9. doi: 10.1038/nm.2472

45. Rother U, Gerken ALH, Karampinis I, Klumpp M, Regus S, Meyer A, et al. Dosing of indocyanine green for intraoperative laser fluorescence angiography in kidney transplantation. *Microcirculation*. (2017) 24:12392. doi: 10.1111/micc.12392

Frontiers in Veterinary Science

Transforms how we investigate and improve animal health

The third most-cited veterinary science journal, bridging animal and human health with a comparative approach to medical challenges. It explores innovative biotechnology and therapy for improved health outcomes.

Discover the latest Research Topics

See more →

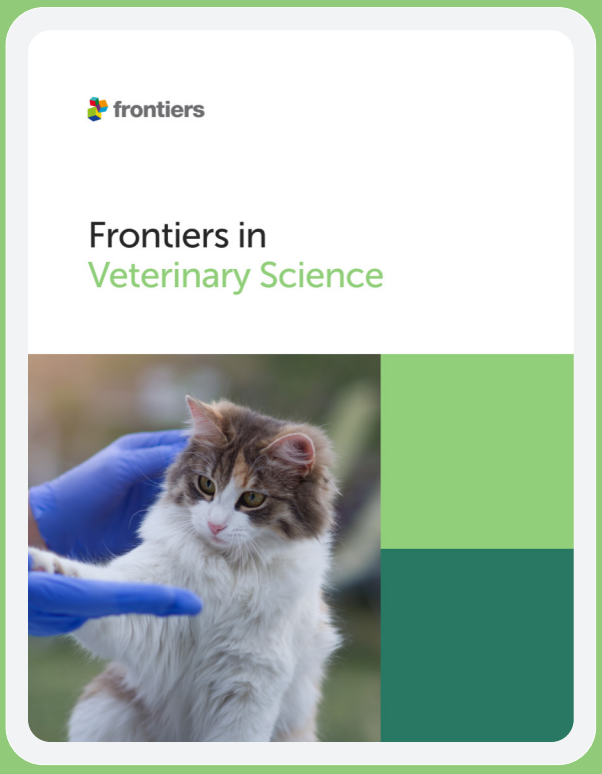

Frontiers

Avenue du Tribunal-Fédéral 34
1005 Lausanne, Switzerland
frontiersin.org

Contact us

+41 (0)21 510 17 00
frontiersin.org/about/contact